Analysis of Liquid-Repellent Surfaces within Heat Exchanger Environments

By

Navdeep Sangeet Singh

A thesis submitted to the University of Birmingham for the degree of DOCTOR OF PHILOSOPHY

School of Engineering
College of Engineering and Physical Sciences
Department of Mechanical Engineering
University of Birmingham
August 2024

Abstract

Steam condensation is omnipresent, and inevitable in many industrial processes. A classic example is seen within condensers that are used to liquify various gasses. In consequence, water-vapor is eventually deposited upon the exterior of heat pipes that passively cool the gas to form a thin film of liquid. This macroscopic film is responsible for the degradation of heat transfer efficiencies at the tubes' solid-vapour interface. Liquid repellent surfaces can microscopically manipulate the hydrodynamics of formulating condensate to transition toward dropwise/jumping-droplet condensation. This effect will save operating and maintenance costs of steam condensers within power-plants, subsequently reducing emissions, operating power, and fuel consumption. The same can be said for an absorber-type (or evaporator) heat exchanger where a hot binary liquid falls over multiple horizontal subcooled heat pipes to be diluted with condensed water-vapour. Conversely, however, in this case, a liquid-adhesive surface is favourable as the expansion of the liquids' surface area increases the rate of dilution and heat transfer rate whilst maintaining a small liquid film thickness. Nonetheless, within the literature, there has been little numerical insight that can adequately demonstrate how surface wettability can alter the flow behaviour of such heat exchanger tubes. Not to mention the effects of droplet impaction which can severely impact the heat transfer rate and flow behaviour. Therefore, for this thesis, various multiphase flow/phase-change simulations are presented for condenser/absorber applications.

Firstly, a two-dimensional numerical simulation of condensation of water upon a heat pipe is presented. By compiling numerous numerical strategies within the literature, the hydro/thermodynamics of the condensate is validated against the Nusselt film theory and experimental data. The tubes' intrinsic contact angle is then altered to signify the how the

flow behaviour is manipulated and its' thermal implications. Then, the contact angle hysteresis of the tube is altered at various intrinsic contact angles to establish its consequence on the tubes' heat transfer rate.

Using this as a foundation, the simulations' domain is then extended to the 3rd dimension where additional horizontal heat pipes are allocated to establish falling-film flow of subcooled water. Again, the results were calibrated through systematic and experimental means within literature. Through meticulously refining the mesh within the vicinity of the falling liquid, a phenomenon known as the Rayleigh-Plateau instability of the liquid jet was depicted which radically altered the flow behaviour and heat transfer coefficients upon the tubes below at various contact angles. This was due to the emergence of additional impacting satellite droplets from the liquid jet which induced film waviness and mixing.

As droplet impaction was found to be the predominant factor for adjusting the heat transfer efficiencies of heat pipes, the effects of impacting droplets on functional surfaces were analysed through numerically accessing the droplet-repellency performance of microscopic doubly-re-entrant pillars. The performance of these pillars were compared to single re-entrant pillars and straight pillars to illustrate the importance of adjusting the overhang angle of the pillars against liquid-repellency. Furthermore, the key dimensions of the doubly re-entrant pillars are adjusted to again demonstrate their significance on droplet repellence. These results give further perception on how to design real-world functional surfaces by revealing which particular surface wettability parameters is able to provide the most dominance to enhance the performance of heat exchanger tubes further.

Acknowledgements

I would very much like to thank my lead supervisor, Dr Nan Gao for being very supportive and patient throughout my Ph.D. studies especially during the COVID-19 pandemic. He has provided me with a considerable amount of experience to immensely improve my writing and research skills which has led me to be publish several journal papers. Additionally, I would like to acknowledge Dr Jason Stafford, my secondary supervisor whom I've conversed with numerous amounts of times to assist me in my numerical simulations and endorse my theoretical approaches to them. Moreover, I want to express my gratitude to the Ph.D. students in my research group who have aided me throughout my Ph.D. – Jitao Zhang who supported in writing my review paper during the lockdown period – Thanaphun Jitniyom who assisted me in conducting experimental work in order to validate my numerical work which led me to a publication.

I am also grateful to the School of Engineering at the University of Birmingham who provided me with a scholarship to fund my Ph.D. programme. Notably, the computations performed in this Thesis would not have been made possible without the University of Birminghams' high-performance computing (HPC) service known as BlueBEAR. Therefore, I would like to show my appreciation to the Advanced Research Computing staff who provide consistent updates and maintenance to the BlueBEAR supercomputer. Finally and most importantly, I would like to express my love to my family especially my mother (Gurmit) who I'm very lucky to have. Her continual nurturing and encouragement throughout my life is what led me here today to obtain my doctorate.

Publication Work Implemented within the Thesis

1. N.S. Singh, J. Zhang, J. Stafford, C. Anthony, N. Gao, Implementing superhydrophobic surfaces within various condensation environments: a review, Advanced Materials Interfaces 8 (2021) 2001442.
2. N.S. Singh, J. Stafford, N. Gao, Dropwise and liquid-jet laminar flow of subcooled water falling over horizontal tube banks, International Journal of Heat and Mass Transfer 206 (2023) 123936.
3. N.S. Singh, T. Jitniyom, M. Navarro-Cía, and N. Gao, Droplet impact on doubly re-entrant structures. Scientific Reports 14 (2024) 2700.
4. N.S. Singh, J. Stafford, N. Gao, Dropwise and filmwise condensation of water on liquid-repellent heat pipes under laminar flow (2025) [In process of being published to International Journal of Multiphase Flow].

List of Figures

Figure 2.1. Schematic diagram of a sessile droplet placed on a solid substrate where three governing surface tension vectors act at the droplets' three-phase contact line. The equilibrium contact angle (θ_Y) characterises the surface wettability.[13] 15

Figure 2.2. Diagram showing (a) Cassie-Baxter state and (b) Wenzel state, illustrating the effects of adverse and favourable pressure gradients within textured surfaces. 17

Figure 2.3. Condensation of toluene over a lubricant-infused surface (LIS) of a heat pipe. (a) shows dropwise condensation at the beginning of condensation which then transition to filmwise condensation after 60 min. (b) depicts the decrease in heat transfer coefficient overtime which is responsible for the transition in condensation regimes observed in (a).[37] 20

Figure 2.4. Jumping-droplet condensation occurring upon a ballistospore mushrooms' spore due to the nucleation of the Buller's drop and the adaxial drop which then coalesce to propel the spore away from the sterigma.[50] 23

Figure 2.5. (a) Results of average droplet diameter with (b) showing the surface coverage for the hydrophobic and superhydrophobic surface against time.[47] 25

Figure 2.6. Coalescence of two unequally sized droplet which then shows an oscillation in the merged droplets' centre of mass in 0.2 ms (contour of the droplet is perturbated) and then being driven away laterally from a superhydrophobic surface.[47] 25

Figure 2.7. (a) SEM image of constructed carbon nanotubes coated with a P2i fluoropolymer coating method (plasma enhanced vapor deposition) to establish their superhydrophobicity. (b) AFM image of carbon nanotubes. (c) Illustrates a droplet in a receding state on the superhydrophobic surface having an apparent contact angle of 166°

± 2°. (d) Environmental scanning electron microscope (ESEM) image of nucleating droplets with a surface inclination angle of 8°. (e) Advancing contact angle of condensing droplets visually measured from ESEM images having different diameters. The dashed line represents the average advancing contact angle of the surface equal to 170.2° ± 2.4°.[57] 28

Figure 2.8. (a) Axisymmetric view of the simulated binary droplet coalescence showing an initial radius *R*, with having a capillary bridge radius $r_b(t)$ as a function of time. $w(t)$ is given as the capillary bridge width, also as a function of time. (b-f) demonstrates the velocity flow field contours during coalescence, where the red the colours indicate the radial velocity component with the blue colours showing velocity flow away from the z-axis.[57] 29

Figure 2.9. (a-b) shows the jumping-droplet velocity against droplet diameter with (c) illustrating the dimensionless jumping-droplet velocity against Ohnesorges number. The jumping velocity results shown in (a) is determined at a wall temperature of 5 °C where (b) is assessed at a wall temperature of 26 °C. The open circles displayed in (a) is the experimental results from the P2i-CNT surface and the open triangles is the experimental results from Boreyko et al.[38] In (b), the squares represent the performance of the P2i-CNT surface whilst the diamonds shows the data for the P2i-CuO surface. For (a-c) the black circles indicates the numerical results. The dashed lines reveal the numerical projection of the momentums' range for the jumping droplets.[57] 31

Figure 2.10. Coalescence-induced jumping droplet on a wooden microgroove. (a-b) shows jumping droplet process of a low surface tension liquid (n-tetradecane) compared against numerical results. (c-d) jumping droplet process for a highly viscous fluid (water-glycol) also compared against numerical results.[65] 32

Figure 2.11. Field emission scanning electron microscopy (FESEM) images of CuO nanoneedles, (a) Topside view of CuO nanoneedles without silane. (b) Horizontal view of nanoneedles also without silane. (c) Topside view of nanoneedles at a larger magnification, illustrating cavities spacings between them. (d) Silane deposited nanoneedles at greater magnification showing an increase in the nanoneedles' thickness (≈10 nm).[35] 34

Figure 2.12. (a) Consistent jumping droplet condensation for a low supersaturation ratio (1.08) at a constant vapour pressure of 2700 ± 68 Pa. (b) Flooded condensation at high supersaturation ratios (1.54) where droplets are in a Wenzel state as nanoneedles are flooded.[35] 36

Figure 2.13. (a) Schematic diagram showing how the highly dense nanowires can minimise condensation upon the surface by establishing a low vapour density from the interstices. (b) Illustrates the procedure of droplet nucleation and removal within the microcavities. (c) SEM image of the two-tier nanowire surface with equally spaced microcavities. (d) Contact angle of the superhydrophobic surface for a 5 µL water droplet.[73] 37

Figure 2.14. Longstanding jumping-droplet condensation achieved on the 3D copper nanowire surface. From the densely packed nanowire array, any microdefects in the nanowire array are eradicated. As the nanowire array allowed greater spatial nucleation control, the heat flux is improved by 100% in comparison to a standard hydrophobic surface.[77] 39

Figure 2.15. Heat transfer performance of a 20-µm porous superhydrophobic surface with nanoscale dendrites benchmarked against a plain and hydrophobic surface. a) heat transfer

coefficient with b) being the heat flux against subcooling temperature up to a range of ~ 34 K.[78] 41

Figure 2.16. Heat transfer coefficient of an absorber tube against the fluids' Reynolds number for a superhydrophilic, hydrophilic and plain tube. The blue line consist of the experimental results conducted by Fujita *et al*. where their results were compared against.[93] 45

Figure 2.17. Falling-film flow behaviour at different Reynolds numbers on a plain copper tube (a), and a micro-porous tube (b) ξ represents the solution wetting ratio of the tube. The numbers shown at the sides of the images represent the number of droplet nucleation sites observed below each tube.[94] 46

Figure 2.18. Direct comparison of simulation results against experimental results by Killion *et al*.[99] for the droplet detachment process from the first tube.[98] 48

Figure 2.19. Motion of droplet spreading whilst impacting upon the second tube, showing the hydrostatic pressure of the liquid at the interface.[98] 49

Figure 2.20. Heat flux performance against the subcooling temperature of the superhydrophobic surface determined over 6 days using a vapour velocity of 12 m/s at 110°C. Heat flux was found to decrease on the 6th day due to surface degradation.[45] . 50

Figure 2.21. Procedure of droplet ejection from within the microcones to coalescence. a) (i) Nucleating droplets are initially retained on the surface, (ii, iii) droplets begin to merge with neighbouring droplets of different size allowing smaller droplets to be swept off, (iv) droplet discharge cycle is replicated seen from the nucleation of new droplets (shown in N1, N2 and N3). b) Laplace pressure gradient of droplets within the microcavities against the normalized height of the microcones at the upper meniscus of the droplet. c) Schematic

diagram of stages of droplet propulsion within the microcones, Ω_{cr} is given as the critical radius. d) Laplace pressure of a nucleating droplet against the normalized height of the microcone at the bottom section of the meniscus.[101] 52

Figure 2.22. Heat transfer coefficients for a hydrophilic (plain), hydrophobic and superhydrophobic surface at different concentrations of noncondensable gas against various subcooling temperatures. a) 1.5%, b) 6.8%, c) 13.7% and d) 27.8%.[78] 55

Figure 2.23. Conduct of condensation on the superhydrophobic and hydrophobic surface at several noncondensable gas concentrations with different subcooling temperatures. On the superhydrophobic surface, jumping-droplet condensation begins to shift towards dropwise condensation at elevated subcooling temperatures and noncondensable gas concentrations.[78] 56

Figure 2.24. Schematic diagram of the transmission of water vapour molecules towards a condensate drop during condensation upon a surface. a) Without the presence of NCG and b) with NCG particulates which inhibits the movement of vapour molecules towards the subcooled surface.[112] 58

Figure 2.25. a) Schematic showing droplet nucleation whilst being cloaked in oil as water vapour penetrates through the oil, b) Interface of the micropillar illustrating favourable droplet growth upon the high surface energy sites, c,d) AFM (Atomic force microscopy) images of TFTS ((tridecafluoro-1,1,2,2-tetrahydrooctyl)-1-trichlorosilane) silane coating indicating its height and phase angle, having a bigger phase angle creates larger surface energy, e,f) ESEM images of micropillars covered with TFTS before and after oil infusion, g,h) contact angle hysteresis of liquid-infused surface with and without oil infusion, i,j) top side optical microscope images of micropillars before and after oil infusion, k)

calculated nucleation rates of droplets against surface contact angle for different surface tension of oils.[114] 59

Figure 2.26. Long aspect ratio nanowires. a) SEM image of copper nanowires from a cross-sectional side view. b) SEM image of the top view of the nanowires with also showing the contact angle of the surface. c) Diagram of the concept design of the nanowires showing a high density of vapour molecules at the interface of the nanowires with a much lower density being resided at the bottom of the nanowires.[119] 61

Figure 2.27. Nanostructures deposited upon the flat copper surface in comparison to an untreated surface. a) Bare copper. b) Small deposition rate of copper nanostructures. c) Large deposition rate of nanostructures on surface. d) SEM image of small deposited rate. e) SEM image of large deposited rate.[120] 62

Figure 2.28. Tube preparation of hydrophobic and superhydrophobic surface with their outlined surface morphologies. a) Process of depositing dendritic nanostructures with then applying the organic polymer upon the surface. b) SEM image and surface wettability of the plain copper tube with, c) for the hydrophobic tube and, d) being the superhydrophobic tube.[78] 63

Figure 2.29. a) Diagram of hierarchical beetle-like surface, containing SiO2 micropillars with nanograss surrounding the pillars. The micropillars' interface are hydrophilic (indicated by the dark red areas), which serves as nucleation sites and increased droplet growth rates. The nanograss regions are coated with fluorosilane (shown on the green regions), to establish superhydrophobicity to facilitate regulated dropwise condensation. The right inset illustrates a droplet being in a Cassie-Baxter state when nucleated on the nanograss and a partial wetting state when grown on the micropillars. b) SEM image of

the fabricated hierarchical micro/nanostructure. Scale bar represents 10 μm. Inset demonstrates the static contact angle of the surface which is 161°.[123] 65

Figure 2.30. Condensation behaviour on a perfectly wetted two-dimensional tube for a subcooling temperature of 50 K. γ here represents the volume fraction of the liquid phase.[126] 70

Figure 2.31. Dropwise condensation within (a) tapered pyramidal micropillars with a half-opening angle of 20° and (b) straight pillars.[128] 72

Figure 2.32. Condensation on square micropillars with different advancing contact angles treated at the walls between 50.8° to 164.5° (a-f). t^* represents the dimensionless time.[131] 74

Figure 2.33. Numerical flow performance of water falling upon a porous tube (a), and a plain tube (b). ε represents the porosity of the porous surface.[133] 76

Figure 2.34. Liquid-contour images of ethylene-glycol/water falling over a horizontal tube at various contact angles. Here, δ is equal to the film thickness.[134] 77

Figure 2.35. Contour image of a droplet that is twice the size of the square tubes impacting at the centre of the tubes' pitch.[137] 79

Figure 2.36. Isometric and planar view of the droplet impact behaviour on cylindrical tubes at numerous contact angles.[138] 81

Figure 2.37. Variation in the liquids' dimensionless contact area (S^*), heat transfer rate (Q) and heat transfer coefficient (h) against contact time (t) for three consecutive droplets impacting the heated tube.[143] 83

Figure 3.1. Computational fluid domain with prescribed boundary conditions and mesh refinement. 110

Figure 3.2. Film thickness validation against Nusselt solution for water with a subcooling temperature of 50 K and imposing $\theta_Y = 0°$. 121

Figure 3.3. Circumferential temperature profiles at (a) 45° and (b) 90° validated against the Nusselt solution at a subcooling temperature of 50 K. 122

Figure 3.4. Simulated heat transfer coefficient against various subcooling temperatures calibrated with Nusselt theory. 123

Figure 3.5. Average heat transfer coefficient and heat flux against time at a subcooling temperature of 50 K validated against Nusselt result. 124

Figure 3.6. Simulated heat transfer coefficient against subcooling temperatures compared against experimental results by Zhang et al. on their original hydrophilic tube ($\theta_Y = 53°$ $\Delta\theta = 28º$).[9] 126

Figure 3.7. Contour image of condensate behaviour for different contact angles a) $\theta_Y = 30°$, b) $\theta_Y = 90°$, c) $\theta_Y = 150°$ and given subcooling temperatures shown at a timeframe of 0.3 s. 129

Figure 3.8. Velocity vectors of condensate behaviour for $\theta_Y = 150°$ at a subcooling temperature of 10 K illustrating the occurrence of jumping-droplet condensation on the tube surface. 130

Figure 3.9. Quarter cross-sectional contour plots of condensate tube illustrating dropwise and filmwise condensation at various contact angles for a subcooling temperature of 10 K given at different timeframes a) 10 ms b) 20 ms c) 30 ms d) 40 ms e) 50 ms f) 60 ms. 132

Figure 3.10. Quarter cross-sectional contour plots of dropwise and filmwise condensation for a superhydrophobic tube (θ_Y = 150°) at various subcooling temperatures demonstrated at different timeframes, a) 10 ms b) 20 ms c) 30 ms d) 40 ms e) 50 ms f) 60 ms. 133

Figure 3.11. Heat transfer coefficient against time at a subcooling temperature of 5 K against various contact angles. 135

Figure 3.12. a) Heat transfer coefficient and b) heat flux of the tube against subcooling temperatures at different contact angles, θ_Y = 0°, θ_Y = 30°, θ_Y = 90°, θ_Y = 150°. 136

Figure 3.13. Contour images of condensate performance by increasing the contact angle hysteresis from 0° to 20° at different equilibrium contact angles at a timeframe of 0.3 s at a subcooling temperature of 10 K. 139

Figure 3.14. Quarter cross-sectional contour plots of condensation behaviour at contact angles a) θ_Y = 90° and b) θ_Y = 150° for numerous contact angle hysteresis and time periods, i) 10 ms, ii) 20 ms, iii) 30 ms at a subcooling temperature of 10 K. 140

Figure 3.15. Heat transfer coefficient against time for several equilibrium contact angles and contact angle hysteresis a) θ_Y = 30°, b) θ_Y = 90°, c) θ_Y = 150° at a given subcooling temperature of 10 K. 142

Figure 4.1. (a-b) Computational fluid domain with defined boundary conditions. 162

Figure 4.2. (a) Mesh refinement near the tube walls with additional inflation layers added at tube wall interface to capture the liquids' film thickness and hydro/thermodynamic flow displayed on the front plane of the second tube. (b) Planar view of mesh topology at the middle section between the first and second tube without mesh refinement (0.25 mm), (c) with mesh refinement (0.1 mm). 163

Figure 4.3. Evolution of droplet formation and Rayleigh-Plateau instability along the liquid bridge that is established during droplet detachment from the first tube. Compared against Killion *et al*. experimental results.[8] 167

Figure 4.4. Film thickness predictions against Nusselt's model. Results are extrapolated from the first tube at the mid-plane (L = 11 mm) when t = 2 s..... 169

Figure 4.5. Circumferential velocity profile calibration around the first tube at different circumferential angles when L = 7.3 mm at t = 2 s..... 170

Figure 4.6. Local heat transfer coefficient within the liquid film across the circumferential direction at a tube length of 11 mm when t = 2 s at the first tube compared against the heat transfer model by Rogers *et al.*[27]..... 172

Figure 4.7. Dimensionless circumferential temperature profiles within the liquid film for different circumferential angles when L = 11 mm at t = 2 s. 173

Figure 4.8. Pressure contours showing capillary ripples generated from the satellite droplets and at different times after first droplet impaction upon the second tube..... 175

Figure 4.9. Velocity contours from initial droplet impaction to Rayleigh-Plateau instability jet break-up at different timescales upon the second tube. 177

Figure 4.10. Velocity vector plot of the liquid film impacting the middle of the second tube (from 30 to 50 ms) in the axial (a-c) and circumferential direction (d-f). 179

Figure 4.11. a) Jet instability behaviour with and without mesh refinement on the second tube just after satellite droplet impaction. b) Axial heat transfer coefficient within the liquid film where Z = 0 mm is taken from the centre of droplet impaction..... 180

Figure 4.12. Velocity contours of first droplet impaction onto second tube following on to Rayleigh-Plateau instability. 182

Figure 4.13. Axial velocity and pressure fluctuations within the central region of the unstable jet over time. 183

Figure 4.14. Contour plots of the flow behaviour around the first tube at multiple contact angles. 187

Figure 4.15. Hydrodynamic flow of liquid falling over the configurated pipes at different static contact angle states namely (a) 0°, (b) 30°, (c) 60°, (d) 90°, (e) 120° and (f) 150°. 188

Figure 4.16. Velocity vector plot of the fluid exiting the inlet in the circumferential direction at different contact angles when t = 0.08 s. (a) 0° (b) 30° (c) 60° (d) 90° (e) 120° (f) 150°. 190

Figure 5.1. Fluid domain design with prescribed boundary and initial conditions: (a) side view and (b) iso view. (c) Key dimensions for doubly re-entrant pillars. (d) SEM image of the fabricated doubly re-entrant pillars, with D=100 µm, H=100 µm, S=200 µm, t_o=10 µm and δ=10 µm. (e) Cross-sectional image of the doubly re-entrant pillar. (f) Schematic illustration of the droplet impact process, where P_d is the total droplet impact pressure (Pa), F_c and P_c are the capillary force (N) and pressure (Pa) (see Appendix B, Chapter 5 for more details), P_{air} is the air pressure within the air-layer (Pa), λ_{max} and $\lambda_{wetting}$ are the maximum spreading diameter and wetting diameter of the droplet (m). 205

Figure 5.2. Comparison between numerical and experimental results of droplet impact at different time periods on doubly re-entrant pillars for the pitch size of 150 µm: (a) Pillars made of bare photoresin: V = 0.32 m/s, λ_c = 1.1 mm, We = 1.6; (b) pillars made of

photoresin coated with Trichloro (1H,1H, 2H, 2H-perfluorooctyl) silane: V = 0.33 m/s, λ_c = 1 mm, We = 1.5. 208

Figure 5.3. Comparison between numerical and experimental results of droplet impact on doubly re-entrant pillars at different time periods for the pitch size of 200 µm: (a) Pillars made of bare photoresin: V = 0.33 m/s, λ_c = 1.1 mm, We = 1.7; (b) Pillars made of photoresin coated with Trichloro (1H,1H, 2H, 2H-perfluorooctyl) silane: V = 0.34 m/s, λ_c = 0.8 mm, We = 1.3 209

Figure 5.4. Comparison between numerical and experimental results of droplet impact on doubly re-entrant pillars at different time periods for the pitch size of 250 µm: (a) Pillars made of bare photoresin, V = 0.31 m/s, λ_c = 1.2 mm, We = 1.6; (b) Pillars made of photoresin coated with Trichloro (1H,1H, 2H, 2H-perfluorooctyl) silane, V = 0.32 m/s, λ_c = 1.1 mm, We = 1.6. 210

Figure 5.5. Numerical and experimental results of $\lambda_{wetting}/\lambda_c$ against contact time for different doubly re-entrant pitch sizes and intrinsic contact angles. a) S = 150 µm, θ_Y = 70°; b) S = 200 µm, θ_Y = 70°; c) S = 250 µm, θ_Y = 70°; d) S = 150 µm, θ_Y = 120°; e) S = 200 µm, θ_Y = 120°; f) S = 250 µm, θ_Y = 120°. 213

Figure 5.6. (a) Droplet impact behaviour at different timesteps on re-entrant and straight pillars having an intrinsic contact angle of θ_Y = 70°. Interfacial pressure profiles within the cavities during droplet impact for straight pillars (b) and re-entrant pillars (c), V = 0.3 m/s, λ_c = 1 mm, We = 1.25. 215

Figure 5.7. Droplet impact behaviours for various doubly re-entrant pillars with an intrinsic contact angle of θ_Y = 105° at (a) 2ms, (b) 4 ms, (c) 6 ms, (d) 8 ms and (e) 10 ms, V = 0.3 m/s, λ_c = 1 mm, We = 1.25. 217

Figure 5.8. (a) Interfacial pressure profiles for each of the configured cases that are not flooded, (b) air pressure contours just after the moment of impact compared between the heights of 50 µm and 100 µm. 218

Figure 5.9. Velocity contours of droplet impacting doubly-re-entrant pillars at different time periods with different overhang lengths. (a) δ = 5 µm, (b) δ = 10 µm, (c) δ = 15 µm. 220

Figure 5.10. Pressure contours of impacting droplets on doubly re-entrant pillars at multiple time steps for various overhang thicknesses: (a) t_o = 5 µm, (b) t_o = 10 µm, (c) t_o = 15 µm. 222

Figure 5.11. $\lambda_{wetting}/\lambda_c$ against contact time for each of the dimensional parameters varied: a) the pitch spacing (S); b) pillar height (H); c) pillar diameter (D); d) length of the vertical overhang (δ); and e) the thickness of the vertical overhang (t_o). θ_Y = 105°. (f) dimensionless contact time (τ^*) against pitch spacing (S) chart highlighting the time taken for the droplet to spread ($\tau_{spreading}$) and recede ($\tau_{receding}$) on each of the configured surfaces..... 225

Figure A.1. General flow behaviour of fluid falling over parallel tubes for several contact angle conditions and time scales. (a) 0° (b) 30° (c) 60° (d) 90° (e) 120° (f) 150°..... 253

Figure B.1. Key dimensions for a) straight circular, b) re-entrant and c) doubly re-entrant pillars..... 256

Figure B.2. a) Mesh topology of fluid domain having a level one octree mesh adaption which is applied within the vicinity of the droplet impact and repulsion area as elucidated from the darker regions, b) Structured mesh refinement applied upon the doubly re-entrant pillar arrays. 257

Figure B.3. Doubly re-entrant unit cell array highlighting the liquid-solid interface of the capillary area during droplet impaction. The working pressures involve the Laplace pressure (P_L), dynamic pressure (P_D), water hammer pressure (P_{wh}) and the breakthrough pressure (P_c).[1,6] 262

Figure B.4. Plots of contact area (a, d and g), interfacial pressure (b, e and h) and penetration depth (c, f and i) of droplet impacting configurated doubly re-entrant pillars at different timescales for an θ_Y = 105°. (a-c): D=100 µm. (d-f): D=150 µm. (g-i): D=200 µm. 267

Figure B.5. Plots of contact area (a, d and g), interfacial pressure (b, e and h) and penetration depth (c, f and i) of droplet impacting configurated doubly re-entrant pillars at different timescales for θ_Y = 105°. (a-c): S=150 µm. (d-f): S=200 µm. (g-i): S=250 µm. 268

Figure B.6. Plots of contact area (a, d and g), interfacial pressure (b, e, and h) and penetration depth (c, f and i) of droplet impacting configurated doubly re-entrant pillars at different timescales for θ_Y = 105°. (a-c): H=100 µm. (d-f): H=50 µm. (g-i): H=30 µm. 269

Figure B.7. Plots of contact area (a, d and g), interfacial pressure (b, e and h) and penetration depth (c, f and i) of droplet impacting configurated doubly re-entrant pillars at different timescales for θ_Y = 105°. (a-c): δ=5 µm. (d-f): δ=10 µm. (g-i): δ=15 µm. 270

Figure B.8. Plots of contact area (a, d and g), interfacial pressure (b, e and h) and penetration depth (c, f and i) of droplet impacting configurated doubly re-entrant pillars at different timescales for θ_Y = 105°. (a-c): t_o=5 µm. (d-f): t_o=10 µm. (g-i): t_o=15 µm. ... 271

Figure B.9. Spreading factor against contact time for various dimensional sizes of the doubly re-entrant pillars with an intrinsic contact angle of θ_Y = 105°. (a): pitch spacing. (b): height. (c): diameter. 272

List of Abbreviations

3D	Three Dimensional
AFM	Atomic Force Microscope
CAH	Contact Angle Hysteresis
CFD	Computational Fluid Dynamics
CLSVOF	Coupled-Level Set Volume-Of-Fluid
CSF	Continuum Surface Force
ESEM	Environmental Scanning Electron Microscope
eDPD	Dissipative Particle Dynamics with energy conservation
FESEM	Field Emission Scanning Electron Microscope
LBM	Lattice-Boltzmann Method
MDPD	Many-body Dissipative Particle Dynamics
MDPDE	Many-body Dissipative Particle Dynamics with Energy conservation methods
NCG	Non-Condensable Gas
PISO	Pressure Implicit Splitting Operators
PRESTO	PREssure Staggering Option
QUICK	Quadratic Upstream Interpolation for Convective Kinematics
RMS	Root Mean Square
SEM	Scanning Electron Microscope
VOF	Volume-Of-Fluid

List of Contents

Abstract.....**i**

Acknowledgements.....**iii**

Publication Work Implemented within the Thesis.....**iv**

List of Figures.....**v**

List of Abbreviations.....**xx**

Chapter 1 - Introduction.....**1**

1.1. Research Inspirations.....2

1.2. Aims and Objectives.....3

1.3. Thesis Summary.....6

1.4. References.....9

Chapter 2 – Review of Current Literature.....**12**

2.1. Preamble.....13

2.2. Concept of Surface Wettability.....14

2.2.1. Youngs' Dupre Model.....14

2.2.2. Cassie-Baxter and Wenzel's Model.....16

2.2.3. Surface Wettability Characterisation.....18

2.3. Functional Surfaces Used within Heat Exchanger Environments.....22

2.3.1. Coalescence-Induced Jumping-Droplet Condensation.....22

2.3.2. How Functional Surfaces are able to Enhance the Heat Transfer Performance of Heat Exchangers?.....33

2.3.3. What Can Affect the Performance of Engineered Surfaces?.....48

2.3.4. Influence of Non-condensable Gasses During Condensation.....53

2.4. Fabrication of Functional Surfaces Used for Heat Pipes.....60

2.4.1. Electrochemical Deposition.....60

2.4.2. Etching.....64

2.5. Utilizing Computational Fluid Dynamics to Provide Further Insight.....67

2.5.1. Introduction to CFD 67

2.5.2. Numerical Condensation and Falling-film Flow 69

2.5.3. Droplet Impingement..... 78

2.6. References 86

Chapter 3 - Dropwise and Filmwise Condensation of Water on Liquid-Repellent Heat Pipes under Laminar Flow 102

3.1. Introduction..... 104

3.2. Methodology 108

3.2.1 Fluid Domain Setup..... 108

3.2.2 Numerical Schemes Implemented 113

3.3. Results and discussion 119

3.3.1 Validation of Simulation Results 119

3.3.2 Effects of Surface Wettability and Subcooling Temperature on Condensate Behaviour and Heat Transfer 126

3.3.3 Implications of Altering the Contact Angle Hysteresis at Given Equilibrium Contact Angles 137

3.4. Conclusion 143

3.5. References 145

Chapter 4 - Dropwise and Liquid-Jet Laminar Flow of Subcooled Water Falling over Horizontal Tube Banks 150

4.1. Introduction..... 152

4.2. Methodology 157

4.2.1 Geometry Setup, Boundary Conditions and Mesh Refinement 157

4.2.2 Governing Equations and Numerical Schemes 164

4.3. Results and Discussion 167

4.3.1 Numerical Validation 167

4.3.2 Implications of Satellite Droplet Impaction on Local Heat Transfer within a Liquid Film..... 174

4.3.3 Falling-Film Flow Behaviour at Different Contact Angles 184
4.4. Conclusion 191
4.5. References 193
Chapter 5 - Droplet Impact on Doubly Re-entrant Structures 197
5.1. Introduction 198
5.2. Methodology 202
5.2.1 Setup of Fluid Domain and Boundary Conditions 202
5.3. Results and Discussion 206
5.3.1 Numerical Validation against Experimental Results. 206
5.3.2 Droplet Repellency Performance Against Pillar Overhangs 213
5.3.3 Parametric Dimensional Analysis of Doubly Re-entrant Pillars Against Liquid-Repellency 215
5.4. Conclusion 226
5.5. References 227
Chapter 6 – Conclusions, Future Prospects and Contributions Made 232
6.1. Contributions Made to Literature 233
6.2. General Conclusions 234
6.3. Future Works 240
6.4. References 245
Appendix A 247
1. Falling-film Flow Behaviour of Water Flowing Over Several Stacked Tubes at Multiple Contact Angle Configurations 248
Appendix B 254
1. Cases Ran for Simulation and Mesh Refinement 255
2. Contact Angle Measurements 257
3. Numerical Methods 259
4. Fabrication of Doubly Re-entrant Pillars 260

5. How Micro-Pillars Repel Impacting Droplets 261
6. Droplet Impact Imagery 265
7. Solid Fraction of Doubly Re-entrant Pillars 266
8. Interfacial Pressure, Penetration Depth and Spreading Diameter 266
9. References 273

Chapter 1

Introduction

1.1. Research Inspirations

Implementing liquid-repellent surfaces on condenser heat pipes have been known to enhance their heat transfer performance considerably through establishing dropwise or jumping-droplet condensation as opposed to filmwise condensation which is naturally seen on most thermally conductive materials used to manufacture heat pipes.[1-4] This can have many profound repercussions on critical engineering processes that utilize condensers within various thermodynamic cycles seen in desalination plans,[5-7] geothermal heat pumps,[8-10] and even nuclear reactors.[11,12] Being able to maintain dropwise or jumping-droplet condensation on heat pipes can allow current heat exchangers to reduce their surface area to provide the same amount of heat transfer required (i.e. less number of heat pipes), thus allowing more compacted heat exchangers to be employed. As a consequence, less power/fuel would be required to operate these heat exchangers resulting in lower operating costs, carbon emissions and taxes.

Nevertheless, such functional liquid-repellent surfaces need to be specifically designed to manipulate the dynamics of the fluid to efficiently repel or thin the formulating liquid in order to amplify heat transfer efficiencies further against condensation or falling-film flow. Two-tiered micro/nanostructures are one of the many complex functional surfaces used within literature to control the dynamics of the fluid by altering the surfaces' properties (for e.g. the contact angle or contact angle hysteresis). Examples of these surfaces are illustrated in Chapter 2. Although, the full potential of these functional surfaces have yet to be revealed through design optimisation. Performing this experimentally is presumed to be quite costly and time consuming due to the fragility of and difficulty of fabricating micro or nanostructures. Thus, numerical simulations are preferred as the properties of the surface can be virtually altered to establish which particular aspect is able to enhance the tubes' heat transfer performance the most through

parametric optimisation for either liquid impingement or condensation. However, there is an absence of numerical studies that are able to simulate liquid impingement on such complex functional surfaces as most numerical work are conducted on plain or straight pillared surfaces (highlighted in Chapter 2.5). Then again, numerically simulating condensation on liquid-repellent heat pipes has not yet been thoroughly analysed or validated within the literature. Certain interfacial flow phenomena that occur on falling-film flow (such as the Rayleigh-Plateau instability) has not been thoroughly portrayed methodologically or even establish its' significance on altering the tubes' heat transfer performance numerically. In addition, most condensation heat transfer studies relating to dropwise condensation have mainly been conducted on micro-scaled surfaces (micro-pillared surfaces) rather than on macroscale surfaces (such as heat pipes). This limits the compatibility of their results to be compared towards heat exchanger tubes since the dynamics of the condensate would be affected by the gravitational acceleration acting along the circumferential direction of the tube. Thus, this would affect the magnitude of the surfaces' heat transfer performance in relation to micro-scale simulations on flat surfaces. Therefore, it is still unclear how certain surface wettability factors (such the contact angle or the contact angle hysteresis) plays a role to enhance the tubes' heat transfer coefficient from establishing when dropwise or even jumping-droplet condensation will transpire at given surface wettability parameters.

1.2. Aims and Objectives

Hence, this thesis will aim to provide further comprehension into answering the issues outlined above. To begin solving these problems, the following objectives are to be achieved.

1. Develop a two-dimensional multiphase flow/phase change simulation of condensation on a heat pipe to assess the importance of altering the surfaces' intrinsic contact angle and contact angle hysteresis against the tubes' heat transfer performance.

The developed model is to be first validated theoretically and experimentally against the Nusselt film theory for condensation and experimental data from literature by comparing the tubes' heat transfer coefficient at various subcooling temperatures using Kleiner *et al*. model as a baseline.[13] Once validated, the tubes' intrinsic contact angle will be varied between hydrophilic and superhydrophobic states (0-150°) and the contact angle hysteresis (0-20°) against the tubes' condensation heat transfer coefficient/heat flux. This will be correlated from identifying when the state of the condensate will transition from filmwise to dropwise and jumping-droplet condensation as the intrinsic contact angle and contact angle hysteresis increases/decreases.

2. Conduct a three-dimensional multiphase flow falling-film simulation to ascertain how the departing droplets may influence the heat transfer performance of the tubes beneath from capturing the Rayleigh-Plateau instability of liquids jets.

Similarly as above, the model needs to be validated against the Nusselt film theory for falling film flow and experimental data using Ding *et al.* model as a starting point.[14] To reveal the Rayleigh-Plateau instability, the number of mesh elements per unit jet width is to be increased between 8-32 points based on Deshpande *et al.* methodology.[15] Using the optimum number of elements, compare the heat transfer performance of the tube beneath with and without mesh refinement to observe the influence of the capturing Rayleigh-Plateau instability and how the increased number of impacting droplets are able to augment the heat transfer performance of secondary tubes. Then adjust the intrinsic

contact angle of the tubes between 0-150° to illustrate how the Rayleigh-Plateau instability is able to alter the state of flow for each contact angle configuration (e.g. from jet-wise to dropwise flow).

3. Assess the droplet repellency performance on doubly re-entrant pillars from parametrically altering the pillars' dimensional and surface properties at various levels to determine which parameter is the most relevant for liquid repellence.

From revealing the implications of impinging droplets on surface heat transfer performance, the droplet impact performance is to be assessed on functional surfaces, specifically on doubly re-entrant pillars as they are known having large breakthrough pressures (capillary pressure) compared to straight or re-entrant pillars. From using Hu *et al.* initial setup, a three-dimensional multiphase flow model will be developed of droplet impact on doubly re-entrant pillars. The model will be validated against experimental data from fabricating doubly re-entrant pillar designs and conducting droplet impact experiments at various pitch sizes and intrinsic contact angles. Then, the droplet repellence performance against the pillars' overhang angle will be accessed (i.e. comparing with straight, re-entrant and double re-entrant pillars) through comparing the interfacial pressure profiles and the penetration depth of the droplet through the pillars' cavities. The doubly re-entrant pillars' height, pitch, diameter, overhang thickness and overhang height will be parametrically varied to determine their predominance on droplet repellency.

Accomplishing these objectives will allow engineers and researchers to numerically undermine which particular surface properties will be able to enhance the performance of heat exchangers for condenser or absorber applications. The outcomes and achievements of this thesis are listed below in their respective chapters

1.3. Thesis Summary

Firstly, Chapter 2 gives a thorough background of how liquid repellent surfaces are utilized for condenser heat pipes and how they are able to enhance their heat transfer performance through demonstrating dropwise and jumping-droplet condensation through their unique functional surface designs. This is then linked towards the numerical work currently seen within the literature illustrating the absence of numerical work on liquid-repellent heat pipes.

Chapter 3 then highlights how altering the tubes' intrinsic contact angle and contact angle hysteresis is able to augment the tubes' heat transfer coefficient and heat flux by shifting the flow behaviour from filmwise condensation to dropwise and even jumping-droplet condensation at various subcooling temperatures up to 50 K. Specifically, the tubes' intrinsic contact angle are adjusted between 0 and 150° and the contact angle hysteresis is changed between 0 and 20° at selected intrinsic contact angles to demonstrate its' potency on altering the condensate flow behaviour and the tubes' heat transfer coefficient. This is demonstrated by conducting a two-dimensional multiphase flow/phase change simulation of laminar condensation of water-vapour upon a heat pipe. The condensate film thickness, circumferential temperature profiles and heat transfer coefficients at different subcooling temperatures are validated against the Nusselt film theory and experimental data from literature by applying a mass transfer model known as the Lee's model and modifying the thermal conductivity of the water-vapour. Nonetheless, as the simulation was conducted on a singular heat pipe, it is worth considering how the departing droplets may alter the heat transfer performance on adjacent tubes beneath the first.

Consequently, Chapter 4, demonstrates three-dimensional falling-film flow of subcooled water across multiple horizontal tube banks at various intrinsic contact angles between 0

and 150°. The local heat transfer coefficients of the film as well as the film thickness and velocity profiles have been correlated against analytical data including the Nusselt film theory. Increasing the contact angle of the tube was shown to reduce the liquids' surface area in axial direction and thicken in the circumferential direction. This caused the flow of the liquid to transition from dropwise to jet flow. Raising the contact angle above 90° however caused the flow to no longer display falling-film flow but just continuous droplets that departed off the tube. Furthermore, a phenomenon known as the Rayleigh-Plateau instability has been depicted from the departing liquid jets which illustrated excellent agreement against experimental results within literature which has been scarcely perceived from other numerical studies.

Capturing the instability of liquid jets was accomplished through increasing the number of mesh elements within the diameter of the liquid jets. This allowed the capillary wave generated at the tip of the liquid jet (just after the pendent droplet impacts the secondary tube) to be appropriately apprehended as it travelled in the direction of recoil. Due to the harmonic sinusoidal nature of the wave, the interface of the liquid jet becomes perturbated, creating regions of high and low pressure. As a consequence, multiple satellite droplets are revealed from the liquid jet to impact the secondary tube. This drastically modified the local heat transfer coefficients of the film and the flow conduct on the tube from inducing film thinning and mixing. More importantly, portraying the Rayleigh-Plateau instability was also able amend the state of the falling-film flow at various contact angles from initially being jet-wise flow to dropwise/jet flow or just dropwise flow entirely. This has further implications on adjusting the overall heat and mass transfer performance in numerical work for absorber and condenser heat exchanger applications.

As the implications of droplet impaction against the tubes' flow behaviour and heat transfer characteristics are assessed, Chapter 5 then further scrutinizes the effects of

droplet impaction on functional surfaces. Explicitly, the chapter reveals three-dimensional simulations of multiphase flow on the droplet repellency performance of water on microscopic doubly re-entrant pillars which is renowned to excel against liquid impingement. The numerical results are quantitively and qualitatively compared against experimental data by evaluating the contour images during droplet impaction and the wetting diameters against contact time. The doubly re-entrant pillars were first fabricated through laser lithography of a liquid photoresin known as IP-S. The pillars were treated with a hydrophobic coating to increase their intrinsic contact angle to allow droplets to easily repel from the surface. The value of the intrinsic contact angles obtained was then inserted within the numerical simulations to allow a direct a comparison.

To thoroughly validate the numerical data, the droplet repellency performance was compared on doubly re-entrant pillars with and without hydrophobic coating for each different pillar spacings selected. Applying a structured hexahedral mesh around each of the doubly re-entrant pillars' cavity is what allowed the simulation to be accurately compared against experimental data. Moreover, the droplet impaction performance on doubly re-entrant pillars are contrasted against re-entrant and straight pillars to determine how altering the overhang angle of the pillar is able to modify the droplet repellency behaviour from reviewing the interfacial pressure profiles within the pillar cavities. In addition, the key dimensions of the doubly re-entrant pillar namely the height, width, diameter, overhang thickness and overhang height are parametrically adjusted to demonstrate their expertise for either repelling or adhering impinging droplets on the surface. The droplet repellency performance is quantified through again analysing the interfacial pressure profiles as well as the droplets' contact area, penetration depth, velocity and pressure contours, and spreading diameters against contact time. The methodology and results presented in this chapter grant further comprehension into

simulating intricate functional surfaces that have yet to be seen in numerical studies in relation to droplet impingement. Not to mention, the dimensional requirements of the micropillars to allow impacting droplets to either wet or repel the substrate depending on the given purpose (such as for condenser or absorber type heat exchangers). Lastly, in Chapter 6, the results across all the chapters are reviewed and put into perspective to demonstrate how the findings of this work can be built upon for future researchers.

1.4. References

1. N. Miljkovic, R. Enright, Y. Nam, K. Lopez, N. Dou, J. Sack, E. N. Wang, Jumping-droplet-enhanced condensation on scalable superhydrophobic nanostructured surfaces, Nano Lett. 13 (2013) 179-187.
2. D. A. McNeil, B. Burnside, G. Cuthbertson, Dropwise condensation of steam on a small tube bundle at turbine condenser conditions, Exp. Heat Transf. 13 (2000) 89-105.
3. P. Marto, D. Looney, J. Rose, A. Wanniarachchi, Evaluation of organic coatings for the promotion of dropwise condensation of steam, Int. J. Heat Mass Transfer 29 (1986) 1109-1117.
4. F. Wang, C. Liang, M. Yang, C. Fan, X. Zhang, Effects of surface characteristic on frosting and defrosting behaviors of fin-tube heat exchangers, Appl. Therm. Eng. 75 (2015) 1126-1132.
5. N. Lukic, L. Diezel, A. P. Fröba, A. Leipertz, Economical aspects of the improvement of a mechanical vapour compression desalination plant by dropwise condensation, Desalination 264 (2010) 173-178.

6. A. Stärk, K. Krömer, K. Loisel, K. Odiot, S. Nied, H. Glade, Impact of tube surface properties on crystallization fouling in falling film evaporators for seawater desalination, Heat Transf. Eng. 38 (2017) 762-774.
7. T. Humplik, J. Lee, S. O'hern, B. Fellman, M. Baig, S. Hassan, M. Atieh, F. Rahman, T. Laoui, R. Karnik, Nanostructured materials for water desalination, Nanotechnology 22 (2011) 292001.
8. A. Bhuvanendran Nair Jayakumari, N. G. Malik, G. Mittal, D. Martelo, N. Kale, S. Paul, A Review on Geothermal Heat Exchangers: Challenges, Coating Methods, and Coating Materials, Coatings 13 (2023) 1988.
9. Y. Sui, Z. Sui, G. Liang, W. Wu, Superhydrophobic Microchannel Heat Exchanger for Electric Vehicle Heat Pump Performance Enhancement, Sustainability 15 (2023) 13998.
10. C. S. Heu, H. Jang, J. Jeon, K.-S. Lee, D. R. Kim, Recent progress on developing anti-frosting and anti-fouling functional surfaces for air source heat pumps, Energy Build. 223 (2020) 110139.
11. R. L. Webb, Enhanced condenser tubes in a nuclear power plant for heat rate improvement, Heat Transf. Eng. 32 (2011) 905-913.
12. M. Jiao, L. Zhang, P. Cheng, M. Zheng, X. Liu, Research on the corrosion resistance of porous coatings for heat transfer enhancement on the head of nuclear reactor pressure vessels, Nucl. Eng. Des. 429 (2024) 113597.
13. T. Kleiner, S. Rehfeldt, H. Klein, CFD model and simulation of pure substance condensation on horizontal tubes using the volume of fluid method, Int. J. Heat Mass Transfer 138 (2019) 420-431.

14. H. Ding, P. Xie, D. Ingham, L. Ma, M. Pourkashanian, Flow behaviour of drop and jet modes of a laminar falling film on horizontal tubes, Int. J. Heat Mass Transfer 124 (2018) 929-942.

15. S. S. Deshpande, L. Anumolu, M. F. Trujillo, Evaluating the performance of the two-phase flow solver interFoam, Comput. Sci. Discov. 5 (2012) 014016.

Chapter 2

Review of Current Literature

*Navdeep Sangeet Singh, Jitao Zhang, Jason Stafford, Carl Anthony and Nan Gao**

School of Engineering, University of Birmingham, Birmingham, B15 2TT, United Kingdom

Some of the content in this chapter (and in the abstract section above) has been published in the journal of Advanced Material Interfaces, (Singh, N. S., Zhang, J., Stafford, J., Anthony, C. & Gao, N. Implementing superhydrophobic surfaces within various condensation environments: a review. Advanced Materials Interfaces 8, 2001442 (2021).).

Author Contributions: N.S.S chose the particular research topic to review. N.S.S and J.Z drafted the review paper. All of the chapters were written by N.S.S except for one which was by J.Z who supported in writing Chapter 2 in the review paper. In this Thesis, Chapters 1.2-1.5 were written by N.S.S. J.Z assisted in conducting the literature review for Chapters 1.2 and 1.4. N.G. directed the manuscript to publication. C.A and J.S, reviewed and gave recommendations on the content of the manuscript. All of the authors evaluated and accepted the manuscript.

2.1. Preamble

Condensation is found to be pervasive in critical engineering process observed within industry. This is frequently seen in various thermodynamic cycles that are a necessity in nuclear and geothermal power plants, HVAC systems (heating ventilation and air conditioning), desalination plants and cryocoolers. Rankine and Kalina cycles are one of the main processes used within these fields.[1,2] 85% of the worlds' power generation is ordained from the recurrent use of these cycles as a substantial amount of heat can be robustly generated between the working hot fluid and the cold source within a small temperature gradient.[3] The surplus amount of heat produced is due to the large amount of enthalpy needed to cause the working fluid to change its' phase, in contrast to the heat transfer rates examined in single phase systems. Fundamentally, the amount of enthalpy required to stimulate a phase change of a fluid is widely known as its latent heat of vaporisation.[4]

For two phase thermodynamic cycles, a condenser is needed to condensate the incoming steam into liquid by discarding its latent heat to the ambient environment isobarically.[5] Such steam-condensers utilise a shell and tube heat exchanger configuration, as it is known for its' robustness, applicability with various hydrocarbons and withstanding high pressures and subcooling temperatures.[6] The shell of the heat exchanger (acting as a pressure vessel), is compacted with numerous heat pipes in order to effectively extract the heat away from the working fluid.[7,8] Overtime, as the fluids' saturation temperatures falls towards the subcooled tubes, the surrounding vapour will become supersaturated, where the vapour pressure is equal or more than the saturation pressure of the local environment. The difference in pressure drives the vapour particulates towards the surface. Here onwards, the vapour particles then agglomerate and grow into macroscopic liquid droplets

which is due to the liquids' intermolecular attraction force and the Gibbs free energy of the surface.[9] Notably, the two primary modes of condensation established from this process are known as dropwise and filmwise. Additionally, for an absorber heat exchanger, a strong solution liquid is fed into the system via an inlet feeder which then falls and collides with various horizontal subcooled tubes. Typically, these compound liquids consist of either LiBr-water (lithium bromide),[10] or 1,1,1,2-Tetrafluroethane-DMAC (dimethyl-acetamide).[11] Simultaneously, water-vapour is also introduced into the system from another reservoir where it eventually becomes liquefied on the cooled pipes. The newly formed condensate then mixes with the working solution to weaken its' concentration as it exists out of the absorber. Similarly, as noted beforehand, the flow behaviour established on these tubes are commonly seen to be dropwise or jet-wise. These two types of flow genres commendably modify the heat transfer performance of heat exchanger tubes and are highly dependent upon the wettability of the surface.

2.2. Concept of Surface Wettability

2.2.1. Youngs' Dupre Model

In 1805, Thomas Young developed a theoretical model to measure the wettability of a solid surface. This is determined by placing a macroscopic sessile droplet on a planar solid substrate and measuring its' equilibrium (or intrinsic) contact angle.[12] The magnitude of the contact angle is directly proportional to the liquids' surface tension. However, naturally, three different mediums exist around the droplet therefore, three different surface tension vectors will co-exist in these phases namely solid-liquid (*sl*), liquid-vapour (*lv*), and solid-vapour (*sv*) illustrated in **Figure 2.1**.

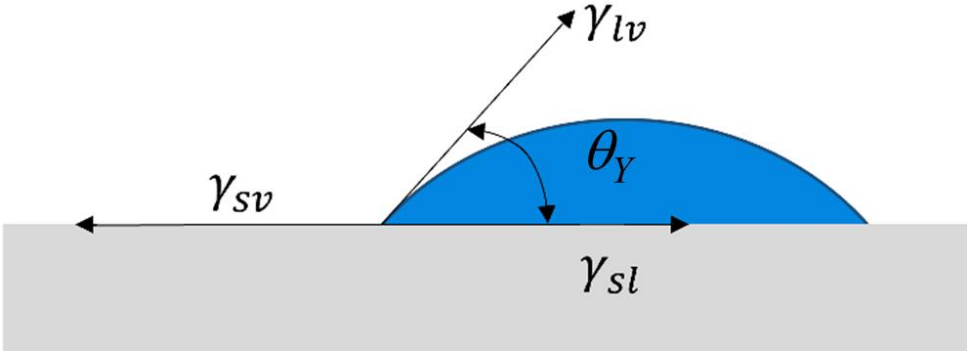

Figure 2.1. Schematic diagram of a sessile droplet placed on a solid substrate where three governing surface tension vectors act at the droplets' three-phase contact line. The equilibrium contact angle (θ_Y) characterises the surface wettability.[13]

These three surface tension vectors is what influences a droplet to be in mechanical equilibrium. Ideally, the correlation between the equilibrium contact angle and the interfacial surface tension forces can be denoted from a force balance equation seen in Equation 2.1.

$$\gamma_{sv} = \gamma_{sl} + \gamma_{lv} \cos \theta_Y \qquad (2.1)$$

Here, θ_Y is represented as the equilibrium contact angle (°), γ_{sv} is the surface tension at the solid-vapour phase (N/m), γ_{sl} is the surface tension between the solid-liquid medium and γ_{lv} is the surface tension at the liquid-vapour interface. Although, Young's equation assumes that the surface is homogenous and uniform with the liquid being in thermal and chemical equilibrium (no impurities exist in the fluid and remains at constant temperature).[14,15] But, in reality, this is not the case as liquid droplets continuously reside in a metastable state.

2.2.2. Cassie-Baxter and Wenzel's Model

Whilst Young's model describes the wettability of an idyllic surface, a practical surface inherently reveals a conditional parameter known as its surface roughness. In 1936, Wenzel considered this property and implemented the factor in Youngs' equation. Firstly, to explain the effect of surface roughness, when a droplet is displaced on a roughened surface, the droplet will infiltrate through surfaces' interstices and occupy its space.[16-19] Therefore, for a completely wetted roughened substrate, the subsided equilibrium contact angle is given in Equation 2.2:

$$cos\,\theta_w = \frac{r_f(\gamma_{sv} - \gamma_{sl})}{\gamma_{lv}} \qquad (2.2)$$

where θ_w is known as the Wenzel contact angle with r_f being the roughness ratio (or the roughness factor) which exemplifies the area of the solid surface to a definite area of the wetted surface. Therefore, the modified Youngs' equation can be further simplified as shown in Equation 2.3:

$$cos\,\theta_w = r_f cos\,\theta_Y \qquad (2.3)$$

Thus, Wenzel's model dictates a more accurate representation of the wettability of a roughened surface rather than of an ideal smooth surface. Nonetheless, whilst Wenzel's model eliminates the assumption of a surface being uniform, it still implies that the wettability of the surface is homogenous. When a droplet is placed on a roughened surface, air is trapped inside the interstices.[20] This gives rise to the static pressure within the grooves and creates a capillary force acting on the droplet, and against the direction of gravity.[21] More information on this issue is presented in Chapter 5. When the pressure inside the channels is greater than the hydrostatic pressure of the droplet, the fluid is

unable to penetrate into the channel creating an adverse pressure gradient (negative pressure) as opposed to a droplet in a Wenzel state displayed in **Figure 2.2**.

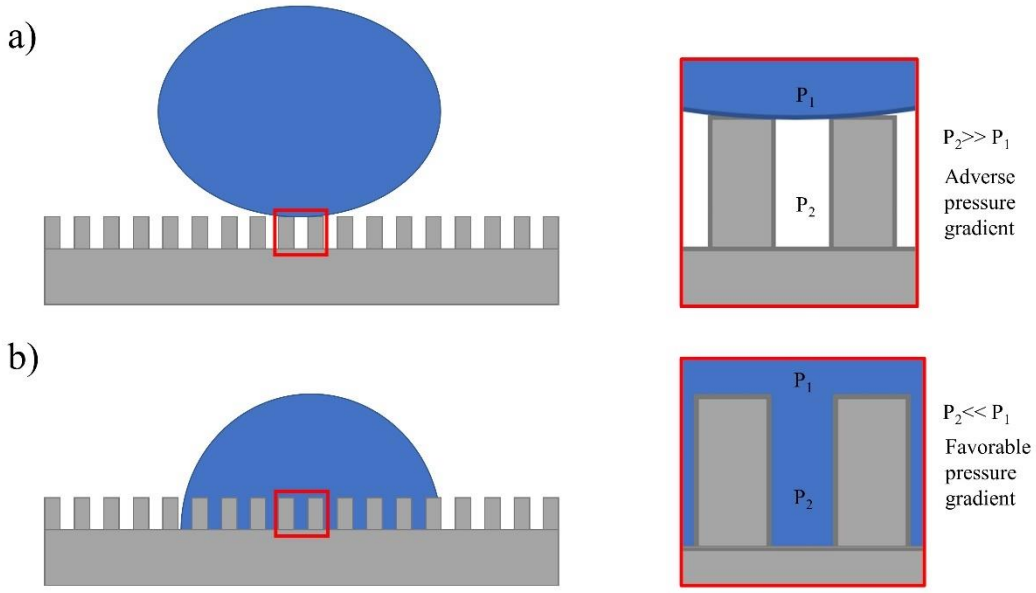

Figure 2.2. Diagram showing (a) Cassie-Baxter state and (b) Wenzel state, illustrating the effects of adverse and favourable pressure gradients within textured surfaces.

Hence, the fluid will heterogeneously wet the substrate. To employ this effect into Young's model, Cassie and Baxter interconnected the apparent contact angle (θ_{CB}) to a multifarious interface illustrated in the Cassie-Baxter equation.[22,23]

$$cos\,\theta_{CB} = \varphi_s cos\,\theta_Y - (1 - \varphi_s) \qquad (2.4)$$

φ_s is given as the solid-liquid fraction regime in a two-dimensional planar area parallel to the inhomogeneous surface. Henceforth, the liquid-air regime (where the droplet has not wetted the surface) can be represented as 1-φ_s. When φ_s is equal to one, the liquid-air regime of the surface becomes zero causing the Cassie-Baxter equation to reduce to the Wenzel equation. Nevertheless, as noted previously from the other wettability models, the Cassie-Baxter equation is not valid in all scenarios. As, it is known for a droplet in a

Cassie-Baxter state to transition to a Wenzel state depending upon the quality of the surfaces' liquid repellency.

2.2.3. Surface Wettability Characterisation

Certain wettability states are desired which will give rise to a Cassie-Baxter or Wenzel state. However, this can be further signified from the value of the contact angle a droplet makes on the surface. A surface that is superhydrophobic is when a stationary water droplet creates a contact angle more than 150° with a hydrophobic surface being more than 90°.[24] Conversely, a hydrophilic surface contains a contact angle less than 90° with superhydrophilic surfaces being smaller than 10°.[25] It is wildly known for superhydrophobic and hydrophobic surfaces to retain a Cassie-Baxter state when no external forces are present, nonetheless, when kinetic forces reside, these two surfaces become distinctively different.

When droplets glide across the surface of a heat pipe (due to gravitational or shear forces), the droplets will retain dynamic contact angles known as its advancing and receding contact angles. The difference between them is noted as the surfaces' contact angle hysteresis (CAH).[14,24] A surface with a low contact angle hysteresis will minimise the contact area between the solid-liquid interface of a droplet whilst in motion. This is due to reduction in the droplets' lateral adhesion force in which the contact angle hysteresis is directly proportional to.[26-28]

$$F_L = wL\gamma_{lv}(\cos\theta_r - \cos\theta_a) \qquad (2.5)$$

w is a dimensionless factor which signifies the eccentricity of the contact area. A circular contact area has a *w* value of π. *L* is given as the diameter of the droplet contact area (m), θ_r is observed as the receding contact angle (°) and θ_a is shown as the advancing contact

angle (°). Superhydrophobic surfaces are known to exhibit low contact angle hysteresis whilst hydrophobic surfaces have a high contact angle hysteresis. Such surfaces are known to exist domestically as discovered by Dettre *et al.* by utilising rough waxed materials.[29] Additionally, it was then discovered to be present intrinsically in nature such as rose petals,[30] lotus leaves,[31] water striders,[32] and water fern,[33] due to their indigenous micro/nanostructures which are able to trap air within their cavities.

Therefore, hydrophobic surfaces are more likely to transition into a Wenzel state which resides in the droplet being "pinned" on the surface.[24] Consequently, utilizing surfaces which contain low contact hysteresis and are superhydrophobic are highly desirable for establishing dropwise condensation. Dropwise condensation has been observed to have increased droplet departure frequency and smaller droplet removal radii compared to filmwise condensation which allegedly increases the tubes' heat transfer coefficient by 4 to 28.6 times more.[3] In filmwise condensation, the presence of a thin macroscopic liquid film is seen upon the tubes which increases the tubes' thermal resistance, resulting in reduced convective heat transfer rates to the surface.

Although overtime, dropwise condensation eventually transition towards filmwise condensation due to the subjugated surface adhesion force seen at high subcooling temperatures or supersaturation pressures. [34-36] The droplets surface tension is then unable to overcome the enhanced adhesion force which results in the fabricated micro/nanostructures to be flooded (i.e. droplets dwelling in a Wenzel state), reducing the structures Laplace pressure gradient. The Laplace pressure gradient phenomenon will be explained thoroughly within the next sub-chapter. Then, the droplets collapse from their own hydrostatic pressure and form a liquid film on-top of the submerged functional structures. This in turn, diminishes the overall heat transfer coefficient of the condenser and therefore its' efficiency.

Figure 2.3 gives an example of the typical time period of which dropwise condensation transitions to filmwise condensation, with its deprivation in heat transfer.

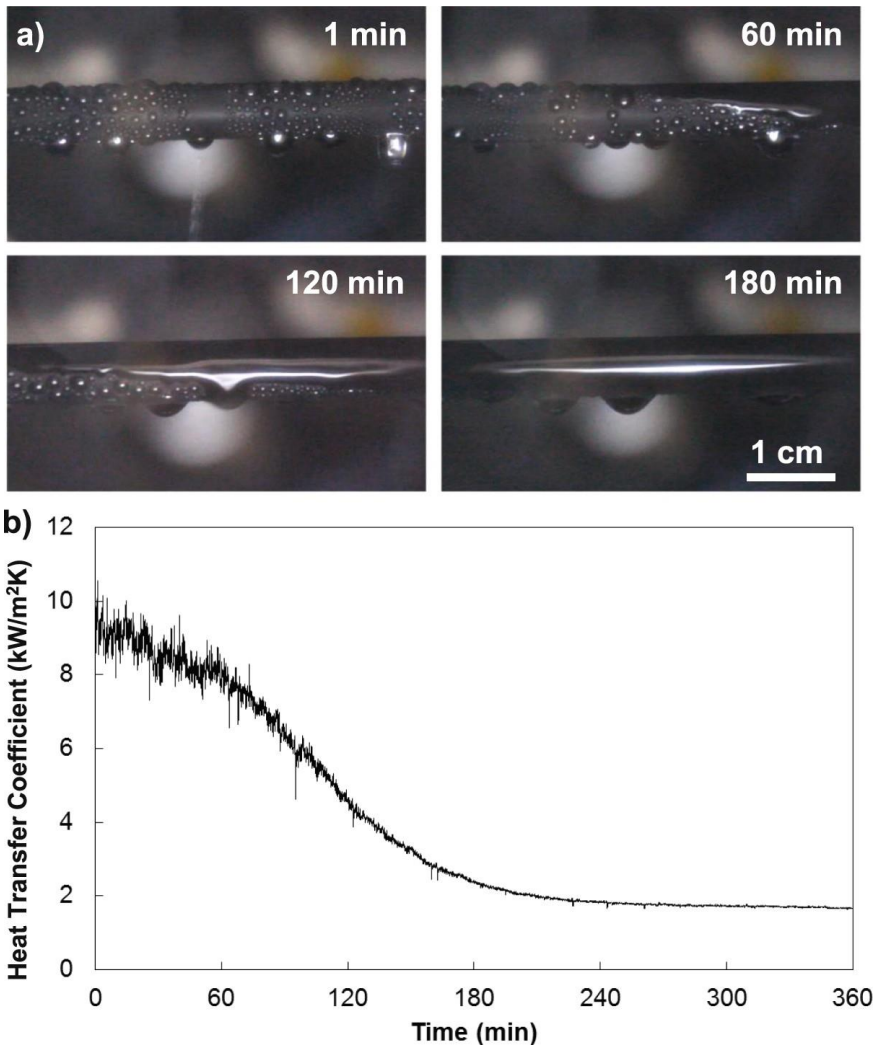

Figure 2.3. Condensation of toluene over a lubricant-infused surface (LIS) of a heat pipe. (a) shows dropwise condensation at the beginning of condensation which then transition to filmwise condensation after 60 min. (b) depicts the decrease in heat transfer coefficient overtime which is responsible for the transition in condensation regimes observed in (a).[37]

Thus, preserving dropwise condensation is a necessity in all condensation heat transfer practices. Additionally, dropwise condensation is able to preserve the operating costs of condensers as the heat transfer surface area required will be compacted. This is shown by

Lukic *et al*. who artificially modified the surface topology of heat pipes using ion beam implementation.[38] As doing so, dropwise condensation was observed which reduced the production cost of water by 35.4% in comparison of using a plain surface. Hence, a smaller surface area could be used to give the same amount of heat transfer at a given subcooling temperature. This will result in lower carbon emissions and carbon taxes,[39] as less operating power is needed to manage the compressed heat exchangers. But most importantly, being able to further comprehend the dropwise condensation phenomena will give rise to innovative superhydrophobic surfaces which are able to withstand excessive environmental pressure. CO_2 emissions would then be declined even more then shown from current sources.[40]

From a wider perspective, many researchers have noted that the lifespan of fragile superhydrophobic micro/nanostructures when applied under condensation environments is usually a few days or at most, a couple of months.[37,41-43] Their short lifecycle is quantified from the abrasion of functional structures under vapour shear flow, the bending of superhydrophobic pillars which eventually stick to the adjacent pillars affected by capillary force (for e.g. formation of large droplets which repeatedly stress delicate structures) and corrosion of surfaces subjected to humid environments.[44,45] Various tactics have been made to enrich or prolong dropwise condensation. For example, lubricant-infused surfaces (LIS), polymer films, hierarchical micro-nanostructures, ion implementation and self-assembled monolayers. However, these functional surfaces raises additional problems which neglects their service. This includes high manufacturing costs, reduced thermal conductivity of coatings, depletion of lubricant overtime, degraded performance at large subcooling temperatures and decreased durability of thin polymer coatings.[3] Notably, Holden *et al.* manged to formulate consistent dropwise condensation for more than 22,00 hours (over 2 years), by prescribing a polymer coating with a

thickness of 60 μm to increase its' resilience. Nonetheless, this generated a large thermal resistance from its profound thickness, therefore, the heat transfer coefficient of the surface was barley improved in respect to the original surface.[3,46]

Recently, over a decade ago, a new form of condensation was discovered known as coalescence-induced jumping droplet condensation which is known to be superior over dropwise condensation but, however, is still under examination.[47] As partly described from its' name, when two microscopic droplets coalesce on a solid substrate, the excessive surface energy formulated is converted in kinetic energy which causes the coalesced droplet to be thrusted away from the surface.[48] As a consequence, this is able to enhance heat transfer coefficients by at least 30% from dropwise condensation.[35] The hydrodynamic aspects of jumping-droplet condensation will be reviewed in the next sub-chapter.

2.3. Functional Surfaces Used within Heat Exchanger Environments

2.3.1. Coalescence-Induced Jumping-Droplet Condensation

The discovery of jumping-droplet condensation was founded by Boreyko *et al.* whom correlated this effect from ballistospore mushrooms.[47] Ballistospore mushrooms are known to eject their spores at the tip of the sterigma which is driven from the coalescence of droplets along the surface of the spore during condensation.[49] The individual droplets that are developed from condensation are known as the Buller's drop that forms on the hilar appendix and the adaxial drop which is nucleated on the spore surface.[49] Once the drops reach a critical radius (where they begin to touch), the droplets then coalesce causing the centre of mass of the merged droplet to shift swiftly, which consequently propels the

droplet away (with the spore being attached to it) due to the change in the droplets' momentum.[50] **Figure 2.4** demonstrates this process, schematically.

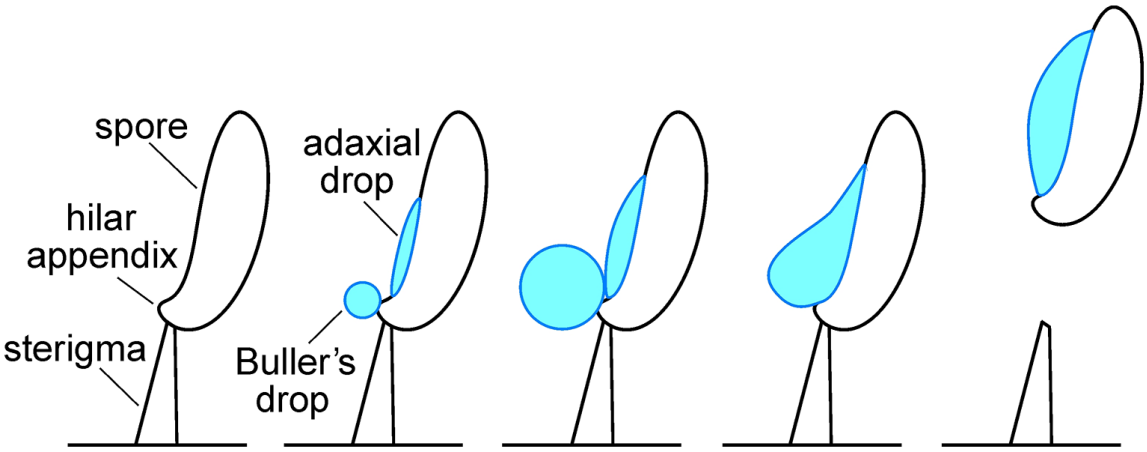

Figure 2.4. Jumping-droplet condensation occurring upon a ballistospore mushrooms' spore due to the nucleation of the Buller's drop and the adaxial drop which then coalesce to propel the spore away from the sterigma.[50]

Originally, this process was known as self-propelled dropwise condensation named by Boreyko *et al.* as droplets were continuously being propelled off the surface as soon as they merged with no external forces being present. It was then found that the additional surface energy created from coalescence was transferred into kinetic energy which instigates droplet propulsion. Dropwise condensation removes droplets away from the surface due to the gravitational force overcoming the droplets' surface tension force, that is, proportional to the surface adhesion force. The effectiveness of droplet removal is mostly responsible upon the orientation of the surface with mainly affecting droplets that reach a diameter equal to their capillary length (for water, this is 2.7 mm at ambient temperature).[51-53]

The self-propelled dropwise condensation was founded on a hierarchical superhydrophobic surface which was produced from depositing carbon nanotubes on

silicon micropillars. The structures were then coated with hexadecanthiol and then employed on a flat copper plate. The performance of the superhydrophobic surface was compared with a plain hydrophobic surface when the surfaces displayed steady state condensation (majority of the surface exhibited condensate drops). As anticipated, the hydrophobic surface presented only dropwise condensation, and showed no change in momentum when droplets coalesced with one another. Conversely, on the superhydrophobic surface, droplets were immediately driven away from surface after coalescence with an average lateral velocity of 1 m/s.[47]

The major distinction between the two surfaces was represented by the droplets' coalesced diameter which was found to be significantly smaller on the superhydrophobic surface, being just over 10 μm. Moreover, the surface coverage of droplets (ratio of surface area obscured by droplets to the overall surface area) for the superhydrophobic surface was much smaller than of the hydrophobic due to the increased droplet removal frequency (as revealed in **Figure 2.5**). Subsequently, the surfaces' thermal resistance to convection was diminished as having smaller droplet departure diameter is associated to an increase in heat transfer.[54] From a kinetic point of view, the self-propelled droplet movement is directly proportional to the inertia and viscous forces that act against the droplet.[55,56] When both droplets reach a critical radius and coalesce, the inertia force developed from the fluctuation in the centre of mass is able to dominate the viscous force of the droplet and be propelled from the surface. This results in the droplet containing a high Reynolds number which corresponds to a large lateral velocity. The autonomous jumping behaviour can be seen clearly in **Figure 2.6.**

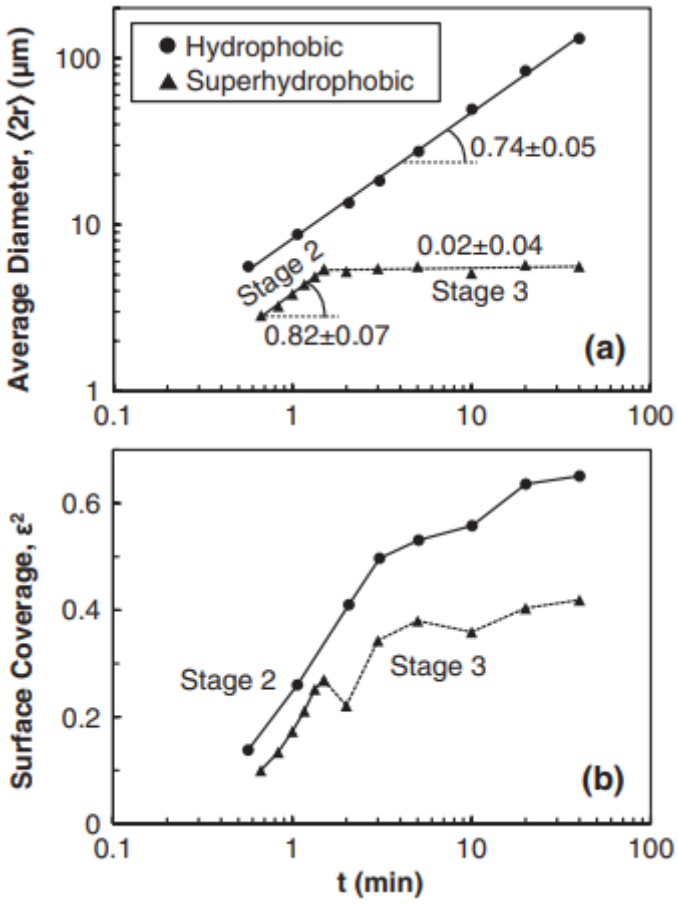

Figure 2.5. (a) Results of average droplet diameter with (b) showing the surface coverage for the hydrophobic and superhydrophobic surface against time.[47]

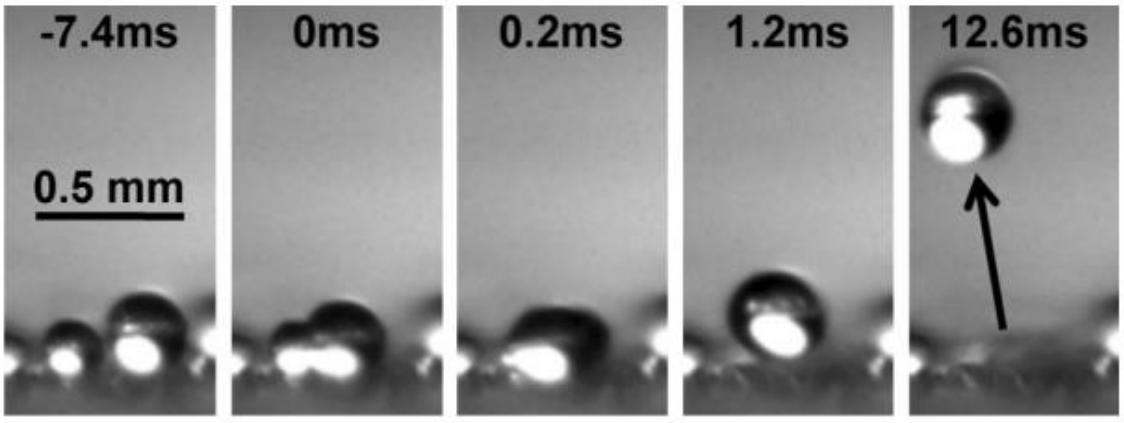

Figure 2.6. Coalescence of two unequally sized droplet which then shows an oscillation in the merged droplets' centre of mass in 0.2 ms (contour of the droplet is perturbated) and then being driven away laterally from a superhydrophobic surface.[47]

The Reynolds number is given as the ratio of the inertial and viscous force of a fluid as shown below:

$$Re = \frac{\rho_l u_o \lambda_c}{\mu_l} \tag{2.6}$$

ρ_l is the density of the fluid (kg/m^3), u_o is the velocity of the merged droplet (m/s), λ_c is known as the hydrodynamic length of a fluid (m) (the diameter of the coalesced droplet), and μ_l is the fluids' dynamic viscosity (Pa·s). Furthermore, to define what influences the critical radius required for self-propulsion, the equation below describes the relationship of how the inertial and viscous forces of a fluid affects the droplets' critical radius:

$$r_{crit} \propto \frac{{\mu_l}^2}{\gamma_{lv}\rho_l} \tag{2.7}$$

r_{crit} is given as the critical radius (m). This relationship dictates that when the inertial force of the droplet increases, the critical radius required for droplet removal decreases in contrast to an increase in the viscous force. Therefore, it can be said, as the Reynolds number of a droplet increases, the critical radius needed for autonomous propulsion declines, due to the Reynolds number being proportionate to the inertial force.

That being said, a deeper comprehension of the mechanism of jumping droplets is still needed to be able to apply this effect within condenser heat pipes. One prime example is from understanding how surface energy is converted into kinetic energy during droplet coalescence which establishes its inertial force for lift off.[47] Enright *et al.* further investigated this theory by analysing the jumping-droplet condensation behaviour within a isobaric enclosed chamber.[57] It was found that merely 6% or less of the surface energy is translated into kinetic energy during droplet impulsion (known as the surface energy conversion efficiency). This result was substantiated against a numerical simulation of

two droplets coalescing. Although, the aspects that affect the efficiency of jumping droplets (i.e. the forces that interplay upon coalesce) remains to be seen.

Importantly, it was found that the diameter of droplets during coalesce affects the magnitude of jumping droplets' velocity. Such studies have to tried to explain this phenomenon by establishing an energy-balance equation to specify the surface to kinetic energy conversion process. Various researches imposed that the viscous dissipation, surface adhesion and the velocity vectors acting on coalescing droplets are the fundamental factors that cause droplets to jump.[58,59] Nevertheless, these factors were not captured qualitatively to validate their cause. On the other hand, Enright *et al.* managed to confine the energy conversion process by fabricating a superhydrophobic surface having a contact angle of ≈170° with negligible contact angle hysteresis to eliminate the presence of surface adhesion.[57] The superhydrophobic surface consisted of fluoropolymer-coated carbon nanotubes where their diameter was equal to 40 nm and pitch distance of 100 nm. From scanning the surface using atomic force microscopy (AFM), the carbon nanotubes were revealed to have a maximum height deviation of 820 nm. The surface wettability properties and morphology can be seen in **Figure 2.7**.

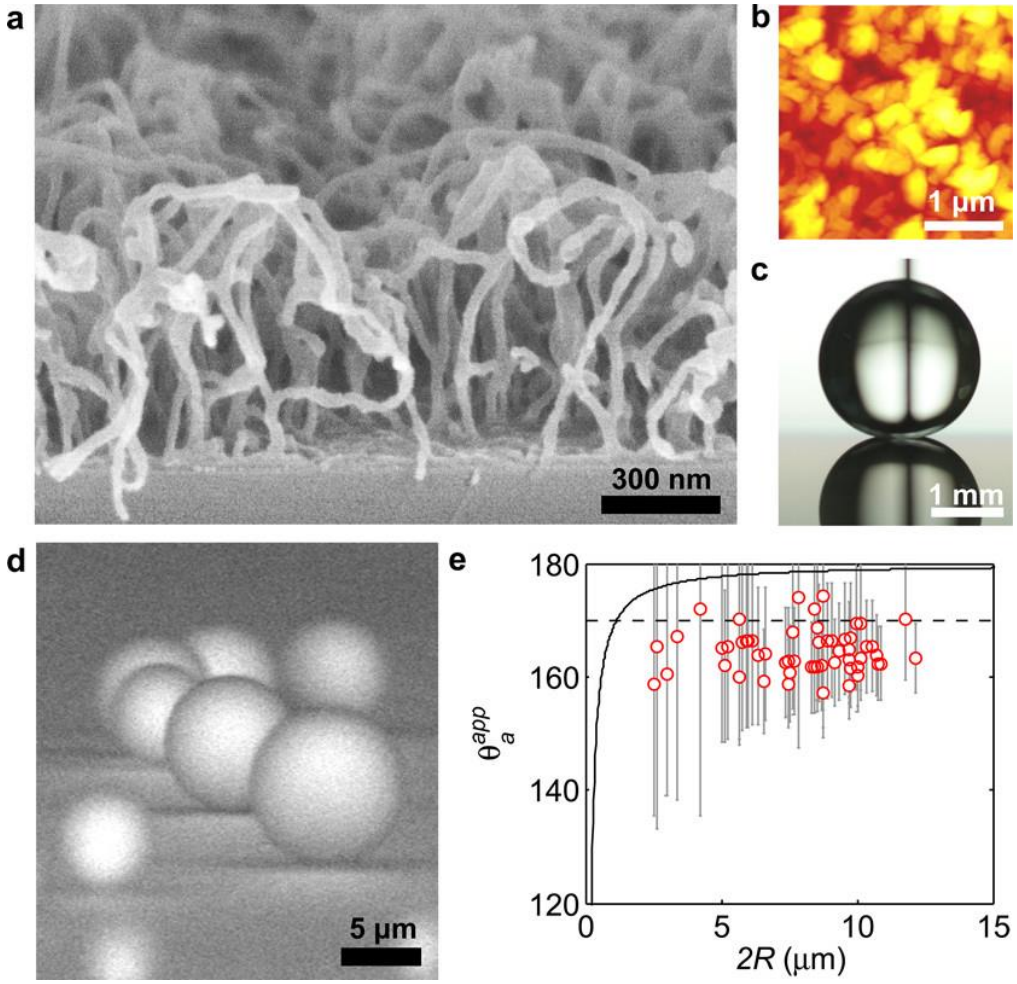

Figure 2.7. (a) SEM image of constructed carbon nanotubes coated with a P2i fluoropolymer coating method (plasma enhanced vapor deposition) to establish their superhydrophobicity. (b) AFM image of carbon nanotubes. (c) Illustrates a droplet in a receding state on the superhydrophobic surface having an apparent contact angle of 166° ± 2°. (d) Environmental scanning electron microscope (ESEM) image of nucleating droplets with a surface inclination angle of 8°. (e) Advancing contact angle of condensing droplets visually measured from ESEM images having different diameters. The dashed line represents the average advancing contact angle of the surface equal to 170.2° ± 2.4°.[57]

To provide additional insight into coalescence procedure, a two-dimensional axisymmetric model was made of two droplets merging with equal diameter. As the

droplets' contours interfere with each other, a capillary bridge is founded which expands outwards from the initial point of contact due to the change in curvature. At the beginning of the bridge formation, viscous forces are dominant however, when bridge radius becomes greater than the critical bridge radius, inertia forces are prevalent.[57,60,61] During coalescence, the liquid begins to flow within the capillary bridge as a low-pressure region is created from the large change in curvature (established from the capillary bridge effect).[55,57] This can be clearly seen in **Figure 2.8** which highlights the velocity contours of the simulated droplet coalescence procedure.

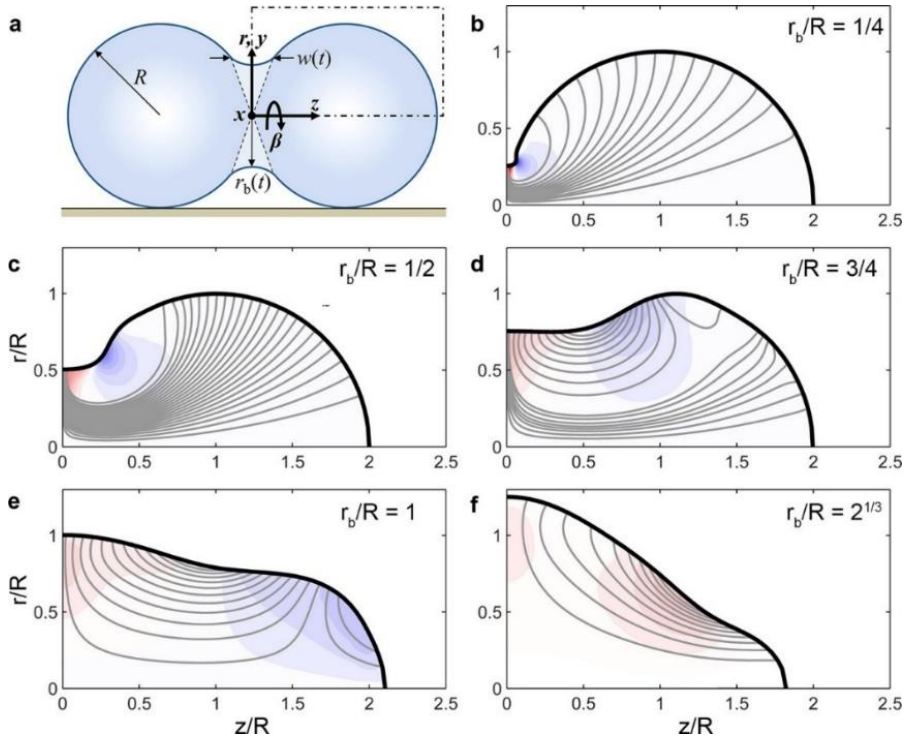

Figure 2.8. (a) Axisymmetric view of the simulated binary droplet coalescence showing an initial radius *R*, with having a capillary bridge radius $r_b(t)$ as a function of time. $w(t)$ is given as the capillary bridge width, also as a function of time. (b-f) demonstrates the velocity flow field contours during coalescence, where the red the colours indicate the radial velocity component with the blue colours showing velocity flow away from the z-axis.[57]

While the capillary bridge is being developed, a capillary wave is formed which proliferates along the droplets' interface moving away from the point of contact. It should be noted that the fluid dynamics of the wave is controlled by surface tension instead of gravity.[62] Due to the periodic nature of the wave, the pressure of the droplet starts to oscillate over and beneath its initial pressure value. Once the wave reaches to the other side of the droplet, it is then reflected back to the point of coalescence.[57] The pressure fluctuations already present within the droplet starts to become enlarged, creating positive and negative radial velocities (as previously shown in **Figure 2.8**).[57] The capillary wave is then dissipated which relaxes the pressure instabilities. As doing so, the droplets' contour and flow field starts to transform due to the change in the droplets' momentum.[57] This change in momentum is founded from a negative momentum flow field within the lower section of the merging droplet and a positive momentum flow field shown within the upper quadrant.[57]

This induces a positive radial flow causing the capillary bridge to impact the surface which creates a region of high-pressure which transforms the dynamic pressure of the droplet into static pressure.[57,63] Subsequently, a hydrostatic force is established along the liquid-vapour interface, that enhances the positive momentum field significantly to propel the droplet away from surface.[57] The following numerical results are validated against experimental results of jumping-droplet velocity against droplet diameter and dimensionless jumping-droplet velocity against Ohnesorges number. Ohnesorges number is known as the ratio of viscous to inertial and surface tension forces shown below.

$$Oh = \frac{\mu_l}{\sqrt{\gamma_{lv}\rho_l\lambda_c}} \tag{2.8}$$

When Ohnesorges number becomes less than one, the surface tension force prevails the viscous force acting on the droplet. Contrariwise, as Ohnesorges number increases (is

more than one), viscous forces are dominant over the surface tension force.[64] Therefore, Ohnesorges number can be used to describe governing kinetic forces that cause droplets to jump, regardless of its independence upon the velocity of the fluid.[64] As Ohnesorges number increases, the tendency for droplets to be ejected starts to weaken which is evidently seen in **Figure 2.9**.

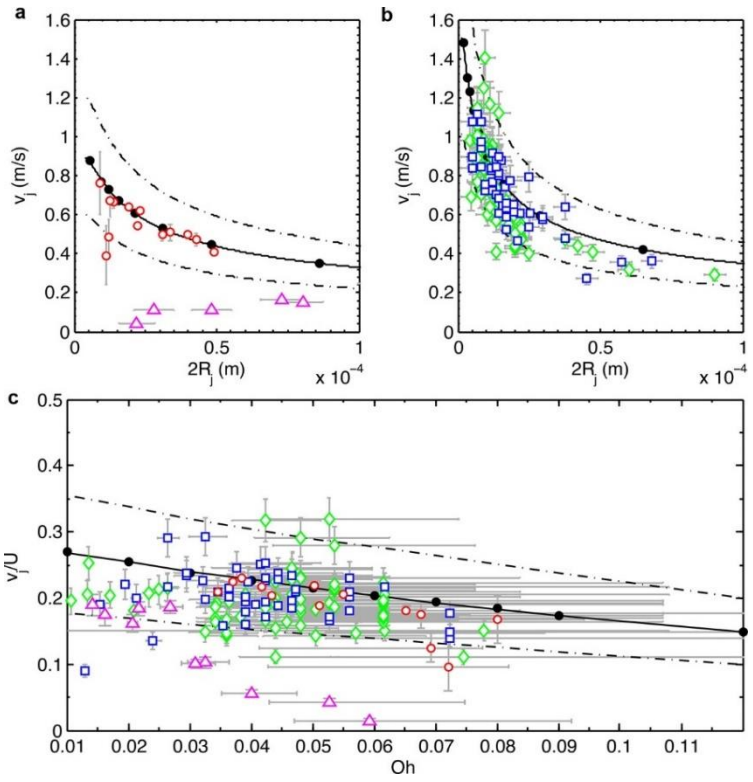

Figure 2.9. (a-b) shows the jumping-droplet velocity against droplet diameter with (c) illustrating the dimensionless jumping-droplet velocity against Ohnesorges number. The jumping velocity results shown in (a) is determined at a wall temperature of 5 °C where (b) is assessed at a wall temperature of 26 °C. The open circles displayed in (a) is the experimental results from the P2i-CNT surface and the open triangles is the experimental results from Boreyko et al.[38] In (b), the squares represent the performance of the P2i-CNT surface whilst the diamonds shows the data for the P2i-CuO surface. For (a-c) the black circles indicates the numerical results. The dashed lines reveal the numerical projection of the momentums' range for the jumping droplets.[57]

From **Figure 2.9c**, it is shown that as *Oh* increases from 0.01 to 0.12 the dimensionless jumping velocity has been halved. This is also illuminated in **Figure 2.9a-b**, where the jumping-droplet velocity declines with larger droplet diameters.

Using this theorem, Vahabi *et al.* managed to create coalescence-induced jumping droplets using multiple hydrocarbon liquids.[65] A wooden microgroove ridge was used to forcibly cause the droplets (adjacent to either side of the groove) to coalesce and eject. N-tetradecane and water-glycol was used to assess whether droplets with low surface tension (26.6 mN/m) or high viscosity (220 mPa·s) were more likely to jump. As both droplets coalesced on the microgroove, a liquid bridge was formulated between them that impacted the microgroove. This caused the symmetry of the droplet to be disturbed which shifted the centre of mass upwards. As a result, the kinetic energy created from coalesce was also released in this direction. **Figure 2.10** demonstrates the aforementioned process for a low surface tension liquid and a fluid with a large viscosity.

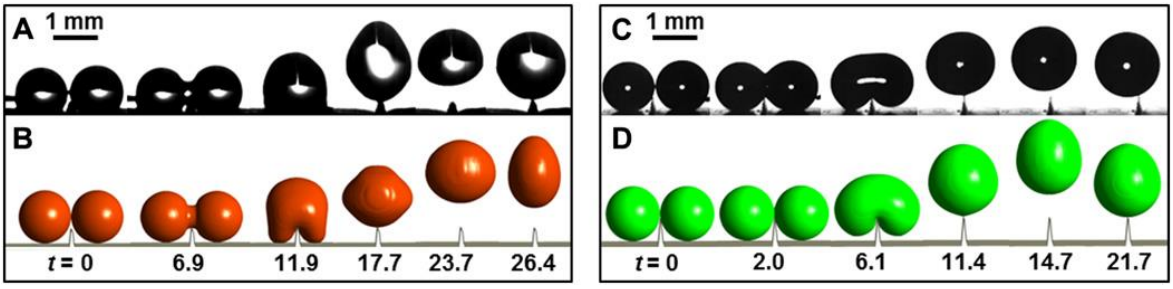

Figure 2.10. Coalescence-induced jumping droplet on a wooden microgroove. (a-b) shows jumping droplet process of a low surface tension liquid (n-tetradecane) compared against numerical results. (c-d) jumping droplet process for a highly viscous fluid (water-glycol) also compared against numerical results.[65]

According to the results, coalescence-induced jumping droplets was perceived for fluids with an Ohnesorges number more than one (viscous force is dominant). The main aspect

that allowed droplets to jump for such viscous liquids was related to the surfaces' high energy conversion efficiency which was equal to 18.8 %. This implies that the inertia force developed from droplet coalescence was more than the adhesive force of the fluid which is proportional to the viscosity of the fluid. Therefore, it can said, that the surface is superomniphobic. Superomniphobic surfaces are known to display contact angles more than 150° for both high and low surface tension fluids.[66] To encapsulate the complex physics associated with jumping droplets, the surface energy conversion efficiency is a vital factor to improve in order to apply jumping droplets in numerous applications. The enhancement in the conversion efficiency is related to the redirection of in-plane velocity vectors to out-of-plane velocity vectors.[65] Hence, superhydrophobic surfaces should be articulated to augment the surfaces' energy conversion efficiency further.

2.3.2. How Functional Surfaces are able to Enhance the Heat Transfer Performance of Heat Exchangers?

As previously mentioned, jumping-droplet condensation has been known to improve the heat transfer performance of heat pipes in comparison to dropwise condensation. This was first noted by Milijkovic *et al.* who established jumping-droplet condensation on a copper pipe.[35] A superhydrophobic surface was formulated on the tube by growing CuO nanoneedles using hydrothermal synthesis. The nanoneedles were then hydrophobized by depositing fluorinated silane upon the structures. The surface morphology of the nanoneedles with and without silane can be seen in **Figure 2.11**.

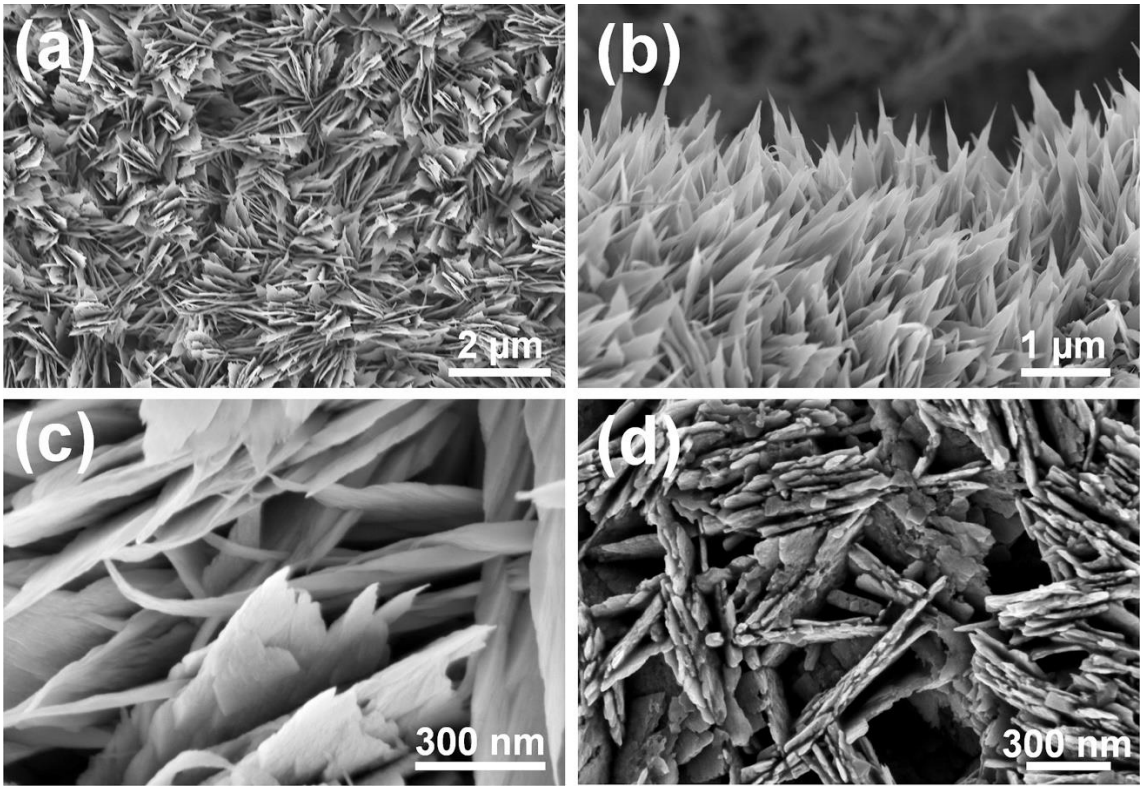

Figure 2.11. Field emission scanning electron microscopy (FESEM) images of CuO nanoneedles, (a) Topside view of CuO nanoneedles without silane. (b) Horizontal view of nanoneedles also without silane. (c) Topside view of nanoneedles at a larger magnification, illustrating cavities spacings between them. (d) Silane deposited nanoneedles at greater magnification showing an increase in the nanoneedles' thickness ($\approx$10 nm).[35]

The combination of low surface roughness (devised from the nanoneedles) and low surface energy (deposition of fluorinated silane) rendered the surface to be highly superhydrophobic, reporting to have an advancing contact angle of 172.0° ± 3.2° with a receding contact angle of 167.8° ± 3.2°.

By subjecting the superhydrophobic tube under subdued supersaturation ratios (1.08), the surface displayed large droplet removal rates as droplets were continuously being ejected from the surface once they coalesced. The critical radius of the droplets were found to be

≈7 μm as they coalesced. In addition, large droplet nucleation number densities were seen which strengthened the droplet removal rates further as more number of droplets are able to coalesce. Conversely, using a hydrophobic copper pipe demonstrated recurrent dropwise condensation where macroscopic droplets were removed off the surface by gravitational forces once they reached their capillary length (equal to 2.7 mm in diameter). The capillary length, κ^{-1}, is known as the ratio of the Laplace pressure to the hydrostatic pressure of a droplet which is distinctive for each fluid as shown below:[67,68]

$$\kappa^{-1} = \sqrt{\frac{\gamma_{lv}}{\rho_l g}} \tag{2.9}$$

where g is the gravitational acceleration (m^2/s). However, at larger supersaturation ratios (1.54) the nucleated droplets on the superhydrophobic surface were pinned on the surface (Wenzel state), which eventually saturated the entire surface and caused the nanoneedles to be submerged. Notably, this effect is shown to be irreversible as water was still confined within the nanocavities after condensation was finished. At nanoscale spacings, surface tension is amplified substantially due to the increase in van der Walls forces between the molecules which makes it difficult to dry the nanocavities (evaporate).[4,69-71] **Figure 2.12** demonstrates the condensation performance on a superhydrophobic tube at different times with two levels of supersaturation ratios.

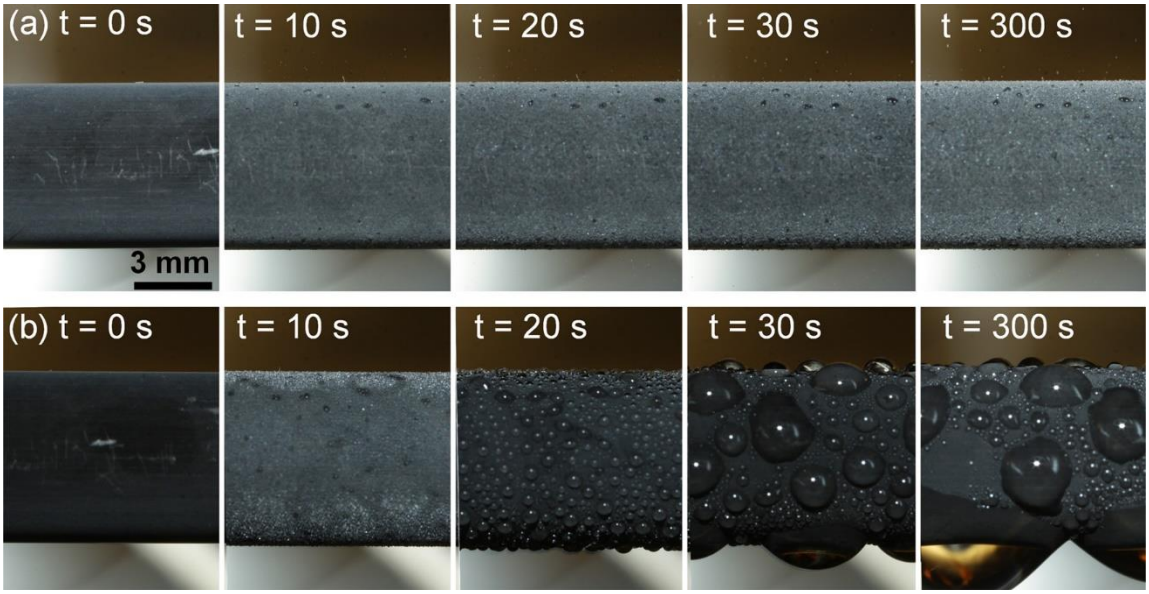

Figure 2.12. (a) Consistent jumping droplet condensation for a low supersaturation ratio (1.08) at a constant vapour pressure of 2700 ± 68 Pa. (b) Flooded condensation at high supersaturation ratios (1.54) where droplets are in a Wenzel state as nanoneedles are flooded.[35]

The superhydrophobic surface illustrated a heat transfer coefficient of 92 ± 12 kW/m^2·K which is 30% higher than the heat transfer coefficient observed from the hydrophobic surface. Although, at high supersaturation ratios, the flooding condensation behaviour caused the heat transfer coefficient to be reduced by 40%. The Wenzel state of the droplets resulted in the droplet departure radius to be enlarged to 2 mm which corresponds to a larger convective thermal resistance that effectively deteriorates the heat transfer. Further to note, the surface temperature is not steady state, but transient, causing the heat transfer results to be additionally affected.[72] Nevertheless, the subcooling temperature used within their experiments was 0.8 K which is too minute to be deemed as a factor against surface flooding.[73] It is still unknown however, what particular aspect of the nanostructures' design allowed jumping-droplet condensation to occur.

To explore this, Wen *et al.* fabricated a two-tier superhydrophobic surface containing nanowires with microcavities.[73] The microcavities allows the nucleation density and droplet departure radius to be regulated by manipulating the Laplace pressure gradient of droplets that nucleate within the cavities.[74] This is shown clearly within **Figure 2.13**.

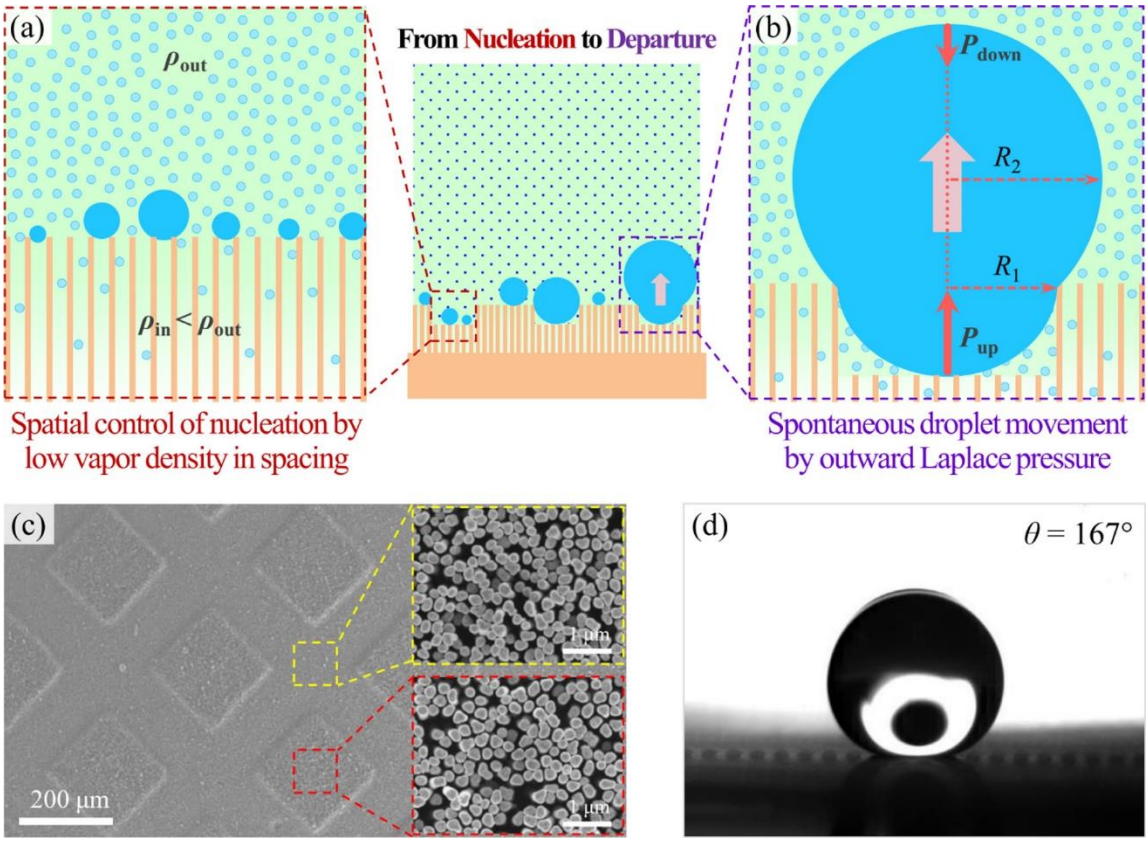

Figure 2.13. (a) Schematic diagram showing how the highly dense nanowires can minimise condensation upon the surface by establishing a low vapour density from the interstices. (b) Illustrates the procedure of droplet nucleation and removal within the microcavities. (c) SEM image of the two-tier nanowire surface with equally spaced microcavities. (d) Contact angle of the superhydrophobic surface for a 5 µL water droplet.[73]

When the droplets inside the microcavities grow larger than the width of the cavity, a pressure gradient is formulated within the droplet causing it to propel itself to the top of

the nanowires. As indicated in **Figure 2.13**, the part of the droplet that is inside the microcavity remains under high pressure whilst the upper section of the droplet (that is outside the microcavity) contains low pressure since the upper radii of the droplet (R_2) is greater than R_1. Using such hierarchical surfaces can control the growth of the droplet between the lower and upper section of the droplet. This allows the Laplace pressure gradient within the droplets to increase so that the large pinning forces formulated at large subcooling temperatures can be overwhelmed.[75,76] Therefore, hierarchical nanoscale structures may be able to stabilize jumping-droplet condensation at large subcooling temperatures ($\geq$ 12 K).[73] Furthermore, Wen *et al*. managed to sustain jumping-droplet condensation for subcooling temperatures as high as 28 K from utilizing three-dimensional superhydrophobic copper nanowire structures.[77] The 3D nanowires enhanced the nucleation rate of droplets and the spatial control of their nucleation sites by introducing large aspect ratio nanowires and minimizing their pitch size. **Figure 2.14** represents an abstract image of the 3D copper nanowire network and its' concept which is validated against its' heat transfer performance.

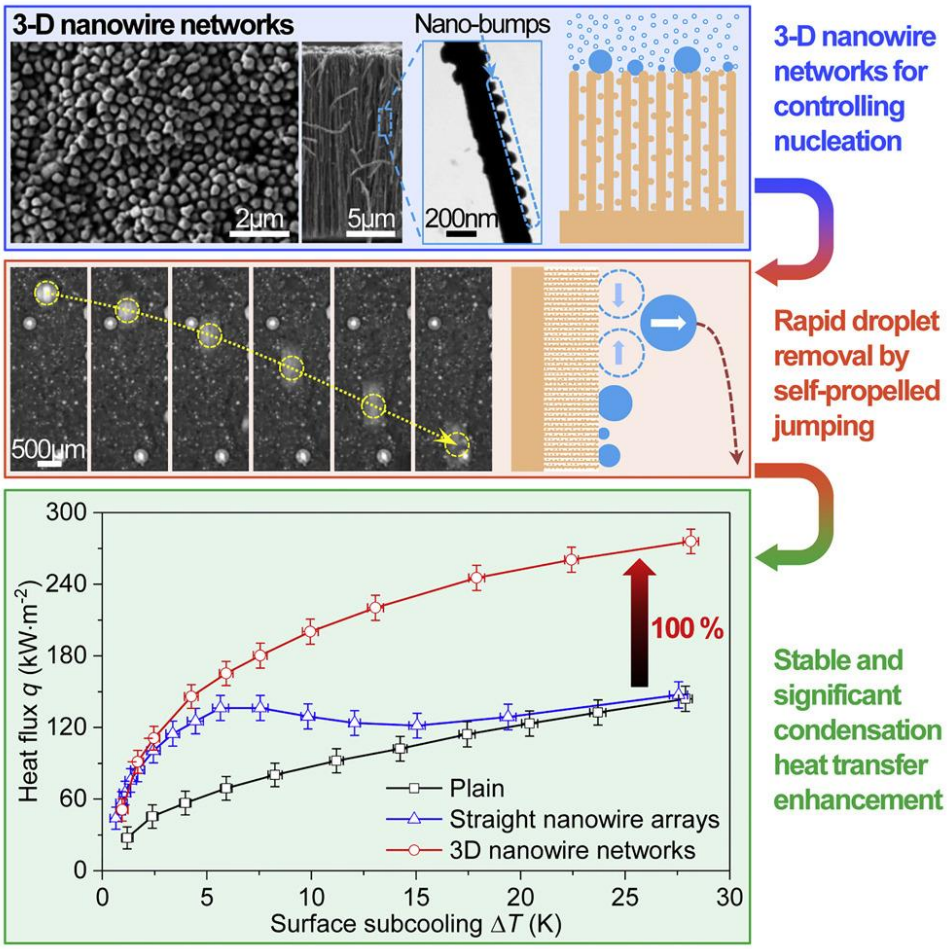

Figure 2.14. Longstanding jumping-droplet condensation achieved on the 3D copper nanowire surface. From the densely packed nanowire array, any microdefects in the nanowire array are eradicated. As the nanowire array allowed greater spatial nucleation control, the heat flux is improved by 100% in comparison to a standard hydrophobic surface.[77]

Moreover, Mou *et al.* generated jumping droplet condensation up to a subcooling temperature of 20 K.[78] This was founded by fabricating a micro porous superhydrophobic surface which contained nanoscale dendritic structures upon its interface. Notably, this surface is comparable to the hierarchical superhydrophobic surface established by Wen *et al.*[73] Two different sized pore diameters, 20 and 50 μm were constructed to determine the optimum size to elongate the jumping-droplet condensation

phenomenon at high subcooling temperatures. Then, dendritic nanostructures were grown on the surface randomly with no specific direction. The concept of using this feature was for droplets to be propelled in various directions which in turn, increases the volume of condensate removed from the surface as neighbouring droplets are carried alongside.[79] Additionally, the dendritic shape of the nanostructures can increase the number of nucleation sites for vapour clusters to form on,[80] which will increase the droplet removal frequency.

The 20 and 50 µm porous superhydrophobic surfaces both showed jumping-droplet condensation having a critical coalescence radius of approximately 10 µm.[36] The major difference between them was the number of jumping droplets, which were found to be greater on the 20 µm porous surface than the 50 µm. This was due to the spacing between the pores being smaller which consequently, increased the rate of droplet coalescence hence its droplet removal frequency. As a result, the heat transfer coefficient on the 20 µm surface was significantly larger than the 50 µm surface with particularly the hydrophobic surface. Nevertheless, when the subcooling temperature was raised over 4 K, the number of jumping-droplets began to decline for both superhydrophobic surfaces. Subsequently, their heat transfer coefficients also began to drop with the 50 µm surface falling even further. Furthermore, increasing the subcooling temperature over 7 K led to a condensate film articulating across the superhydrophobic surfaces. Increasing the subcooling temperature further only increased the film thickness as more droplets were being pinned on the surface. In spite of this, the superhydrophobic surfaces still managed to create fractional jumping-droplet condensation up to 19 K. At this point, both surfaces' heat transfer coefficient and heat flux had fallen below of the hydrophobic surface which consistently showed dropwise condensation throughout.

To elaborate upon the surfaces' heat performance, Zhang *et al.* used such porous micro/nano superhydrophobic surface at even larger subcooling temperatures, where its performance was compared against a plain and a hydrophobic surface.[78] **Figure 2.15** represents the heat transfer coefficient and heat flux for each surface with additionally validating the results against Nusselt's model for the plain surface.

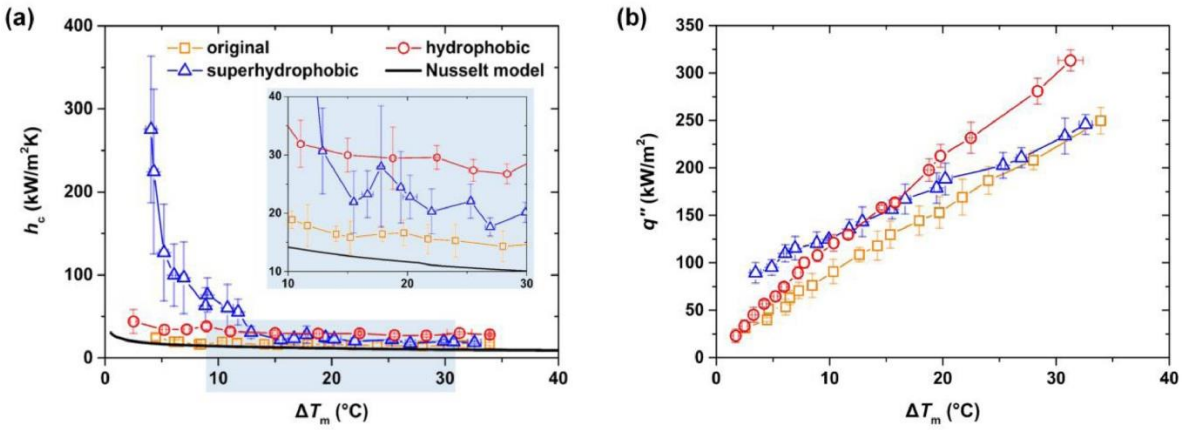

Figure 2.15. Heat transfer performance of a 20-µm porous superhydrophobic surface with nanoscale dendrites benchmarked against a plain and hydrophobic surface. a) heat transfer coefficient with b) being the heat flux against subcooling temperature up to a range of ~ 34 K.[78]

The immediate illustration of surface flooding at lower subcooling temperatures was due to the use of porous structures. Surfaces that are mainly porous will effortlessly be flooded when brought under condensation. This effect is known as capillary condensation.[81,82] In correspondence to the Kelvin equation,[82] it is known that the vapour pressure within a porous (or cylindrical) interstice is lower than the saturation pressure from the surrounding environment as seen in equation below. The declination in pressure is given due to the concave meniscus developed as the liquid soaks the capillary walls.

$$RT_w \ln \frac{P_v}{P_{sat}} = -\frac{2\gamma_{lv} V_m \cos\theta_p}{r_p} \qquad (2.10)$$

r_p is known as the radius of the capillary (μm), θ_p is the contact angle at the liquid-solid interface (walls of the pore), V_m is given as the liquid molar volume (m^3/mol), T_w is the temperature of the surface (K), R is wildly known as the specific gas constant (J/mol·K), P_v is the vapour pressure (Pa) with P_{sat} being the saturation pressure (Pa). Notably, on the right hand side of the equation, a minus sign is added to define the negative radius of curvature developed on a concave meniscus.[83] As the pressure of the environment is greater than the pressure within the pores, the difference in pressure (generally known as the Laplace pressure) drives the vapours through the pores causing capillary condensation. As a consequence, the local pinning force of droplets (or the surfaces' adhesion force) becomes greater at small subcooling temperatures. Nucleating droplets will then start to transition from a Cassie-Baxter to Wenzel state.[84]

Peng *et al*. demonstrated jumping-droplet condensation on a hierarchical microgrooved superhydrophobic surface, however, it was noted that the some droplets naturally coalesced before they jumped whilst some were "forced".[85] The usage of such microgrooved surfaces was stimulated by the works of Vahabi et al. mentioned in the previous chapter whom developed the concept idea.[65] As stated previously, microgrooved surfaces are able to redirect the planar velocity vectors within the droplet towards the lateral direction. Subsequently, this increases the magnitude of the lateral jumping velocity of droplets after coalescence. Testing this superhydrophobic surface under subcooling temperatures less than 5 K revealed a 90% increase in heat flux compared to a hydrophobic surface. Interestingly, at subcooling temperatures beyond 17.9 K, coalescence-induced jumping droplet condensation changed to coalescence-induced sweeping condensation where droplets were swept off the surface at a much larger diameter ranging from 500 to 800 μm. The sweeping process was found to be independent of gravity as shown from the Bond number of droplets given as:

$$Bo = \frac{\rho_l g {\lambda_c}^2}{\gamma_{lv}} \quad (2.11)$$

Bond number is defined as the ratio of gravitational to surface tension force of a droplet. The Bond number calculated from the experiment was determined to be between 0.038 and 0.098, which shows that the surface tension force is responsible for the droplets being swept off the surface. This transition from droplets jumping to sweeping led to a 24% reduction in heat flux as subcooling temperatures were elevated to 24 K. Yet, the superhydrophobic surface still outperformed the hydrophobic surface, due to the droplets' high nucleation rates and small departure diameters. Since the hydrophobic surface allowed droplets to be driven off mainly by gravity, removing droplets was found to be more difficult as droplets remained on the surface longer. Remarkably, droplets that nucleated within the microgroove were "stretched". A droplet that is stretched contains a positive Laplace pressure gradient due to the difference in internal pressure between the upper and lower menisci. The idea behind stretching a droplet was related to the works of Wen *et al.*[73] Furthermore, when a stretched droplet merges with a smaller spherical droplet at the surfaces' interface, a sudden pressure drop will be experienced in the upper menisci. The pressure gradient developed from this procedure increases the driving force for droplet propulsion.[86]

Not much attention has been made towards using liquid-repellent surfaces within binary fluid mixtures, as further comprehension is required of its intuitive physics compared to singular condensate fluids. It is observed that binary fluid mixtures have a surface tension gradient across its hydrodynamic length.[87] This factor promotes a Marangoni flow which affects the kinetics and internal dynamics of how condensate droplets move along the surface.[88,89] Utaka *et al*. investigated condensate drop movements of a binary fluid mixture, which consisted of water and ethanol, on a brass surface coated with TiO_2 having

a surface area of 20 x 20 mm^2.[90] It was found that Marangoni dropwise condensation was created upon the brass surface, due to the difference between the surface tension of the fluids. This established a surface tension gradient across the interior of the condensate droplets. Condensate drops were found to move along the surface from the difference in bulk surface temperature gradient, shown from either side of the droplet.[87] The main difference between conventional dropwise condensation and Marangoni condensation are that the thickness of the condensate film is not uniform in Marangoni condensation.[90] Thicker condensate areas are formed as the surface temperature is higher than the condensate in thinner areas, due to the difference in surface tension across its length. The movement of the droplet can be enhanced from increasing the Marangoni force's instability, after amplifying its bulk temperature gradient. In consequence, as the Marangoni force increases, the droplet velocity also increases, which gives rise to thermocapillary stresses within the liquid that promotes a shear stress gradient along the droplet.[91,92] Hence, the kinetics and kinematics that Marangoni drops produce on the surface must be recognized for functional surfaces to control its performance. Droplet movement in fluid mixtures is shown to be mainly dominant towards thermocapillary forces than just capillary forces.

On the other hand, for an absorber heat exchanger, a completely wetted surface (superhydrophilic) is favoured due to the increased absorption rate of water-vapour upon the mixed liquid. This is exemplified by Zheng *et al.* who fabricated superhydrophilic tubes by fabricating un-coated nanoneedles through chemical etching.[93] As such, the superhydrophilic tube demonstrated a contact angle of less than 5°. The heat transfer performance of the superhydrophilic tube were then compared against a modified hydrophilic tube and a plain copper tube by measuring the tubes' heat transfer coefficient. It was discovered that, for low inlet mass flow rates, the heat transfer coefficient of the

superhydrophilic tubes was at least twice as high compared to the hydrophilic and plain surface as the liquid was able to spread and wet the entirety of the tube whilst also producing a thin liquid film. Increasing the inlet velocity further did not change the surface coverage of the liquid but, instead, increased the film thickness of the liquid which consequently reduced the heat transfer coefficient to become equal to that of a plain or hydrophilic surface as demonstrated in **Figure 2.16** where the mass flow rate of the fluid is characterised as the Reynolds number.

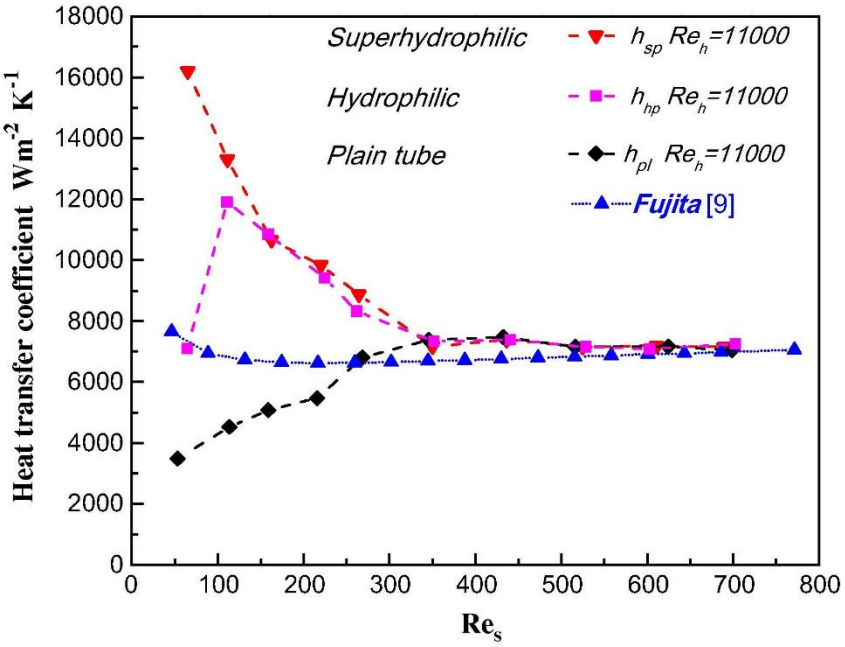

Figure 2.16. Heat transfer coefficient of an absorber tube against the fluids' Reynolds number for a superhydrophilic, hydrophilic and plain tube. The blue line consist of the experimental results conducted by Fujita *et al*. where their results were compared against.[93]

Going back towards micro-porous surfaces, Lee *et al.* utilized micro-porous structures upon a copper tube to enhance the heat transfer coefficient of absorber heat pipes.[94] As opposed to the works of Zhang *et al.* the micro-pores in this case were left bare without any nano-scale topology to allow the liquid to be distributed across the tube through

capillary action within the porous network as previously explained through the Kelvin equation.[95] The micro-porous layer was generated through sintering copper powders on the interface of copper tubes which illustrated an average porous diameter of 75 µm. By comparing the modified tube to a plain copper tube, the porous tube showed to amplify the heat transfer rates by twice as much. This was accomplished by increasing the liquids' affinity at low Reynolds numbers (mass flow rates) in contrast to the plain tube. **Figure 2.17** visualises the falling-film flow performance of water upon the functional and plain tubes at various Reynolds numbers.

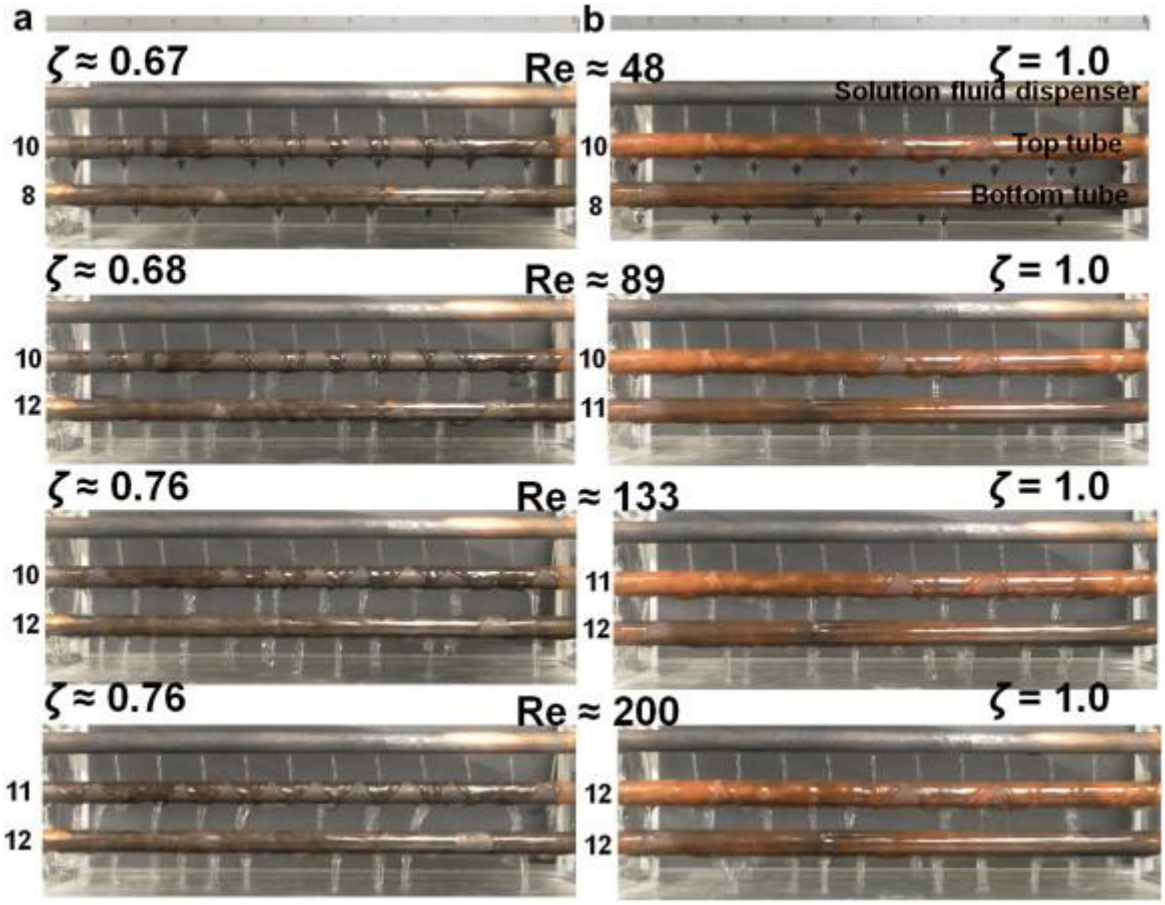

Figure 2.17. Falling-film flow behaviour at different Reynolds numbers on a plain copper tube (a), and a micro-porous tube (b) ζ represents the solution wetting ratio of the tube. The numbers shown at the sides of the images represent the number of droplet nucleation sites observed below each tube.[94]

To further note, Kim *et al.* created roughened tubes by introducing micro-scale hatches upon the tubes' surface.[96] It was hypothesised that, the micro-hatches would allow the liquid to spread effortlessly as the liquid trapped within the micro-channels would act as an adhesion promoter. The concept of this idea is shown to be analogous to the previously discussed micro-porous surfaces. Therefore, in comparison to a smooth tube, the micro-hatched tube demonstrated increased wettability ratios up to 100% coverage for all tube rows. Subsequently, this allowed increased rates of heat and mass transfer as observed from the increased rate of water-vapour absorption for minimal inlet flow rates. Another way to promote hydrophilicity of a heat pipe is through plasma treating the surface which was conducted by Yoon *et al.*[97] The heat and mass transfer performance of the tube were compared with a bare and floral tube where the surface topology of the tube is modified at a macro-scale. Regardless, as expected, the hydrophilic tube promoted up to 35% higher heat transfer coefficients than of the bare and floral tube. This was attributed to the increased wetted area of the tube at a given mass flow rate.

Whether functional surfaces are used either for condensation or absorber applications, both systems aim to reduce the film thickness of the condensate upon the heat pipes to diminish the thermal resistance of the surface in order to increase the heat transfer coefficient of the surface. The main difference is that absorbers ideally want a surface that can fully cover the interface of the tube as thinly as possible to enhance heat and mass transfer rates whilst the other (the condenser) desires to minimise the liquid coverage to only improve heat transfer rates. Thus a superhydrophobic surface or a superhydrophilic surface is ideal for each individual system. Nonetheless, as discussed beforehand, such functional surfaces do not contain a long life span due to external forces damaging the fragile micro/nanostructures which are established within heat exchangers. Such scenarios are explained within the next sub-chapter.

2.3.3. What Can Affect the Performance of Engineered Surfaces?

Functional surface damage within heat exchangers is often caused by either vapour shear flow or droplet impaction.[98] The additional hydrodynamics these aspects invoke upon the surface will reduce the stability liquid-repellent surfaces.[45] It is worthy to note that, heat exchangers will contain various flow regimes parallel to the surface of the tubes. Such flow regimes are highlighted as stratified, annular, and spray flows.[8] These regimes should be tested upon functional surfaces to determine their compliance for industrial standards. Ding *et al.* configurated a numerical simulation of the flow regimes experienced on heat pipes against several horizontal stacked tubes.[98] The methodology used to capture the liquid-gas interface of the fluid was a Volume-of-Fluid method which was then validated against Killion *et al.* experiment as presented in **Figure 2.18**.

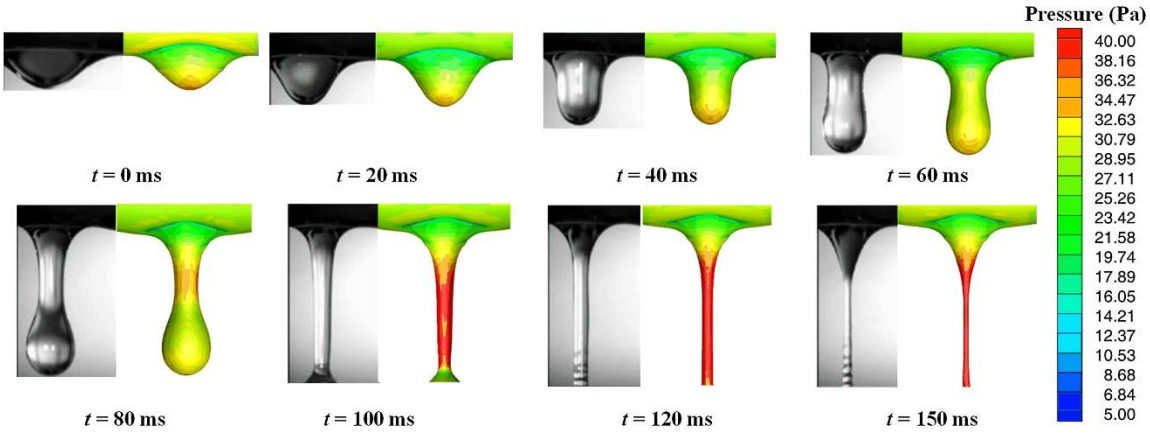

Figure 2.18. Direct comparison of simulation results against experimental results by Killion *et al.*[99] for the droplet detachment process from the first tube.[98]

By altering the contact angle of the surface and the inlet flow rate, two different types of flow patterns were seen upon the tubes which were dropwise, and jet flow. It was found that dropwise flow tended to shift towards filmwise flow (jet flow) when the Reynolds number of the flow increased that is proportionate to inlet velocity over the surface. Although, the transition time between the two flows is dependent upon the fluids' Galileo

number,[98] which is equal to the ratio of the fluids' gravitational force to the viscous force. More details of the Galileo number in contrast to falling-films will be shown in Chapter 4.

Remarkably, for horizontal tubes, droplets will only begin to detach off its' surface once the gravitational force becomes larger than the surface tension force at the fluids' interface. When detached droplet descends and impacts the tube beneath, the droplet will spread both circumferentially and axially. In this instance, surface tension, inertia, and gravitational forces dictate the flow pattern of the flattened droplet.[98] This is elucidated in **Figure 2.19**. Further details on droplet impaction will be elaborated on in Chapter 2.5.3.

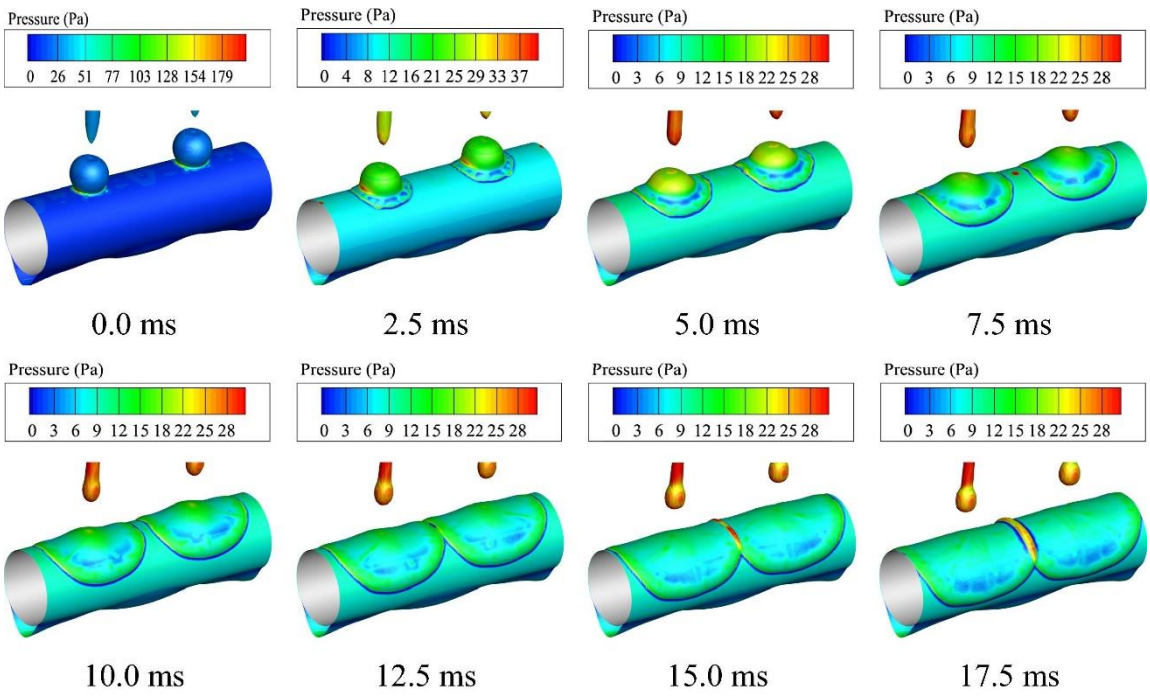

Figure 2.19. Motion of droplet spreading whilst impacting upon the second tube, showing the hydrostatic pressure of the liquid at the interface.[98]

Focusing on vapour shear flow, Torresin *et al.* studied the effect of forced convection upon a superhydrophobic copper nanostructured during condensation.[45] Vapour velocities were configured across the surface to determine its impact upon the surfaces'

heat flux and heat transfer coefficient. This was done by measuring the droplet removal rates once steady state condensation began. Introducing vapour shear flow adds the effect of drag force on the surface. Therefore, when the drag force dominates the surfaces' adhesion force, droplets started to be removed off the surface at smaller diameters.[45] This translates to an increase in heat and mass transfer as smaller droplets contain a lower thermal resistance.[75,100] It is noteworthy that the superhydrophobic nanostructures retained its heat transfer performance for 5 days (as shown in **Figure 2.20**).

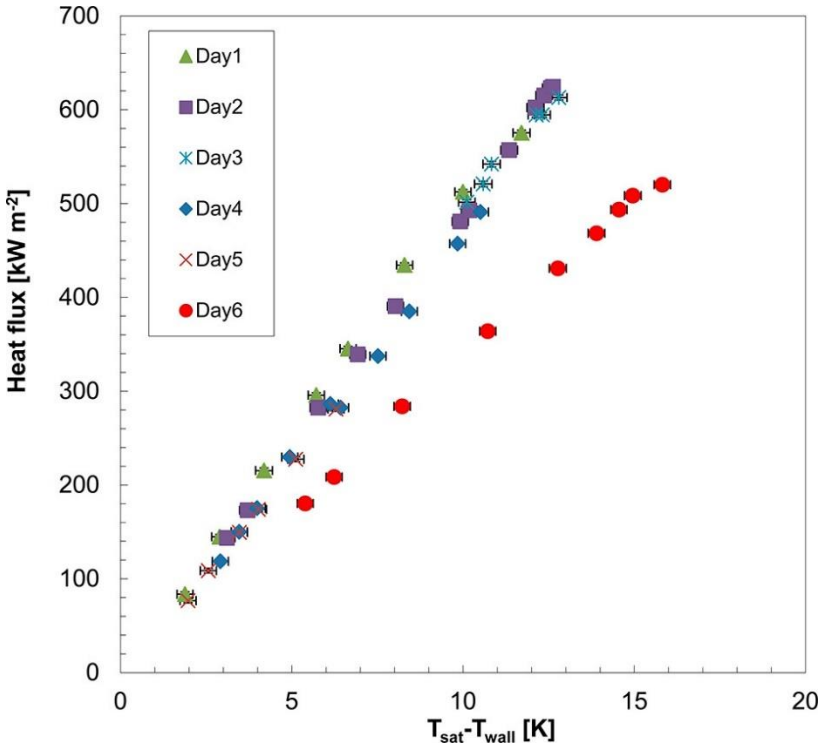

Figure 2.20. Heat flux performance against the subcooling temperature of the superhydrophobic surface determined over 6 days using a vapour velocity of 12 m/s at 110°C. Heat flux was found to decrease on the 6th day due to surface degradation.[45]

On the 6th day however, the heat flux began to fall by 33% as the nanostructures became damaged due to excessive vapour shear flow. Due to the damaged superhydrophobic surface, the condensation behaviour transitioned from dropwise to filmwise condensation.

Likewise, Sharma *et al.* established dropwise condensation on a superhydrophobic copper microcones with papillae-shaped nanostructures upon its interface.[101] Due to the shape of the microcones, when droplets nucleate within the cavities, a favourable Laplace pressure gradient is created from the change in the upper and lower meniscus radius. A meniscus was allowed to form at the bottom of the microcones due to nanostructured surface which minimised the surfaces' adhesion force.[102] The notion of manipulating the Laplace pressure gradient of droplets is similar to the micro/nanostructured surfaces mentioned in Chapter 2.3.2. The mechanics of droplet discharge from the microcones' design is illustrated in **Figure 2.21**. The ejection of droplets was determined by the asymmetrical coalescence which was aided by the truncated microcone design. From coalescence, the Laplace pressure gradient within the merged droplet became unbalanced, which allowed droplets to be ejected from the microcavities effortlessly as the droplets' pinning force was overwhelmed.[103]

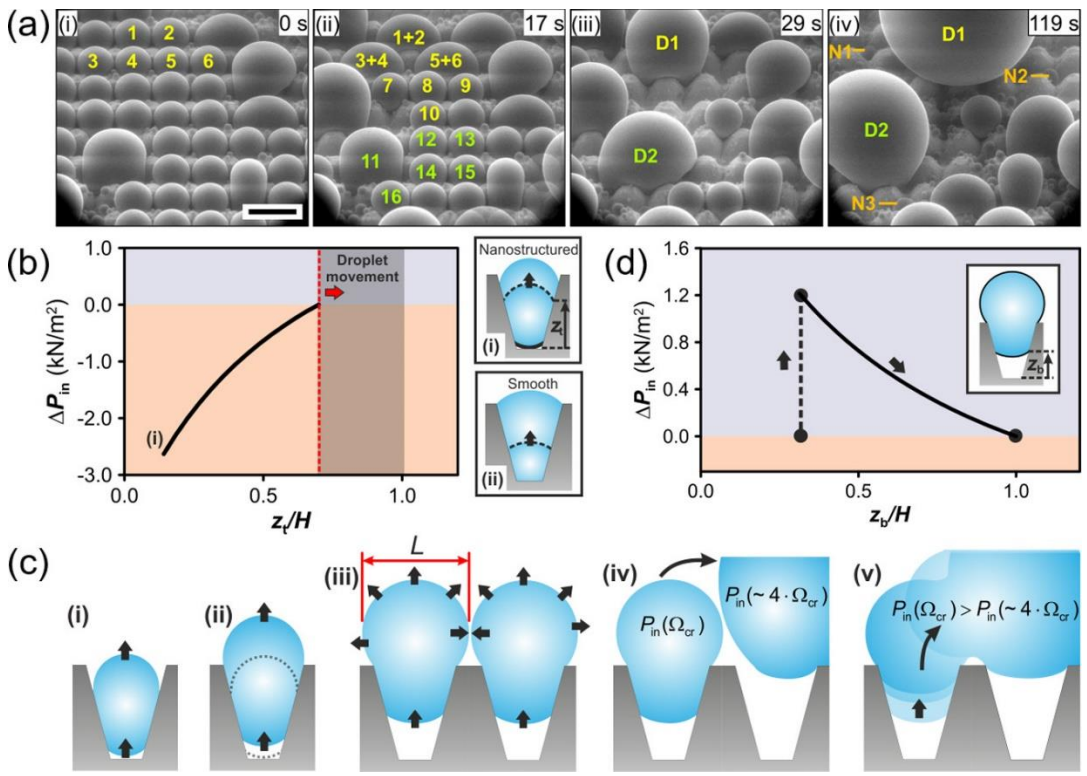

Figure 2.21. Procedure of droplet ejection from within the microcones to coalescence. a) (i) Nucleating droplets are initially retained on the surface, (ii, iii) droplets begin to merge with neighbouring droplets of different size allowing smaller droplets to be swept off, (iv) droplet discharge cycle is replicated seen from the nucleation of new droplets (shown in N1, N2 and N3). b) Laplace pressure gradient of droplets within the microcavities against the normalized height of the microcones at the upper meniscus of the droplet. c) Schematic diagram of stages of droplet propulsion within the microcones, Ω_{cr} is given as the critical radius. d) Laplace pressure of a nucleating droplet against the normalized height of the microcone at the bottom section of the meniscus.[101]

The superhydrophobic surface was then tested under various vapour velocities to see its effect on droplet shedding.[101] Increasing the vapour velocity from 3 to 9 m/s caused an increase in the heat transfer coefficient by 37%. Its amplification is elucidated from the reduction in the droplet departure diameter from 2.5 to 1.3 mm. Therefore, it can be said that increasing the vapour velocity across the surface will increase the surfaces' heat flux

due to droplets being removed off the surface at smaller diameters. This notably improves the heat transfer area due to the enhancement in droplet discharge.[104] To see the surfaces' longstanding performance, the superhydrophobic surface was subjected to vapour velocities of 9 m/s for 5 days. Resembling Torresin *et al.* results,[45] the surface became damaged after 5 days as filmwise condensation was seen at the centre of the sample. However, it should be stated that noncondensable gasses may affect the heat transfer results due to the presence of a diffusion barrier that is retained adjacent to the surface.[105] The implications of noncondensable gasses is explained in the next sub-chapter.

2.3.4. Influence of Non-condensable Gasses During Condensation

Noncondensable gasses (NCG) are ubiquitous in condensation environments even when placed under vacuum.[106] Whilst condensation occurs, a thin layer of noncondensable gas is articulated over the cooled surface.[107] The thin boundary layer acts as a diffusion barrier for vapour molecules to protrude through making it more difficult to reach the subcooled surface. As a consequence, the rate of heat and mass transfer of the condenser is severely diminished as the rate of condensate produced is less.[108] This is due to the vapour pressure near the surface to be reduced as it is replaced by the pressure of the diffusion barrier.[109] In turn, the saturation temperature adjacent to the surface is decreased, causing the working fluid to cooled further in order for condensation to happen. Therefore, the heat transfer coefficient and heat flux of the condenser is reduced significantly. This can be as much as 50% just by having 0.5% of NCG within the vicinity.[110,111] In order to compensate for the loss, the total heat transfer surface area of the condenser must be at least twice its original value. As previously stated, the capital costs of the heat exchanger will undoubtedly increase.

To further discuss on Zhang *et al.* works as mentioned in Chapter 2.3.2, they also investigated the effect of NCG on their hierarchical microporous superhydrophobic surface with a pore diameter of 20 μm.[78] When the surface was exposed to 1.5% concentration of NCG, jumping-droplet condensation was seen on the superhydrophobic surface. As expected, dropwise and filmwise condensation was established on the hydrophobic and hydrophilic surfaces. Although, when the NCG concentration kept increasing up to 27.8%, the heat transfer coefficient for all surfaces showed to decrease. This was due to apparent increase in the number of Wenzel droplets the superhydrophobic surface illustrated. **Figure 2.22** gives the heat transfer coefficient results for all three surfaces at different NCG concentrations.

By increasing the NCG concentration level, the NCG boundary layer thickness proportionally rises which is the reason why the heat transfer coefficient decreases at larger concentrations. As indicated by **Figure 2.22**, the superhydrophobic surface demonstrated the largest amount of heat transfer due to the presence of jumping droplets which enhanced the vapour diffusion to the surface.

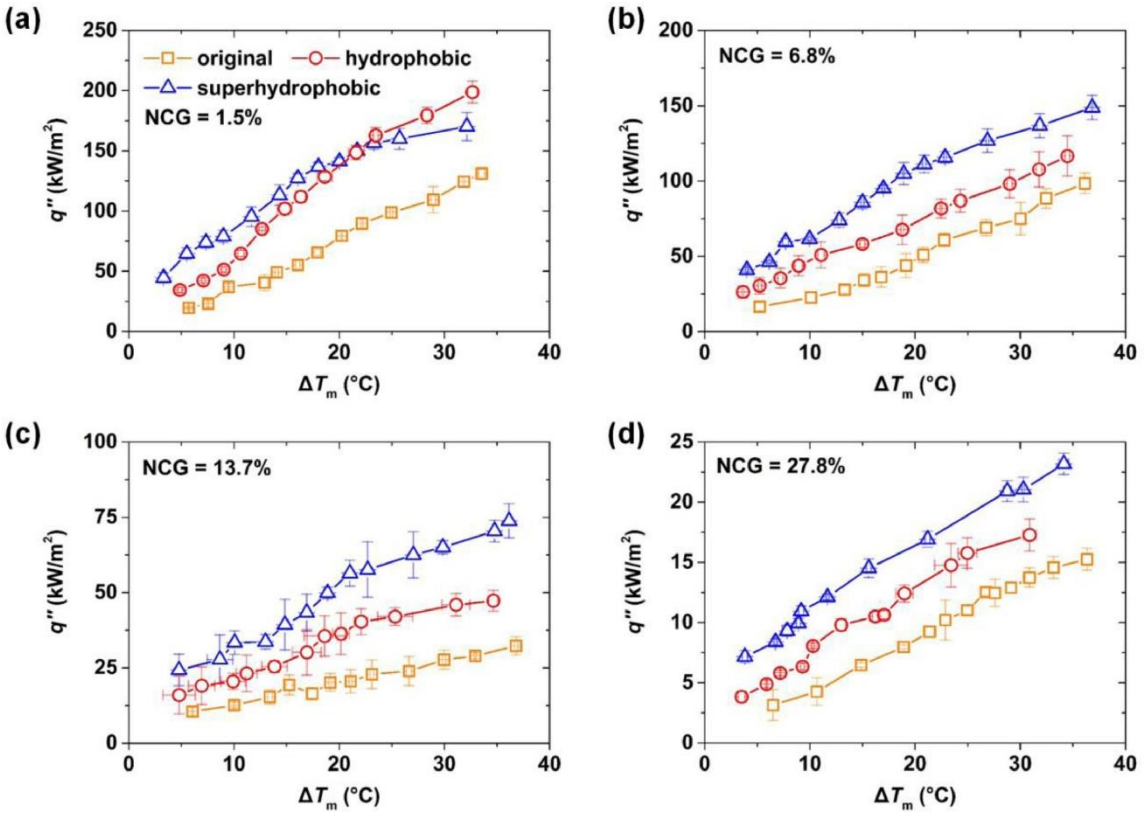

Figure 2.22. Heat transfer coefficients for a hydrophilic (plain), hydrophobic and superhydrophobic surface at different concentrations of noncondensable gas against various subcooling temperatures. a) 1.5%, b) 6.8%, c) 13.7% and d) 27.8%.[78]

The propelled droplets were able to penetrate through the NCG boundary layer of which dropwise condensation was unable to do so. This was seen on the hydrophobic surface where droplets were simply swept off the surface by gravity. The effect of NCG concentrations on the superhydrophobic and hydrophobic surface visually can be seen in **Figure 2.23**. It should be noted that, the NCG became ensnared within the microporous structures which prevented surface flooding (filmwise condensation) to occur at high subcooling temperatures. Nonetheless, the heat transfer coefficient was still lowered at large NCG concentrations.

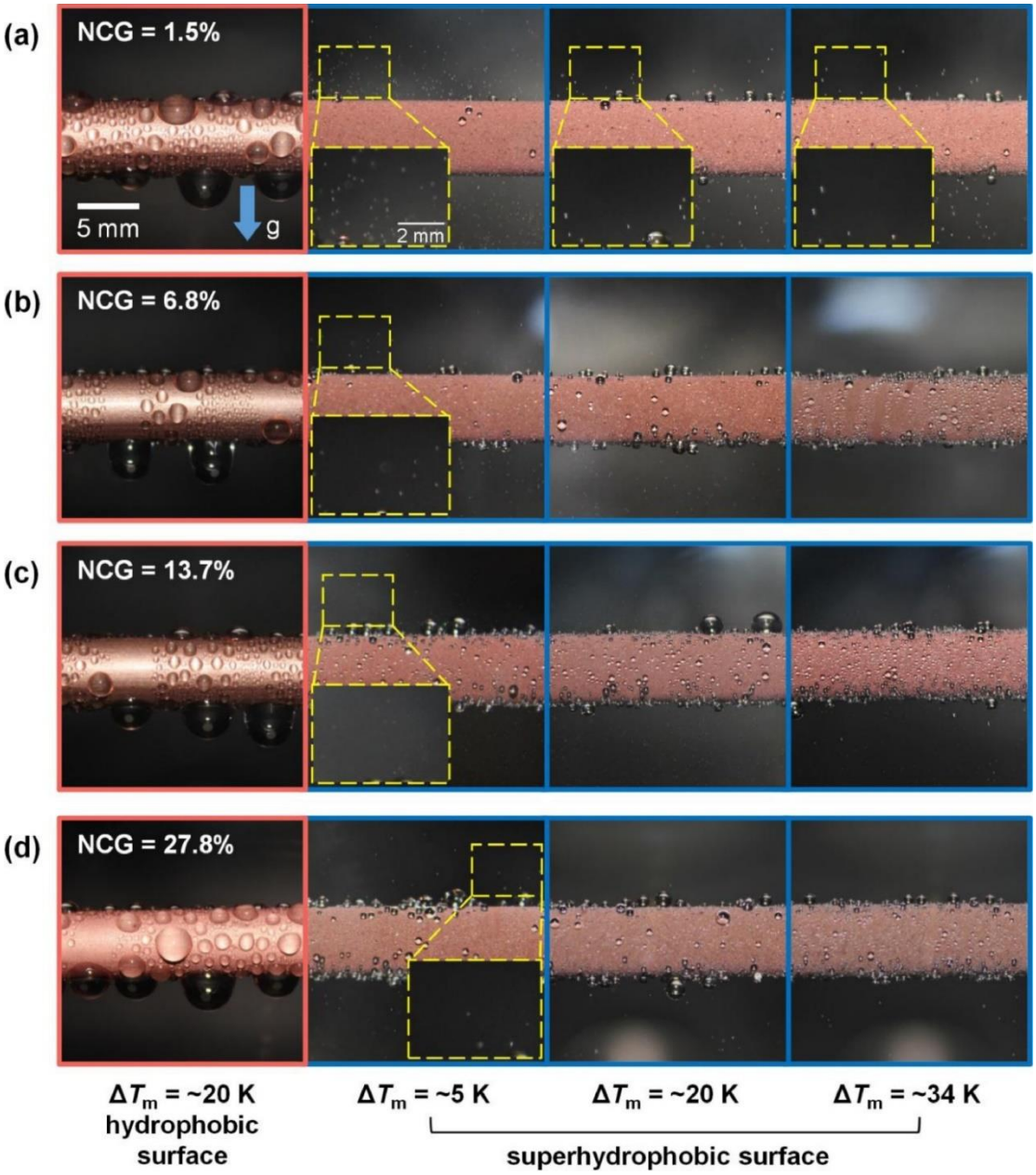

Figure 2.23. Conduct of condensation on the superhydrophobic and hydrophobic surface at several noncondensable gas concentrations with different subcooling temperatures. On the superhydrophobic surface, jumping-droplet condensation begins to shift towards dropwise condensation at elevated subcooling temperatures and noncondensable gas concentrations.[78]

To further elaborate, Zheng *et al.* conducted a numerical simulation of dropwise condensation under NCG that was substantiated against experimental results.[112] The

nucleation of droplets were determined from the heat and mass transfer process between the hot vapour and the cold surface where condensation took place. As droplets grew at numerous diameters, the Knudsen layer theorem was used to describe the transition between the continuum and kinetic limit. The droplet growth model presented was cross verified against the heat flux results from other condensation experiments. From the existence of the NCG diffusion barrier given adjacent to the surface, the nucleation density of droplets was found to decline. **Figure 2.24** depicts how NCG particles affect the rate of water vapour transport towards the condensate droplet whilst nucleation occurs. Therefore it can be said that the presence of NCG creates a diffusion resistance to water vapour molecules which decreases the formation and growth of condensate drops. This can be also seen from Ma *et al*. who observed for a hydrophilic and hydrophobic when increasing the NCG concentration to 30%, the nucleation energy barrier of the surface increased up to four times the amount of pure water vapour.[113]

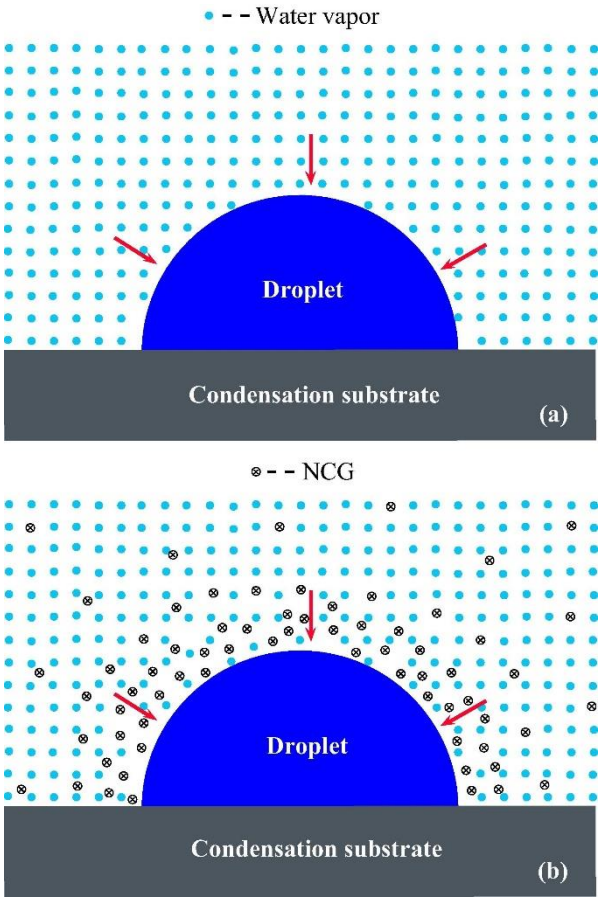

Figure 2.24. Schematic diagram of the transmission of water vapour molecules towards a condensate drop during condensation upon a surface. a) Without the presence of NCG and b) with NCG particulates which inhibits the movement of vapour molecules towards the subcooled surface.[112]

Using a different liquid-repellent surface, Xiao *et al.* managed to boost condensation heat transfer rates for a liquid infused heterogenous surface (in this case oil).[114] Permeating oil within the surface allows the surfaces' adhesion force to become considerably lower as cited by literature.[37,115,116] Having a hierarchical surface energy domain i.e. areas of high-surface energy with reduced interfacial energy (water-oil interface), causes droplets to nucleate within the oil. This can be seen clearly in **Figure 2.25** where the surface morphology and surface wettability results are presented.

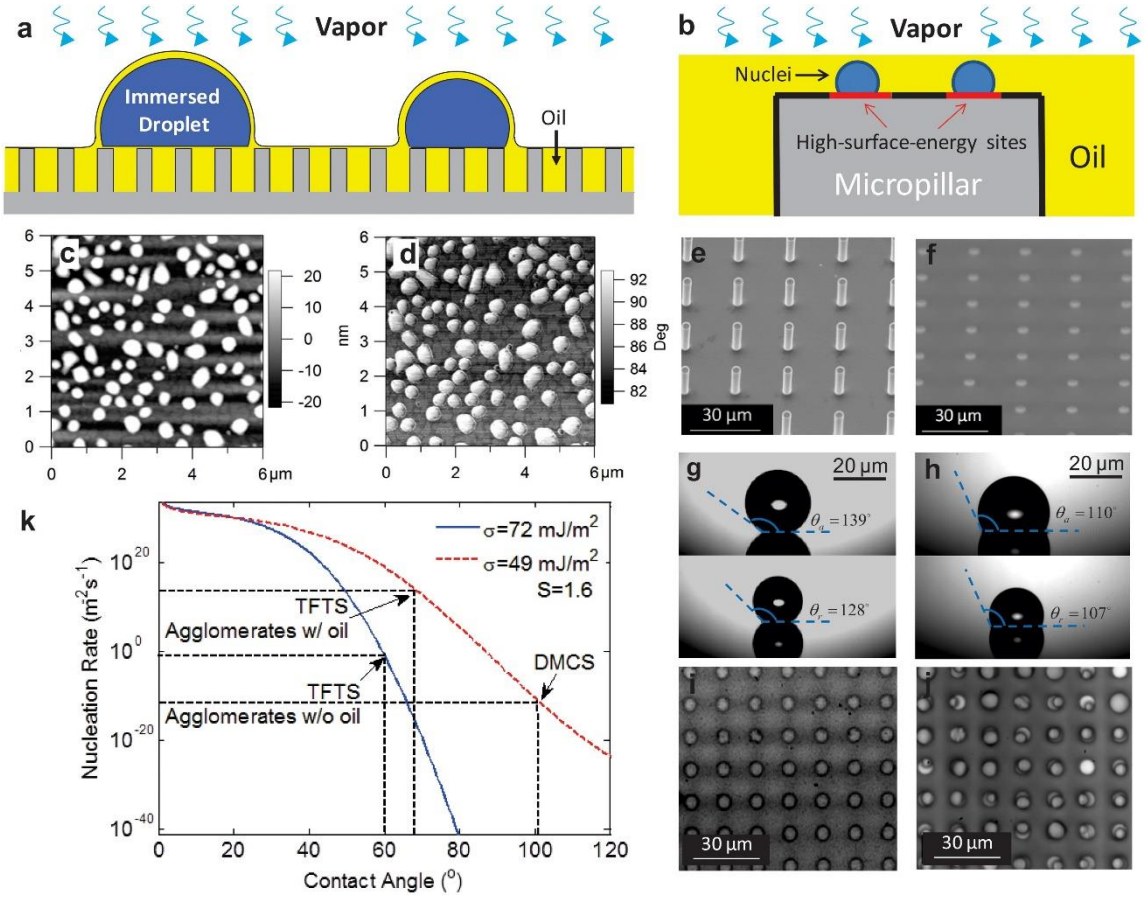

Figure 2.25. a) Schematic showing droplet nucleation whilst being cloaked in oil as water vapour penetrates through the oil, b) Interface of the micropillar illustrating favourable droplet growth upon the high surface energy sites, c,d) AFM (Atomic force microscopy) images of TFTS ((tridecafluoro-1,1,2,2-tetrahydrooctyl)-1-trichlorosilane) silane coating indicating its height and phase angle, having a bigger phase angle creates larger surface energy, e,f) ESEM images of micropillars covered with TFTS before and after oil infusion, g,h) contact angle hysteresis of liquid-infused surface with and without oil infusion, i,j) top side optical microscope images of micropillars before and after oil infusion, k) calculated nucleation rates of droplets against surface contact angle for different surface tension of oils.[114]

Having larger droplet nucleation rates and droplet removal increased the heat transfer performance further in the presence of NCG. It was determined that the enhanced

nucleation density was responsible for 80% of the increase in heat transfer coefficient.[114] In contrast, for a plain superhydrophobic surface without any liquid-infusion, surface flooding was observed with large amounts of Wenzel droplets upon the surface created by using high supersaturation ratios. In any case, more research is necessary for liquid-infused surfaces to appear within condenser heat pipes. For example, the thickness of the oil impregnated upon the surfaces' interface will establish a thermal resistance to heat transfer. Additionally, the oil will eventually be drained away from the surface as the formulating droplets will sweep the oil away with them.[114] These factors must be diminished to sufficiently stabilize the liquid repellent properties of the surface.

2.4. Fabrication of Functional Surfaces Used for Heat Pipes

As mentioned within the previous chapters, superhydrophobic surfaces are necessary to promote dropwise or jumping-droplet condensation. This will give rise to greater droplet departure frequencies, droplet nucleation rates and nucleation densities which will avoid or postpone the formation of filmwise condensation.[117] There are many methods of fabricating various functional surfaces.[24,118] Such surfaces require the establishment of micro/nanoscale structures as formerly presented in the examples. Therefore, this chapter will examine several methods of manufacturing micro/nanostructures

2.4.1. Electrochemical Deposition

This technique widely used for depositing a thin layer of metal upon another compatible metal or any electrically conductive material for constructing micro or nanostructures. The sacrificial material (also known as the anode) is placed within a electrolyte solution alongside the material to be deposited on (cathode).[118] The shape and size of the structures are determined by controlling the deposition parameters. Similarly to Xu *et al.* former works,[77] Wen *et al.* created copper nanowires by using electrodeposition on a

nanowire template.[119] The dimensions of the nanowires were 20 µm in height having a diameter range of 200-240 nm with a pitch distance of 100-140 nm. Establishing such large nanowire lengths was done by optimising the electrodeposition time with the pitch distance being dependent on the design of the template mould. Afterwards, the nanowires were hydrophobized to obtain a contact angle of 139° ± 3°. The nanowires were purposely designed to have high aspect ratios to inhibit vapour molecules from protruding through the interstices between the nanowires which will prevent surface flooding at high subcooling temperatures. **Figure 2.26** demonstrates the surface morphology of the copper nanowires with a diagram illustrating the notion of using such large aspect ratio nanowires.

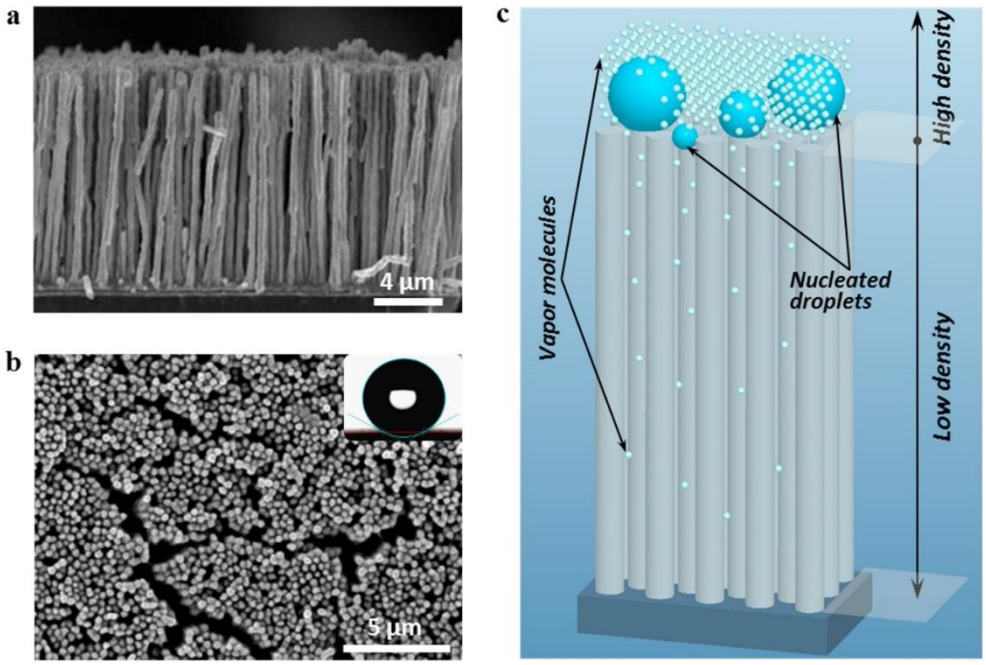

Figure 2.26. Long aspect ratio nanowires. a) SEM image of copper nanowires from a cross-sectional side view. b) SEM image of the top view of the nanowires with also showing the contact angle of the surface. c) Diagram of the concept design of the nanowires showing a high density of vapour molecules at the interface of the nanowires with a much lower density being resided at the bottom of the nanowires.[119]

Copper heat pipes are traditionally used within heat exchangers due to their high thermal conductivity and ease of manufacturing. Accordingly, many studies that use electrodeposition to fabricate superhydrophobic surfaces have been able to do so on copper plates. Zhao *et al.* founded superhydrophobic copper nanostructures to enhance the condensation heat transfer performance.[120] An electrolyte solution of 100 mM of $CuCl_2$ was utilized to electrodeposit the nanostructures upon the surface as seen in **Figure 2.27**. Afterwards, a monolayer of fluorinated silane is applied upon the nanostructures to make them hydrophobic. This gave a contact angle of 160° and 158° respectively.

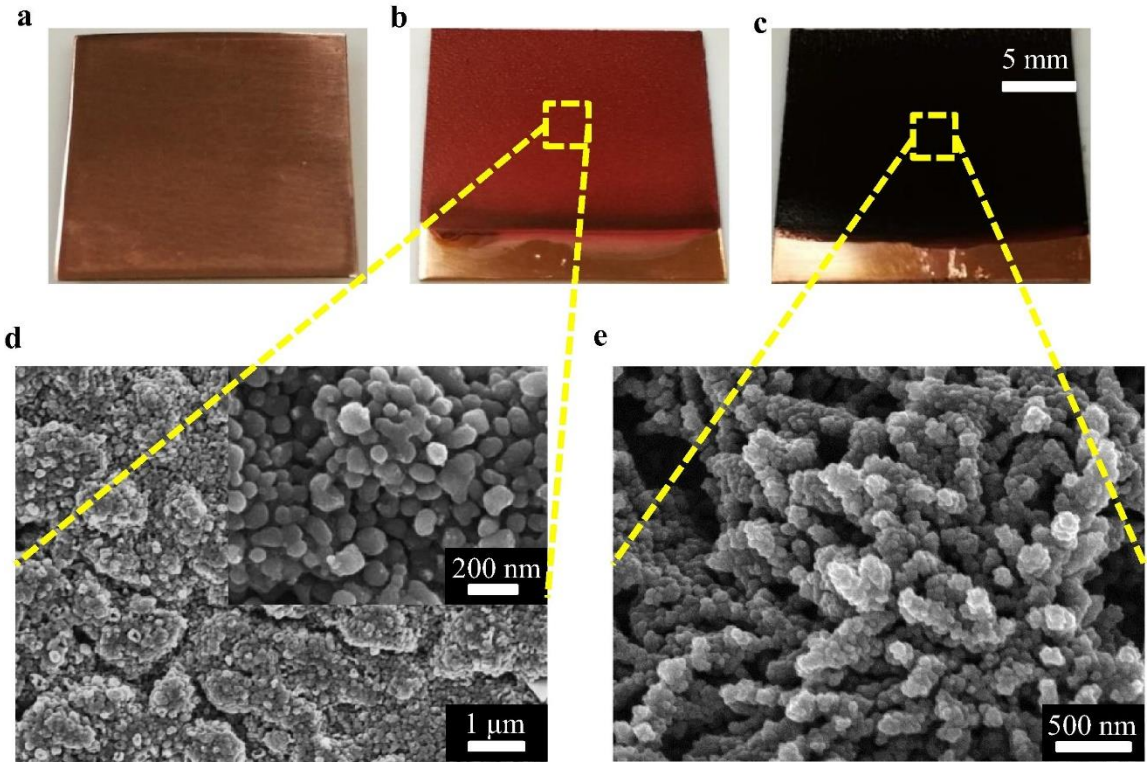

Figure 2.27. Nanostructures deposited upon the flat copper surface in comparison to an untreated surface. a) Bare copper. b) Small deposition rate of copper nanostructures. c) Large deposition rate of nanostructures on surface. d) SEM image of small deposited rate. e) SEM image of large deposited rate.[120]

Referring back to the works of Zhang *et al.*, electrodeposition of such structures can be applied upon copper tubes to determine its' condensation performance.[78] The dendritic nanostructures that were applied upon the micropores was done by electrodeposition. Once the micropores were established on the tube, the tube was then placed in an electrolyte solution of 0.2 mol of $CuSO_4$ and 1.0 mol of H_2SO_4 to deposit the dendritic structures. Thereafter, the tube was rinsed in DI water and then hydrophobized using an organic polymer known as n-hexadecyl mercaptan which was then left to cure in air. Another tube was also hydrophobized on a plain copper tube using the organic polymer stated above. **Figure 2.28** displays the fabrication technique with the tubes' defined surface topology and wettability.

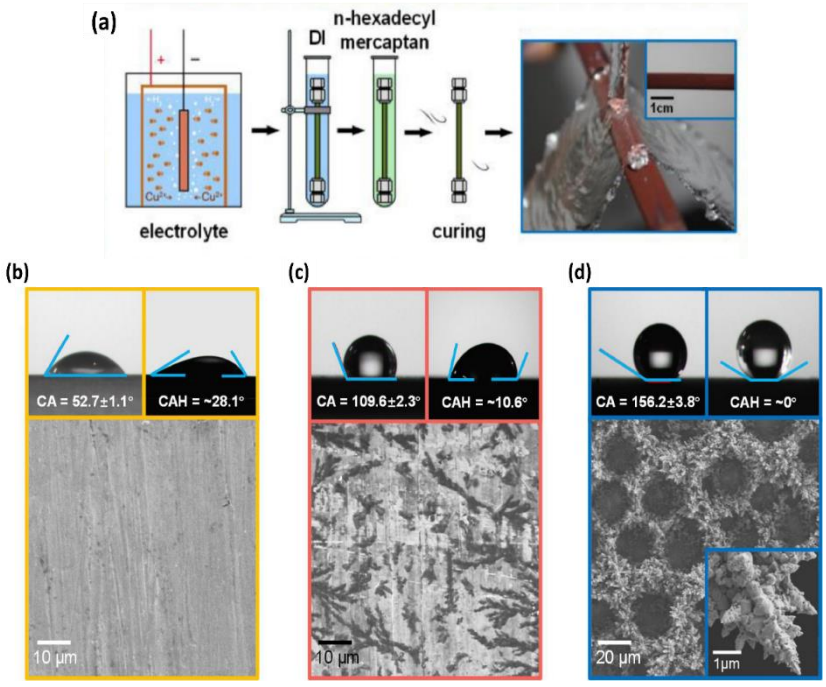

Figure 2.28. Tube preparation of hydrophobic and superhydrophobic surface with their outlined surface morphologies. a) Process of depositing dendritic nanostructures with then applying the organic polymer upon the surface. b) SEM image and surface wettability of the plain copper tube with, c) for the hydrophobic tube and, d) being the superhydrophobic tube.[78]

As illustrated, the plain copper tube was determined to be hydrophilic with a contact angle of 53° and CAH of 28°. Applying the organic polymer upon the tubes caused the surface to be hydrophobic having a contact angle of approximately 110° with a CAH of roughly 11°. Utilizing the hierarchical microporous surface with a pore diameter of 20 μm and the dendritic nanostructures bestowed a contact angle of 156° with a CAH of roughly 0° making the surface superhydrophobic. Therefore it can be said that superhydrophobic surfaces can easily be constructed using electrodeposition on various types of surface geometries including heat exchanger tubes.

2.4.2. Etching

Etching is one of the main methods used to establish superhydrophobic surfaces within academia and industry. Usually, chemical or physical techniques are needed to strip the part of the surface that is not needed to allow ordinary or sporadic patterns to be present.[121] In this case, the surface roughness can be altered by changing certain etching parameters during the process. Parin *et al.* managed to create dropwise condensation upon etched aluminium surfaces.[122] From adjusting the concentrations of $AlCl_3$, $FeCl_3$ and $CuCl_2$, various surface morphologies can be obtained. Once the etching process was done, the surface became superhydrophobic when the surface structures were coated in fluorosilane.

Remarkably, Hou *et al.* made a hierarchical superhydrophobic surface by etching silicon wafers in the formation of shell-like structures of the Namib desert beetle as displayed in **Figure 2.29**.[123]

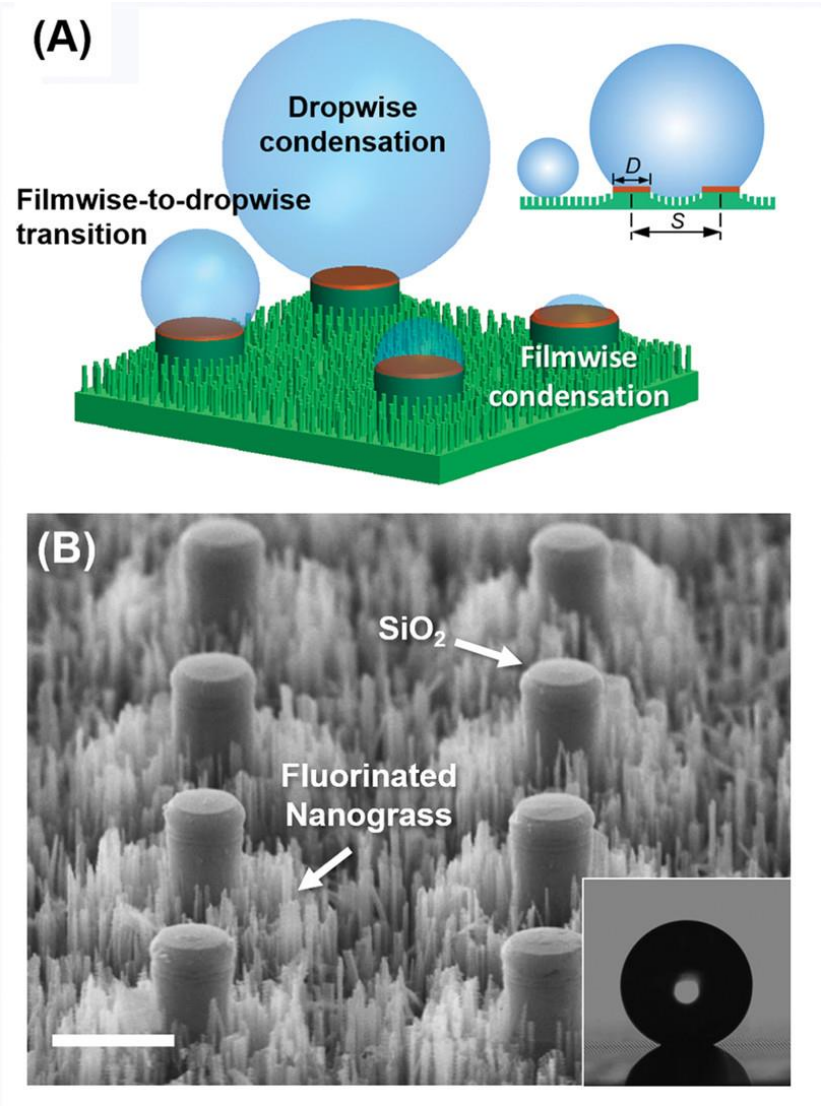

Figure 2.29. a) Diagram of hierarchical beetle-like surface, containing SiO2 micropillars with nanograss surrounding the pillars. The micropillars' interface are hydrophilic (indicated by the dark red areas), which serves as nucleation sites and increased droplet growth rates. The nanograss regions are coated with fluorosilane (shown on the green regions), to establish superhydrophobicity to facilitate regulated dropwise condensation. The right inset illustrates a droplet being in a Cassie-Baxter state when nucleated on the nanograss and a partial wetting state when grown on the micropillars. b) SEM image of the fabricated hierarchical micro/nanostructure. Scale bar represents 10 μm. Inset demonstrates the static contact angle of the surface which is 161°.[123]

To fabricate SiO_2 micropillars upon silicon wafers, photolithography and oxide etching was implemented. The etching agent used was tetramethylammonium hydroxide. Hereafter, deep reactive ion etching was done to construct the nanograss around the cavities of the micropillars. Then, the entire surface was coated with fluorosilane to facilitate the hydrophobicity of the structures. However, to ascertain the hydrophilicity of the micropillar tops, buffered oxide etching was applied to remove the hydrophobic coating upon the pillars and re-ordain the surface wettability of SiO_2. This indigenous combination of hydrophobic and hydrophilic regions seen on the backs of Namib desert beetles are able to collect condensate water droplets.[124] Regardless of the hydrophilic regions on the surface, the surface still remained to be superhydrophobic with an apparent contact angle of 161° ± 4° (seen on the inset of **Figure 2.29b**). Such surfaces are able to control the performance of dropwise condensation by adjusting their droplet nucleation sites and departure rates.

Whilst the fabrication of these unique functional surfaces appear to be interesting, the full potential of these surfaces have yet to be seen through design optimisation. Numerical simulations (or computational fluid dynamics) on the other hand can provide such perception from modifying the liquid-repellency properties of the surface against condensation or falling-film flow to signify which particular properties of the surface are able to enhance the tubes' heat transfer performance the most. Conducting this experimentally would take an enormous amount of time and capital and operating costs due to the fragility and difficulty of fabricating functional surfaces on multiple heat pipes as noted in Chapter 1. Nonetheless, current numerical simulations presented within literature are mainly shown to be limited towards simple straight pillars or within a micro-scaled environment which will be discussed in the next sub-chapter.

2.5. Utilizing Computational Fluid Dynamics to Provide Further Insight

2.5.1. Introduction to CFD

Computational fluid dynamics allows us to virtually predict the fluid flow behaviour and its' heat and mass transfer characteristics depending on the given boundary and initial conditions. Using Newtons laws of conservation, a set of conservation equations are derived and solved numerically within a modelled physical domain to visualise the physical phenomena of the fluid. These conservation equations are known as the Navier-Stokes equations which are implemented in order to simulate the velocity, temperature and pressure of the fluid (highlighted in Chapter 3.2.2). It is worth noting that the general form for all conservation equations are given as such:[125]

$$\underbrace{\frac{\partial}{\partial t}(\rho\phi)}_{Transient\ term} + \underbrace{\nabla\cdot(\rho\vec{v}\phi)}_{Convection\ term} = \underbrace{\nabla\cdot\left(\Gamma^{\phi}\nabla\phi\right)}_{Diffusion\ term} + \underbrace{Q^{\phi}}_{Source\ term} \qquad (2.12)$$

where ϕ is a general scalar variable, $\vec{v}$ is the velocity vector, Γ^{ϕ} is known as the diffusion coefficient, Q^{ϕ} is given as the source term and ∇ is given as a vector differential operator which denotes the standard derivative of a scalar or vector quantity in a given coordinate system (in this case, the cartesian coordinate system). Consequently, this allows the gradient or the divergence of a scalar or vector field to be formed. As underlined above, each term in the transport equation represents the transient, convection, diffusion and source term respectively.

The transient term (or the unsteady state term) indicates that the scalar variable is time-dependent and can change in magnitude at a given finite time step. The convection term allows us to interpret the transport of a given scalar variable across a velocity field

established within the physical domain (for e.g. temperature or the volume fraction of a particular phase). The diffusion term is used to model to the transference of a scalar quantity which is driven by the motion of fluid particles within the domain. Notably, the magnitude of diffusivity determines whether the flow is laminar or turbulent which is directly proportional to the fluid properties and its' velocity (similar to the Reynolds number). The source term refers to external body forces that may arise and act upon the fluid and altar the scalar variable such as gravitational forces, surface tension forces or mass transfer. Nonetheless, solving the conservation equations analytically proves to be challenging due to the non-linearity of the convection term (for e.g. when replacing ϕ with $\vec{v}$ in order to derive the conservation of linear momentum).[125]

At the moment, the solution to the equations can only be approximated through numerically integrating the equations over a fluid domain that has been discretised into many finite control volumes (or mesh elements). In other words, the partial differential equations are discretised into a set of linear algebraic equations (in a matrix form) which are then solved using a numerical scheme to compute the value of ϕ at each control volume. There are many numerical integration techniques used to solve partial difference equations over finite elements which are known as the finite difference method, the finite element method and the finite volume method. For CFD applications, the finite volume method is more ideal due to its compatibility against complex geometries and discontinuous flow. Therefore in this Thesis, the finite volume method is utilized to solve the governing equations through a commercial software known ANSYS Fluent. Further details on the finite volume method and its' implementation can be seen from Moukalled *et al.*[125]

2.5.2. Numerical Condensation and Falling-film Flow

Some numerical case-studies have been discussed upon in previous chapters but, nonetheless, the numerical techniques involved have not yet been conversed. Modelling condensation accurately proves to be computationally challenging as the simulation can easily become unstable due to large temperature gradients initially observed between the solid and vapour interface before condensate arises. Even so, once a thin condensate film is developed, the mass transfer rate of the vapour to the subcooled tube must be precisely calculated in order to produce the correct film thickness for the given settings. Notably, Kleiner *et al.* managed to accurately determine the vapour mass transfer rate by calculating the heat flux balance between the liquid-vapour interface to ensure that the temperature at the liquid-vapour interface remains equal to the saturation temperature.[126] More details on the mass transfer rate will be reviewed in Chapter 3. Their simulations model consisted of a two-dimensional tube with a wall thickness to model the heat flux between the inner and outer wall to establish a temperature gradient across the two. In addition, to counteract numerical instabilities gained from large temperature gradients, the number of iterations (calculations) per time step was selected to be ten. By implementing these numerical strategies, their condensation simulations produced stable solutions up to a subcooling temperature of 50 K. This was perceived by comparing the tubes' film thickness and heat transfer coefficients to the Nusselt film theory.[126] An example of their simulated condensation behaviour is illustrated below in **Figure 2.30**.

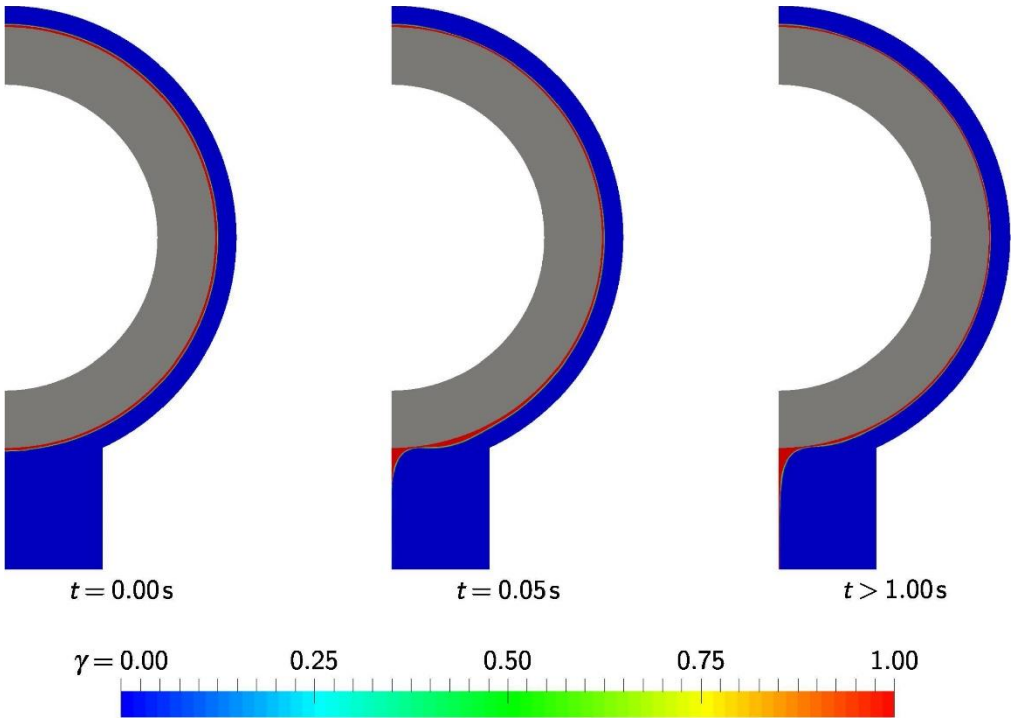

Figure 2.30. Condensation behaviour on a perfectly wetted two-dimensional tube for a subcooling temperature of 50 K. γ here represents the volume fraction of the liquid phase.[126]

However, as seen from **Figure 2.30**, a pre-existing liquid interface is required to initiate the condensation process as the heat flux balance is calculated between the liquid and vapour phase. This presents limitations within their methodology as filmwise condensation is not initially conceived for hydrophobic or superhydrophobic surfaces as explained previously. Thus, altering the surface wettability of the tube in this model would not provide an accurate representation of the flow behaviour. Instead, Kleiner *et al.* used their existing model to study condensation of pentane on macro-scaled finned tubes with varying fin angles.[127] To accurately portray the condensate film thickness, structured hexahedral mesh refinement layers were added on the tube and fin interfaces. Altering the fin angles from 90° to 73° (measured anti-clockwise) showed an enhancement in heat transfer coefficient due to the reduction in surface flooding as the spacing between the

fins are reduced. Although, lessening the fin angle below 73° began to reduce the heat transfer coefficient as the progression of the film thickness along the film flank became dominant over the decline in surface flooding. In spite of using macro-scaled structures for augmenting condensation heat transfer rates, the physical phenomena demonstrated within the results may be analogous to micro-scale structures.

In correspondence to Sharma *et al.* condensation study on functional microcone pillars in Chapter 2.3.3,[101] Standardo *et al.* locally modelled condensation within pyramidal micropillar cavities using the Volume-of-Fluid method to analyse the droplet ejection efficiency against the pillars' half-opening angle through the Laplace pressure imbalance phenomenon as discussed previously.[128] This was instituted by allocating a small hydrophilic dot (θ_Y = 20°) within the centre of the pillar cavity to essentially create a nucleation site for the droplet to grow upon. The rest of the pillar interfaces were treated with an intrinsic contact angle of 166.9° to allow the nucleating droplet to easily glide the out of the pillars. It was noted that a half-opening angle of 20° was able to provide maximal droplet ejection due to the optimal capillary pressure gradient developed within droplet as it elongates towards the pillars' interface. This can be seen through the lowered droplet departure volume as opposed to straight pillars where the droplet departure volume was much larger. **Figure 2.31** illustrates the dropwise condensation performance on the pyramidal micropillars and straight pillars.

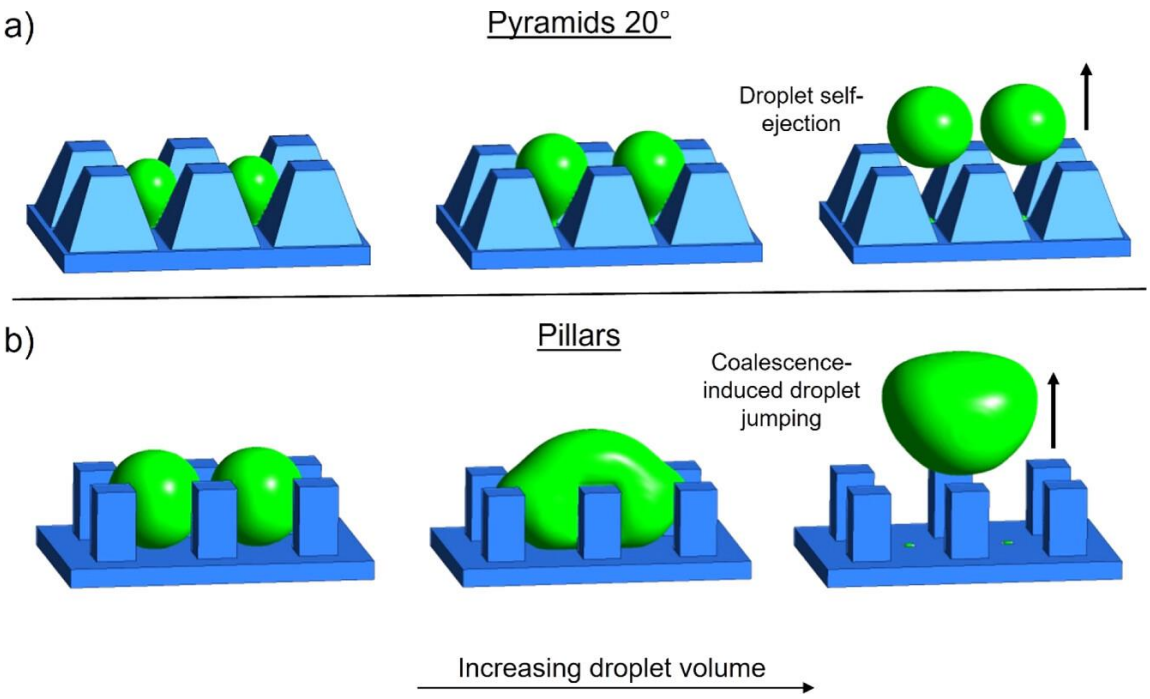

Figure 2.31. Dropwise condensation within (a) tapered pyramidal micropillars with a half-opening angle of 20° and (b) straight pillars.[128]

Within the pyramidal micropillars, the droplets are stretched and self-ejected without coalescence with the adjacent droplet. Conversely, with the straight pillars as the droplets cannot be self-driven out of the cavities, the droplets continue to nucleate within the cavity until reaching a critical radius to coalescence with the neighbouring droplet. This allows the droplet to be swiftly removed off the surface through jumping-droplet condensation. While this study does provide perception into designing pillars for discharging nucleating droplets, it does not accurately display real-world condensation behaviour as droplets would nucleate across the pillar interfaces which would thus affect the dynamics of the droplet growth within the pillar interstices as illustrated within the previous chapters.

Nevertheless, further focusing on microscopic condensation, Yin *et al.* conducted water-vapour condensation on three-dimensional micropillar structured surfaces with various intrinsic contact angles using the Lattice-Boltzmann method.[129] Unlike the Volume-of-

Fluid method which employs the Navier-Stokes equations, the Lattice-Boltzmann method (LBM) applies a set of kinetic equations in order to simulate the kinetic and kinematic movement of fictitious microscopic fluid particles within confined lattices.[130] This allows fluid dynamic simulations to be observed within micro-scaled structures with ease. It was found that, increasing the intrinsic contact angle of the micropillars reduced the droplets' contact length and the droplet nucleation density (i.e. the number of nucleation sites). This is attributed to the difficulty of fluid particles to coalescence and grow due to the reduction in interfacial adhesion forces. More details on this issue is revealed in Chapter 3. As a result, the rate of droplet departure from the micro-pillars were increased. The same can be said when increasing the pitch spacing of the pillars to a critical value in which the nucleating droplet appeared to cover the entire micropillar substrate which formed a Wenzel droplet.

Wang *et al.* also used the LBM to simulate dropwise condensation on micro-pillared surfaces whilst modifying the pillars' advancing contact angle and surface subcooling temperature to demonstrate their significance in altering the condensate flow dynamics and surface heat transfer properties.[131] As expected, increasing the advancing contact angle from a hydrophilic (θ_a = 50.8°) to a superhydrophobic (θ_a = 164.5°) state allowed the nucleating droplets within the pillars to transition from a pinned Wenzel state to a mobile Cassie-Baxter state. It should be noted that, for hydrophilic surfaces, droplets that nucleate and coalesce end up forming a liquid puddle on the surface as the pillar interstices are flooded. As the intrinsic contact angle increases towards the hydrophobic state, the liquid retained within the pillars began to climb up the interstices and form droplets at the interfaces since the liquids' surface tension force is able to overcome the surface's adhesion force. A phenomenon equivalent to this is explained in Chapter 5.3.1. The performance of the condensate is visually demonstrated below in **Figure 2.32**.

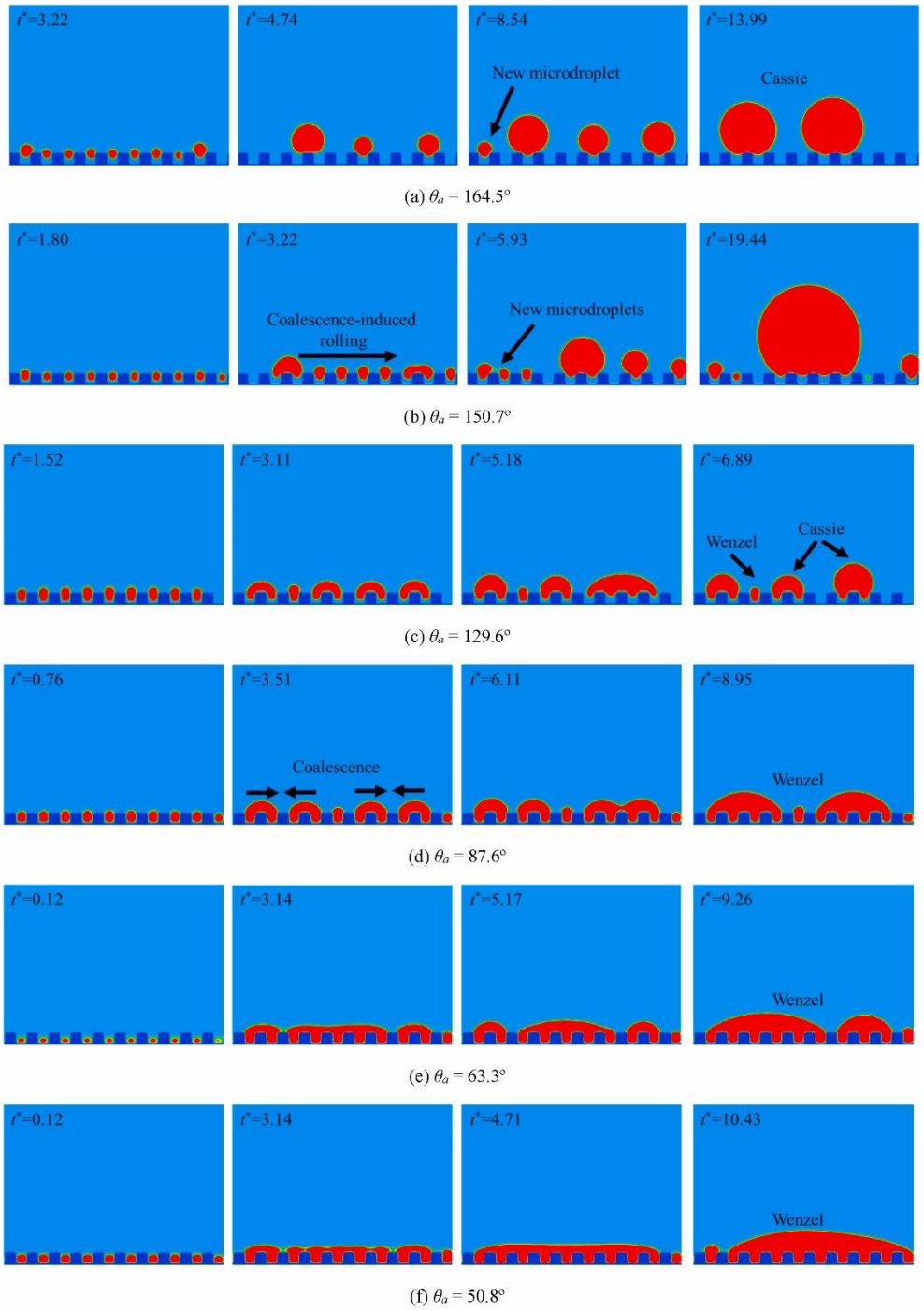

Figure 2.32. Condensation on square micropillars with different advancing contact angles treated at the walls between 50.8° to 164.5° (a-f). *t** represents the dimensionless time.[131]

Furthermore, increasing the subcooling temperature of the surface increased the rate of condensation which resulted in droplets being detached from the pillar interstices at a faster rate which amplified the surface heat flux. However, the droplets that emerged from

the pillars were larger in volume as a result. This may lead to filmwise condensation at a critical subcooling temperature as droplets will end up collapsing under their own weight (hydrostatic pressure). However, one of the main disadvantages of using the Lattice-Boltzmann method over the Volume-of-Fluid method is that, it is difficult to simulate free surface flows (gravity-driven flow) or modelling/meshing complex geometry as the LBM uses voxels to mesh the domain rather than polyhedral meshes.[132]

Moving on towards falling-film flow, Zhao *et al.* conducted a multiphase flow falling-film simulation upon a single horizontal tube where the Volume-of-Fluid method was used to track the liquid-gas interface.[133] Remarkably, a virtual porous layer was implemented at the tube wall to dictate whether it will increase the wettability and heat transfer coefficient of the tube. To validate their model, the film thickness and the average heat transfer coefficient of the tube was compared against experimental results from literature illustrating a maximum deviation of 5% for their porous and plain tube. As a result, their simulations managed to accurately predict the film spreading process across the tube for their porous and plain surface as illustrated in **Figure 2.33**. This was predominantly accomplished by employing a structured hexahedral mesh around the computational fluid domain and conducting a mesh independence analysis where the number of mesh elements were increased to the point where the wetting ratio on the tube did not change. This provides an optimal mesh density value against computational efficiency and accuracy.

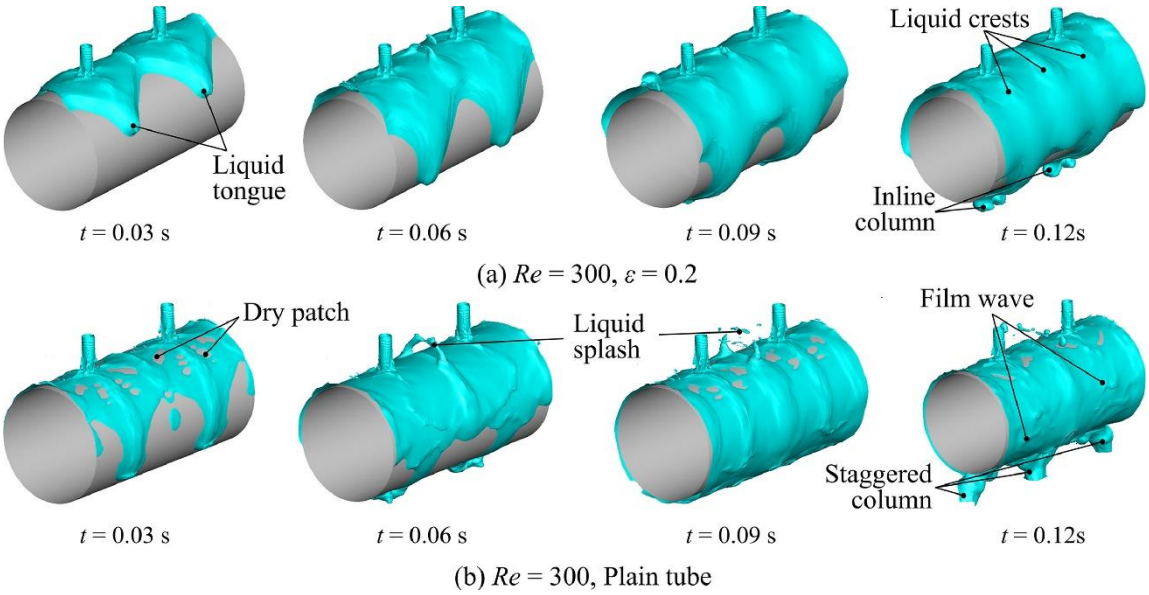

Figure 2.33. Numerical flow performance of water falling upon a porous tube (a), and a plain tube (b). ε represents the porosity of the porous surface.[133]

To further specify the effects of surface wettability, Karmakar *et al.* conduced a falling-film simulation of ethylene glycol and water upon a subcooled heat pipe.[134] The intrinsic contact angle of the tube were varied from a superhydrophilic to superhydrophobic state whilst maintaining a contact angle hysteresis of 2°. It was observed that, for jet-wise flow, increasing the contact angle from 2 to 175° caused a reduction in the axial film thickness whilst the circumferential film thickness increased. This can be seen within **Figure 2.34**.

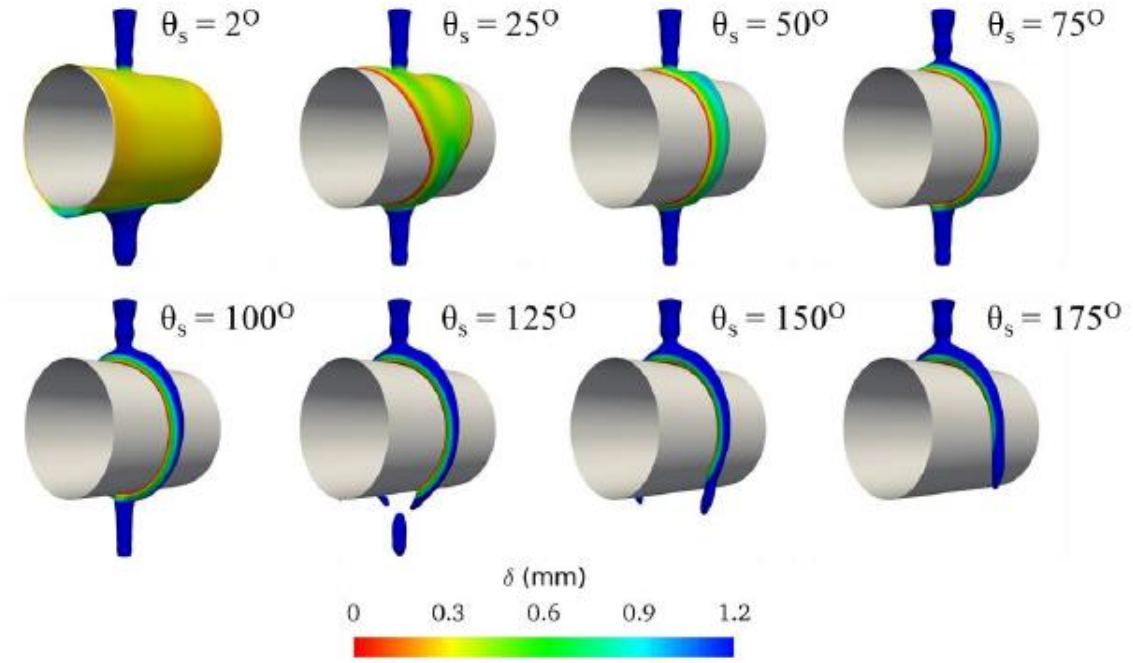

Figure 2.34. Liquid-contour images of ethylene-glycol/water falling over a horizontal tube at various contact angles. Here, δ is equal to the film thickness.[134]

Nonetheless as the surface area of the liquid across the tube is lessened, the overall heat transfer rate of the tube inevitably decreased. Notably, the advection of the liquid-gas interface was captured using a Volume-of-Fluid method where the transport equation was discretised and solved algebraically.

Karmakar *et al.* then allocated two additional tubes stacked below each other to investigate the heat transfer properties on the impacting tubes.[135] For dropwise flow, it was found that as the pendent droplet from the first tube impacted the second tube, the local heat transfer coefficient within the impingement region began to decrease due to the rise in film thickness. However, due to the Rayleigh-Plateau instability of the liquid jet, multiple satellite droplets were formed and impacted the tube. This significantly amplified the local heat transfer coefficients within the impingement region by twice as much since the satellite droplets induced film thinning and mixing. In spite of this, their methodology did

not explain the importance of capturing the Rayleigh-Plateau instability nor how this phenomenon was numerically established. Further details upon this issue will be discussed in Chapter 4. A numerical study by Zhao *et al.* studied the flow behaviour of completely wetted tube bundle arrangements against the tubes' heat transfer properties.[136] It is perceived that a triangular tube arrangement was able to augment the average heat transfer coefficient of the tube bundle compared to a traditional square tube arrangement. This is predominantly due to the added number of droplets departing and splashing amongst other tubes which increases the number of surface waves generated on the liquid film. As formerly stated, this is able to enhance the heat transfer coefficient of the tubes beneath the first.

2.5.3. Droplet Impingement

From examining the preceding case-studies, it is shown that droplet impaction is renowned to be pervasive on heat exchanger tubes. Therefore, it is necessary to depict its' fundamental physical phenomena to allow one to insightly design such functional surfaces that can accurately engineer the hydrodynamics of the fluid to either repel or wet the surface to increase heat transfer efficiencies. Alinejad *et al.* simulated droplet impaction on three-dimensional tubes by employing the Volume-of-Fluid method using OpenFOAM.[137] The setup consisted of a Newtonian droplet impacting the centre of two adjacent square tubes for different dimensional configurations and droplet sizes under the influence of gravitational acceleration. Additionally, surface wettability of the tube was considered by allocating an advancing contact angle of 110° with a receding contact angle of 40° with an intrinsic contact angle of 75°. Evidently, for large sized droplets, (twice the width of the tube) that impacted in between the tubes caused the droplet to rupture and leave behind several small liquid filaments on the square tubes. A primary pendent droplet

is then seen to depart underneath the tube interstice. **Figure 2.35** displays this phenomenon clearly. On the other hand, for droplets that are less than or equal to the width of the tube, only left behind two small satellite droplets in which, the pendent droplet either escaped through the gap or became stuck in between the tubes. Therefore, in relation to falling-film flow, controlling the diameter of pendent droplets that depart off the primary tube could adjust the coverage of the liquid on the tube for given tube contact angles. The same can be said for numerically apprehending small satellite droplets that may formulate from liquid filaments.

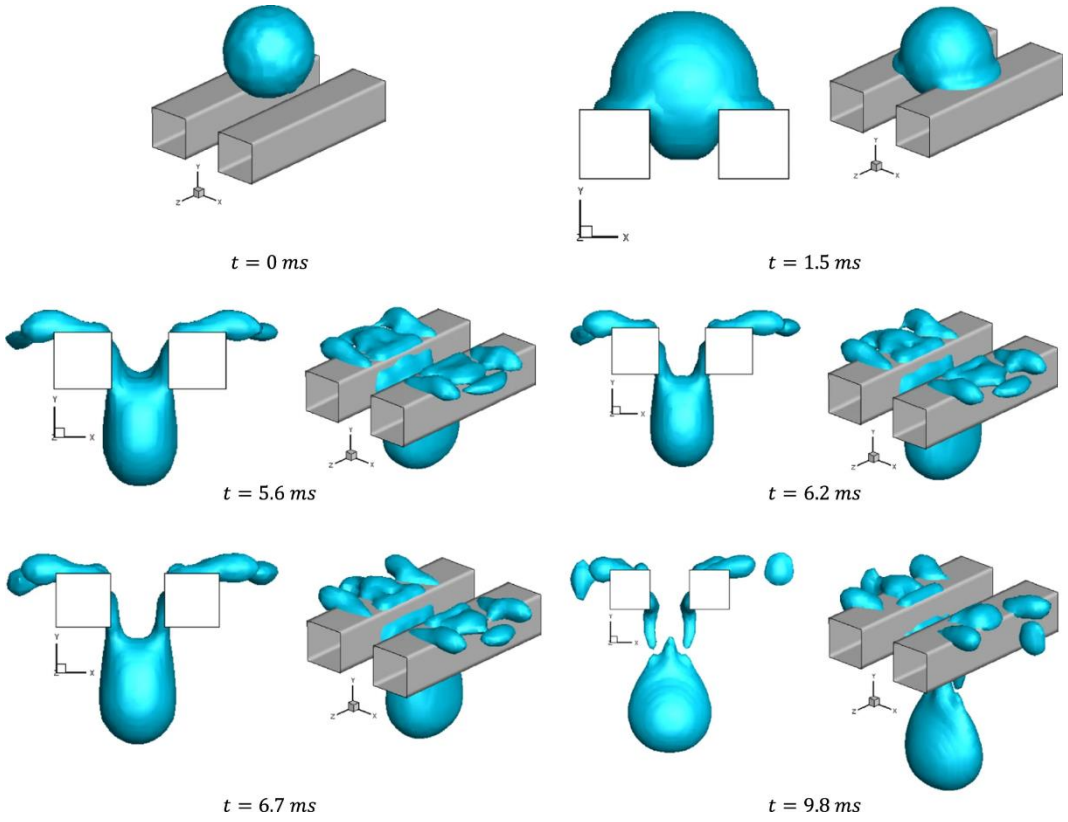

Figure 2.35. Contour image of a droplet that is twice the size of the square tubes impacting at the centre of the tubes' pitch.[137]

Furthermore, Wang *et al.* investigated droplet impact on cylindrical tubes.[138] A numerical method known as Many-body dissipative particle dynamics (MDPD) was employed to simulate droplet impact by modelling the interactive forces involved between

liquid particles and solid walls.[139] Thus, the MDPD method is mainly limited to mesoscale simulations. As a result, the effects of gravitational forces are ignored within the model due to the small length scales involved. Nevertheless, droplet impact on hydrophilic, hydrophobic and superhydrophobic tubes with various tube diameters were considered. For a hydrophilic tube, as the droplet impacts the tube, the droplet splits into two liquid strands on either side of the tube. As the liquid progresses down the tube, the liquid strands eventually meet and coalesce beneath the tube to form a pendent droplet which detaches off the tube as it falls. Interestingly, for a hydrophobic tube, the same liquid strands still formulates however, the angle between the strands appear to be more obtuse from each other. As a consequence, the liquid strands do not meet but instead, detach off the tube individually from each side. The same occurrence is seen for a superhydrophobic tube however, the angle between the liquid strands are much wider apart. The fluid behaviour described is observed in **Figure 2.36**. The same particular trend is noted when increasing the tube diameter.

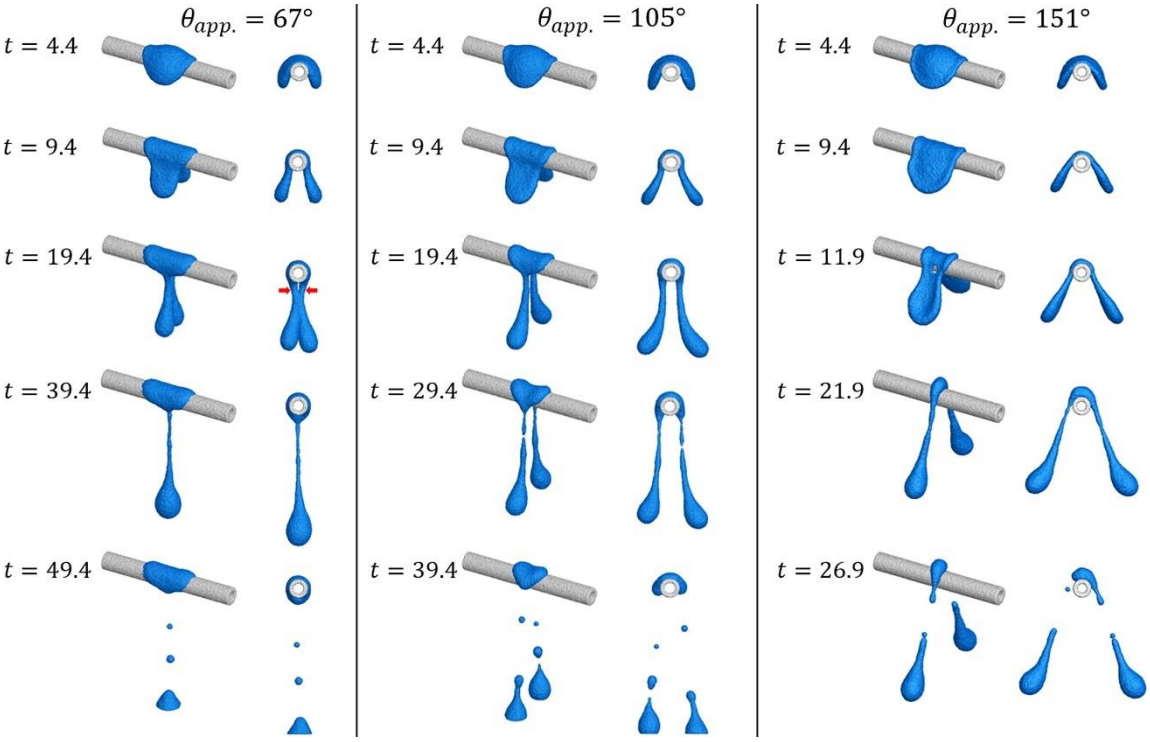

Figure 2.36. Isometric and planar view of the droplet impact behaviour on cylindrical tubes at numerous contact angles.[138]

This leads to further questions as to how tube sizes and bundle arrangements could be used to catch or avoid the falling-film against different tube contact angles to amplify heat transfer coefficients further within real-world settings.

Moreover, droplets that formulate and fall from various heat pipes may not be completely spherical but, rather displaying irregular sphere-like shapes as presented from previous case studies. In other words, the eccentricity of the droplets will be different in each instance (how much the droplet is stretched). Therefore, Yun *et al.* numerically investigated the bouncing behaviour of ellipsoidal liquid drops on curved surfaces by utilizing the Volume-of-Fluid method.[140] It was illustrated that, increasing the droplets' eccentricity (parallel to the direction of the tube) reduced the contact time of the droplet as opposed to increasing the eccentricity perpendicular to the tube. This is primarily due to the escalation in the rate of change of momentum in the circumferential and axial

direction of the droplet. Furthermore, the overall enhancement in the droplets' momentum is seen to be more prevalent on curved surfaces rather than flat surfaces as the contact time was demonstrated to increase when raising the eccentricity of the curved surface (i.e. flattening the surface) for all drop ellipticities tested. Again, from analysing these observations, one can strategize to formulate ellipsoidal droplets from functional surfaces on heat pipes to test this hypothesis under real-world environmental conditions viewed within heat exchangers as droplets that impact heat pipes will not be implicitly dry.

On that note, Chen *et al.* investigated droplet impact of two drops impacting each other a superhydrophobic tube at various droplet velocities using ANSYS Fluent.[141] To capture the liquid-vapour interface, a coupled level-set and Volume-of-Fluid method was provided (CLSVOF). The level set method is able to enhance the resolution of the liquid-gas interfaces' curvature by introducing a level set function within the continuity equations.[142] At low droplet velocities (less than 1 m/s), as the falling droplet impacted the secondary droplet already on the tube, the droplets both coalesced and rebounded from tube as the falling droplet pulled the secondary droplet away from the tube during the receding stage. This phenomenon is shown to be similar to jumping-droplet condensation. Increasing the droplet velocity beyond 1 m/s caused the droplets to break up due to the enlargement in liquid pressure at the centre of impact. This induced the droplet to spread further axially as the pressure gradient is increased. Further increasing the velocity towards 1.5 m/s generated splashing as the liquid film at the trailing edge began to rupture and form small satellite droplets. This is governed by the Rayleigh-Plateau instability phenomena as raising the droplets' impact velocity amplified the capillary wave velocity within the liquid. In any case, superhydrophobic tubes are demonstrated to repel incoming droplets even if the substate is already partially wetted which can further enhance heat transfer coefficients on condenser tubes. To further observe its' implications on heat

transfer, Luo *et al.* conducted a numerical simulation of three impacting droplets on a heated hydrophilic tube (intrinsic contact angle of 30°) using ANSYS Fluent.[143] As the droplets successively impact the heated tube, the tubes' heat transfer coefficient began to peak at the instance of impingement similar to Karmakar *et al.* results.[135] As mentioned beforehand, this is due to the liquid film being thinned as the droplets impact the film. Once the droplets begin to spread however, the heat transfer coefficient begins to decline as the liquid surface area rises from the added mass of the droplets. This can be seen from **Figure 2.37** which illustrates the alteration in the heat transfer rate and the contact area against time as the three droplets impinge the tube.

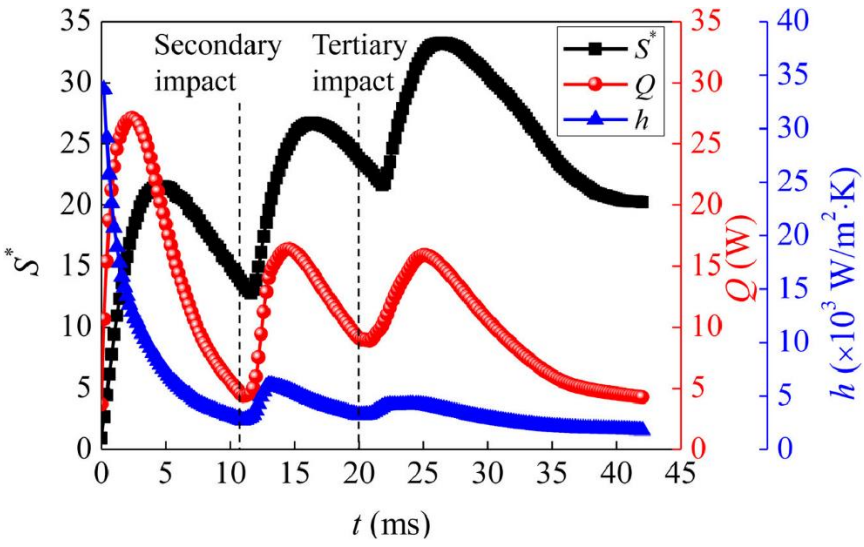

Figure 2.37. Variation in the liquids' dimensionless contact area (*S**), heat transfer rate (*Q*) and heat transfer coefficient (*h*) against contact time (*t*) for three consecutive droplets impacting the heated tube.[143]

However, it remain unknown how consecutive droplet impacts affect the heat transfer performance on a superhydrophobic surface. Therefore, Ma *et al.* numerically examined the heat transfer implications of two droplets impacting a heated flat superhydrophobic surface using the Volume-of-Fluid method within a two-dimensional axisymmetric

domain.[144] By altering the intrinsic contact angle of the surface between 130 to 170°, it is prominent that the transient heat transfer rate between the liquid-solid interface for binary or singular droplet impact tends to reduce as the maximum spreading diameter falls as the contact angle is increased. Notably, the difference between the heat transfer rates at different contact angles is magnified for binary droplet impact rather than a singular impacting droplet. For contact angles of 130°, the heat transfer rate is 21.8% higher for binary droplets than of a singular droplet impact. Whereas for 150° and 170°, the heat transfer rate is 20.2% and 31.1% lower, correspondingly.[144] This is due to the jumping droplet behaviour illustrated from binary droplet coalescence on superhydrophobic surfaces. As a result, the merged droplet was able to be propelled away from the surface swiftly in comparison to a singular droplet impact or the hydrophobic surface. Although this study illustrates the thermodynamic behaviour of impacting droplets on a superheated surface (surface temperatures above saturation), the fluid dynamic behaviour observed can be made to be analogous on cooled surfaces as the heat transfer performance quantified at the observed contact angles would be inverted.

To examine consecutive impacting droplets on cooled surfaces, Wang *et al.* simulated multiple droplets impacting a cold superhydrophobic substrate by employing the Many-body dissipative particle dynamics with energy conservation method (MDPDE).[145] The MDPDE method is essentially the combination of the MDPD and the eDPD method (dissipative particle dynamics with energy conversation).[146] This allows the simulation to create heat exchange between the fluid particles from allocating the energy conversion equations.[147] It should be noted that, the surface temperatures were assigned to be below zero degrees (up to -21°C) to test the anti-icing performance of superhydrophobic surfaces. It is perceived that, consecutive droplets impacting a superhydrophobic surface were able to facilitate a pancake rebound where the droplet is able to lift off the surface

without retracting.[148,149] This was due to the trailing droplet impacting and coalescing into the leading droplet whilst in its' maximum spreading stage. Hence, this led the inertial force generated in the horizontal direction to be converted into the vertical direction of the leading droplet. Subsequently, this allowed the merged droplet to be rapidly detached off the substrate whilst minimising ice nucleation within the liquid. Nonetheless, this feature was shown to be more effective at large Weber numbers (We ~ 100). The Weber number represents the ratio of the inertial to surface tension forces of the liquid which is showed dimensionally as:

$$We = \frac{\rho_l V^2 \lambda_c}{\gamma_{lv}} \tag{2.13}$$

where V is the velocity of the droplet (m/s). Thus, droplets that contain a large Weber number (much greater than one) will cause the liquids' inertial force to prevail over the surface tension force. As a consequence, the droplet is able to swiftly flatten when impacting the surface and not recede. Nevertheless, a superhydrophobic surface with a large droplet Weber number is required to observe pancake droplet rebound. Although, employing Weber numbers that are too large (greater than 100) can cause the merged droplet to splash and breakup on the surface. Yet, in relation to heat pipes, establishing pancake droplet rebound within heat exchanger environments is particularly important for further expanding heat transfer efficiencies. In summary, numerical simulations are able to reveal further intuition into how manipulating the liquids' morphology are able to alter the heat transfer performance of the heat pipes at multiple contact angles. This enables researchers to strategize and design functional surfaces that are capable of mimicking the profound phenomena presented.

2.6. References

1. S. Quoilin, M. Van Den Broek, S. Declaye, P. Dewallef, V. Lemort, Techno-economic survey of Organic Rankine Cycle (ORC) systems, Renew. Sustain. Energy Rev. 22 (2013) 168-186.
2. A. Elsayed, M. Embaye, R. Al-Dadah, S. Mahmoud, A. Rezk, Thermodynamic performance of Kalina cycle system 11 (KCS11): feasibility of using alternative zeotropic mixtures, Int. J. Low-Carbon Technol. 8 (2013) 69-78.
3. Shoukat Alim Khan, Furqan Tahir, Ahmer Ali Bozdar Baloch, M. Koc, Review of Micro–Nanoscale Surface Coatings Application for sustaining dropwise condensation, Coatings 9 (2019) 117.
4. M. B. Kirkham, Principles of Soil and Plant Water Relations (Second Edition) Elsevier (2014) 27-40.
5. A. Di Gianfrancesco, Materials for ultra-supercritical and advanced Ultra-Supercritical Power Plants, Woodhead Publishing (2016) 1-49.
6. B. I. Master, K. S. Chunangad, A. Boxma, D. Kral, P. Stehlik, Most Frequently Used Heat Exchangers from Pioneering Research to Worldwide Applications, Heat Transf. Eng. 27 (2006) 4-11.
7. C. Philpott, J. Deans, The enhancement of steam condensation heat transfer in a horizontal shell and tube condenser by addition of ammonia, Int. J. Heat Mass Transfer 47 (2004) 3683-3693.
8. G. Yang, H. Hu, G. Ding, J. Chen, W. Yang, S. Hu, X. Pang, Experimental investigation on heat transfer characteristics of two-phase propane flow

condensation in shell side of helically baffled shell-and-tube condenser, Int. J. Refrig. 88 (2018) 58-66.

9. S. Anand, S. Y. Son, Sub-Micrometer Dropwise Condensation under Superheated and Rarefied Vapor Condition, Langmuir 26 (2010) 17100-17110.
10. S. M. Hosseinnia, M. Naghashzadegan, R. Kouhikamali, CFD simulation of water vapor absorption in laminar falling film solution of water-LiBr — Drop and jet modes, Appl. Therm. Eng. 115 (2017) 860-873.
11. L. Harikrishnan, M. Maiya, S. Tiwari, Investigations on heat and mass transfer characteristics of falling film horizontal tubular absorber, Int. J. Heat Mass Transfer 54 (2011) 2609-2617.
12. Y. Thomas, An essay on the cohesion of fluids, Philos. Trans. R. Soc. London 95 (1805) 65-87.
13. N. S. Singh, J. Zhang, J. Stafford, C. Anthony, N. Gao, Implementing superhydrophobic surfaces within various condensation environments: a review, Adv. Mater. Interfaces 8 (2021) 2001442.
14. D. Bonn, J. Eggers, J. Indekeu, J. Meunier, E. Rolley, Wetting and spreading, Rev. Mod. Phys. 81 (2009) 740-793.
15. P.-G. De Gennes, Wetting: statics and dynamics, Rev. Mod. Phys. 57 (1985) 827.
16. M. Callies, D. Quéré, On water repellency, Soft matter 1 (2005) 55-61.
17. R. N. Wenzel, Surface roughness and contact angle, J. Phys. Chem. 53 (1949) 1466-1467.
18. R. N. Wenzel, Resistance of solid surfaces to wetting by water, Ind. Eng. Chem. 28 (1936) 988-994.
19. A. Marmur, Wetting on hydrophobic rough surfaces: to be heterogeneous or not to be?, Langmuir 19 (2003) 8343-8348.

20. D. Liao, M. He, H. Qiu, High-performance icephobic droplet rebound surface with nanoscale doubly reentrant structure, Int. J. Heat Mass Transfer 133 (2018) 341-351.

21. R. K. Annavarapu, S. Kim, M. Wang, A. J. Hart, H. Sojoudi, Explaining Evaporation-Triggered Wetting Transition Using Local Force Balance Model and Contact Line-Fraction, Sci. Rep. 9 (2019) 405.

22. A. B. D. Cassie, S. Baxter, Wettability of porous surfaces, Trans. Faraday Society 40 (1944) 546-551.

23. A. B. D. Cassie, Contact angles, Discuss. Faraday Soc. 3 (1948) 11-16.

24. P. Roach, N. J. Shirtcliffe, M. I. Newton, Progess in superhydrophobic surface development, Soft matter 4 (2008) 224-240.

25. K.-Y. Law, Definitions for Hydrophilicity, Hydrophobicity, and Superhydrophobicity: Getting the Basics Right, J. Phys. Chem. Lett. 5 (2014) 686-688.

26. C. Extrand, A. Gent, Retention of liquid drops by solid surfaces, J. Colloid Interface Sci. 138 (1990) 431-442.

27. J. C. Scott, Wetting, spreading and adhesion, J. Fluid Mech. 94 (1978) 794-797.

28. N. Gao, F. Geyer, D. W. Pilat, S. Wooh, D. Vollmer, H.-J. Butt, R. Berger, How drops start sliding over solid surfaces, Nat. Phys. 14 (2018) 191-196.

29. R. H. Dettre, R. E. Johnson Jr, Contact Angle Hysteresis II. Contact Angle Measurements on Rough Surfaces, Adv. Chem. 43 (1964) 136-144.

30. C. Cao, Y. Feng, J. Zang, G. P. López, X. Zhao, Tunable lotus-leaf and rose-petal effects via graphene paper origami, Extreme Mech. Lett. 4 (2015) 18-25.

31. W. Barthlott, C. Neinhuis, Purity of the sacred lotus, or escape from contamination in biological surfaces, Planta 202 (1997) 1-8.

32. X. Gao, L. Jiang, Water-repellent legs of water striders, Nature 432 (2004) 36.

33. M. J. Mayser, H. F. Bohn, M. Reker, W. Barthlott, Measuring air layer volumes retained by submerged floating-ferns Salvinia and biomimetic superhydrophobic surfaces, Beilstein J. Nanotechnol. 5 (2014) 812-821.

34. Q. Sheng, J. Sun, Q. Wang, W. Wang, H. S. Wang, On the onset of surface condensation: formation and transition mechansims of condensation mode, Sci. Rep. 6 (2016) 30764.

35. N. Miljkovic, R. Enright, Y. Nam, K. Lopez, N. Dou, J. Sack, E. N. Wang, Jumping-Droplet-Enhanced Condensation on Scalable Superhydrophobic Nanostructured Surfaces, Nano Lett. 13 (2013) 179-187.

36. L.-W. Mou, T.-Y. Zhang, J.-Y. Zhang, J.-Q. Li, L.-W. Fan, Realization of coalescence-induced condensate droplet jumping on a hierarchical porous superhydrophobic surface over a wide range of subcooling up to 20 K, AIP Adv. 9 (2019) 045125.

37. D. J. Preston, Z. Lu, Y. Song, Y. Zhao, K. L. Wilke, D. S. Antao, M. Louis, E. N. Wang, Heat transfer enhancement during water and hydrocarbon condensation on lubricant infused surfaces, Sci. Rep. 8 (2018) 540.

38. N. Lukic, L. Diezel, A. P. Fröba, A. Leipertz, Economical aspects of the improvement of a mechanical vapour compression desalination plant by dropwise condensation, Desalination 264 (2010) 173-178.

39. C.-S. Hong, E.-B. Lee, Power Plant Economic Analysis: Maximizing Lifecycle Profitability by Simulating Preliminary Design Solutions of Steam-Cycle Conditions, Energies 11 (2018) 2245.

40. K. Ummel, CARMA revisited: an updated database of carbon dioxide emissions from power plants worldwide, Center for Global Development Working Paper (2012) 30.

41. G. A. O'neill, J. Westwater, Dropwise condensation of steam on electroplated silver surfaces, Int. J. Heat Mass Transfer 27 (1984) 1539-1549.

42. K. Cheng, S. Kim, S. Lee, K. J. Kim, Internal dropwise condensation: Modeling and experimental framework for horizontal tube condensers, Int. J. Heat Mass Transfer 83 (2015) 99-108.

43. P. Marto, D. Looney, J. Rose, A. Wanniarachchi, Evaluation of organic coatings for the promotion of dropwise condensation of steam, Int. J. Heat Mass Transfer 29 (1986) 1109-1117.

44. S. Tawfick, A. J. Hart, M. De Volder, Capillary bending of Janus carbon nanotube micropillars, Nanoscale 4 (2012) 3852-3856.

45. D. Torresin, M. K. Tiwari, D. Del Col, D. Poulikakos, Flow Condensation on Copper-Based Nanotextured Superhydrophobic surfaces, Langmuir 29 (2013) 840-848.

46. K. Holden, A. Wanniarachchi, P. Marto, D. Boone, J. Rose, The use of organic coatings to promote dropwise condensation of steam, J. Heat Transfer 109 (1987) 768-774.

47. J. B. Boreyko, C.-H. Chen, Self-Propelled Dropwise Condensate on Superhydrophobic Surfaces, Phys. Rev. Lett. 103 (2009) 184501.

48. P. Zhang, Y. Maeda, F. Lv, Y. Takata, D. Orejon, Enhanced Coalescence-Induced Droplet-Jumping on Nanostructured Superhydrophobic Surfaces in the Absence of Microstructures, ACS Appl. Mater. Interfaces 9 (2017) 35391-35403.

49. A. Pringle, S. N. Patek, M. Fischer, J. Stolze, N. P. Money, The captured launch of a ballistospore, Mycologia 97 (2005) 866-871.

50. M. O. Hassett, M. W. Fischer, N. P. Money, Mushrooms as Rainmakers: How Spores Act as Nuceli for Raindrops, PloS One (2015) 0140407.

51. I. Tanasawa, Advances in Condensation Heat Transfer, Adv. Heat Transf. 21 (1991) 55-139.

52. H.-Y. Kim, H. J. Lee, B. H. Kang, Sliding of Liquid Drops Down an Inclined Solid Surface, J. Colloid Interface Sci. 247 (2002) 372-380.

53. P. Dimitrakopoulos, J. Higdon, On the Gravitational Displacement of three-dimentional fluid droplets from inclined solid surfaces, J. Fluid Mech. 395 (1999) 181-209.

54. J. H. Lienhard V, J. H. Lienhard IV, A Heat Transfer Textbook, Phlogiston Press (2003).

55. J. Eggers, J. R. Lister, H. A. Stone, Coalesence of liquid drops, J. Fluid Mech. 401 (1999) 293-310.

56. M. Wu, T. Cubaud, C.-M. Ho, Scaling law in liquid drop coalescence driven by surface tension, Phys. Fluids 16 (2004) 51-54.

57. R. Enright, N. Miljkovic, J. Sprittles, K. Nolan, R. Mitchell, E. N. Wang, How Coalescing Droplets Jump, ACS Nano 8 (2014) 10352-10362.

58. C. Lv, P. Hao, Z. Yao, Y. Song, X. Zhang, F. He, Condensation and jumping relay of droplets on lotus leaf, Appl. Phys. Lett. 103 (2013) 021601.

59. F.-C. Wang, F. Yang, Y.-P. Zhao, Size effect on the coalescence-induced self-propelled droplet, Appl. Phys. Lett. 98 (2011) 053112.

60. J. D. Paulsen, J. C. Burton, S. R. Nagel, Viscous to inertial crossover in liquid drop coalescence, Phys. Rev. Lett. 106 (2011) 114501.

61. J. D. Paulsen, J. C. Burton, S. R. Nagel, S. Appathurai, M. T. Harris, O. A. Basaran, The inexorable resistance of inertia determines the initial regime of drop coalescence, Proc. Natl. Acad. Sci. U.S.A. 109 (2012) 6857-6861.

62. R. Fitzpatrick, Oscillations and waves: an introduction, CRC Press (2013).

63. Y. Nam, H. Kim, S. Shin, Energy and hydrodynamic analyses of coalescence-induced jumping droplets, Appl. Phys. Lett. 103 (2013) 161601.

64. D. Li, Encyclopedia of microfluidics and nanofluidics, Springer Science & Business Media (2008).

65. H. Vahabi, W. Wang, J. M. Mabry, A. K. Kota, Coalescence-induced jumping of droplets on superomniphobic surfaces with macrotexture, Sci. Adv. 4 (2018) eaau3488.

66. A. K. Kota, G. Kwon, A. Tuteja, The design and applications of superomniphobic surfaces, NPG Asia Mater. 6 (2014) 109.

67. T. Liu, C.-J. Kim, Contact angle measurement of small capillary length liquid in super-repelled state, Sci. Rep. 7 (2017) 1-8.

68. P.-G. Gennes, F. Brochard-Wyart, D. Quéré, Capillarity and wetting phenomena: drops, bubbles, pearls, waves, Springer (2004).

69. G. Yang, D. Chai, Z. Fan, X. Li, Capillary condensation of single-and multicomponent fluids in nanopores, Ind. Eng. Chem. Res. 58 (2019) 19302-19315.

70. G. Rickayzen, Molecular theory of capillarity, Phys. Bull. 34 (1983) 437.

71. R. C. Tolman, The effect of droplet size on surface tension, J. Chem. Phys. 17 (1949) 333-337.

72. J. Xie, Q. She, J. Xu, C. Liang, W. Li, Mixed dropwise-filmwise condensation heat transfer on biphilic surface, Int. J. Heat Mass Transfer 150 (2020) 119273.

73. R. Wen, S. Xu, D. Zhao, Y.-C. Lee, X. Ma, R. Yang, Hierarchical superhydrophobic surfaces with micropatterned nanowire arrays for high-efficiency jumping droplet condensation, ACS Appl. Mater. Interfaces 9 (2017) 44911-44921.

74. M. He, Y. Ding, J. Chen, Y. Song, Spontaneous uphill movement and self-removal of condensates on hierarchical tower-like arrays, ACS Nano 10 (2016) 9456-9462.

75. J. Rose, Dropwise condensation theory and experiment: a review, Proc. Inst. Mech. Eng., Part A 216 (2002) 115-128.

76. N. Miljkovic, E. N. Wang, Condensation heat transfer on superhydrophobic surfaces, MRS Bull. 38 (2013) 397-406.

77. R. Wen, S. Xu, X. Ma, Y.-C. Lee, R. Yang, Three-dimensional superhydrophobic nanowire networks for enhancing condensation heat transfer, Joule 2 (2018) 269-279.

78. T.-Y. Zhang, L.-W. Mou, J.-Y. Zhang, L.-W. Fan, J.-Q. Li, A visualized study of enhanced steam condensation heat transfer on a honeycomb-like microporous superhydrophobic surface in the presence of a non-condensable gas, Int. J. Heat Mass Transfer 150 (2020) 119352.

79. X. Qu, J. B. Boreyko, F. Liu, R. L. Agapov, N. V. Lavrik, S. T. Retterer, J. J. Feng, C. P. Collier, C.-H. Chen, Self-propelled sweeping removal of dropwise condensate, Appl. Phys. Lett. 106 (2015) 221601.

80. W. Xu, Z. Lan, B. Peng, R. Wen, X. Ma, Heterogeneous nucleation capability of conical microstructures for water droplets, RSC Adv. 5 (2015) 812-818.

81. W. Thomson, On the Equilibrium of Vapour at a Curved Surface of Liquid, Proc. R. Soc. Edinb. 7 (1872) 63-68.

82. L. R. Fisher, J. N. Israelachvili, Experimental studies on the applicability of the Kelvin equation to highly curved concave menisci, J. Colloid Interface Sci. 80 (1981) 528-541.

83. Q. Chang, Colloid and Interface Chemistry for Water Quality Control, Academic Press (2016).

84. W. Xu, Z. Lan, B. Peng, R. Wen, X. Ma, Effect of nano structures on the nucleus wetting modes during water vapour condensation: from individual groove to nano-array surface, RSC Adv. 6 (2016) 7923-7932.

85. Q. Peng, L. Jia, J. Guo, C. Dang, Y. Ding, L. Yin, Q. Yan, Forced jumping and coalescence-induced sweeping enhanced the dropwise condensation on hierarchically microgrooved superhydrophobic surface, Appl. Phys. Lett. 114 (2019) 133106.

86. A. Aili, H. Li, M. H. Alhosani, T. Zhang, Unidirectional fast growth and forced jumping of stretched droplets on nanostructured microporous surfaces, ACS Appl. Mater. Interfaces 8 (2016) 21776-21786.

87. Y. Utaka, T. Kamiyama, Condensate drop movement in Marangoni condensation by applying bulk temperature gradient on heat transfer surface, Heat Transfer — Asian Research: Co‐sponsored by the Society of Chemical Engineers of Japan and the Heat Transfer Division of ASME 37 (2008) 387-397.

88. D. Tam, V. Von Arnim, G. McKinley, A. Hosoi, Marangoni convection in droplets on superhydrophobic surfaces, J. Fluid Mech. 624 (2009) 101-123.

89. A. Phadnis, K. Rykaczewski, The effect of Marangoni convection on heat transfer during dropwise condensation on hydrophobic and omniphobic surfaces, Int. J. Heat Mass Transfer 115 (2017) 148-158.

90. S. N. Kazi, An overview of heat transfer phenomena, IntechOpen (2012).

91. Y. Li, M. Yoda, An experimental study of buoyancy-Marangoni convection in confined and volatile binary fluids, Int. J. Heat Mass Transfer 102 (2016) 369-380.

92. S. H. Davis, Thermocapillary instabilities, Annu. Rev. Fluid Mech. (1987) 403-435.

93. Y.Zheng, X.Ma, Y. Liu, R. Jiang, K. Wang, Z. Lan, Q. Liang, Experimental study of falling film evaporation heat transfer on superhydrophilic horizontal-tubes at low spray density, Appl. Therm. Eng. 111 (2017) 1548-1556.

94. S. Lee, B. Köroğlu, C. Park, Experimental investigation of capillary-assisted solution wetting and heat transfer using a micro-scale, porous-layer coating on horizontal-tube, falling-film heat exchanger, Int. J. Refrig. 35 (2012) 1176-1187.

95. T. Y. Zhang, L. W. Mou, J. Y. Zhang, L. W. Fan, J. Q. Li, A visualized study of enhanced steam condensation heat transfer on a honeycomb-like microporous superhydrophobic surface in the presence of a non-condensable gas, Int. J. Heat Mass Transfer 150 (2020) 119352.

96. J.-K. Kim, C. W. Park, Y. T. Kang, The effect of micro-scale surface treatment on heat and mass transfer performance for a falling film H2O/LiBr absorber, Int. J. Refrig. 26 (2003) 575-585.

97. J. Yoon, E. Kim, K. Choi, W. Seol, Heat transfer enhancement with a surfactant on horizontal bundle tubes of an absorber, Int. J. Heat Mass Transfer 45 (2002) 735-741.

98. H. Ding, P. Xie, D. Ingham, L. Ma, M. Pourkashanian, Flow behaviour of drop and jet modes of a laminar falling film on horizontal tubes, Int. J. Heat Mass Transfer 124 (2018) 929-942.

99. J.D. Killion, S. Garimella, Gravity-driven flow of liquid films and droplets in horizontal tube banks, Int. J. Refrig. 26 (2003) 516-526.

100. J. Rose, L. Glicksman, Dropwise condensation—the distribution of drop sizes, Int. J. Heat Mass Transfer 16 (1973) 411-425.

101. C. S. Sharma, C. Stamatopoulos, R. Suter, P. R. Von Rohr, D. Poulikakos, Rationally 3D-textured copper surfaces for laplace pressure imbalance-induced enhancement in dropwise condensation, ACS Appl. Mater. Interfaces 10 (2018) 29127-29135.

102. W. Xu, Z. Lan, B. Peng, R. Wen, Y. Chen, X. Ma, Directional movement of droplets in grooves: suspended or immersed?, Sci. Rep. 6 (2016) 18836.

103. C. S. Sharma, J. Combe, M. Giger, T. Emmerich, D. Poulikakos, Growth rates and spontaneous navigation of condensate droplets through randomly structured textures, ACS Nano 11 (2017) 1673-1682.

104. L. Ventola, L. Scaltrito, S. Ferrero, G. Maccioni, E. Chiavazzo, P. Asinari, Micro-structured rough surfaces by laser etching for heat transfer enhancement on flush mounted heat sinks, J. Phys. Conf. Ser. 525 (2014) 012017.

105. M. Nitsche, R. O. Gbadamosi, Heat exchanger design guide: a practical guide for planning, selecting and designing of shell and tube exchangers, Butterworth-Heinemann (2015).

106. S. Al-Shammari, D. Webb, P. Heggs, Condensation of steam with and without the presence of non-condensable gases in a vertical tube, Desalination 169 (2004) 151-160.

107. P. Donkers, K. Gao, J. Houben, H. Huinink, B. Erich, O. Adan, Effect of non-condensable gasses on the performance of a vacuum thermochemical reactor, Energies 13 (2020) 362.

108. S. T. Revankar, D. Pollock, Laminar film condensation in a vertical tube in the presence of noncondensable gas, Appl. Math. Model. 29 (2005) 341-359.

109. E. Sparrow, W. Minkowycz, M. Saddy, Forced convection condensation in the presence of noncondensables and interfacial resistance, Int. J. Heat Mass Transfer 10 (1967) 1829-1845.

110. W. Minkowycz, E. Sparrow, Condensation heat transfer in the presence of noncondensables, interfacial resistance, superheating, variable properties, and diffusion, Int. J. Heat Mass Transfer 9 (1966) 1125-1144.

111. D. F. Othmer, The condensation of steam, Ind. Eng. Chem. 21 (1929) 576-583.

112. S. Zheng, F. Eimann, C. Philipp, T. Fieback, U. Gross, Modeling of heat and mass transfer for dropwise condensation of moist air and the experimental validation, Int. J. Heat Mass Transfer 120 (2018) 879-894.

113. R. Wen, X. Zhou, B. Peng, Z. Lan, R. Yang, X. Ma, Falling-droplet-enhanced filmwise condensation in the presence of non-condensable gas, Int. J. Heat Mass Transfer 140 (2019) 173-186.

114. R. Xiao, N. Miljkovic, R. Enright, E. N. Wang, Immersion condensation on oil-infused heterogeneous surfaces for enhanced heat transfer, Sci. Rep. 3 (2013) 1988.

115. H. Tsuchiya, M. Tenjimbayashi, T. Moriya, R. Yoshikawa, K. Sasaki, R. Togasawa, T. Yamazaki, K. Manabe, S. Shiratori, Liquid-infused smooth surface for improved condensation heat transfer, Langmuir 33 (2017) 8950-8960.

116. S. Sett, P. Sokalski, K. Boyina, L. Li, K. F. Rabbi, H. Auby, T. Foulkes, A. Mahvi, G. Barac, L. W. Bolton, Stable dropwise condensation of ethanol and hexane on rationally designed ultrascalable nanostructured lubricant-infused surfaces, Nano Lett. 19 (2019) 5287-5296.

117. A. Ghosh, S. Beaini, B. J. Zhang, R. Ganguly, C. M. Megaridis, Enhancing dropwise condensation through bioinspired wettability patterning, Langmuir 30 (2014) 13103-13115.

118. Y. Y. Yan, N. Gao, W. Barthlott, Mimicking natural superhydrophobic surfaces and grasping the wetting process: A review on recent progress in preparing superhydrophobic surfaces, Adv. Colloid Interface Sci. 169 (2011) 80-105.

119. R. Wen, Q. Li, J. Wu, G. Wu, W. Wang, Y. Chen, X. Ma, D. Zhao, R. Yang, Hydrophobic copper nanowires for enhancing condensation heat transfer, Nano Energy 33 (2017) 177-183.

120. Y. Zhao, H. Zhang, W. Wang, C. Yang, Wetting transition of sessile and condensate droplets on copper-based superhydrophobic surfaces, Int. J. Heat Mass Transfer 127 (2018) 280-288.

121. E. Jiaqiang, Y. Jin, Y. Deng, W. Zuo, X. Zhao, D. Han, Q. Peng, Z. Zhang, Wetting models and working mechanisms of typical surfaces existing in nature and their application on superhydrophobic surfaces: A review, Adv. Mater. Interfaces 5 (2018) 1701052.

122. R. Parin, A. Martucci, M. Sturaro, S. Bortolin, M. Bersani, F. Carraro, D. Del Col, Nano-structured aluminum surfaces for dropwise condensation, Surf. Coat. Technol. 348 (2018) 1-12.

123. Y. Hou, M. Yu, X. Chen, Z. Wang, S. Yao, Recurrent filmwise and dropwise condensation on a beetle mimetic surface, ACS Nano 9 (2015) 71-81.

124. A. R. Parker, C. R. Lawrence, Water capture by a desert beetle, Nature 414 (2001) 33-34.

125. F. Moukalled, L. Mangani, M. Darwish, F. Moukalled, L. Mangani, M. Darwish, The finite volume method, Springer (2016).

126. T. Kleiner, S. Rehfeldt, H. Klein, CFD model and simulation of pure substance condensation on horizontal tubes using the volume of fluid method, Int. J. Heat Mass Transfer 138 (2019) 420-431.

127. T. Kleiner, A. Eder, S. Rehfeldt, H. Klein, Detailed CFD simulations of pure substance condensation on horizontal annular low finned tubes including a parameter study of the fin slope, Int. J. Heat Mass Transfer 163 (2020) 120363.

128. L. Stendardo, A. Milionis, G. Kokkoris, C. Stamatopoulos, C. S. Sharma, R. Kumar, M. Donati, D. Poulikakos, Out-of-Plane Biphilic Surface Structuring for Enhanced Capillary-Driven Dropwise Condensation, Langmuir 39 (2023) 1585-1592.

129. X. Yin, G. Liang, J. Wang, S. Shen, Vapor condensation on micropillar structured surface with lattice Boltzmann method, Int. Commun. Heat Mass Transf. 138 (2022) 106357.

130. W. Fang, K. Zhang, Q. Jiang, C. Lv, C. Sun, Q. Li, Y. Song, X.-Q. Feng, Drop impact dynamics on solid surfaces, Appl. Phys. Lett. 121 (2022) 210501.

131. X. Wang, B. Xu, Z. Chen, Y. Yang, Q. Cao, Lattice Boltzmann simulation of dropwise condensation on the microstructured surfaces with different wettability and morphologies, Int. J. Therm. Sci. 160 (2021) 106643.

132. D. Wang, J. Bernsdorf, Lattice Boltzmann simulation of steady non-Newtonian blood flow in a 3D generic stenosis case, Comput. Math. Appl. 58 (2009) 1030-1034.

133. C.-Y. Zhao, J.-D. Wu, G.-D. Wang, D. Qi, J.-M. Jiang, Numerical study of falling film flow and heat transfer on the horizontal tube with a porous coating layer, Int. J. Heat Mass Transfer 221 (2024) 125046.

134. A. Karmakar, S. Acharya, Wettability effects on falling film flow and heat transfer over horizontal tubes in jet flow mode, J. Heat Transfer 142 (2020) 122301.

135. A. Karmakar, S. Acharya, Numerical simulation of falling film sensible heat transfer over round horizontal tubes, Int. J. Heat Mass Transfer 190 (2022) 122727.

136. C.-Y. Zhao, Z.-L. Yao, D. Qi, W.-T. Ji, A.-G. Li, W.-Q. Tao, Numerical investigation of tube bundle arrangement effect on falling film fluid flow and heat transfer, Appl. Therm. Eng. 201 (2022) 117828.

137. J. Alinejad, M. M. Peiravi, Numerical analysis of secondary droplets characteristics due to drop impacting on 3D cylinders considering dynamic contact angle, Meccanica 55 (2020) 1975-2002.

138. Y. Wang, Y. Wang, S. Wang, Droplet impact on cylindrical surfaces: Effects of surface wettability, initial impact velocity, and cylinder size, J. Colloid Interface Sci. 578 (2020) 207-217.

139. Y. Wang, Q. Shangguan, D. Zhang, Many-body dissipative particle dynamics simulation of the anisotropic effect of droplet wetting on stripe-patterned heterogeneous surfaces, Appl. Surf. Sci. 494 (2019) 675-683.

140. S. Yun, Enhancing the asymmetry of bouncing ellipsoidal drops on curved surfaces, Langmuir 36 (2020) 14864-14871.

141. H. Chen, X. Liu, K. Wang, H. Liu, S. Shen, Numerical study on dynamic characteristics of double droplets impacting a super-hydrophobic tube with different impact velocities, Int. J. Comput. Fluid Dyn. 33 (2019) 222-233.

142. Y. Guo, L. Wei, G. Liang, S. Shen, Simulation of droplet impact on liquid film with CLSVOF, Int. Commun. Heat Mass Transf. 53 (2014) 26-33.

143. J. Luo, S.-Y. Wu, L. Xiao, Z.-L. Chen, Hydrodynamics and heat transfer of multiple droplets successively impacting on cylindrical surface, Int. J. Heat Mass Transfer 180 (2021) 121749.

144. Y. Ma, Z. Zhou, F. Zhang, Y. Cheng, J. Xu, Numerical investigation of impacting heat transfer of binary droplets on superhydrophobic substrates, Int. J. Therm. Sci. 192 (2023) 108381.

145. C. Wang, H. Zhang, D. Zhu, B. Huang, Z. Xu, P. Hao, F. He, H. Zhao, X. Zhang, Successive impact of droplets on the superhydrophobic surface, Int. J. Multiphase Flow (2024) 104758.

146. Z.-H. Cao, K. Luo, H.-L. Yi, H.-P. Tan, Energy conservative dissipative particle dynamics simulation of mixed convection in eccentric annulus, Int. J. Heat Mass Transfer 74 (2014) 60-76.

147. Z. Li, Y.-H. Tang, H. Lei, B. Caswell, G. E. Karniadakis, Energy-conserving dissipative particle dynamics with temperature-dependent properties, J. Comput. Phys. 265 (2014) 113-127.

148. Y. Liu, L. Moevius, X. Xu, T. Qian, J. M. Yeomans, Z. Wang, Pancake bouncing on superhydrophobic surfaces, Nat. Phys. 10 (2014) 515-519.

149. C. Qian, F. Zhou, T. Wang, Q. Li, D. Hu, X. Chen, Z. Wang, Pancake jumping of sessile droplets, Adv. Sci. 9 (2022) 2103834.

Chapter 3

Dropwise and Filmwise Condensation of Water on Liquid-Repellent Heat Pipes under Laminar Flow

Navdeep Sangeet Singh, Jason Stafford and Nan Gao**

School of Engineering, University of Birmingham, Birmingham, B15 2TT, United Kingdom

This chapter is in the process of being published to a journal.

Author Contributions: N.S.S formulated the research idea. N.S.S conducted, extracted and assessed all the numerical simulation data. N.S.S prepared the manuscript. N.G and J.S are currently reviewing and guiding the manuscript to publication.

Abstract

Utilizing liquid-repellent surfaces on condenser heat pipes has been widely known to augment the heat transfer coefficient of the tube by regulating the hydrodynamics of the formulating condensate towards dropwise or jumping-droplet condensation. An example is employing superhydrophobic surfaces with minimal contact angle hysteresis to allow droplets to swiftly glide off the tubes' surface. However, it remains unclear as to whether the contact angle or the contact angle hysteresis plays the main role to augment the tubes' heat transfer efficiencies at various subcooling temperatures. Therefore, in this study, numerous two-dimensional numerical simulations are demonstrated to describe the condensate flow behaviour and heat transfer rates of a condensing tube at various equilibrium contact angles, contact angle hysteresis and subcooling temperatures. By modifying the vapour thermal conductivity alongside employing the Lee's model, the heat transfer coefficients, film thickness and temperature profiles have shown particularly good agreement against the Nusselt solution for a fully wetted tube. A maximum film thickness error of only 2% was shown against the Nusselt solution up to a subcooling temperature of 50 K. Additionally at the same subcooling temperature, the circumferential temperature profiles illustrated a interfacial temperature deviation of less than 1 K at the liquid-gas interface. This led to the heat transfer coefficients only showing an error of 10.5% up to a subcooling temperature of 10 K. Furthermore, the simulated heat transfer coefficients provided only a 13% maximum error in comparison to experimental results. Adjusting the equilibrium contact angle of the tube between 0 to 150° amplified heat transfer coefficients by 140% due to the transition between filmwise to dropwise condensation and even jumping-droplet condensation. In addition, altering the contact angle hysteresis of the tube from 0 to 20° gave a 27% reduction in heat transfer coefficients at selected equilibrium

contact angles as multiple droplets began to become pinned on the tube rather than being swept or propelled off.

3.1. Introduction

Steam condensation is ubiquitous amongst essential thermal engineering processes that include condensers. These condensers can be seen in various industries such as chemical or nuclear power plants, heating ventilation and air conditioning systems, distillation, and food processing.[1-5] Generally, condensers contain several heat pipes that are cooled below saturation conditions to effectively withdraw the latent heat from the steam. As a consequence, the steam will begin to liquify upon the tube surface resulting in a thin liquid film or numerous nucleating droplets. The former is widely known as filmwise condensation and the latter as dropwise condensation. However, these modes of condensation greatly affect the heat transfer performance of condensers and are typically achieved through altering the wettability of the surface as thoroughly discussed in Chapter 1.

Most thermally conductive materials that are used for heat pipes are notably hydrophilic which in most cases, promotes filmwise condensation whilst hydrophobic or superhydrophobic surfaces ideally generate dropwise condensation.[6-9] Thus, for condensation applications, dropwise condensation is heavily preferred as the heat transfer coefficient of the tubes are at least 4 times higher than of filmwise condensation.[10] This is ascribed to the thin macroscopic liquid film on the surface which generates a thermal resistance towards heat transfer hence, reducing the rate of heat flux towards the tube surface. Whereas, with dropwise condensation, droplets continuously nucleate and slide off the tube causing more of the bare surface to be exposed between the vapour-solid interface.[9] Recently, however, a phenomenon known as coalescence-induced jumping-

droplet condensation has been shown to further improve heat transfer efficiencies by as much as 100% from dropwise condensation.[11] This is due to the droplets being removed swiftly off the surface at a much smaller droplet diameter as they are propelled off the surface rather than being swept by the falling film flow. To ascertain jumping-droplet condensation, a superhydrophobic surface is required with minimal contact angle hysteresis (less than 5°) which is crucial for droplet propulsion.[9,12,13]

For surfaces with large contact angle hysteresis, the lateral adhesion force of the surface becomes substantial which prohibits the movement of droplets hence, allowing droplets to be pinned on the surface. Therefore it can be said that, in order for droplets to jump off the surface, the inertia force generated from droplet coalescence must overcome the adhesion force of the surface.[14] For this reason, it is ideal for surfaces to have a high contact angle and low contact angle hysteresis to minimise the adhesion force in the static and kinetic regime. An example can be seen by Zhang *et al.* who fabricated microporous superhydrophobic surfaces on copper heat pipes with a CAH close to 0°.[15] Their results exhibited jumping-droplet condensation up to a subcooling temperature of 20 K. The subcooling temperature is the deviation between the saturation and wall temperature. When comparing against a hydrophobic or hydrophilic surface, the results showed dropwise and filmwise condensation due to low contact angles and high contact angle hysteresis (~28°). In addition, Milijkovic *et al*. created superhydrophobic nanostructures upon a tube with a CAH of less than 5° which was compared against a hydrophobic and hydrophilic tube with CAH being up to 40°.[12] The superhydrophobic tube illustrated jumping-droplet condensation compared to the hydrophobic and hydrophilic surface which again demonstrated dropwise and filmwise condensation at various vapour pressures resulting in a 30% increase in heat transfer coefficients.

Remarkably, the same can be said for establishing dropwise condensation as having a large contact angle hysteresis will be prevent droplets from sliding off the tube and thus creating filmwise condensation. Although, in this case, a superhydrophobic or even a hydrophobic surface is not necessary to create dropwise condensation. This is demonstrated by Cha *et al.* who managed to generate dropwise condensation from hydrophilic surfaces by modifying the surfaces' contact angle hysteresis to be lower than 3°.[16] It was postulated that decreasing the contact angle hysteresis towards zero allowed the droplet departure radius to become independent of the surfaces' equilibrium contact angle. As a result, the heat transfer performance of the modified hydrophilic surface became equivalent to a hydrophobic surface with large contact angle hysteresis. Nevertheless, it is still unclear how much the contact angle hysteresis affects the condensate behaviour at different equilibrium contact angles. In this case, numerical simulations are ideal to investigate such concerns to depict the kinetic forces involved during condensation. However as seen from literature, validating phase change simulations presents a challenge as most methods require the usage of experimental correlations which introduces limitations within the model.[17-20]

To appropriately simulate condensation, the phase change rate must be correctly calculated, which is essentially the mass transfer rate from one phase to another. There are various mass transfer models used to simulate the mass transfer rate such as the Energy jump condition,[21] Schrage's model,[22] and Lee's model.[23] Nonetheless, the former two methods require a pre-existing interface (in this case, a liquid film) to determine the mass transfer rate. This would not be ideal for our case as filmwise condensation is not guaranteed when altering the surfaces' contact angle. Thus, the Lee's model is widely used amongst various phase change simulations. It should be noted that, the Lee's model intends to minimize the interfacial temperature deviation between the saturation

temperature and the temperature of the film (at the liquid-vapour interface) through the use of an empirical coefficient which is known as the mass transfer intensity factor.[24] Further details on the approach to determine this factor, as well as the overall numerical implementation, can be found in Chapter 3.2.2. Maintaining the interfacial temperature towards saturation is essential to obtain the correct heat transfer rate to the liquid film otherwise, an artificial temperature gradient is created between the liquid-vapour phase which will present false heat transfer results.[25] It is noteworthy that the value of the empirical coefficient is typically calibrated from a case-by-case basis and usually ranges between 0.1 to 10^7 s^{-1}.[24]

Using large mass transfer intensity factor values ($\geq 10^5$ s^{-1}) has been found to reduce the temperature deviation between the saturation temperature, however at the same time, instability is introduced due to the prompt increase in mass transfer rate. In spite of this, Shen *et al.* managed to devise a strategy to increase the stability of condensation simulations on a flat plate for large empirical coefficient values.[25] This was achieved by modifying the thermal conductivity of the vapour which in turn, affects the temperature gradient at the liquid-vapour interface (further details are shown in Chapter 3.2). As a consequence, the interfacial temperature deviation was reduced to only 1.1 K between the saturation temperature whilst also maintaining condensation stability. Therefore, for this study, the condensation heat transfer properties on a two-dimensional tube are investigated by altering the surfaces' static and dynamic contact angles at several subcooling temperatures. By employing Shen *et al.* methodology, the simulation results tend to agree well with the Nusselt theory up to a subcooling temperature of 50 K. This is quantified by comparing the temperature profiles at different circumferential angles, film thickness and more importantly, the heat transfer coefficients against subcooling temperature and time. The surfaces' equilibrium contact angle is then adjusted from 0 to 150° at different

subcooling temperatures to clarify the transition from filmwise to dropwise condensation and even jumping-droplet condensation. Furthermore, a dynamic contact angle model based on Yokoi *et al.* model is implemented in the simulation to adjust the advancing and receding contact angles of the surface (details are shown in Chapter 3.2.2).[26] This is to demonstrate how much the contact angle hysteresis can alter the heat transfer coefficient of the tube by altering the surfaces' adhesion force within the dynamic regime at given equilibrium contact angles.

3.2. Methodology

3.2.1 Fluid Domain Setup

Figure 3.1 displays the dimensions and the design of the fluid domain with its associated boundary conditions and mesh refinements. Notably, the setup of the domain follows a similar approach to Kleiner *et al.* model where the size of the fluid domain in the radial direction (R_2) is kept short (equal to 0.975 mm) to minimise the computational time and resources.[27] Moreover, only half of the tube is considered as the fluid flow is deemed to be symmetric. The radius of the tube is given as 8.025 mm (shown as R_1) which equates to a diameter of 19.05 mm. Furthermore, the length of the fluid domain at the bottom of the tube (R_3) is set to 5.475 mm in order to observe the detachment of condensate off the tube surface. A pressure-outlet is then prescribed at the outer edges of the domain which has a gauge pressure of 0 Pa to certify no non-condensable gasses are present during condensation. In this instance, the tube is only subjected to atmospheric pressure (101325 Pa). To accurately compare the film thickness against the Nusselt solution, a wall-slip boundary condition is imposed at the bottom left side of the tube containing an equilibrium contact angle of 0° to minimise the effect of surface tension at the bottom of the tube, as it is neglected from the Nusselt solution. Additionally, a no-slip boundary condition is

selected at the wall as the slip velocity experienced at the tube wall is viewed to be insignificant for characteristic length scales involved. Importantly, the fluid domain is initially patched with a water-vapour volume fraction of $\alpha_v = 1$ to ensure the entire domain is filled with vapour and the temperature of the vapour is equal to the saturation temperature of water (373 K). This is to ensure that condensation occurs as soon as the simulation starts. Additionally, a constant wall temperature is imposed on the tube wall boundary condition in the range between 372 – 323 K. Once compared with the Nusselt solution, the wall-slip boundary condition is then changed to a symmetry boundary condition to include the effects of surface tension within the fluid at the bottom of the tube.

To specify the contact angle hysteresis upon the tube, a UDF (User-defined Function) model developed by Yokoi *et al.* is implemented at the wall boundary condition where the advancing, receding and equilibrium contact angles can be adjusted accordingly.[26] As shown in **Figure 3.1**, the domain is meshed with hexahedral elements where size of each element is equal to 30 µm based on the mesh sensitivity analysis conducted by Kleiner *et al*. which was benchmarked against the Nusselt film theory.[27] To appropriately depict the film thickness, mesh refinement layers are added at the wall boundary where the number of layers are based on the minimal Nusselt film thickness calculated. The smallest film thickness value (seen at the top of the tube) was then divided by ten to give ten mesh refinement layers which equated to 2.5 µm width layers. Mesh refinement layers is also applied along the symmetry plane at the bottom of the tube in order to capture the Rayleigh-Plateau instability of the liquid jet/droplet detachment as this will notably affect the number of droplets released from the tube surface.[28]

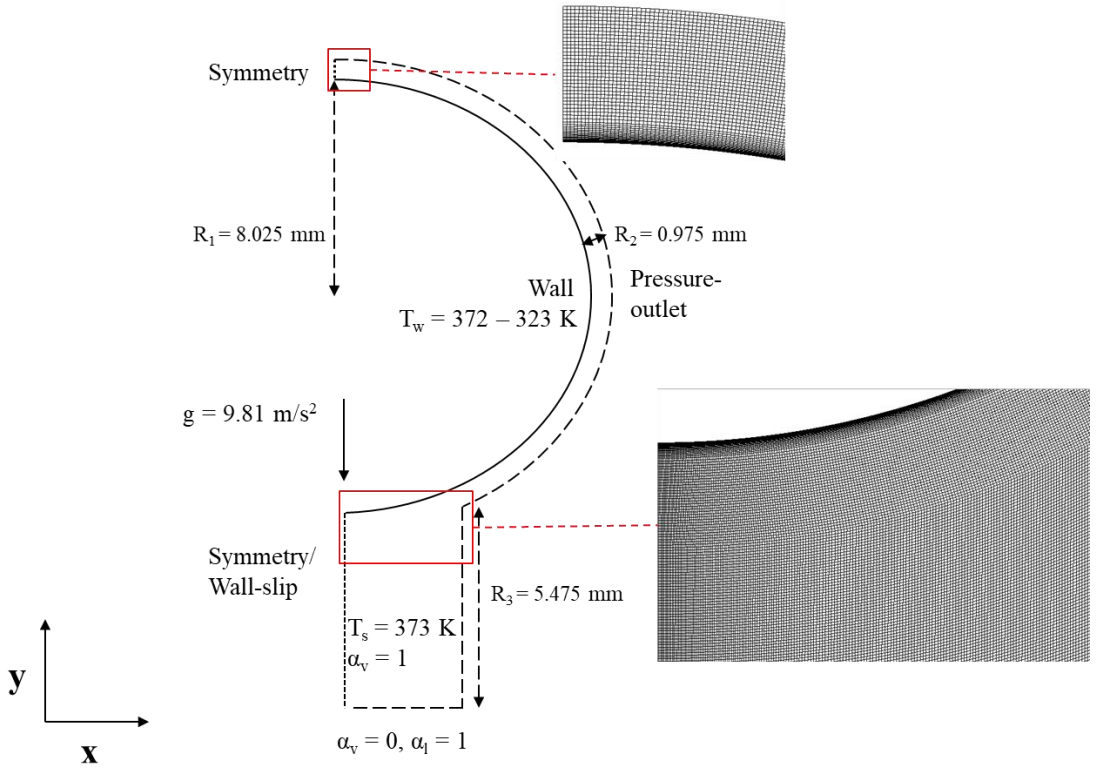

Figure 3.1. Computational fluid domain with prescribed boundary conditions and mesh refinement.

To ensure the condensate flow remains within the laminar region, the films Reynolds number (Re_f) is initially calculated. Here, the films' Reynolds number is determined to be:[28]

$$Re_f = \frac{4\Gamma}{\mu_l} \tag{3.1}$$

where Γ is the specific film flow rate (kg/m·s) given as:

$$\Gamma = \frac{\dot{m}}{2L_t} \tag{3.2}$$

$\dot{m}$ is stated as the mass flow rate (kg/s) and L_t is the tube length (m). Based on Newtons' law of cooling for phase change, the mass flow rate is calculated as:

$$\dot{m} = \frac{qA}{\Delta h_v} = \frac{q2\pi R_t L_t}{\Delta h_v} \tag{3.3}$$

here q equals the mean heat flux of the tube (W/m^2), A is the surface area of the tube (m^2), Δh_v is the latent heat of vaporisation (J/kg) and R_t is the radius of the tube (m). For filmwise condensation, the mean heat flux is derived as:[29]

$$q = 0.728\left(\frac{\rho_l(\rho_l - \rho_v)g\Delta h_v {k_l}^3 (T_s - T_w)^3}{\mu_l d_t}\right)^{\frac{1}{4}} \tag{3.4}$$

k_l is the thermal conductivity of the liquid (W/m·K), ρ_v is the density of the vapour (kg/m^3) d_t is the diameter of the tube (m) and T_s is the saturation temperature (K). T_s-T_w represents the subcooling temperature (ΔT). Substituting both the specific mass flow rate (Equation 3.2) and the mass flow rate equations (Equation 3.3) into the films' Reynolds number gives:

$$Re_f = \frac{4qR_t\pi}{\mu_l \Delta h_v} \tag{3.5}$$

From Equation 3.5, the highest films Reynold number is given as 80 for a subcooling temperature of 50 K which demonstrates laminar flow. It is worth noting however, that even within the laminar region, interfacial waves may arise due to the increase in inertia forces at large subcooling temperatures.[30] This may alter the heat transfer rate during condensation as the waves will induce film thinning and mixing. To ascertain whether the interfacial waves will predominantly affect the film behaviour, Brauer *et al.* developed a correlation for laminar filmwise condensation to determine the critical Reynolds number for when this will occur:[31]

$$Re_f > 9.3Ga^{*0.1} \tag{3.6}$$

*Ga** represents the modified Galileo number for falling-film flow which illustrates the ratio of gravitational forces to the viscous forces of a fluid which can be stated as:

$$Ga = \frac{g{\lambda_c}^3{\rho_l}^2}{\mu_l^2} \tag{3.7}$$

For falling-film flow, the hydrodynamic length is commonly expressed as the capillary length (κ^{-1}) (Equation 2.9 in Chapter 2.3.2). Inserting the capillary length into the Galileo number and squaring it, generates a modified Galileo number, *Ga**, which is shown as:[30]

$$Ga^* = \frac{\rho_l \gamma_{lv}^3}{\mu_l^4 g} \tag{3.8}$$

From Equation 3.6, using water at saturation temperature, interfacial waves will begin to induce film thinning when the film Reynolds number becomes greater than 166. Thus, from the calculated Reynolds number, the effect of interfacial waviness is negligible upon the flow behaviour of the condensate and will not affect the heat transfer characteristics. As noted previously, the fluid used for condensation at the liquid and vapour phase is water and water-vapour respectively. The fluid properties used are constant and given at saturation conditions (T_s = 373 K) where ρ_l = 958 kg/m^3 ρ_v = 0.58 kg/m^3 μ_l = 0.28 mPa·s, μ_v = 12.3 µPa·s, $C_{p,l}$ = 2077 J/kg·K, $C_{p,v}$ = 4217 J/kg·K, k_l = 0.68 W/m·K, k_v = 24.6 mW/m·K, Δh_v = 2256.5 kJ/kg and γ_{lv} = 59 mN/m. μ_v is the dynamic viscosity of vapour (Pa·s), k_v is the thermal conductivity of the vapour (W/m·K), $C_{p,l}$ is known as the isobaric specific heat capacity of the liquid (J/kg·K) and $C_{p,v}$ is the isobaric specific heat capacity of the vapour (J/kg·K).

3.2.2 Numerical Schemes Implemented

To appropriately capture the liquid-vapour interface, of an incompressible, laminar fluid, the Volume-of-Fluid (VOF) method is implemented to establish the volume fraction (α) of the liquid and vapour phase at each cell. Furthermore, to initiate condensation, a phase transport equation is utilized to create the mass transfer between the vapour and liquid phase. This is shown as:

$$\frac{1}{\rho_v}\left(\frac{\partial}{\partial t}(\alpha_v \rho_v) + \nabla \cdot (\alpha_v \rho_v \overrightarrow{v_v}) = \dot{m}_{lv} - \dot{m}_{vl}\right) \tag{3.9}$$

where $\dot{m}_{lv}$ is the mass transfer rate from the liquid to vapour phase (evaporation), and $\dot{m}_{vl}$ is the mass transfer rate from the vapour to liquid phase (condensation) (kg/m^{3}s). It should be noted that, ANSYS Fluent considers the mass transfer rate from the vapour to liquid phase as being negative. For this case, $\dot{m}_{lv}$ is equal to 0 as it is assumed there is no mass transfer from the liquid to the vapour phase. To determine $\dot{m}_{vl}$, the Lee's model is introduced which calculates the mass transfer rate based on the difference between the interfacial temperature of the film and saturation temperature.[23] Additionally, Lee's model assumes that the mass transfer rate is isobaric and in a quasi-thermo-equilibrium state.[24] The simplified equation used for the mass transfer rate is given as:

$$\dot{m}_{vl} = r\alpha_v \rho_v \frac{T_s - T_v}{T_s} \tag{3.10}$$

where r is the mass transfer intensity factor (s^{-1}) and T_v is the temperature of the vapour (K). Notably, this equation is only valid if $T_v < T_s$. As previously stated, the mass transfer intensity factor is an important feature to maintain the interfacial temperature towards the saturation temperature and it is usually determined empirically through trial and error.

Through trail-and-error, a maximum coefficient value of r = 5 x 10^5 was found to produce stable rates of condensation without creating divergence. Increasing the condensation frequency further caused the stability of the simulation to decrease rapidly. However, it was found that the coefficients' magnitude is still not large enough to maintain the interfacial temperature towards the saturation temperature, in other words, the heat transfer results were below that predicted by the Nusselt theory. To minimise the interfacial temperature deviation further without creating instability, the vapour thermal conductivity is amplified using a correlation factor conceived by Shen *et al.*[25] Their model simplifies the energy equation to a one-dimensional conduction equation by assuming that the heat transfer rate is steady state, convection is negligible compared to the latent heat and α_v = 1 before reaching the liquid film at the vapour-liquid interface. By increasing the vapour thermal conductivity, the temperature gradient along the vapour phase is reduced, which lessened the interfacial temperature deviation based on energy conservation at the liquid-vapour film interface which is illustrated as:[25]

$$k_l \frac{\partial(T_l)}{\partial y} = k_v \frac{\partial(T_v)}{\partial y} \tag{3.11}$$

From Nusselt's solution, it is assumed that the temperature gradient near the film is equal to zero as convection is neglected. Hence, the vapour thermal conductivity is modified as:[25]

$$k_v{}^* = nk_v \tag{3.12}$$

where n is a coefficient determined empirically. Through trail-and-error, an optimum n value was found to be 6000 by comparing the heat flux and heat transfer coefficient of the tube surface against the Nusselt solution.

Furthermore, the momentum conservation equation is introduced which is solved in the mixture phase (where $0 < \alpha_v < 1$) to establish the velocity field within the fluid domain.

$$\frac{\partial}{\partial t}(\rho\vec{v}) + \nabla \cdot (\rho\vec{v}\vec{v}) = -\nabla p + \nabla \cdot [\mu(\nabla\vec{v} + \nabla\vec{v}^T)] + \rho\vec{g} + \overrightarrow{F_{vol}} \quad (3.13)$$

Additionally, the density and viscosity terms in the momentum equation are modified to take into account of the mixture phase as follows:

$$\rho = \alpha_l\rho_l + (1 - \alpha_l)\rho_v \quad (3.14)$$

$$\mu = \alpha_l\mu_l + (1 - \alpha_l)\mu_v \quad (3.15)$$

$(1 - \alpha_l) = \alpha_v$ based on the VOF method. $\overrightarrow{F_{vol}}$ is a source term which represents the surface tension force upon the liquid-vapour interface. Here, the surface tension force is modelled using the continuum surface tension force (CSF) model by Brackbill *et al*.[32] For only two phases present, this is shown as:

$$\overrightarrow{F_{vol}} = \gamma_{lv}\frac{\rho K\nabla\alpha_l}{\frac{1}{2}(\rho_v + \rho_l)} \quad (3.16)$$

K is known as the surface curvature of the liquid-vapour interface which, in other words, can be defined as the divergence of the unit normal vector:[32]

$$K = \nabla \cdot \hat{n} \quad (3.17)$$

$\hat{n}$ is given as the unit normal vector which is calculated by determining the volume fraction gradient of the liquid phase.

$$\hat{n} = \frac{\nabla\alpha_l}{|\nabla\alpha_l|} \quad (3.18)$$

To prescribe the effect of the contact angle on the tube surface, the wall adhesion model is employed at the wall which applies an adhesion force to the surface based on the

magnitude of the contact angle imposed. However, for the contact angle hysteresis studies, a dynamic contact angle (θ_d) is used instead of the equilibrium contact angle. To illustrate the effect of the surface adhesion force, the wall adhesion model amends the unit normal vector as:

$$\hat{n} = \hat{n}_w \cos\theta_d + \hat{t}_w \sin\theta_d \tag{3.19}$$

$\hat{n}_w$ and $\hat{t}_w$ are the unit vectors that are normal to and tangent from the wall correspondingly. Based on the works of Yokoi *et al.*[26], the dynamic contact angle is calculated based on the velocity of the droplets' three-phase contact line (U_{cl}) and the selected advancing and receding contact angles. As the velocity of the contact line increases (advances), the advancing contact angle tends to saturate to its' maximum value. The same can be said for when the velocity of the contact line decreases (receding). As such, the dynamic contact angle is determined as follows:[26]

$$\theta_d(U_{cl}) = \begin{cases} \min\left[\theta_Y + \sqrt[3]{\frac{Ca}{k_a}}\ , \theta_a\right] & if\ U_{cl} \geq 0 \\ \max\left[\theta_Y + \sqrt[3]{\frac{Ca}{k_r}}\ , \theta_r\right] & if\ U_{cl} < 0 \end{cases} \tag{3.20}$$

where *Ca* is equal to the capillary number given as the ratio of the fluids' viscous force to the surface tension force ($Ca = \mu_l U_{cl}/\gamma_{lv}$), k_a and k_r are coefficients based on the material used for advancing and receding contact angles. As the material of the surface is not considered in our study, the values of k_a and k_r are selected based on Yokoi *et al.* experimental parameters where k_a = 9 x 10^{-9} and k_r = 9 x 10^{-8}.[26] Incorporating other dynamic contact angle models (for e.g. the Cox-Voinov law) would not be valid in this instance as their model is limited to small capillary numbers and contact angles.[33] For larger intrinsic contact angles (i.e. up to 150°) jumping-droplet condensation may be

conceived which can result in large inertial forces to be generated as droplets depart off the tube which would increase the capillary number of the fluid further. Furthermore, the energy equation is introduced which is solved within the mixture phase as:

$$\frac{\partial\left(\rho e+\frac{v^2}{2}\right)}{\partial t}+\nabla\cdot\left[\vec{v}\left(\rho(e+\frac{v^2}{2})+p\right)\right]=\nabla\cdot[k\nabla T]+S_h \qquad (3.21)$$

Where e is given as the internal energy of the system (J) which is calculated as $e=C_{\mathrm{v}}(T)$, with C_{v} equalling the isochoric specific heat capacity (J/kg·K). v is equal to the velocity of the fluid within the mixture phase (m/s). p is the ideal gas pressure (Pa) calculated as $(p=(\kappa-1)\rho e)$ where κ is given as the specific heat ratio $(\kappa=\frac{C_p}{C_{\mathrm{v}}})$. S_h is the energy source term which considers the amount of latent heat released through condensation. Therefore, the energy source term is given as:

$$S_h=-\dot{m}_{vl}\Delta h_v \qquad (3.22)$$

Similarly, the thermal conductivity, k, is calculated in the mixture phase as:

$$k=\alpha_l k_l+(1-\alpha_l)k_v \qquad (3.23)$$

Although, as previously mentioned, from Shen *et al.* model, the vapour thermal conductivity is modified by multiplying it by a coefficient which modifies the thermal conductivity in the mixture phase as:

$$k^*=\alpha_l k_l+(1-\alpha_l){k_v}^* \qquad (3.24)$$

Initially, when a thin film of condensate is formed on the tube, the temperature gradient along the film is substantially large for its' given thickness. An example of this is shown in **Figure 3.5**. As a consequence, this brings forth numerical instability due to the prompt increase in heat flux on the tube hence, increasing the rate of condensation. This will give

rise to capillary waves generated within the bulk of the fluid which in turn, can create surface waves. To counteract this phenomenon, the Courant number (or the Courant–Friedrichs–Lewy condition) was fixed to apply an adaptive time stepping method that automatically changed the timestep based on the magnitude of the capillary waves' velocity. In other words, the larger the capillary waves' velocity is, the smaller the timestep must be for a given Courant number. This relationship can be expressed as:[34]

$$Co = \frac{a\Delta t}{\Delta x} \tag{3.25}$$

where a is the capillary wave velocity (m/s), Δt is the timestep (s) and Δx is the size of the mesh cell (m). A Courant number of 0.4 is chosen to warrant the stability of the simulation.[27]

To capture the diffusion of the vapour to the liquid film during condensation, the compressive numerical scheme is used.[35] The compressive scheme is a diffusive interface-capturing scheme which is ideal for phase change simulations as using sharper discretisation schemes may not be able to adequately capture the advection of the vapour to the surface or liquid film. As a result, this will lead to unrealistic sharpening of the diffusive zone (where $0 < \alpha_v < 1$). To alleviate this issue, the compressive scheme employs a slope limiter value which can be altered between 0 and 2 depending on the degree of sharpness required. Hence, the volume fraction on the face elements is calculated as:

$$\alpha_f = \alpha_d + \beta \nabla \alpha_d \cdot d\vec{r} \tag{3.26}$$

α_f is the face VOF value, α_d is the donor cell VOF value, β is the slope limiter value, $\nabla \alpha_d$ is the donor cell VOF gradient value and $d\vec{r}$ is the cell to face distance. For our case, a slope limiter value of 2 is selected with a sharp/dispersed interface modelling option as the diffusion of the vapour only needs to be depicted sufficiently in the early stages of

condensation to produce a thin film or droplets. Thereafter, the liquid-vapour interface should be suitably sharp in order to govern the film thickness.

Pressure and velocity correction gradients within the continuity equations are coupled using the PISO (Pressure-Implicit with Splitting of Operators) algorithm. The PISO algorithm repeats the calculations multiple times in a single time-step to ensure the continuity equations illustrate a normalized residual mean value of $\leq 10^{-3}$. Consequently, a value of 10 iterations per time step is chosen to sustain the stability of the simulations. Furthermore, the mass, momentum and energy continuity equations are discretised spatially through using the PRESTO (PREssure Staggering Option) and QUICK (Quadratic Upstream Interpolation for Convective Kinematics) schemes. As the simulations are transient (time-dependent), the transient scheme used was a first-order upwind since higher order schemes are limited to implicit discretisation schemes in ANSYS Fluent.

3.3. Results and discussion

3.3.1 Validation of Simulation Results

In order to validate the thermodynamic and fluid dynamic behaviour of the tubes' condensate, the results are compared against the Nusselt solution for film thickness, temperature profile, heat transfer coefficient against various subcooling temperatures and time which can be seen below. **Figure 3.2** displays the numerical film thickness observed for a perfectly wetted tube (θ_Y = 0°) with a subcooling temperature of 50 K compared against the Nusselt solution calculated for a two-dimensional plane. Whilst neglecting the effects of inertia, convection, and shear stress within the liquid film, the Nusselt film thickness for filmwise condensation is expressed as:[29]

$$\delta_f = \psi \left(\frac{3\mu_l k_l d_t (T_s - T_w)}{2\Delta h_v \rho_l (\rho_l - \rho_v) g} \right)^{\frac{1}{4}} \quad (3.27)$$

ψ is known as the stream function which is given as:[29]

$$\psi = \frac{4}{3\sqrt[4]{2}\,\theta} \left(\int_0^{\theta} \sqrt[3]{\sin\theta}\, d\theta \right)^{\frac{3}{4}} \quad (3.28)$$

where θ is the circumferential angle of the tube (°). As shown, the simulation data shows good agreement with the Nusselt solution between circumferential angles of 0 to 170° (clockwise) showing a maximum error of 2%. However, after 170°, the film thickness begins to deviate significantly from the Nusselts' calculation as the liquid film begins to neck towards the bottom of the tube as shown by the concave interface. This is attributed to the effects of surface tension of the fluid which is neglected within the Nusselt solution. As the fluid becomes squashed within this region, a negative pressure gradient is produced which causes the fluid to accelerate along the tube resulting in a reduction in film thickness.[27] Additionally, this is also seen along the liquid jet at the bottom of the tube as convex and concave regions are established due to the Rayleigh-Plateau instability.

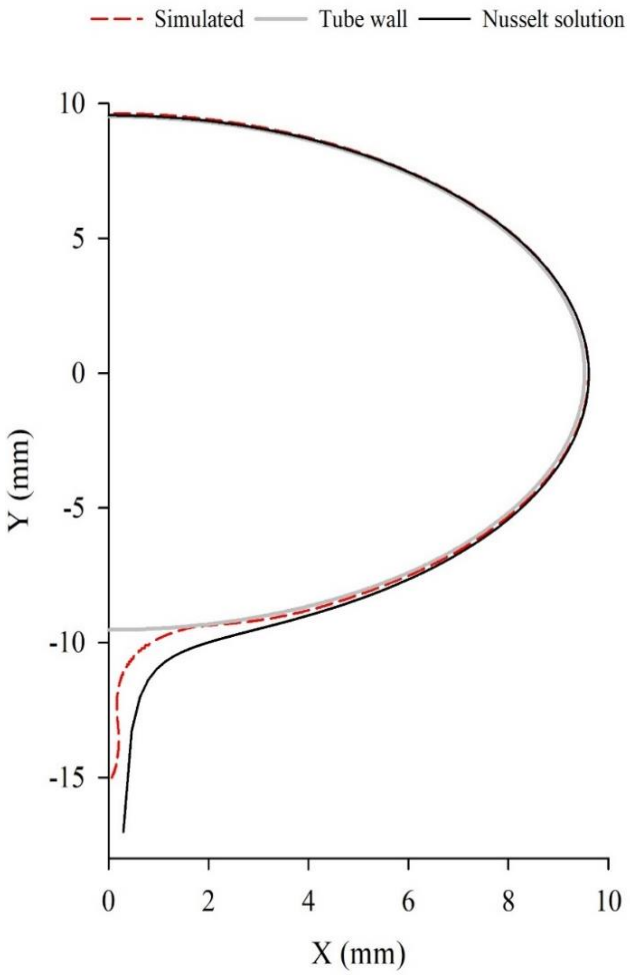

Figure 3.2. Film thickness validation against Nusselt solution for water with a subcooling temperature of 50 K and imposing θ_Y = 0°.

As noted formerly, since convection within the fluid is neglected, heat transfer is predominantly driven by conduction which results in a linear temperature profile along the circumferential direction of the film. Thus from the Nusselt theory, the circumferential temperature profile is given as:[36]

$$T_\theta = T_s - (T_s - T_w)\left(1 - \frac{r_i}{\delta_f}\right) \tag{3.29}$$

where r_i is the radial coordinate within the condensate film (m). **Figure 3.3a** and **b** demonstrate the circumferential temperature profile of the liquid film at a tube angle of 45

and 90° compared against the Nusselt theory for a subcooling temperature of 50 K. The simulated temperature profiles agree very well with the calculated result illustrating the interfacial temperature deviations to be less than 1 K between the simulation and the Nusselt film theory as shown from the zoomed highlighted region. This was achieved using selected settings for the mass transfer intensity factor and the modified vapour thermal conductivity coefficient.

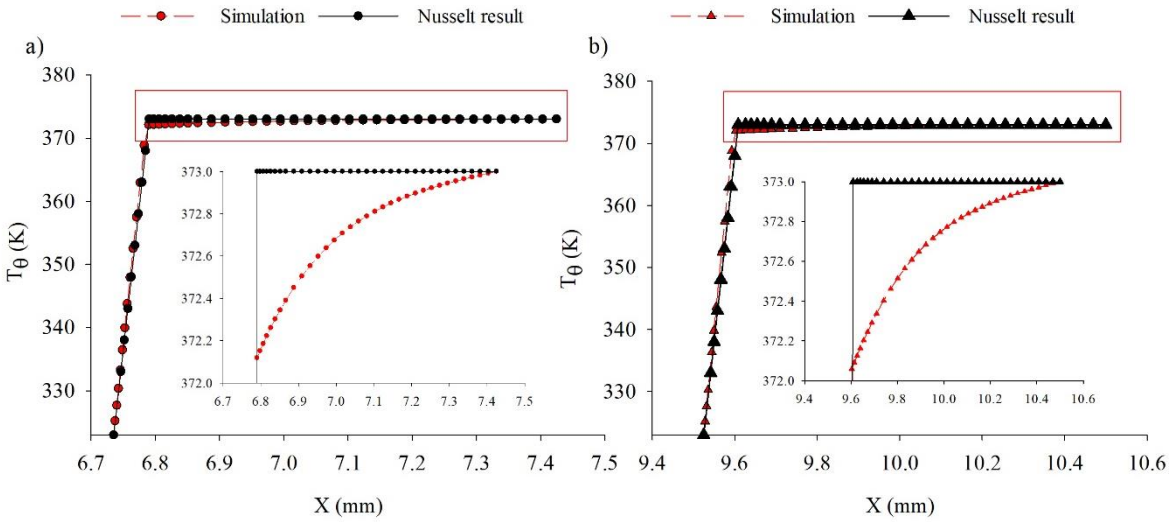

Figure 3.3. Circumferential temperature profiles at (a) 45° and (b) 90° validated against the Nusselt solution at a subcooling temperature of 50 K.

In order to validate the heat flux and heat transfer coefficients presented, the tube was simulated at various subcooling temperatures (wall temperatures) to determine the heat transfer coefficient against Nusselt's result. The heat transfer coefficient can be calculated as:

$$h = \frac{q}{(T_s - T_w)} \tag{3.30}$$

To accurately determine the heat transfer coefficient, the RMS (Root Mean Square) value was taken from the data after the heat transfer coefficient reaches a steady state value

where the condensate reaches its' maximum film thickness (after 0.5 s). **Figure 3.4** displays the simulated heat transfer coefficients at various subcooling temperatures between 372 – 323 K which is compared against the Nusselt result. Again, the simulation results correlates down to a subcooling temperature of 10 K with a maximum error of 10.5 %. The larger error seen in the heat transfer coefficients below 5 K is attributed to the effects of surface tension as noted previously. As the subcooling temperature of the film decreases, the inertia force generated within film reduces as a consequence (seen from the film Reynolds number). Because of this, the effects of surface tension become more dominant which, in turn, reduces the film thickness more so compared to the Nusselt solution. Due to the reduction in film thickness, the heat transfer coefficient is amplified further which deviates the heat transfer coefficient from the Nusselt result.

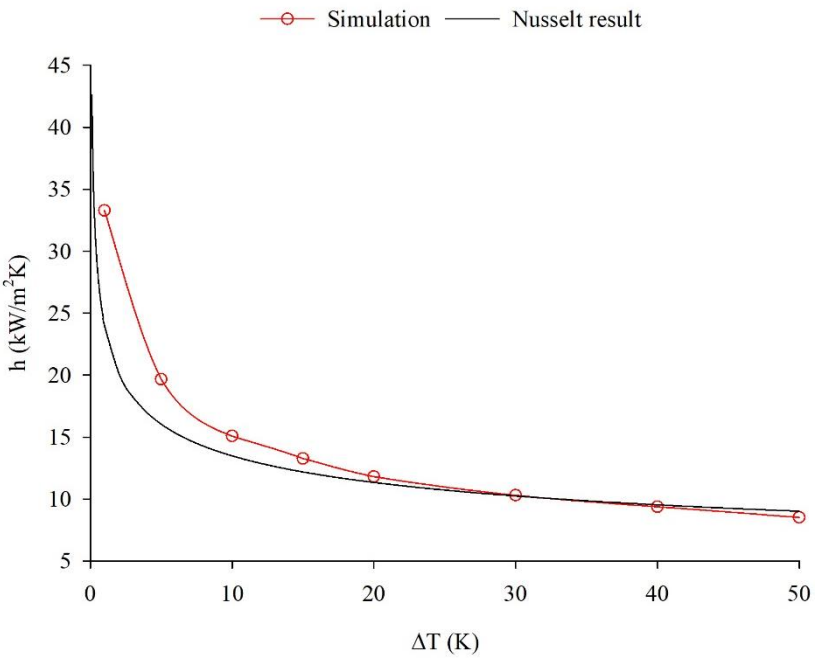

Figure 3.4. Simulated heat transfer coefficient against various subcooling temperatures calibrated with Nusselt theory.

Figure 3.5 demonstrates the heat transfer coefficient and heat flux of the tube against time for a subcooling temperature of 50 K compared against the Nusselt solution up to 2 s. As

also seen from **Figure 3.4**, the heat transfer coefficient and heat flux compare well against the Nusselt solution once it reaches its steady state value after approximately 0.5 s presenting an error of only 5.5 %. Initially, the heat transfer coefficient and heat flux is substantially large due to the large temperature gradient between the vapour and the bare solid region. Once a thin condensate film is formed upon the tube, the heat flux and heat transfer coefficient begins to settle down as the temperature gradient between the tube and vapour slowly reduces from the increase in thermal resistance of the film. When the liquid film begins to run off the tube, the heat flux and heat transfer coefficients then saturates as the liquid film reaches its' maximum thickness.

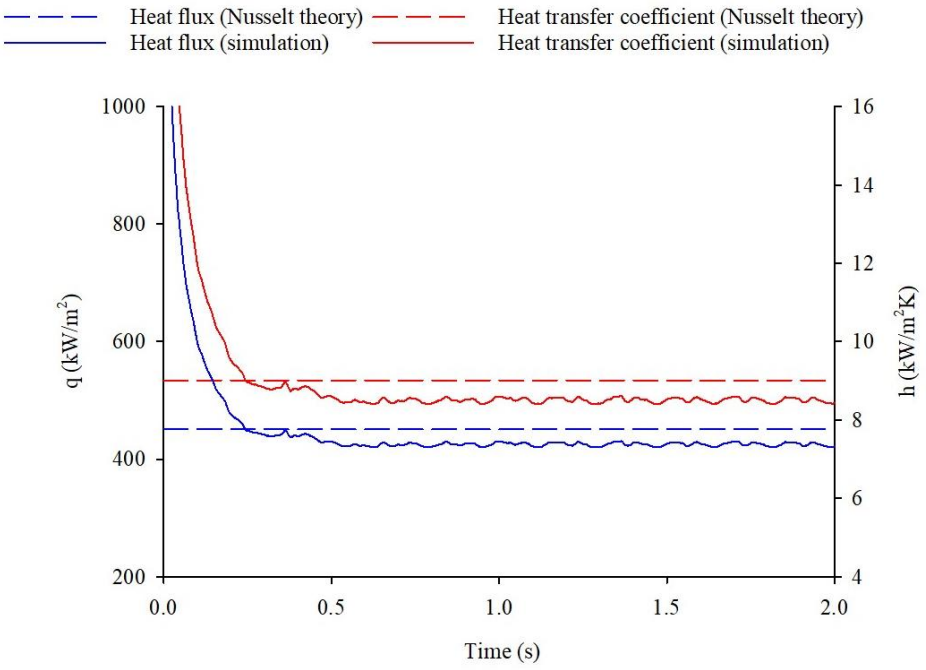

Figure 3.5. Average heat transfer coefficient and heat flux against time at a subcooling temperature of 50 K validated against Nusselt result.

To validate the simulated heat transfer coefficients presented against experimental data, **Figure 3.6**, demonstrates the comparison between numerical and experimental heat transfer coefficients against various subcooling temperatures captured by Zhang *et al.*[9]

As anticipated, the simulated heat transfer coefficients show a satisfactory agreement against the experimental data, illustrating a maximum error of 13 % up to a subcooling temperature of 30 K. The large divergence seen between subcooling temperatures of 5 to 10 K is due to the large error in experimentally measuring the small temperature rise within a small volume of condensate.[9] Nonetheless, the primary error observed is associated with the three-dimensional flow along the axial direction which is neglected within the simulations. Due to the formation of multiple elongated droplets seen along the bottom of the tube within the experiments, the overall heat transfer coefficient is less as more condensate is accumulated at the bottom of the tube which promptly increases the thermal resistance of the tube. This, consequently, reduced the heat transfer coefficient by approximately 2-3 kW/m^2K for each subcooling temperature in relation to the two-dimensional results. It should be noted that, their subcooling temperature was defined as the logarithmic mean temperature difference (ΔT_{LMDT}) instead of the difference between the saturation and wall temperature. This also adds further discrepancies within the heat transfer coefficient comparison.

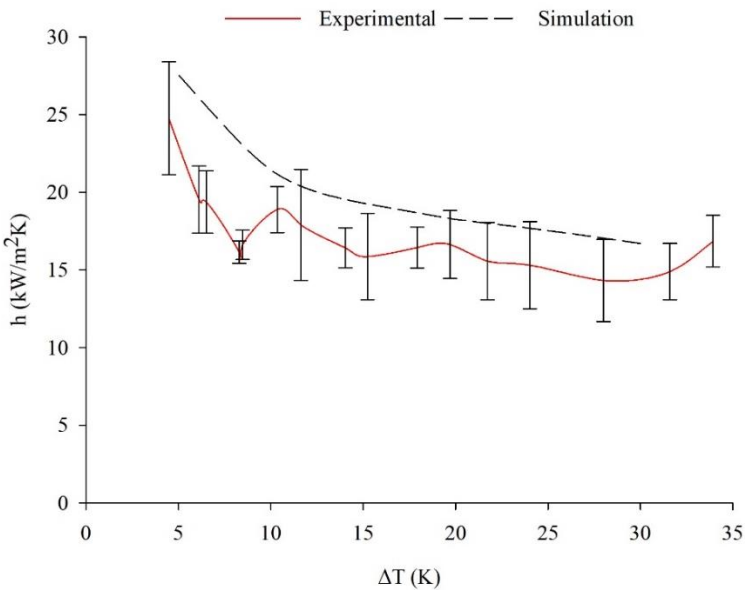

Figure 3.6. Simulated heat transfer coefficient against subcooling temperatures compared against experimental results by Zhang et al. on their original hydrophilic tube (θ_Y = 53° $\Delta\theta$ = 28º).[9]

3.3.2 Effects of Surface Wettability and Subcooling Temperature on Condensate Behaviour and Heat Transfer

As discussed previously, altering the tubes' surface wettability can have a profound effect upon the heat flux and heat transfer coefficient of the tube as more of the bare surface becomes exposed at larger contact angles. This is exemplified in **Figure 3.7** which demonstrates the condensate behaviour for a hydrophilic (θ_Y = 30°) (**Figure 3.7a**), hydrophobic (θ_Y = 90°) (**Figure 3.7b**) and superhydrophobic (θ_Y = 150°) (**Figure 3.7c**) tube at various subcooling temperatures. At an equilibrium contact angle of 30° (**Figure 3.7a**) the condensate behaviour illustrates dropwise condensation for a subcooling temperature of 5 K where the droplets contain a large contact length (seen more clearly in **Figure 3.9**). However, increasing the subcooling temperature further slowly shows the transition towards filmwise condensation as increasing the subcooling temperature causes

the nucleation density of the droplets to rise further (i.e. increasing the number of droplets).[37] This is attributed to heterogenous droplet nucleation theory as shown below:[38]

$$r_{min} = \frac{2T_s\gamma_{lv}}{\rho_l \Delta h_v \Delta T} \tag{3.31}$$

where r_{uin} is the minimum droplet nucleation radius observed (m). Notably, this is assuming that the temperature of the vapour is uniform. Therefore, the nucleation density is said to be given as:[39]

$$N_s = \frac{0.037}{{r_{min}}^2} \tag{3.32}$$

To summarise, increasing the subcooling temperature causes the droplet nucleation radius to decrease which in turn, increases the nucleation density. This escalates the number of coalescing droplets which results in a formation of a liquid film for low equilibrium contact angles (less than 90°). Nonetheless, it should be noted that, as the size of droplets is heightened at higher subcooling temperatures, the gravitational forces within the fluid will begin to dominate the capillary forces (also seen in **Figure 3.10**). The Bond number can be used to explain this relationship as shown in Chapter 2.3.2 (Equation 2.11). Particularly, for dropwise condensation, when gravitational forces become prevalent, formulating droplets will not demonstrate hemispherical or spherical shapes but instead illustrate unstable or random film patterns which can be seen at subcooling temperatures beyond 5 K for all contact angles.[16]

Nonetheless, for a hydrophobic tube (**Figure 3.7b**), the condensate performance clearly demonstrates dropwise condensation for subcooling temperatures of 5 K and beyond. Noticeably, the contact length of the droplets is shortened compared to the hydrophilic

tube as the surface adhesion force is reduced. At larger subcooling temperatures, the number of nucleating droplets is shown to increase with the droplets ending up breaking off the tube as they glide down. Although, for a superhydrophobic tube (**Figure 3.7c**), the contact length of droplets is reduced even further showing an almost spherical shape. Due to the amply reduced surface adhesion force, some nucleating droplets were seen to jump off the tube within the early stages of condensation. This is observed more clearly in **Figure 3.8** which represents the velocity vector contour plots of jumping-droplet condensation for a subcooling temperature of 10 K. When two adjacent nucleating droplets reach a critical radius, the droplets will begin to merge seen at 0.3 ms. Consequently, the merged droplets' centre of mass will tend to fluctuate vertically which induces a change in momentum.[40] This is demonstrated from the velocity vectors as they begin to increase away from the surface at 0.6 ms. The change in momentum generates an inertia force which allows the droplet to lift off the surface after 0.9 ms as it is dominant over the surfaces' adhesion force. To summarise, jumping droplet condensation can be established by reducing the droplets' characteristic length scale to a critical radius (as examined in Chapter 2.3.1).

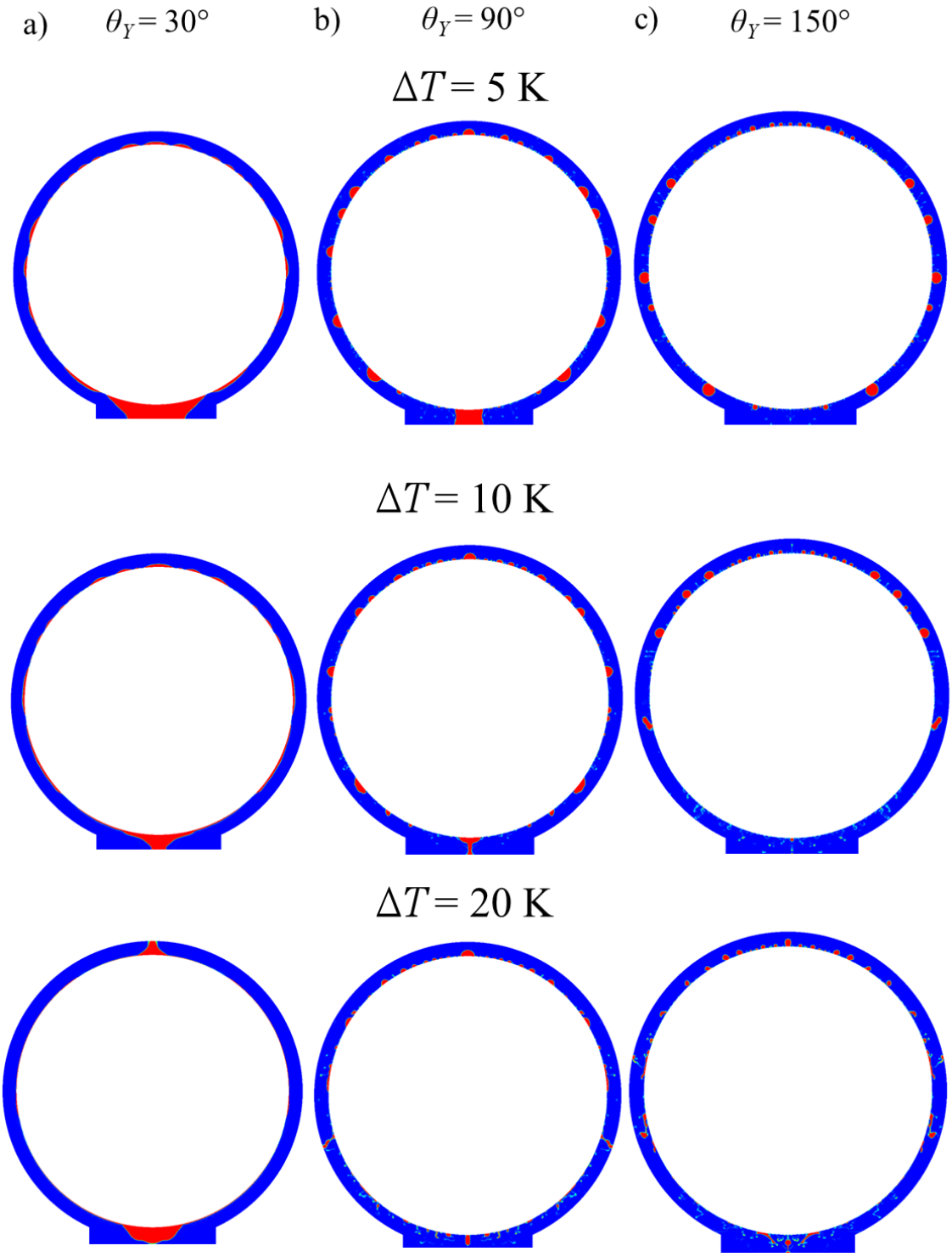

Figure 3.7. Contour image of condensate behaviour for different contact angles a) θ_Y = 30°, b) θ_Y = 90°, c) θ_Y = 150° and given subcooling temperatures shown at a timeframe of 0.3 s.

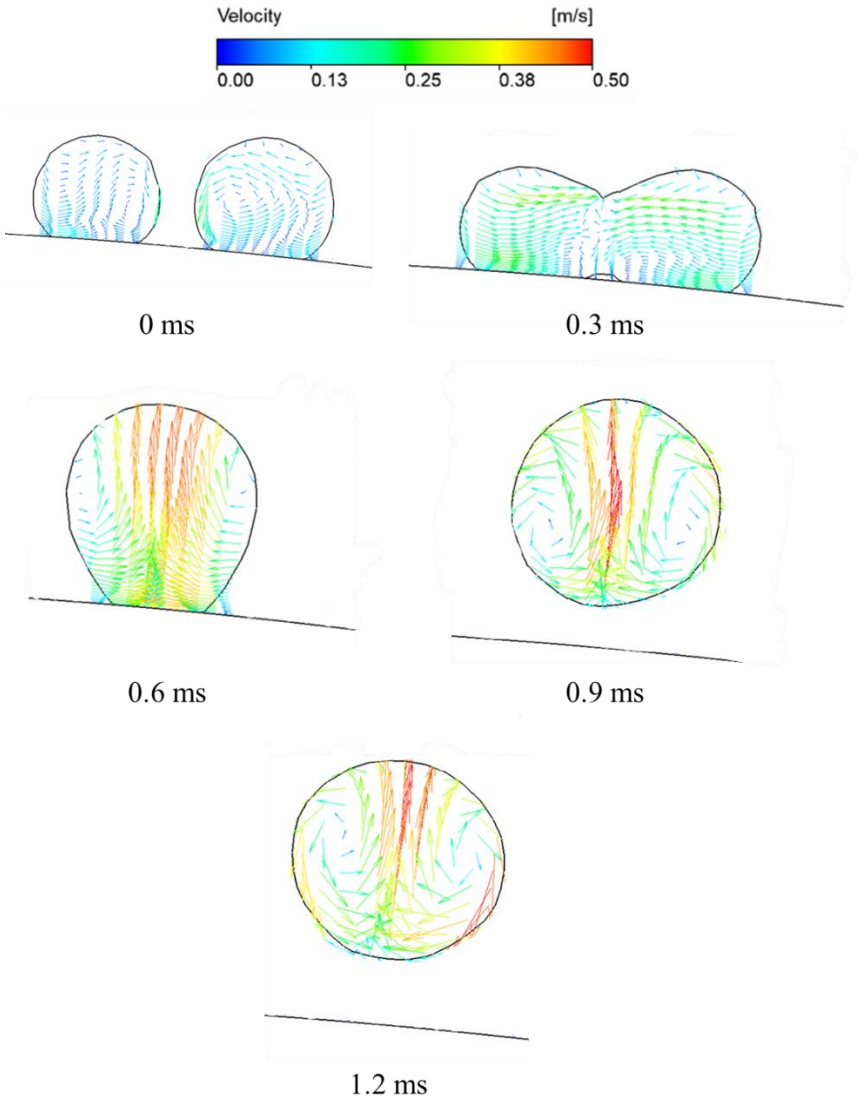

Figure 3.8. Velocity vectors of condensate behaviour for θ_Y = 150° at a subcooling temperature of 10 K illustrating the occurrence of jumping-droplet condensation on the tube surface.

To undermine the key differences in the condensate flow behaviour between the contact angles, **Figure 3.9** shows the contour plots of the condensate performance on the tube at various timeframes and contact angles between 0 and 150°. Initially, at 10 ms (**Figure 3.9a**) contact angles below 30° demonstrate filmwise condensation whilst dropwise and jumping-droplet condensation is formulated for contact angles above 90° as formerly noted. Notably, at 20 and 30 ms (**Figure 3.9b** and **Figure 3.9c**) for the superhydrophobic

tube, some minuscule and macroscopic droplets are seen to jump off the surface, although the majority of the tube primarily displays dropwise condensation. For contact angles below 30°, the condensate film slowly increases in thickness whilst at 30°, the liquid film shows signs of nucleating droplets with large characteristic length scales. Eventually, after 30 ms (**Figure 3.9d-f**), the beading film begins to run off the tube as the pinned droplets increase in size whilst for contact angles above 90°, the droplets glide off the tube at much smaller length scales, especially for the contact angle of 150°. Nevertheless, it should be stated that the nucleation density of the droplets manages to decline between contact angles of 90 to 150°. This is associated with the increase in droplet nucleation radius as it becomes difficult for the vapour to conglomerate on the surface at high contact angles.[41]

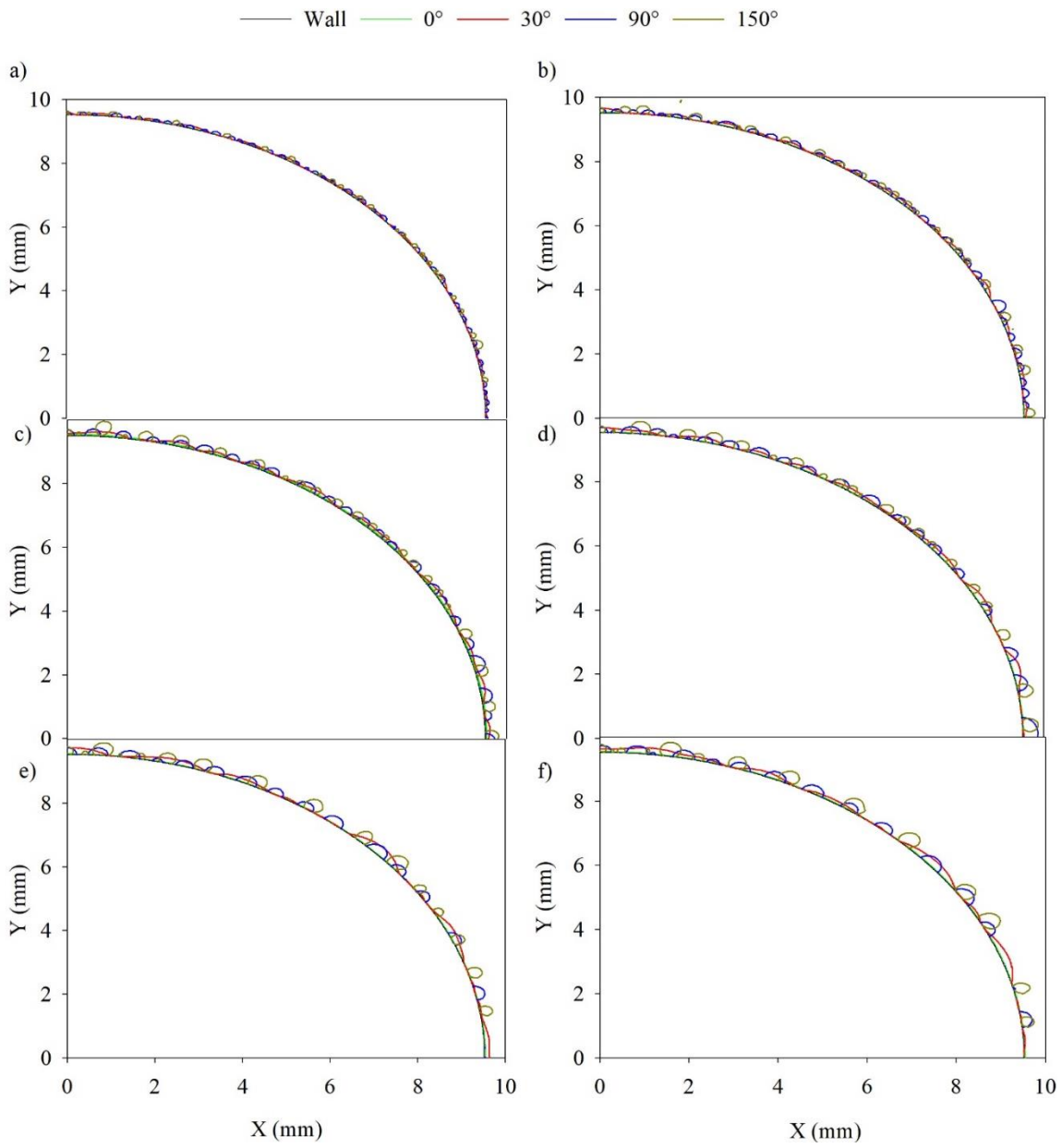

Figure 3.9. Quarter cross-sectional contour plots of condensate tube illustrating dropwise and filmwise condensation at various contact angles for a subcooling temperature of 10 K given at different timeframes a) 10 ms b) 20 ms c) 30 ms d) 40 ms e) 50 ms f) 60 ms.

Figure 3.10 displays the condensate flow of a superhydrophobic under various subcooling temperatures and timeframes. As expected, increasing the subcooling temperature causes the nucleation density to rise due to the reduction in droplet nucleation radius as highlighted beforehand. In addition, droplets tend to grow at a faster rate as the subcooling

temperature increases. This is due to the enhancement in heat flux between the vapour-solid interface which in turn, escalates the droplet coalescence frequency which raises the overall size of the droplets upon the tube.[42] Due to the large size of the droplets, droplets begin to have less mobility and instead collapse into a liquid film as their hydrostatic pressure becomes substantial (seen in **Figure 3.10f**). This phenomenon is particularly seen at subcooling temperature beyond 20 K.

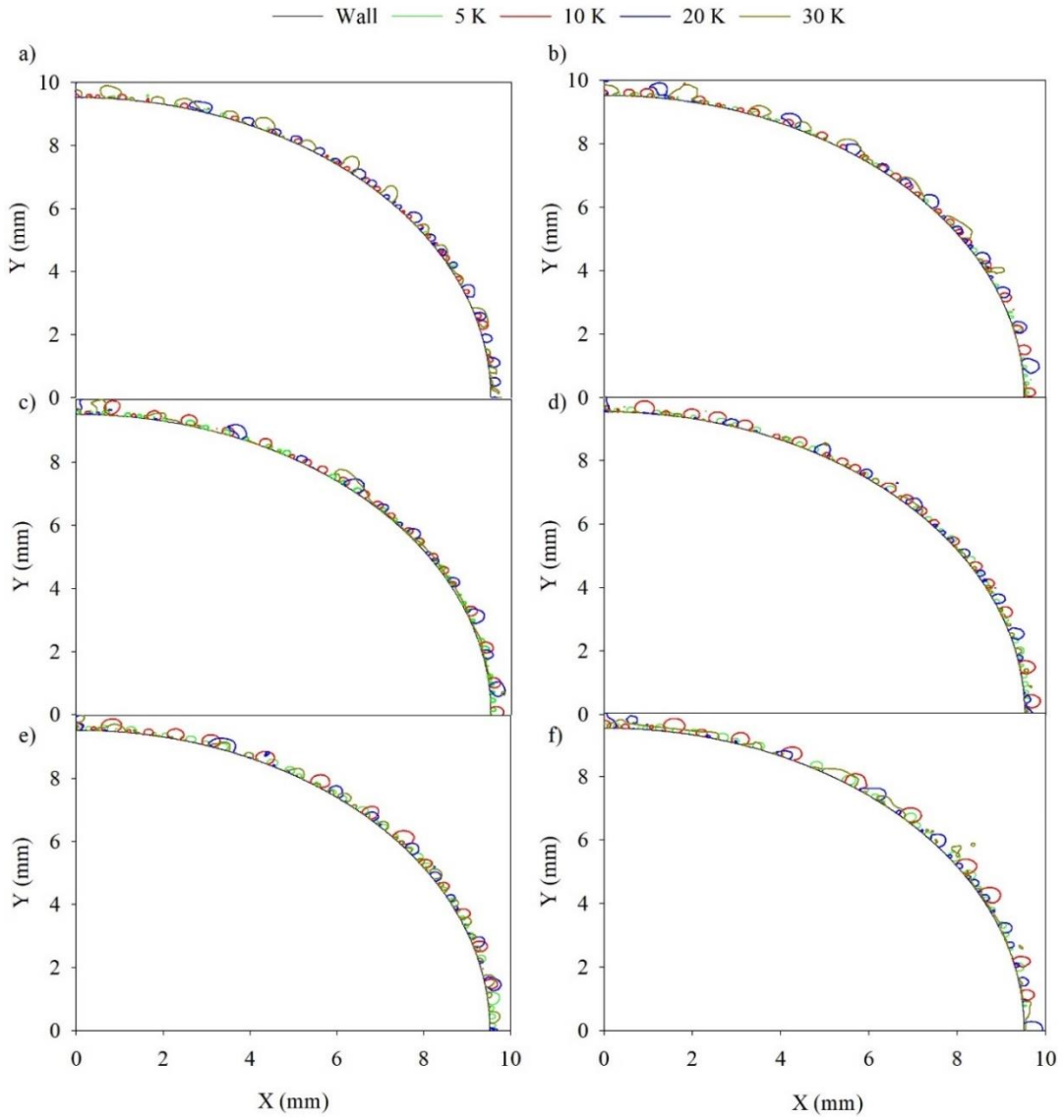

Figure 3.10. Quarter cross-sectional contour plots of dropwise and filmwise condensation for a superhydrophobic tube (θ_Y = 150°) at various subcooling temperatures demonstrated at different timeframes, a) 10 ms b) 20 ms c) 30 ms d) 40 ms e) 50 ms f) 60 ms.

To correlate the behaviour of the condensate observed towards the tubes' heat transfer characteristics, **Figure 3.11** demonstrates the heat transfer coefficient against time for various contact angles at a subcooling temperature of 5 K. It should be noted that, for contact angles more than 0°, the heat transfer coefficient inclines to reach steady state at a faster rate at approximately 0.1 s compared to 0.3 s. This is primarily due to the formation of droplets at the tube surface which begin to shed off the surface swiftly as opposed to a contact angle of 0° where a thin sheet of liquid is formed instead. The fluctuations shown in the heat transfer coefficient from contact angles 30° and above are due to droplet shedding and nucleation upon the tube surface, indicating dropwise condensation. At a contact angle of 0°, the heat transfer coefficient shows little to no variation in heat transfer which demonstrates the flow to be filmwise condensation as a continuous film remains present at the tube's interface. Nonetheless, from increasing the contact angle from 0° to 30°, the flow behaviour began to transition from filmwise to dropwise condensation as indicated from the previous contour plots. This increased the heat transfer coefficient value from 19.7 kW/m^{2}K to 232 kW/m^{2}K, indicating a 92 % increase. Adjusting the contact angle further to 90° gave a further 37 % enhancement in the heat transfer coefficient (from 232 kW/m^{2}K to 367 kW/m^{2}K) as a liquid film was no longer present on the tube but instead displaying macroscopic droplets which eventually glided off the tube. Finally, altering the contact angle towards 150° demonstrated an 11 % improvement (367 kW/m^{2}K to 413 kW/m^{2}K) as the contact length of the droplets were significantly reduced which allowed droplets to be amply removed off the tube.

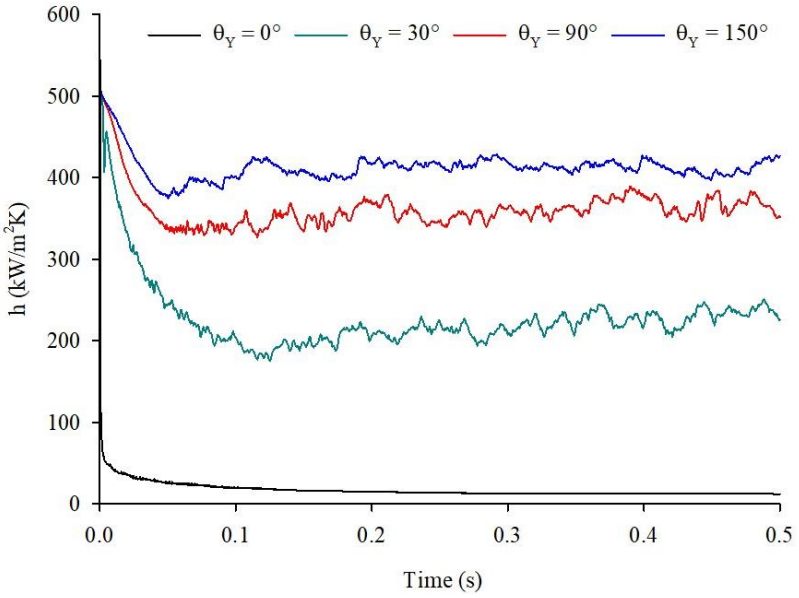

Figure 3.11. Heat transfer coefficient against time at a subcooling temperature of 5 K against various contact angles.

Correspondingly, to illustrate the effect of the subcooling temperature upon the heat transfer against the surface contact angles, **Figure 3.12**, displays the heat transfer coefficient and heat flux against subcooling temperature which are compared against numerous equilibrium contact angles. At a contact angle of 30°, it is shown that the heat transfer coefficient and heat flux remain predominantly high compared to the contact angle of 0° at low subcooling temperatures. Nevertheless, after a subcooling temperature of 10 K, both the heat transfer coefficient and heat flux rapidly starts to decline where eventually it becomes equal to the performance of a superhydrophilic surface. This is notably due to the increase in nucleation density and droplet coalescence which is directly proportional to the rise in subcooling temperature as noted beforehand. Since the flow behaviour of the condensate was already in a dropwise/filmwise state (i.e. droplets formulating on thin film sheets) at low subcooling temperatures (less than 10 K),

increasing the subcooling temperature further allowed the condensate to fully transition towards filmwise condensation which dramatically reduced the heat transfer coefficient by 95% (between subcooling temperatures 1 to 30 K).

The same can be said for contact angles of 90 and 150°, however as the condensate behaviour repeatedly illustrated dropwise condensation (with some jumping-droplet condensation seen at contact angles of 150°), increasing the subcooling temperature allowed the heat transfer coefficient and heat flux to increase as amplifying the nucleation density and droplet coalescence rate is favourable for expanding the rate of droplet removal. On the other hand, increasing the rate of condensation also increases the probability of droplets being too large to be removed by themselves and instead collapse under their own weight which is exemplified beyond subcooling temperatures of 20 K where the heat transfer coefficient and heat flux start to slightly decline.

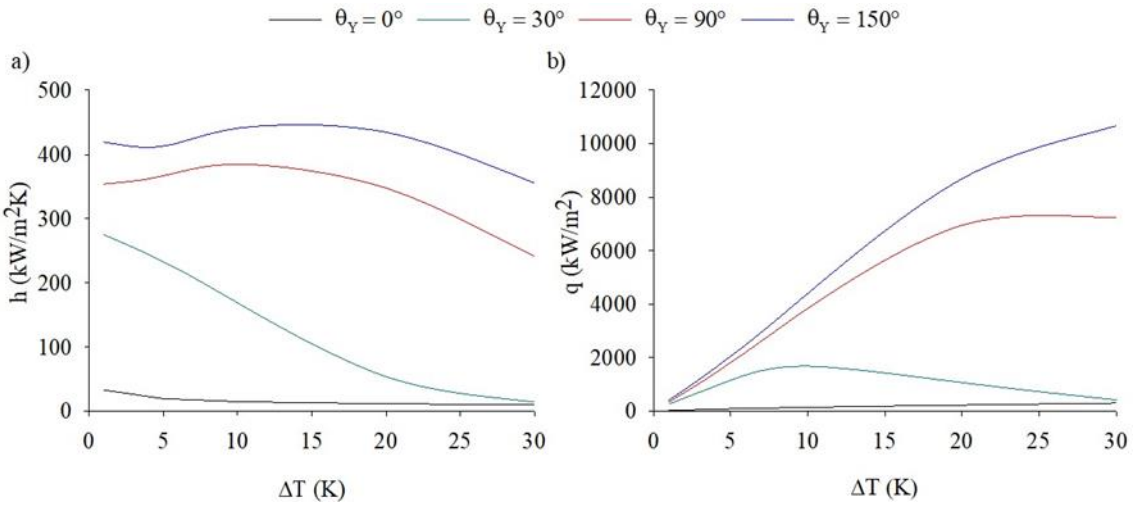

Figure 3.12. a) Heat transfer coefficient and b) heat flux of the tube against subcooling temperatures at different contact angles, $\theta_Y = 0°$, $\theta_Y = 30°$, $\theta_Y = 90°$, $\theta_Y = 150°$.

Increasing the contact angle further towards 180° may amplify the heat transfer coefficients and heat flux further due to the presence of jumping-droplet condensation being dominant resulting in droplets being removed off the surface with greater ease and

at lower droplet diameters. However as mentioned beforehand, increasing the intrinsic contact angle would lower the rate of droplet nucleation resulting in less droplet coalesce rates. Having larger droplet coalesce and nucleation rates is vital to increase the efficiency of jumping-droplet condensation as previously discussed in Chapter 2. This may be counteracted through amplifying the subcooling temperature although, the rate of change in the nucleation density would be lowered at very large contact angles (up to 180°) which would result in lower rates of heat flux/heat transfer coefficients at each subcooling temperature increment. This leads to further questions as to how the dynamic contact angles of the surface could be adjusted to provide the optimum heat transfer coefficient/heat flux at large contact angles. The implications of dynamic contact angles on condensation heat transfer are illustrated below.

3.3.3 Implications of Altering the Contact Angle Hysteresis at Given Equilibrium Contact Angles

In a real-world scenario, all surfaces inherently contain a contact angle hysteresis which can impact the droplets' adhesion to the surface in the dynamic regime (i.e. when the droplet is moving). Therefore, it is ideal for numerical simulations to apprehend this factor as this would determine whether droplets remain pinned on the tube or slide off depending on the degree of contact angle hysteresis. This phenomenon is presented in **Figure 3.13** which illustrates the contour images for the condensate behaviour for each static contact angle (30-150°) where the contact angle hysteresis altered between 2-20°. For an equilibrium contact angle of 30°, increasing the CAH from 2-20° causes the contact length of the droplet to rise, which increases the maximum droplet radius observed (r_{max}). This is directly correlated to Dimitrakopoulos *et al.* theoretical model where the contact angle hysteresis is directly proportional to the maximum droplet radius shown as:[37,43]

$$r_{max} = \sqrt{\frac{6\gamma_{lv}(\cos\theta_r - \cos\theta_a)\sin\theta_Y}{\rho_l g\pi(2 - 3\cos\theta_Y + \cos^3\theta_Y)}} \quad (3.33)$$

Increasing the contact angle hysteresis towards 20° for an equilibrium contact angle of 90° causes droplet to slowly agglomerate at the top of the tube as it now becomes difficult for droplets to be displaced along the tube, regardless of their hydrostatic pressure. Furthermore, at a static contact angle of 150°, between CAH of 2 to 10° shows little change in the dynamic adhesion of droplets as the contact length is already sufficiently small due to the superhydrophobicity of the tube which still allows droplets to roll off effortlessly. However, when increasing the contact angle hysteresis towards 20°, droplets begin to stick onto the tube for a longer period of time before they are removed off the surface. A more precise comparison can be seen from the contour plots in **Figure 3.14**.

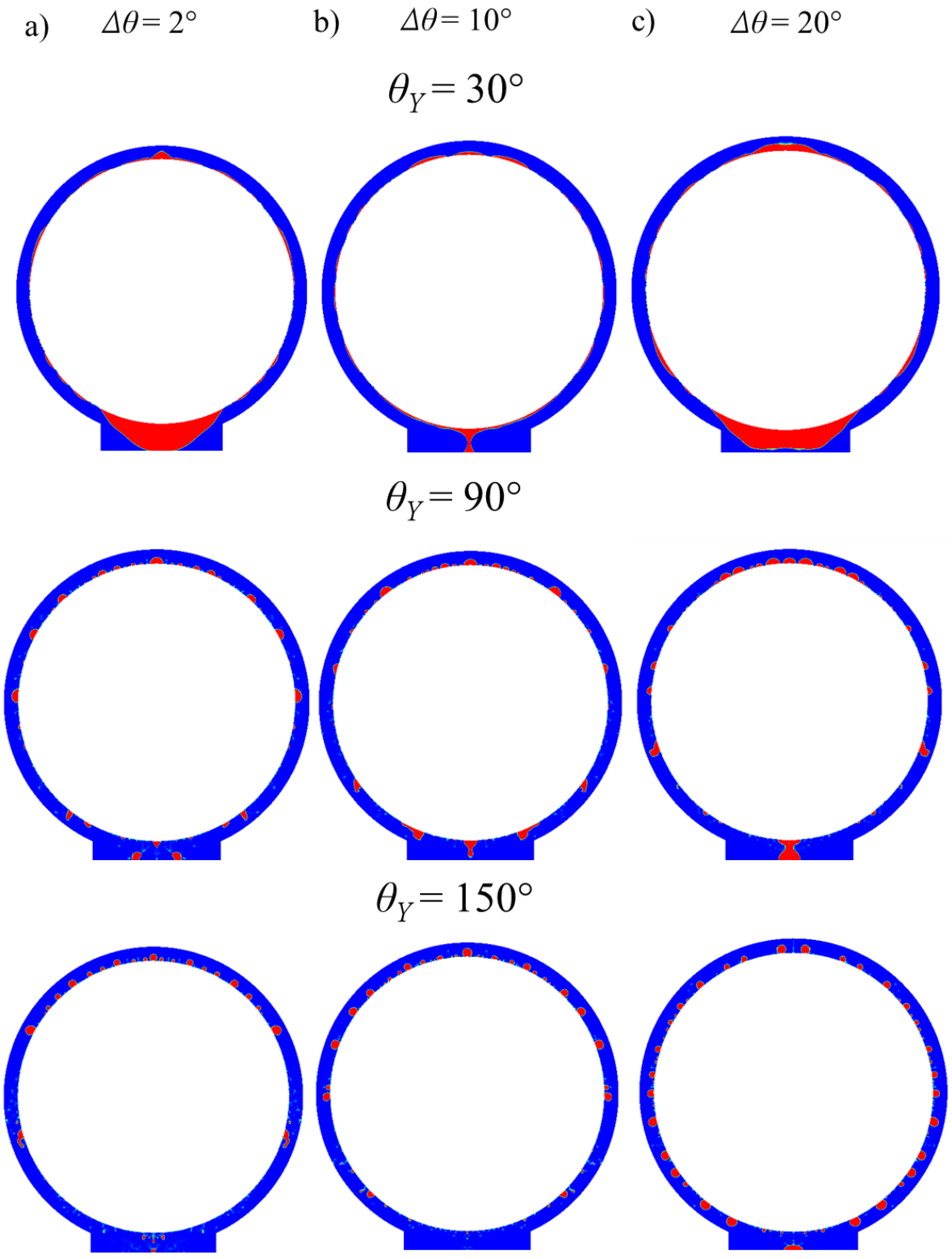

Figure 3.13. Contour images of condensate performance by increasing the contact angle hysteresis from 0° to 20° at different equilibrium contact angles at a timeframe of 0.3 s at a subcooling temperature of 10 K.

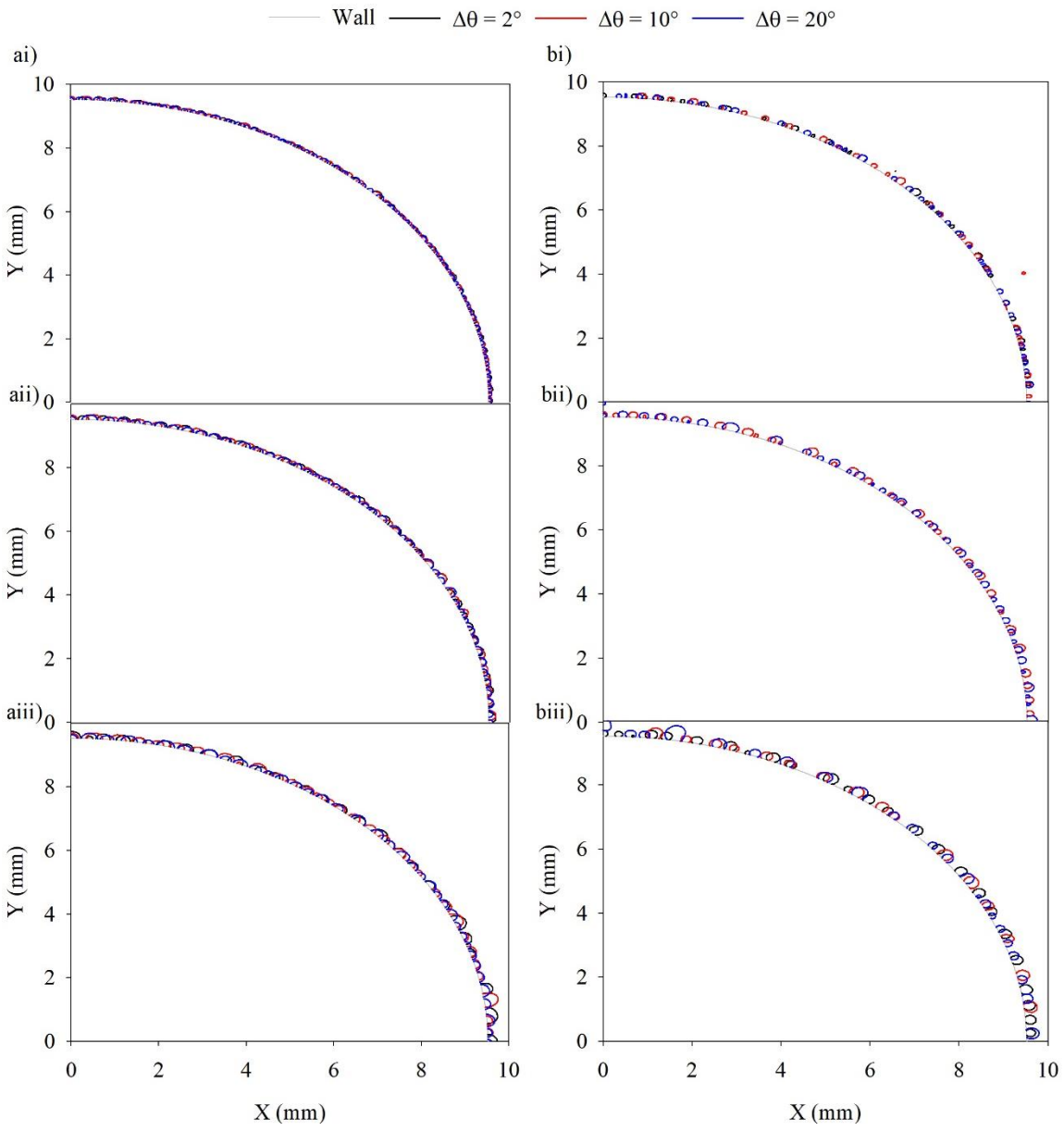

Figure 3.14. Quarter cross-sectional contour plots of condensation behaviour at contact angles a) $\theta_Y = 90°$ and b) $\theta_Y = 150°$ for numerous contact angle hysteresis and time periods, i) 10 ms, ii) 20 ms, iii) 30 ms at a subcooling temperature of 10 K.

Therefore, it can be said that, increasing the contact angle hysteresis of the tube will promptly reduce the heat transfer coefficient of the tube due to the rise in droplet size which consequently increases the thermal resistance of the tube. The variations in heat transfer coefficients for different equilibrium contact angles and contact hysteresis are

plotted against time in **Figure 3.15**. As anticipated, increasing the contact angle hysteresis from 2 to 20° for a given equilibrium contact angle reduces the heat transfer coefficient of the tube. The magnitude of reduction, however, appears to gradually decrease as the equilibrium contact angle approaches 150°. For example, at a contact angle 30°, increasing the contact angle hysteresis from 2 to 20° resulted the heat transfer coefficient to decrease from 161 kW/m^{2}K to 118 kW/m^{2}K which corresponds to a 27% reduction in heat transfer coefficient. Though, for an equilibrium contact angle of 90° changing the contact angle hysteresis from 2° to 20° again only decreased the heat transfer coefficient from 388 kW/m^{2}K to 365 kW/m^{2}K which equates to a 6% decline. Then again, increasing the contact angle hysteresis from 2 to 10° showed no change in the heat transfer performance illustrating an average heat transfer coefficient of 443 kW/m^{2}K. Remarkably, however, further increasing the hysteresis towards 20° resulted in a substantial drop in heat transfer coefficient to 384 kW/m^{2}K which demonstrates a 13% change.

The large alteration in heat transfer coefficient for low equilibrium contact angles is associated to the increase in nucleation density and smaller minimum droplet radiuses. The combination of large kinetic adhesion forces (from increasing the CAH) with increased droplet coalescence rates causes the heat transfer coefficient to decrease more abruptly as these conditions provide a stable foundation for establishing filmwise condensation, specially at larger subcooling temperatures. On the other hand, increasing the contact angle hysteresis higher than 10° for a superhydrophobic tube provided a critical transition of where droplets become less mobile resulting in a subsequent decline in heat transfer coefficient. This may lead to further questions as to whether the nucleation density or the contact angle hysteresis is responsible for immobilising condensing droplets.

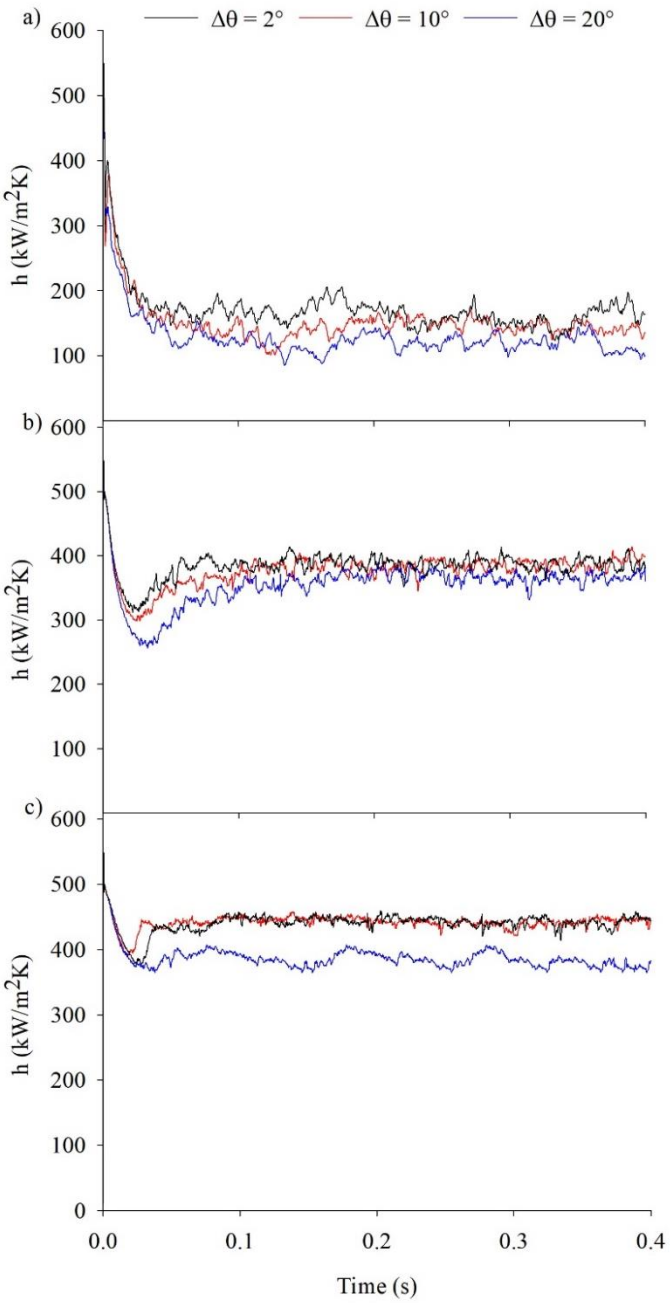

Figure 3.15. Heat transfer coefficient against time for several equilibrium contact angles and contact angle hysteresis a) θ_Y = 30°, b) θ_Y = 90°, c) θ_Y = 150° at a given subcooling temperature of 10 K.

3.4. Conclusion

Multiphase numerical simulations with phase-change have been carried out to reveal the condensation heat transfer characteristics of the tube at various equilibrium contact angles, subcooling temperatures and contact angle hysteresis based on their flow behaviour. Initially, the film thickness, circumferential temperature profiles, heat flux and heat transfer coefficients are shown to be in good agreement with the Nusselt solution at different subcooling temperatures. Further to that, numerical heat transfer coefficients against various subcooling temperatures are also shown to be in agreement with experimentally obtained heat transfer coefficients despite the dimensional differences. When ignoring the effects of contact angle hysteresis, increasing the equilibrium contact angle of the tube from a hydrophilic to a superhydrophobic state resulted in a transition between filmwise to dropwise condensation and even jumping-droplet condensation although only a few droplets were seen to be propelled off the tube at the early stages of condensation.

Therefore, a contact angle greater than 150° may be required to stabilize the occurrence of jumping-droplet condensation whilst maintaining low contact angle hysteresis (less than 10°). As a result, heat transfer coefficients and heat flux were found to substantially increase especially at large subcooling temperatures (~20 K) for surfaces that illustrated dropwise condensation. This is due to the increase in droplet nucleation density which lead to increased rates of droplet coalescence which allowed droplets to be swiftly removed off the tube. After 20 K, the increase in nucleation density and droplet coalescence reached a critical point to where droplets grew too large in size before they could slide off the tube. Hence, the droplets eventually subsided into a liquid film which predominantly reduced the heat transfer coefficient of the tube as the flow begins to transition from dropwise to filmwise condensation. Notably, as filmwise condensation

was already established for contact angles less than 30° increasing the subcooling temperature only reduced the heat transfer coefficients further as only the thickness of the film rose.

To further note, when increasing the contact angle hysteresis of the tube, droplets began to become less mobile and agglomerate at given equilibrium contact angles. This caused the tubes' heat transfer coefficient to be reduced even further. Although, this was shown to be more prevalent at low static contact angles due to the increase in droplet coalescence rates and nucleation density which is primarily observed for hydrophilic surfaces. Nevertheless, for a superhydrophobic tube, increasing the contact angle hysteresis towards 20° showed a noticeable reduction in heat transfer performance of 13% due to the formulating droplets being pinned on the tube. In any case, future numerical studies related to condensation should consider the aspect of contact angle hysteresis when modelling functional surfaces as the degree of the contact angle hysteresis will dictate whether the flow pattern is either dropwise or filmwise condensation at given equilibrium contact angle. If the contact angle hysteresis is not considered within numerical simulations, the surface is deemed to have a hysteresis of 0°. This will create misrepresentation of the flow behaviour of the condensate when comparing to experimentally modified surfaces which in turn, will alter the observed heat transfer coefficients.

3.5. References

1. R. L. Webb, Enhanced condenser tubes in a nuclear power plant for heat rate improvement, Heat Transf. Eng. 32 (2011) 905-913.
2. J. F. Kim, A. Park, S.-J. Kim, P. Lee, Y. Cho, H. Park, S. Nam, Y. Park, Harnessing clean water from power plant emissions using membrane condenser technology, ACS Sustain. Chem. Eng. 6 (2018) 6425-6433.
3. R. Agrawal, D. M. Herron, Efficient use of an intermediate reboiler or condenser in a binary distillation, AlChE J. 44 (1998) 1303-1315.
4. L. Lu, W. Cai, Y. C. Soh, L. Xie, S. Li, HVAC system optimization — condenser water loop, Energy Convers. Manage. 45 (2004) 613-630.
5. L. Wang, Energy efficiency technologies for sustainable food processing, Energy Effic. 7 (2014) 791-810.
6. K. Rykaczewski, A. T. Paxson, M. Staymates, M. L. Walker, X. Sun, S. Anand, S. Srinivasan, G. H. McKinley, J. Chinn, J. H. J. Scott, Dropwise condensation of low surface tension fluids on omniphobic surfaces, Sci. Rep. 4 (2014) 4158.
7. J. Y. Ho, K. F. Rabbi, S. Sett, T. N. Wong, N. Miljkovic, Dropwise condensation of low surface tension fluids on lubricant-infused surfaces: droplet size distribution and heat transfer, Int. J. Heat Mass Transfer 172 (2021) 121149.
8. J. Xie, J. Xu, W. Shang, K. Zhang, Dropwise condensation on superhydrophobic nanostructure surface, part II: Mathematical model, Int. J. Heat Mass Transfer 127 (2018) 1170-1187.
9. T.-Y. Zhang, L.-W. Mou, J.-Y. Zhang, L.-W. Fan, J.-Q. Li, A visualized study of enhanced steam condensation heat transfer on a honeycomb-like microporous superhydrophobic surface in the presence of a non-condensable gas, Int. J. Heat Mass Transfer 150 (2020) 119352.

10. N. S. Singh, J. Zhang, J. Stafford, C. Anthony, N. Gao, Implementing superhydrophobic surfaces within various condensation environments: A review, Adv. Mater. Interfaces 8 (2021) 2001442.

11. R. Wen, S. Xu, X. Ma, Y.-C. Lee, R. Yang, Three-dimensional superhydrophobic nanowire networks for enhancing condensation heat transfer, Joule 2 (2018) 269-279.

12. N. Miljkovic, R. Enright, Y. Nam, K. Lopez, N. Dou, J. Sack, E. N. Wang, Jumping-droplet-enhanced condensation on scalable superhydrophobic nanostructured surfaces, Nano Lett. 13 (2013) 179-187.

13. D. Xing, R. Wang, F. Wu, X. Gao, Confined growth and controlled coalescence/self-removal of condensate microdrops on a spatially heterogeneously patterned superhydrophilic–superhydrophobic surface, ACS Appl. Mater. Interfaces 12 (2020) 29946-29952.

14. J. B. Boreyko, C.-H. Chen, Self-Propelled Dropwise Condensate on Superhydrophobic Surfaces, Phys. Rev. Lett. 103 (2009) 184501.

15. Y. Song, C. D. Díaz-Marín, L. Zhang, H. Cha, Y. Zhao, E. N. Wang, Three-Tier Hierarchical Structures for Extreme Pool Boiling Heat Transfer Performance, Adv. Mater. 34 (2022) 2200899.

16. H. Cha, H. Vahabi, A. Wu, S. Chavan, M.-K. Kim, S. Sett, S. A. Bosch, W. Wang, A. K. Kota, N. Miljkovic, Dropwise condensation on solid hydrophilic surfaces, Sci. Adv. 6 (2020) eaax0746.

17. S.-S. Jeon, S.-J. Kim, G.-C. Park, Numerical study of condensing bubble in subcooled boiling flow using volume of fluid model, Chem. Eng. Sci. 66 (2011) 5899-5909.

18. Y. Zhang, A. Faghri, M. B. Shafii, Capillary blocking in forced convective condensation in horizontal miniature channels, J. Heat Transfer 123 (2001) 501-511.

19. E. Krepper, B. Končar, Y. Egorov, CFD modelling of subcooled boiling—concept, validation and application to fuel assembly design, Nucl. Eng. Des. 237 (2007) 716-731.

20. R. Zhuan, W. Wang, Simulation on nucleate boiling in micro-channel, Int. J. Heat Mass Transfer 53 (2010) 502-512.

21. F. Gibou, L. Chen, D. Nguyen, S. Banerjee, A level set based sharp interface method for the multiphase incompressible Navier–Stokes equations with phase change, J. Comput. Phys. 222 (2007) 536-555.

22. R. W. Schrage, A theoretical study of interphase mass transfer, Columbia University Press (1953).

23. W. H. Lee, Multiphase transport fundamentals, reactor safety, applications, Hemisphere Publishing (1980).

24. C. R. Kharangate, I. Mudawar, Review of computational studies on boiling and condensation, Int. J. Heat Mass Transfer 108 (2017) 1164-1196.

25. Q. Shen, D. Sun, S. Su, N. Zhang, T. Jin, Development of heat and mass transfer model for condensation, Int. Commun. Heat Mass Transf. 84 (2017) 35-40.

26. K. Yokoi, D. Vadillo, J. Hinch, I. Hutchings, Numerical studies of the influence of the dynamic contact angle on a droplet impacting on a dry surface, Phys. Fluids 21 (2009)

27. T. Kleiner, S. Rehfeldt, H. Klein, CFD model and simulation of pure substance condensation on horizontal tubes using the volume of fluid method, Int. J. Heat Mass Transfer 138 (2019) 420-431.

28. N. S. Singh, J. Stafford, N. Gao, Dropwise and liquid-jet laminar flow of subcooled water falling over horizontal tube banks, Int. J. Heat Mass Transfer 206 (2023) 123936.

29. J. Rose, Condensation heat transfer fundamentals, Chem. Eng. Res. Des. 76 (1998) 143-152.

30. M. K. Dobson, Heat transfer and flow regimes during condensation in horizontal tubes, University of Illinois at Urbana-Champaign (1994).

31. X. Hu, The intertube falling-film modes: transition, hysteresis, and effect on heat transfer, University of Illinois at Urbana-Champaign (1995).

32. J. U. Brackbill, D. B. Kothe, C. Zemach, A continuum method for modeling surface tension, J. Comput. Phys. 100 (1992) 335-354.

33. M. Kansal, V. Bertin, C. Datt, J. Eggers, J. H. Snoeijer, Viscoelastic wetting: Cox–Voinov theory with normal stress effects, J. Fluid Mech. 985 (2024) A17.

34. R. Courant, K. Friedrichs, H. Lewy, On the partial difference equations of mathematical physics, IBM J. Res. Dev. 11 (1967) 215-234.

35. O. Ubbink, Numerical prediction of two fluid systems with sharp interfaces, University of London (1997)

36. L. C. Burmeister, Convective heat transfer, John Wiley & Sons (1993).

37. X. Liu, P. Cheng, Dropwise condensation theory revisited Part II. Droplet nucleation density and condensation heat flux, Int. J. Heat Mass Transfer 83 (2015) 842-849.

38. V. P. Carey, Liquid-vapor phase-change phenomena: an introduction to the thermophysics of vaporization and condensation processes in heat transfer equipment, CRC Press (2020).

39. J. Rose, Further aspects of dropwise condensation theory, Int. J. Heat Mass Transfer 19 (1976) 1363-1370.

40. M. O. Hassett, M. W. Fischer, N. P. Money, Mushrooms as rainmakers: how spores act as nuclei for raindrops, PloS one 10 (2015) 0140407.

41. X. Liu, P. Cheng, Dropwise condensation theory revisited: Part I. Droplet nucleation radius, Int. J. Heat Mass Transfer 83 (2015) 833-841.

42. Y. Guo, R. Wang, D. Zhao, L. Gong, S. Shen, Numerical Simulation of Vapor Dropwise Condensation Process and Droplet Growth Mode, Energies 16 (2023) 2442.

43. P. Dimitrakopoulos, J. Higdon, On the gravitational displacement of three-dimensional fluid droplets from inclined solid surfaces, J. Fluid Mech. 395 (1999) 181-209.

Chapter 4

Dropwise and Liquid-Jet Laminar Flow of Subcooled Water Falling over Horizontal Tube Banks

Navdeep Sangeet Singh, Jason Stafford and Nan Gao

School of Engineering, University of Birmingham, Birmingham, B15 2TT, United Kingdom

This chapter was published in the journal of International Journal of Heat and Mass Transfer (Singh, N. S., Stafford, J. & Gao, N. Dropwise and liquid-jet laminar flow of subcooled water falling over horizontal tube banks. International Journal of Heat and Mass Transfer 206, 12336 (2023).).

Author Contributions: N.S.S and J.S conceptualized the research idea. N.S.S performed, designed and analysed all the numerical simulations data. N.S.S prepared the manuscript. N.G and J.S proofread and guided the preparation of the manuscript. All of the authors reviewed and authorised the manuscript.

Abstract

Falling-film heat exchangers are widely used to promote heat and mass transport within industrial environments. In contemporary condensers, for example, liquid films continuously form over a tube row and impact multiple tubes beneath, resulting in a rich variety of two-phase flow phenomena, including the classical Rayleigh-Plateau instability. It is widely known that altering the contact angle of the tubes influences the heat exchangers' heat and mass transfer characteristics by changing the falling-films' flow behaviour (i.e. dropwise or jet). Therefore, resolving interfacial flow characteristics, such as the Rayleigh-Plateau instability, is crucial for falling-film studies as this instability may change the state of the falling-film from being jet flow to dropwise/jet flow or even just dropwise. To explore this aspect, three-dimensional direct numerical simulations are used in the present work to replicate the jet instability behaviour. By employing certain mesh refinement strategies demonstrated from various case studies, the interfacial flow behaviour and jet instability have been captured, showing good agreement with experimental and theoretical data previously published. This is determined from the increased jet bifurcation and a maximum error of 2.2% of the film thickness in comparison to Nusselt's result within the bulk region of the tube. In addition, the average and local heat transfer coefficients across the first tube were compared with numerical solutions to give an average error of 3.2 and 14 %. Jet instability is found to be directly related to the amplitude of the axial pressure variations which is augmented by the growth rate of the capillary wave that travels upstream. Specifically, for contact angles of 30 and 60°, the flow is in a dropwise and dropwise/jet state due to the emergence of the Rayleigh-Plateau instability. Notably, the additional satellite droplets that materialize from the unstable jet led to an increase in the local heat transfer coefficient of the film compared to without the Rayleigh instability improvement.

4.1. Introduction

The occurrence of liquid films/drops plummeting over a bundle of tubes is frequently observed within many heat exchangers such as condensers, evaporators and absorbers that are heavily used in the fields of refrigeration/cryogenics, desalination, LNG (liquid natural gas) phase change, food production plants and power plants.[1-4] For example, in a horizontal tubular absorber, as the working hot binary liquid mixture and water-vapour enter the system via a feeder, the coolant pipes siphon the latent heat away from the vapour to be liquefied. The subcooled condensate then simultaneously mixes with the operating hot liquid to dilute its concentration as it flows and falls across the heat pipes. [5] Due to the inherent variation of surface roughness across most thermal conductive materials, some areas of the pipes are left exposed, which reduces the rate of heat and mass transfer of vapour to the liquid-film i.e. the vapour's absorption rate.[6]

In addition, the hydrodynamics of the film is another contributing factor as to whether it will increase or decrease the heat or mass transfer depending on the nature of its flow (i.e. sheet, jet or dropwise regimes).[7] The ability to capture and examine the behaviour of falling films is of great interest to guide improvement in overall efficiency of heat exchangers via surface topology modification. By investigating gravity-driven flow of falling films over multiple horizontal tube banks,[8] Killion *et al*. has noted that droplet nucleation sites will form as soon as the liquid beneath the first tube starts to thicken. Specifically, as liquid is continuously driven into the droplets, the hydrostatic force starts to become dominant over the surface tension and pulls the droplet orthogonally from the tube. Hereafter, the inertial force between the liquid filament and the circumference of the droplet continuously increases under gravitational acceleration. Consequently, the capillary bridge (still being attached to the droplet) begins to shrink to a point where its surface tension overcomes the viscous force causing the bridge to collapse.[8]

It should be noted that the difference in overall interfacial tension force between the tip and the bulk of the jet forces the jet to retreat towards the tube.[9,10] This is then followed by a capillary wave (formulated at the tip) that propagates along the liquid jet. When the wavelength surpasses the circumference of the jet, the surface area of the filaments will decrease resulting in a reduction in surface energy. The diminished surface energy is then converted into kinetic energy which dissipates along the stream causing the jet to be perturbated.[10,11] These oscillations directly affect the Laplace pressure gradient within the fluid, forming regions of high and low pressures along the convex and concave curvatures.[12] As a result, along the high-pressure regions, the jet bifurcates into many satellite droplets.[12] Droplets that formulate from a perturbated liquid column is associated with the Rayleigh-Plateau instability.[13-15]

In order to apprehend and understand such comprehensive physics within the Rayleigh time-scale,[16] numerical simulations are required to locally analyse the hydrodynamic flow pattern to distinguish which properties or parameters will globally affect the proficiency of heat and mass exchangers. Further, interpreting the Rayleigh-Plateau instability is of the utmost importance to encapsulate within numerical simulations as the capillary ripples generated on the film will induce film waviness. The increased waviness of the film will provoke hydrodynamic instabilities which can increase the departure rates of droplets beneath the tube. Furthermore, such physical interaction will cause the interfacial area to increase as the additional capillary waves generated will stretch the liquid film further.[8] This will enhance the overall heat transfer as the thermal resistance between the bulk liquid and solid is reduced with the reduction in film thickness. To capture this phenomenon numerically, high-level mesh refinement is required within the liquid filament to resolve the capillary waves during the evolution of the Rayleigh-Plateau instability.

A study by Deshpande *et al*. focused on a mesh independence analysis on the retraction of a laminar liquid column by altering the number of grid points across the diameter of the jet.[17] Within the initial stages of instability, it was found that the mesh resolution was independent upon the retraction velocity and jet contour. However, as the amplitude of the capillary wave started to increase, the larger number of grid points per diameter (between 8 and 32) showed greater rapid bulging of the liquid column and jet bifurcation. At a grid resolution of 32 points within a particular timeframe, droplet pinching was observed although lower grid resolutions did not apprehend this. It should be noted that during jet instability, the diameter at the convex regions of the jet will decrease to its smallest mesh size. Therefore, the neck diameter at that particular region is limited to the number of grid points acting along its interface as it is directly proportional to the interfacial tension force.[17] Ultimately, the required number of grid points varies, depending on the film Reynolds and Weber numbers. In the context of falling-films, the films' Reynolds number at the inlet here is given as follows: [18]

$$Re_{f(in)} = \frac{4\Gamma_{in}}{\mu_l} \tag{4.1}$$

where Γ_{in} is the inlet specific film flow rate (kg/m·s), given by the following equation,

$$\Gamma_{in} = \frac{\dot{m}_{in}}{2L_t} \tag{4.2}$$

where $\dot{m}_{in}$ is the mass flow rate at the inlet (kg/s). Shinjo *et al*. stated that the mesh spacing should typically be at least a fifth of the jets' diameter to capture the profile of instability.[19] Nevertheless, as the film Reynolds number increases (i.e. the inlet velocity) the Weber number will simultaneously increase as it is proportional to the film velocity. In turn, this will increase the instability of the liquid jet and reduce the diameter of the subsequent satellite droplets following from Rayleigh-Plateau instability. As a

consequence, further mesh refinement is needed to capture these droplets which may require a few hundred million grid points for a singular liquid jet. On the other hand, to find out whether numerical results are correctly captured with the selected grid spacing requires the inspection of the waviness of the jet in which the formation of oscillating droplets can be identified. This will indicate how precise the interfacial surface tension has been captured.[19]

Many have attempted to model and compare the kinematics of falling films in comparison to experimentally obtained results. Hosseinnia *et al*. numerically investigated how the falling-film flow regime affects the absorption rate of water vapour within a lithium bromide (LiBr) solution whilst traveling over cooled heat pipes.[20] However, the Rayleigh-Plateau instability seen on the liquid-jet was only slightly captured, that is, only a few subsequent liquid drops were broken from the jet after droplet detachment. As mentioned previously, this will ultimately affect the flow regime beneath the second pipe and hence the water vapour absorption rate. Ding *et al*. also compared numerical simulations against the experiments from Killion *et al*., and extended their investigations to explore the effect of surface wettability on the hydrodynamics.[18] Nevertheless, as the Rayleigh-Plateau instability was under-resolved, it remains unclear how the true flow regime on the second tube (and so on) will be as a function of surface wettability. As briefly mentioned, changing the surface wettability of tube walls can significantly improve the heat transfer characteristics of heat exchanger systems. However, the wettability requirements for each type of system (for example, absorbers and condensers) are distinctive. In a partial wetting regime, droplets that are associated with a microscopic thin film absorbed within their vicinity will have reduced tendency to move laterally and longitudinally.[21]

To elaborate on different heat exchanger wettability requirements, an absorber heat exchanger (or an evaporator) will favour a completely wetted surface as opposed to condenser heat pipes as discussed in Chapter 1. This is reflected from the previous work by Köroglu *et al*., who fabricated functional hydrophilic and hydrophobic surfaces upon copper heat pipe banks to investigate the heat transfer enhancement on a falling-film evaporator.[22] It was noted that the functional hydrophilic surface exhibited better performance in comparison to the plain and hydrophobic surface. This was due to the increased affinity of the surfaces to water, promoting a thin liquid film along the interface. In respect to absorbers, the hydrophilic surface property increased the diffusion rate of the vapour onto the surface, which explains the improvement in the heat transfer rate. Subsequently, Zheng *et al*. studied the same effect on a falling-film evaporator but further modified the surface to reach a superhydrophilic condition.[6] As anticipated, the heat transfer coefficient of the superhydrophilic surfaces outperformed the hydrophilic surface by at least twice the amount at low film flow rates due to complete surface wetting at low spray densities.

In this study, direct numerical simulations are designed to resolve the Rayleigh-Plateau instability and other interfacial flow features of the falling-film within the dropwise regime by focusing on mesh refinement within the liquid-jet. The flow phenomena on the first and second tubes is directly compared to the experimental results by Killion *et al*.[8] In addition, the local heat transfer coefficient within the film is accessed to explore the effects of additional satellite droplets impacting the tube. Moreover, effects of static contact angles are parametrically investigated across a wide range of surface conditions from superhydrophilic to superhydrophobic states. The distinction between the wettability states are quantified from the hydrodynamics of the flow pattern (i.e. capillary wave propagation), changes in droplet departure diameter, film waviness and instability,

transition periods from dropwise to jet flow and the film thickness across the impacted tubes.

4.2. Methodology

4.2.1 Geometry Setup, Boundary Conditions and Mesh Refinement

Firstly, to validate the numerical predictions, a similar tube configuration as the experiments of Killion *et al*. was generated.[8] The system consisted of six horizontal brass tubes in a 300-mm long column. The outer tube diameter (d_t) and the longitudinal tube spacing (s_t) (distance between the tube faces) was 12.7 mm and 25.4 mm (double the tube diameter). To feed the water over the tubes, a distributer was placed 1 mm above the first tube. This was to ensure that the fluid impacting the tube would be evenly distributed i.e. verifying that the planar shear stresses at the walls would be negligible so that certain parabolic velocity profiles may not be created and disturb the flow.

To reduce computational power and time, only three horizontal tubes are selected for the simulation model where their length is equivalent to the Rayleigh-Taylor instability wavelength. The Taylor wavelength is known as the distance between the droplets on the pipe where they start to nucleate from and leave. This was first noted by Hu *et al*.[7] who observed this behaviour and discussed the accuracy of the different correlations of other researchers used to determine the Taylor wavelength on horizontal tubes. However, as suggested by Ding *et al*.[18], most studies ignored the effects of the film Reynolds and Galileo numbers on the Taylor instability. Nevertheless, Armbruster *et al*. took this into consideration and correlated the Taylor wavelength equation with a standard deviation of ±7.5% as:[23]

$$\lambda = \frac{2\pi\sqrt{2}}{\sqrt{\frac{\rho_l g}{\gamma_{lv}}\left(1 + \left(\frac{\frac{Re_{f(in)}}{2}}{Ga^{\frac{1}{4}}}\right)^{0.8}\right) + \frac{2}{d_t^2}}} \quad (4.3)$$

To ensure that dropwise flow is initially maintained from the tube banks, the film Reynolds number must be within a certain threshold. According to Hu *et al*., the regime for which dropwise flow will occur is:[7]

$$Re_{f(in)} = 0.074Ga^{*0.302} \quad (4.4)$$

with a mean deviation of ±11%.[7] In addition, the transition regime of which dropwise flow will evolve into jet flow (i.e. dropwise/jet flow) is verified as:

$$Re_{f(in)} = 0.096Ga^{*0.301} \quad (4.5)$$

having a mean deviation of ± 11.2%.[7] For water at approximately room temperature and at atmospheric pressure, the critical Reynolds number where dropwise flow is maintained is given as $Re_{f(in)}$ = 116 from Equation 4.4. Based on this, the critical inlet specific film-flow rate from Equation 4.1 is Γ_{in}= 0.029 kg/m·s. It should be noted that the Reynolds number must be kept less than 100 as this is typically the Reynolds number margin observed from the experiments by Killion *et al*. to establish droplet-to-droplet/jet behaviour.[8] To make a direct comparison against the simulation results by Ding *et al*., a Reynolds number of $Re_{f(in)}$ = 80 was selected which corresponded to an inlet specific film-flow rate of Γ_{in} = 0.02 kg/m·s. The tube length was chosen as 22 mm (rounded up from 21.7 mm) for these flow conditions based on the Taylor wavelength (Equation 4.3). The dimensions of the inlet feeder were fixed at 1 x 2 mm^2 (L_z x L_x) and positioned 1 mm above the first tube. This arrangement limits the effects of shear forces created from the feeder which could perturb the liquid flow around the tube and invalidate the results.[18,20]

The length of the domain in the flow direction was also chosen to match that of the numerical study by Ding *et al*.[18] which corresponds to 99.9 mm.

To further note, in order to predict and validate the heat transfer model prescribed, the Nusselt number can be used to describe the heat and mass transfer characteristics for each of the falling film regimes. The Nusselt number is widely known as the ratio of the convective to the conductive heat transfer rate of a fluid, which is normally expressed as:

$$Nu = \frac{h\lambda_c}{k_l} \tag{4.6}$$

For falling films, the length scale here is denoted based on the characteristic film thickness (δ_{ch}), which is given as:[7,24]

$$\delta_{ch} = \sqrt[3]{\frac{{v_l}^2}{g}} \tag{4.7}$$

with v_l being the kinematic viscosity of the liquid (m^2/s). Therefore, substituting δ_{ch} for λ_c one obtains a modified Nusselt number, Nu^*,

$$Nu^* = \frac{h}{k_l}\sqrt[3]{\frac{{v_l}^2}{g}} \tag{4.8}$$

From the experimental observations made by Hu *et al*., the resulting Nusselt number correlation established for dropwise flow is expressed as:[7]

$$Nu^* = 0.113{Re_{f(in)}}^{0.85} Pr^{0.85} Ar^{-0.27} \left(\frac{s_t}{d_t}\right)^{0.04} \tag{4.9}$$

with a mean deviation of ± 6.1%.[7] Here, Pr is known as the Prandtl number and Ar is given as the Archimedes number. The Prandtl number illustrates the ratio of the momentum diffusion rate to the thermal diffusion rate of the fluid which is given as:

$$Pr = \frac{\mu_l C_{p,l}}{k_l} \tag{4.10}$$

Likewise to the Galileo number, the Archimedes number represents the ratio of the gravitational to the viscous forces of a fluid but instead as a function of the tube diameter.[7] Therefore, the length scale in this case is equivalent to the tube diameter (λ_c = d_t), and one finds the Archimedes number as,

$$Ar = \frac{{\rho_l}^2 g {d_t}^3}{\mu_l^2} \tag{4.11}$$

Also, the dimensionless parameters stated within the Nusselt correlation equations were governed in this work to a certain range for which Hu *et al*. experiments were conducted up to, with $Re_{f(in)}$ = 4 – 2060, Pr = 4.8 – 75.6, Ar = 6.7 × 10^5 – 1.8 × 10^8 and the ratio between the tube spacing and diameter, $\left(\frac{s_t}{d_t}\right)$ = 0.3 – 5.2.[7]

Constant thermodynamic and fluid properties for water and air were implemented which are evaluated at the inlet temperature (T_{in} = 293 K), where ρ_l = 998.2 kg/m^3, μ_l = 1.003 mPa·s, $C_{p,l}$ = 4182 J/kg·K, k_l = 0.6 W/m·K, ρ_v = 1.225 kg/m^3, μ_v = 0.0179 mPa·s, $C_{p,\mathrm{v}}$ = 1006.43 J/kg·K, k_v = 25.87 mW/m·K and γ_{lv} = 72 mN/m. A symmetric boundary condition was imposed which permitted simulations of the complex two-phase flows while also reducing the computational domain size and resource demands. As shown in **Figure 4.1a**, a velocity-inlet ($u_{l,y}$) is prescribed at the 1 x 1 mm^2 sectioned area with a secondary velocity-inlet opted around the domain of the feeder. A liquid volume fraction of 1 (α_l) is imposed at the inlet feeder to ensure only water-liquid enters the domain from that area whilst a vapour volume fraction (α_v) of 1 is selected for the secondary velocity inlet as this particular region will represent the atmosphere. A constant liquid inlet velocity of $u_{l,y}$ = 0.44 m/s was imposed at the feeder which was calculated from Equation 4.2 using

the operating Reynolds number ($Re_{f(in)}$ = 80). At the minor inlet, u_y = 0 m/s since no external airflow is present there. Symmetry boundary conditions are applied at the lateral cross-section of the tubes and at the front, back and side faces of the domain to reduce the number of mesh elements required by duplicating the current geometry normal to these directions.

It should be nonetheless noted, for large contact angles (≥ 90°), the symmetry boundary conditions on the left-hand side of **Figure 4.1a** must be changed to pressure-outlet as some formulating droplets on the tubes escape the fluid domain. From **Figure 4.1b** a pressure-outlet is enforced at the bottom of the domain having a gauge (or static) pressure of 0 Pa since the environment surrounding the tubes is only exposed to atmospheric pressure (101325 Pa). An intrinsic contact angle of 0° (θ_Y = 0°) was initially subjected on each of the three tube walls, which will create a more accurate representation of the fluid flow near the top section of the tubes. As the effect of contact angle hysteresis is not included in this study, the contact angle hysteresis is assumed to be 0°, where the advancing and receding contact angles are equal to the equilibrium contact angle. Subsequently, a no-slip condition (V_w = 0 m/s) was also applied at the walls, whereas the finite slip velocity practically experienced by the fluid at the solid-liquid interface is considered to be negligible for the characteristic length scale. Finally, a uniform heat flux, supplied to the tube walls was equal to 50 kW/m^2 based on the experimental parameter range by Hu *et al.*[7]

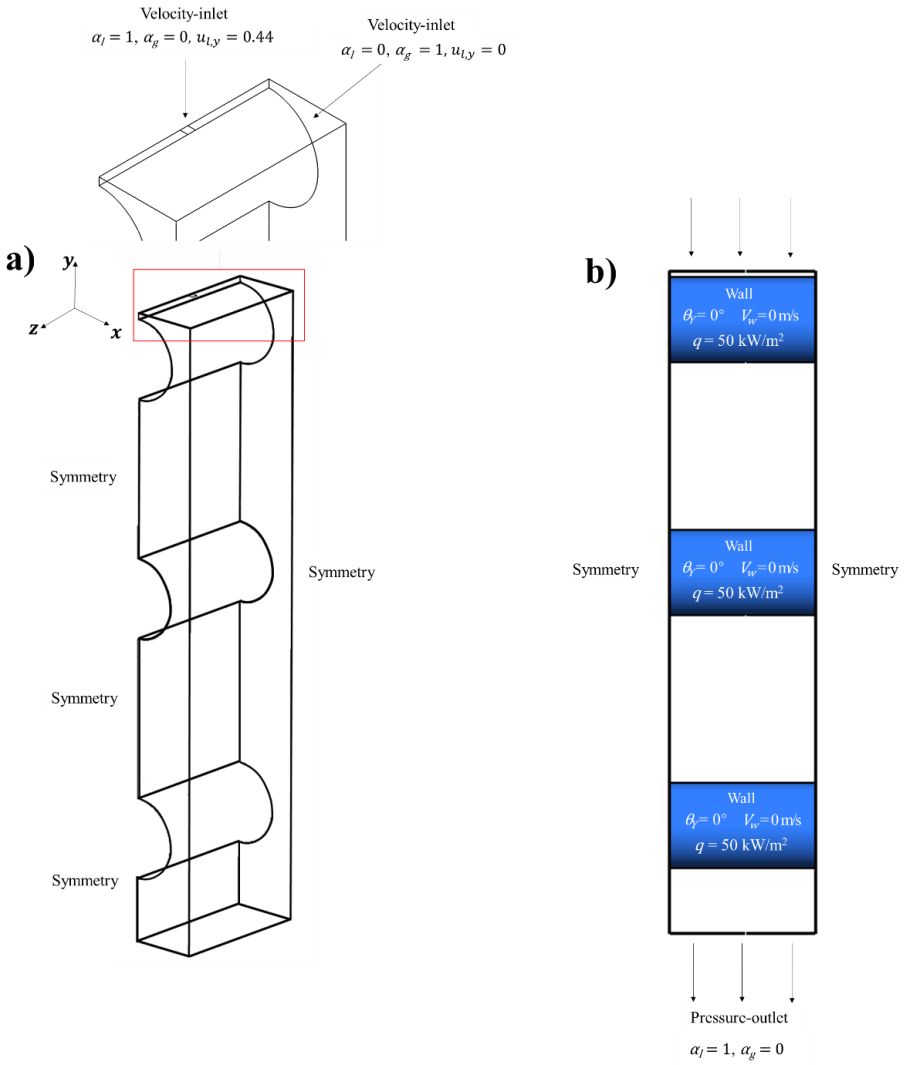

Figure 4.1. (a-b) Computational fluid domain with defined boundary conditions.

The fluid domain had been meshed using hexahedral elements as shown in **Figure 4.2**. According to mesh sensitivity analyses conducted by Ding *et al.* and Hosseinnia *et al.*, respectively, the global mesh size was selected to be 0.25 mm with the local mesh size being 0.2 mm around the face of the tube walls.[18,20] From their grid independence analysis, decreasing the base mesh below 0.25 mm resulted in a film thickness variation of less than 0.5 % when $Re_f = 80$.[18] To sufficiently capture the hydrodynamic and thermal boundary layers around the tube walls, additional refinement layers were added as seen in **Figure 4.2a**. Sixteen grid points per unit jet length were used to capture the fine-scale interfacial flow features of the jet, equivalent to a cell length of 0.1 mm displayed in

Figure 4.2b-c (based on the smallest jet length observed that was 1.6 mm).[17] Increasing grid resolution to 24 and 32 grid points resulted in limited improvements in resolving the jet instability and droplet breakup. The concluded cell length was then used to locally refine the mesh near the jet at the front and lateral planar faces.

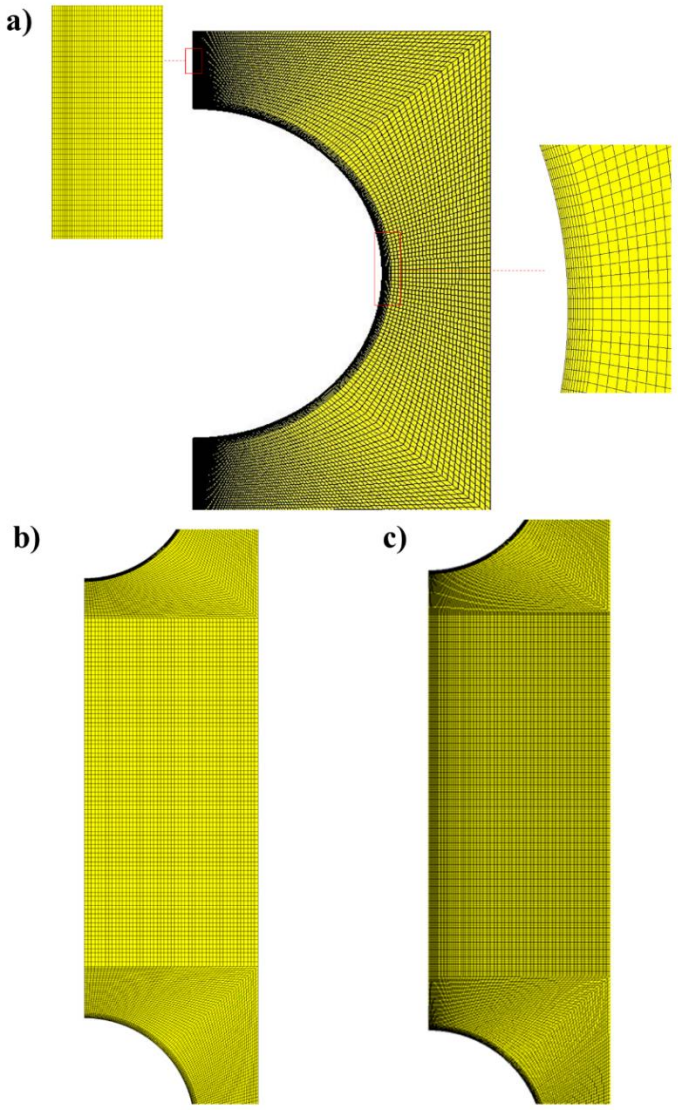

Figure 4.2. (a) Mesh refinement near the tube walls with additional inflation layers added at tube wall interface to capture the liquids' film thickness and hydro/thermodynamic flow displayed on the front plane of the second tube. (b) Planar view of mesh topology at the middle section between the first and second tube without mesh refinement (0.25 mm), (c) with mesh refinement (0.1 mm).

4.2.2 Governing Equations and Numerical Schemes

Most of the continuity equations and numerical schemes in this study are employed from the previous chapter which includes the Volume-of-Fluid method, the mass, momentum, energy conversation equations (Equation 3.9, 3.13-3.15, 3.21 and 3.23) to develop the velocity and temperature fields within the fluid domain. The CSF and wall adhesion model (Equation 3.16-3.19) is also added to model the surface tension force at the liquid-vapour interface and the surfaces' adhesion force based on the magnitude of the intrinsic contact angle. However, in this case, unlike Equation 3.9, the mass continuity equation does not contain any source terms as no mass transfer is present. Thus, Equation 3.9 is modified as:

$$\frac{1}{\rho_x}\left(\frac{\partial}{\partial t}(\alpha_x\rho_x) + \nabla\cdot(\alpha_x\rho_x\overrightarrow{v_x})\right) = 0 \qquad (4.12)$$

where *x* stands for the liquid phase (l) or vapour phase (v). The same is also said for Equation 3.21, where the energy source term is not considered as no phase change is established between the two phases (i.e. no latent heat is released). Therefore, Equation 3.21 is altered as follows:

$$\frac{\partial\left(\rho e + \frac{v^2}{2}\right)}{\partial t} + \nabla\cdot\left[\vec{v}\left(\rho(e+\frac{v^2}{2}) + p\right)\right] = \nabla\cdot[k\nabla T] \qquad (4.13)$$

Likewise, in Equation 3.19, as the dynamic contact angle is not investigated in this chapter (i.e. the contact angle hysteresis), the wall adhesion model uses the intrinsic contact angle (θ_Y) instead of the dynamic contact angle (θ_d) to alter the unit normal vector at the wall. Hence, Equation 3.19 is represented here as:

$$\hat{n} = \hat{n}_w \cos\theta_Y + \hat{t}_w \sin\theta_Y \quad (4.14)$$

To further note, the mass, momentum and energy equations are solved using an explicit discretisation scheme to reduce the complexity of solving the equations. As a consequence, this reduces the robustness of the simulation stability and requires small time-steps to counteract this problem. In terms of numerical stability, to sufficiently capture the capillary wave propagation rate along the jet without divergence, the simulation must record the fluid dynamics within a unit cell as the capillary waves propagate through each cell. To achieve this, an adaptive time-stepping method was required to adjust the timestep in accordance with the wave velocity (e.g. the faster the waves propagate, the smaller the timestep must be). This relationship can be expressed as Courant–Friedrichs–Lewy condition otherwise known as the Courant number as formerly highlighted in Chapter 3.2.2 (Equation 3.25). To elaborate further however, when the Courant number is greater than one, numerical instability will start to arise as fluid particles begin to navigate through two or more elements at a given timestep. This causes the numerical diffusion (or the viscous diffusion coefficient) to become negative which makes the solution to the governing equations multiply indeterminately. To ensure numerical constancy of the governing equations, a maximum Courant number of 0.4 was set. The global timestep was automatically adjusted during the simulation to meet this requirement.

In order to ascertain the average heat transfer coefficient across the tube, the local heat transfer coefficient must first be solved. Notably, the heat transfer coefficient will vary across the circumferential and axial direction (θ, z) as the liquid spreads. Based on Newton's law of cooling, the local heat transfer coefficient is given as:

$$h(\theta, z) = \frac{q}{T_w(\theta, z) - T_{in}} \quad (4.15)$$

Thus, the average heat transfer coefficient, $\bar{h}$, is computed by doubly integrating the local heat transfer coefficient on the surface area of the tube assuming the entirety of the surface provides a uniform heat flux:

$$\bar{h} = \frac{1}{2\pi R_t L_t} \iint h(\theta, z)\, dA \tag{4.16}$$

By calculating the average heat transfer coefficient, the average Nusselt number, $\overline{Nu}$, of the tube surface is obtained by substituting $\bar{h}$ into h from the modified Nusselt equation (4.17).

$$\overline{Nu} = \frac{\bar{h}}{k_l} \sqrt[3]{\frac{{v_l}^2}{g}} \tag{4.17}$$

Furthermore, the coupling of the pressure and velocity correction gradients in the simulation were solved using the same numerical scheme provided in Chapter 3.2.2 (PISO). Although in this case, a normalized residual mean square value of $\leq 10^{-5}$ was utilized.[18] In addition, the mass, momentum and energy equations were spatially discretised using the PRESTO and the second-order upwind scheme. Correspondingly, the Geo-Reconstruct scheme is used to interpolate the advection between the liquid and gas interface by assuming a piecewise-linear slope.[25] Finally, the transient scheme used to solve the unsteady-state differential in the mass and momentum equations was first-order upwind as mentioned beforehand in Chapter 3.2.2.

4.3. Results and Discussion

4.3.1 Numerical Validation

Figure 4.3 illustrates the droplet detachment process assessed at different timesteps and evaluated against experimental results by Killion *et al*.[8] The simulation results show good agreement with the hydrodynamics observed in the necking progression of the pendent droplet. After the droplet detaches itself from the liquid bridge (at 130 ms), the break-up of the liquid filament is initiated by the harmonic oscillations generated from the jet recoil. The simulations adequately capture this phenomenon due to the mesh refinement around the liquid-jet, while also capturing the axial motion of the droplet during droplet nucleation (from 0 to 10 ms). A pendent droplet that nucleates on a horizontal tube tends to elongate towards the axial direction due to the competing surface tension and gravitational forces.[8] However, once the gravitational force overcomes the surface tension force, the pendulous droplet departs away from the tube. Due to its initial axial translation, the shape of the droplets appears to be asymmetrical (seen from 90 ms onwards).

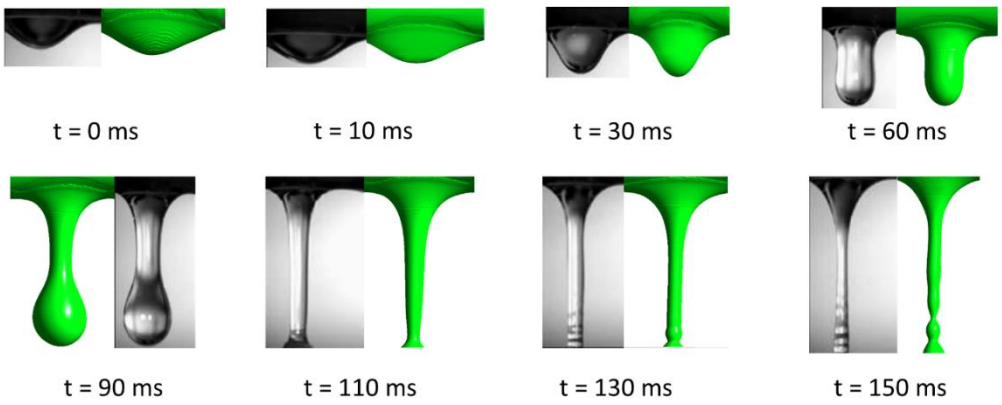

Figure 4.3. Evolution of droplet formation and Rayleigh-Plateau instability along the liquid bridge that is established during droplet detachment from the first tube. Compared against Killion *et al*. experimental results.[8]

To quantitatively validate the hydrodynamics of the falling-film around the first tube, the Nusselt solution can be used to verify the expected film thickness and velocity profile within a two-dimensional plane. The Nusselt's film thickness for falling-films upon a tube can be expressed as:[26]

$$\delta_f = \left(\frac{3\mu_l \Gamma_{in}}{{\rho_l}^2 g \cos\theta}\right)^{\frac{1}{3}} \tag{4.18}$$

Additionally, the circumferential and radial velocity profiles around the tube can be calculated as:

$$u_\theta = \frac{\rho_l g}{\mu_l} \sin\theta \left(\delta_f r_i - \frac{{r_i}^2}{2}\right) \tag{4.19}$$

$$u_r = -\frac{\rho_l g}{R_t \mu_l} \cos\theta \left(\frac{\delta_f {r_i}^2}{2} - \frac{{r_i}^3}{6}\right) - \frac{\rho_l g}{2R_t \mu_l} {r_i}^2 \sin\theta \frac{d\delta_f}{d\theta} \tag{4.20}$$

From **Figure 4.4**, the three-dimensional numerical film thickness located at the mid-plane (11 mm) is displayed when t = 2 s and plotted against the two-dimensional Nusselt's film thickness. As shown, the numerical film thickness is validated against the Nusselt's solution with a maximum error of 2.2% between 7 and 129° (clockwise). However, exceptions are made at the top of the tube and towards the bottom of the tube. The enlarged necking seen at the top of the tube is attributed to the surface tension effect of the inlet feeder. And the droplet formation (seen roughly 38° from the tube counter-clockwise) is due to the symmetry boundary condition enforced which creates a contact angle of 90° at the symmetric interface. This makes the solid-gas surface tension become equal to the solid-liquid surface tension (as seen from Equation 2.1, in Chapter 2.2.1) which allows the fluid to be seemingly in contact with air (from a real-world perspective). It should be

noted that the Nusselt's solution ignores the effects of surface wettability which results in no droplet formation and only filmwise flow.

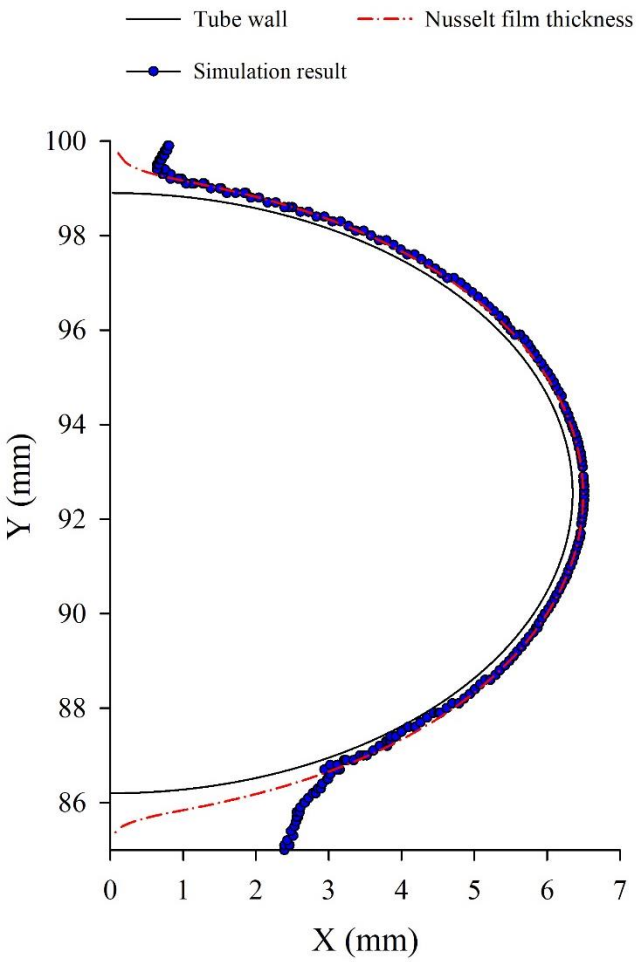

Figure 4.4. Film thickness predictions against Nusselt's model. Results are extrapolated from the first tube at the mid-plane (L = 11 mm) when t = 2 s.

Furthermore, the circumferential velocity profiles at a tube length of 7.3 mm across the first tube is shown in **Figure 4.5**. The velocity profiles chosen for validation was selected away from the middle of the tube due to the droplet formation, which will alter the velocity profiles presented due to the three-dimensional flow affecting the circumferential velocity around the tube as stated by Ding *et al.*[18] Nonetheless, the simulated velocity profiles coincide with the Nusselt's velocity profiles well for circumferential angles of 45° and

90° with a maximum error of 10.6 % for 45° and 9 % for 90°. The deviation between the theoretical and simulation results is due to the effect of film waviness along the axial direction which is neglected in the Nusselt solution.

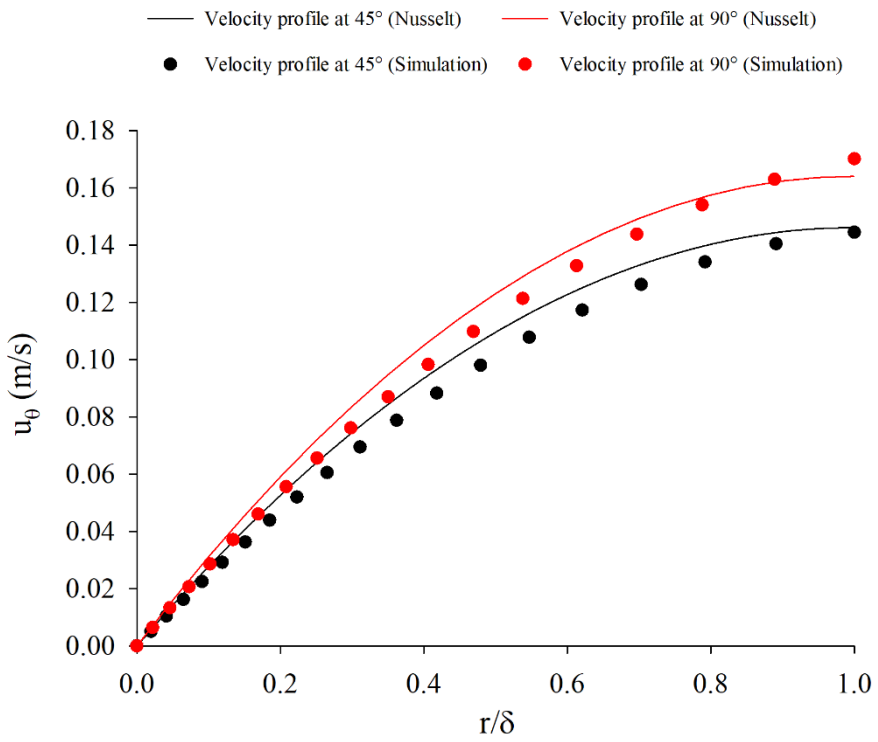

Figure 4.5. Circumferential velocity profile calibration around the first tube at different circumferential angles when L = 7.3 mm at t = 2 s.

To validate the heat transfer model, the average Nusselt number was recorded on the first tube and then time-averaged across 2 seconds (total simulation time). The following result gave an average Nusselt number of $\overline{Nu}_{sim}$ = 0.26 (rounded up to 2 decimal places), whilst the calculated result from Hu *et al.* gave a value of $\overline{Nu}_{cal}$ = 0.27.[7] This corresponded to an error of 3.2 %. Since Hu *et al.* correlated Nusselt equation with a mean deviation of 6.1 %, the error presented is satisfactory as it is confined within the boundaries of the mean deviation. Moreover, the local heat transfer coefficient of the film was also compared against a two-dimensional analytical model by Rogers *et al.*[27] From their model, a heated tube surrounded by a running liquid film is partitioned into two regions known as the

developing thermal boundary layer region and the fully-developed thermal boundary layer region. The developing thermal boundary layer region is known to begin just after liquid impingement zone where the thermal boundary layer thickness continuous to grow within the viscous (or hydrodynamic) boundary layer (for fluids with a Prandtl number greater than one).[7] When the thermal boundary layer intersects the outer liquid film, the thermal boundary layer is considered to be fully developed causing the rate of change in the local heat transfer to approach zero (i.e. thermal boundary layers expand towards the outside of the film). In this study, the local heat transfer coefficient has been determined using the relationship for thermally developing boundary layers:[7,27]

$$\frac{hd_t}{k_l} = 0.831 Re_{f(in)}^{\frac{1}{9}} Ar^{\frac{2}{9}} Pr^{\frac{1}{3}} \left(\frac{\sin\theta}{P(\theta)}\right)^{\frac{1}{3}} \quad (4.21)$$

where $P(\theta)$ is given to be,[7,27]

$$P(\theta) = \int_0^{\theta} \sqrt[3]{\sin\theta}\ d\theta \quad (4.22)$$

Figure 4.6 displays the circumferential local heat transfer coefficient within the liquid film at the middle section of the first tube which is compared against the analytical model of Rogers *et al.*[27] The theoretical model disregards film waviness, surface tension and liquid impingement which partly explains the large variation in the results at certain tube angles.[24] Between 0 and 6°, the heat transfer coefficient rises to its peak due to the effect of liquid impingement of the inlet feeder (the stagnation zone). Notably, the stagnation zone in this case is proportional to the width and the height of the inlet feeder. After the stagnation zone, the fluid enters the impingement region (6 to 30°) where the velocity gradient reduces due to the viscous force acting against the fluid (as illustrated in **Figure 4.16a**). This region is analogous to the wall-jet formed in classical jet impingement flows

,[28] extending the development region to much larger circumferential angles (~100°) and resulting in numerically simulated heat transfer coefficients that are comparable to the analytical prediction.

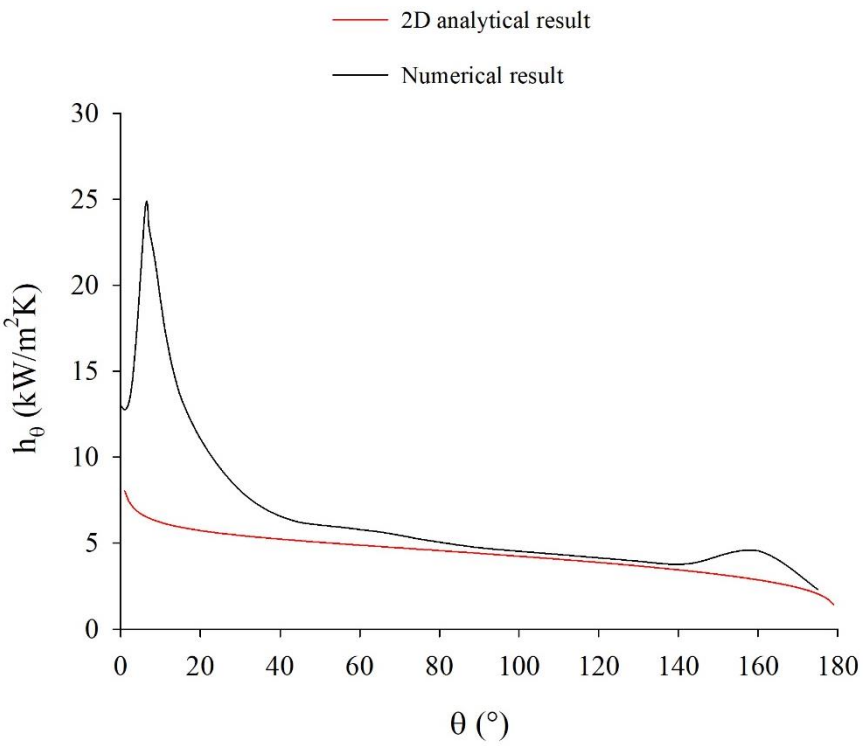

Figure 4.6. Local heat transfer coefficient within the liquid film across the circumferential direction at a tube length of 11 mm when t = 2 s at the first tube compared against the heat transfer model by Rogers *et al.*[27]

In this developing thermal boundary layer section, the thermal boundary thickness represented by the dimensionless temperature profile in **Figure 4.7** continues to increase within the liquid film. Within this region, the average difference in heat transfer coefficient is 14 % compared to Rogers *et al*. theoretical model.[27] After 145°, the thin film can no longer follow the tube contour due to flow separation and droplet formation at the end of tube. This increases the fluid velocity within the small intermediate region leading to an increase in the heat transfer coefficient from 145° to 180°. Since the analytical model

disregards surface tension, this phenomenon is non-existent causing no change in the heat transfer coefficient gradient. The dimensionless temperature profile was determined as:

$$T^* = \frac{T - T_w}{T_b - T_w} \tag{4.23}$$

where T_b is equal to the bulk temperature of the fluid (K) which is defined as the average temperature within the liquid at a defined axis.

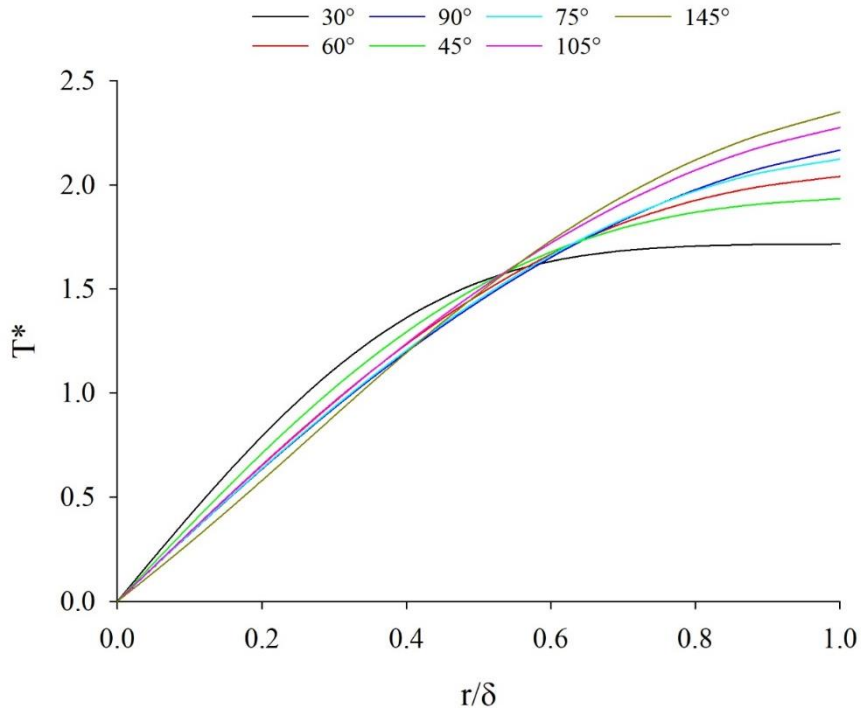

Figure 4.7. Dimensionless circumferential temperature profiles within the liquid film for different circumferential angles when L = 11 mm at t = 2 s.

4.3.2 Implications of Satellite Droplet Impaction on Local Heat Transfer within a Liquid Film.

As previously discussed, the improved capture of the jet ligament break-up will establish additional capillary ripples within the fluid which can be clearly seen in **Figure 4.8**. At 0 ms, the droplet has successfully detached itself from the liquid filament and has started spreading more rapidly than the impact speed in the circumferential and axial directions. This is indicated from the low static pressure the fluid experiences upon impact and the negative pressure gradient between the head and the puddle of the droplets. From this, the kinetic energy of the fluids starts to increase according to Bernoulli's principle and is shown from the capillary velocity contours in **Figure 4.9**, which was also mentioned by Killion *et al*.[8] It should be noted, however, that this observation is only valid for isentropic flows. After 10 ms, the droplet has now flattened into a saddle wave which then impinges onto the second saddle wave adjacent to it and formulates a liquid hoop around the tube. The hoop appears to spread circumferentially and not axially as the impact force from each of the saddle waves cancels one another, caused by the adjacent droplet impacting the tube at approximately the same time as the other. The velocity of saddle waves then starts to decline as it continuously spreads over a large portion of the tube due to the viscous forces being dominant.

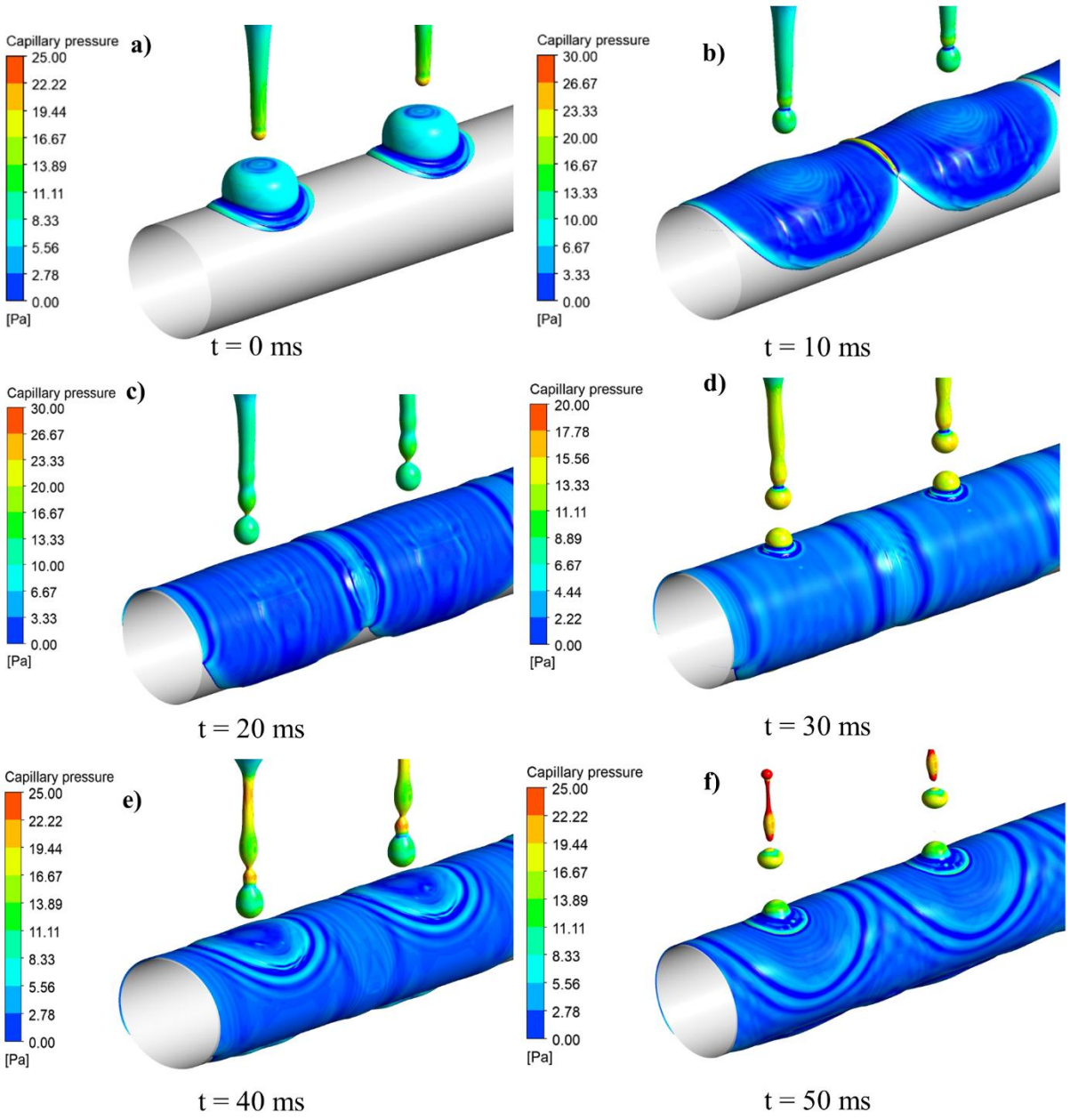

Figure 4.8. Pressure contours showing capillary ripples generated from the satellite droplets and at different times after first droplet impaction upon the second tube.

From 20 ms onwards, satellite droplets start to form from the jet and impact the film which gives rise to capillary ripples generated in the circumferential and axial direction. This is also noted by Killion *et al*., although due to lighting conditions, only axial waves could be seen.[8] The circumferential waves then travel towards the bottom of the tube where they constructively interfere with the nucleating droplet and affect the morphology and

departure rate of the droplets (as illustrated in **Figure 4.16**). The increased number of waves generated due to the further number of satellite droplets captured will increase the disturbance of the droplet causing it to depart faster than if the Rayleigh instability was not captured. It is noteworthy that these capillary waves have been displayed to promote film mixing and thinning which further increase the heat and mass transfer rates in conventional absorption systems.[8,29-31] However, the magnitude of wave velocity starts to slow as the subsequent droplet impact the film (seen in **Figure 4.9**) due to their hydrostatic pressure being smaller than the other (size of the droplets declines).

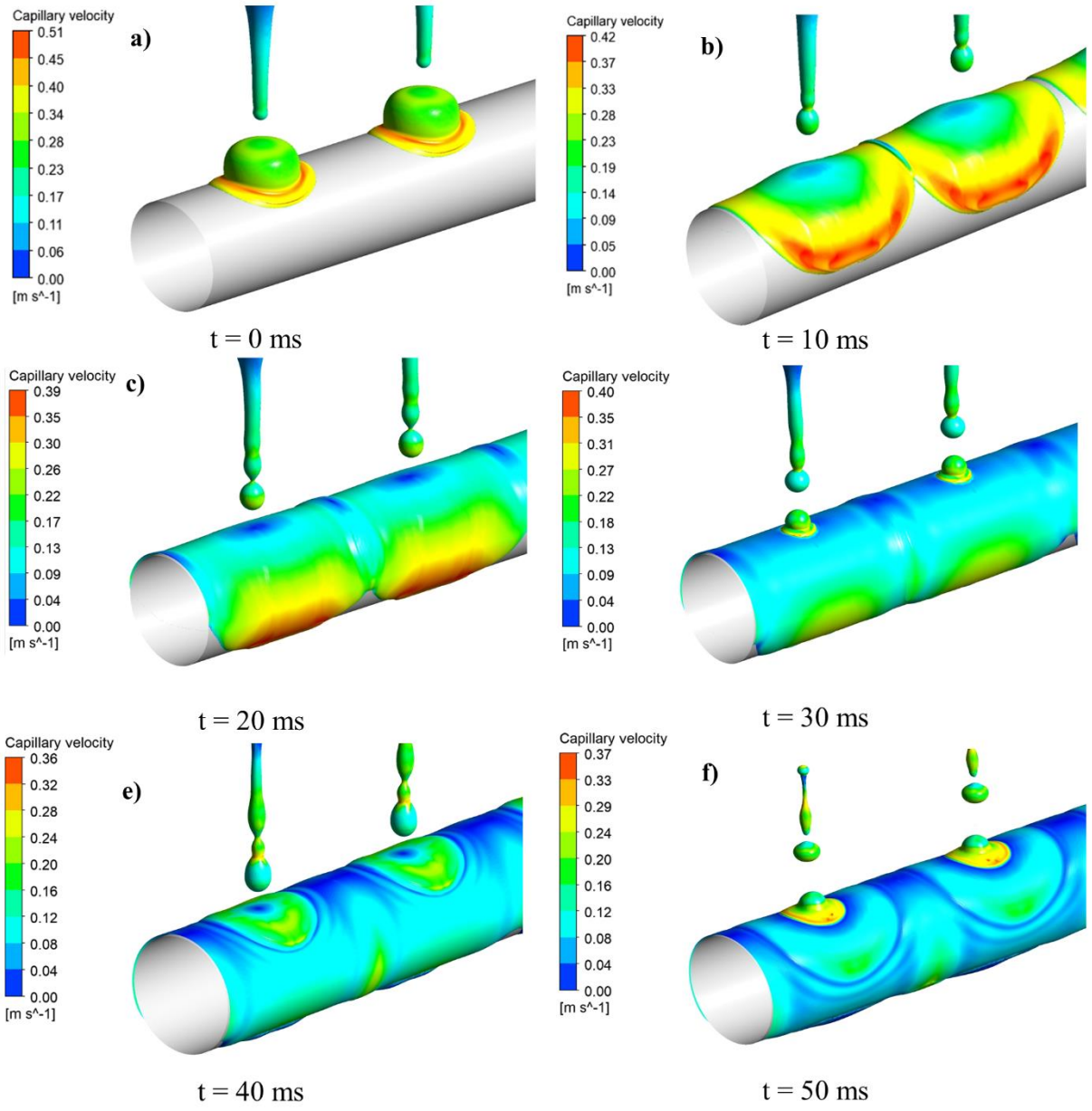

Figure 4.9. Velocity contours from initial droplet impaction to Rayleigh-Plateau instability jet break-up at different timescales upon the second tube.

The film mixing phenomenon within the fluid can be seen in **Figure 4.10** from the velocity vector fields in the axial and circumferential directions on the second tube. In **Figure 4.10a and d**, initially as the satellite droplet impacts the film, the velocity vector field within the film shows little or no movement in the bulk region of the film. In the vicinity of droplet impaction, the capillary velocity begins to increase as the generated saddle wave spreads across the film in all directions. Whilst the wave spreads, the wave dynamically

creates regions of high and low pressures (seen from the squashed regions of the fluid) which enhances the flow of the liquid as shown in **Figure 4.10b-c, e-f.**

To illustrate how film mixing can alter the local heat transfer rate, **Figure 4.11** shows the axial local heat transfer coefficient within the liquid film just after the first satellite droplet impacts the film which is compared before (**Figure 4.11a**) and after the Rayleigh instability improvement (**Figure 4.11b**). At 0 ms, the local heat transfer coefficient is lower within the droplet impaction regime in both cases compared to the rest of the tube. This is due to the increased film thickness which is found to be inversely proportional to the local heat transfer rate.[24] As the droplet flattens into a saddle wave (5 ms), the liquid film within intermediate region begins to thin, which amplifies the local heat transfer coefficient causing the liquid film to cool. Between 5 to 10 ms, the capillary wave continues to spread across the tube which is seen in both graphs as the maxima point of the wave shifts axially along the tube. However, at the same time, the heat transfer coefficient declines as the saddle wave begins to settle within the film. Notably, for the improved Rayleigh capture state, another satellite droplet is detached from the ligament, whilst for the flow state without mesh refinement, the jet is still formulating a satellite droplet. At 20 ms, for the mesh refinement state, the satellite droplet impacts the tube, generating another capillary wave with the rest of the jet being broken into multiple satellite droplets. This promptly increases the local heat transfer coefficient as shown previously when the first satellite droplet impacted the film. For the flow state without mesh refinement, the heat transfer coefficient continues to decline as the capillary wave travels further along the tube with a second satellite droplet just beginning to be detached. This demonstrates how the additional capillary waves generated from the satellite droplets can enhance the local heat transfer rate by promoting film mixing, thinning and cooling.

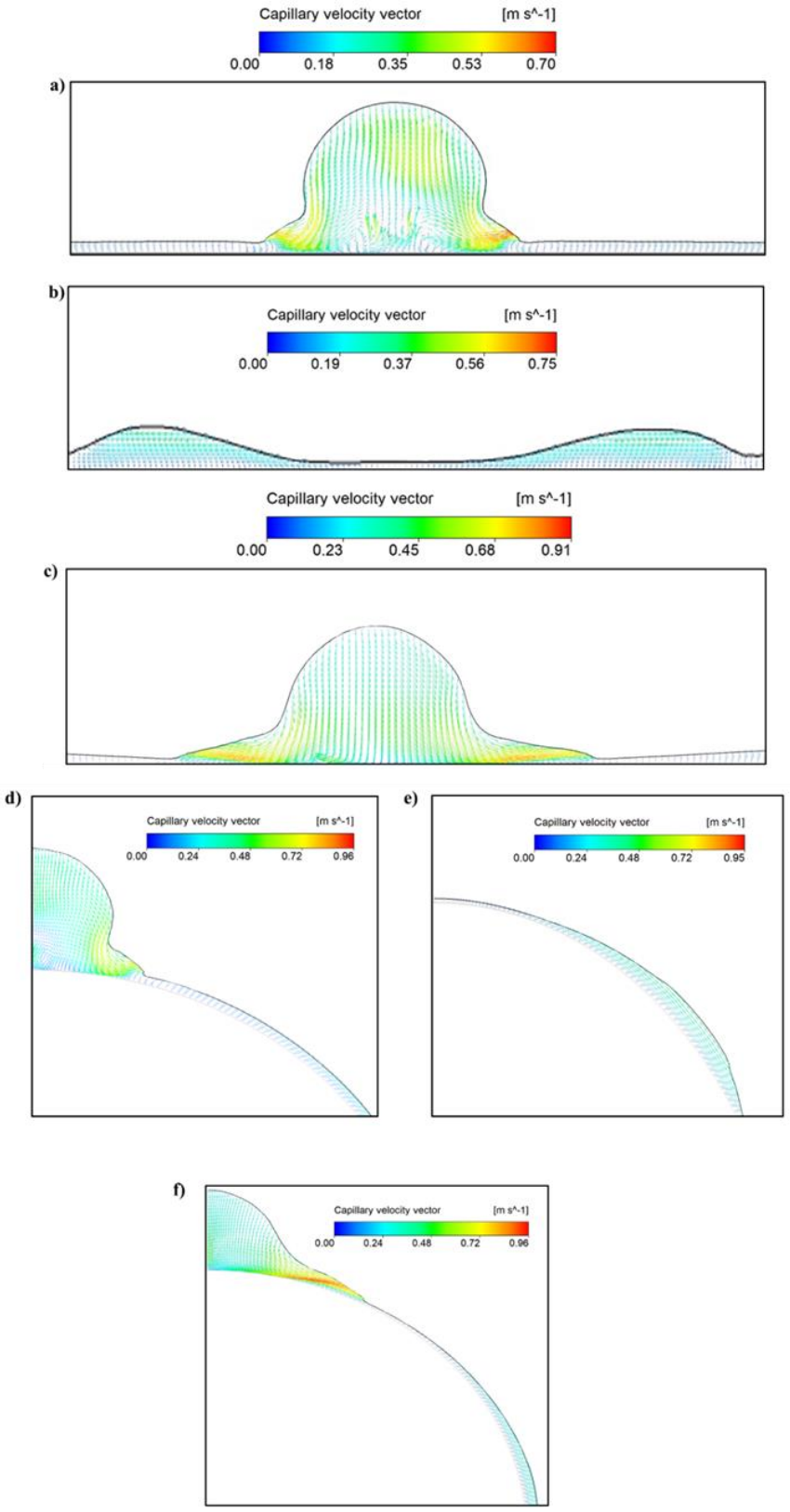

Figure 4.10. Velocity vector plot of the liquid film impacting the middle of the second tube (from 30 to 50 ms) in the axial (a-c) and circumferential direction (d-f).

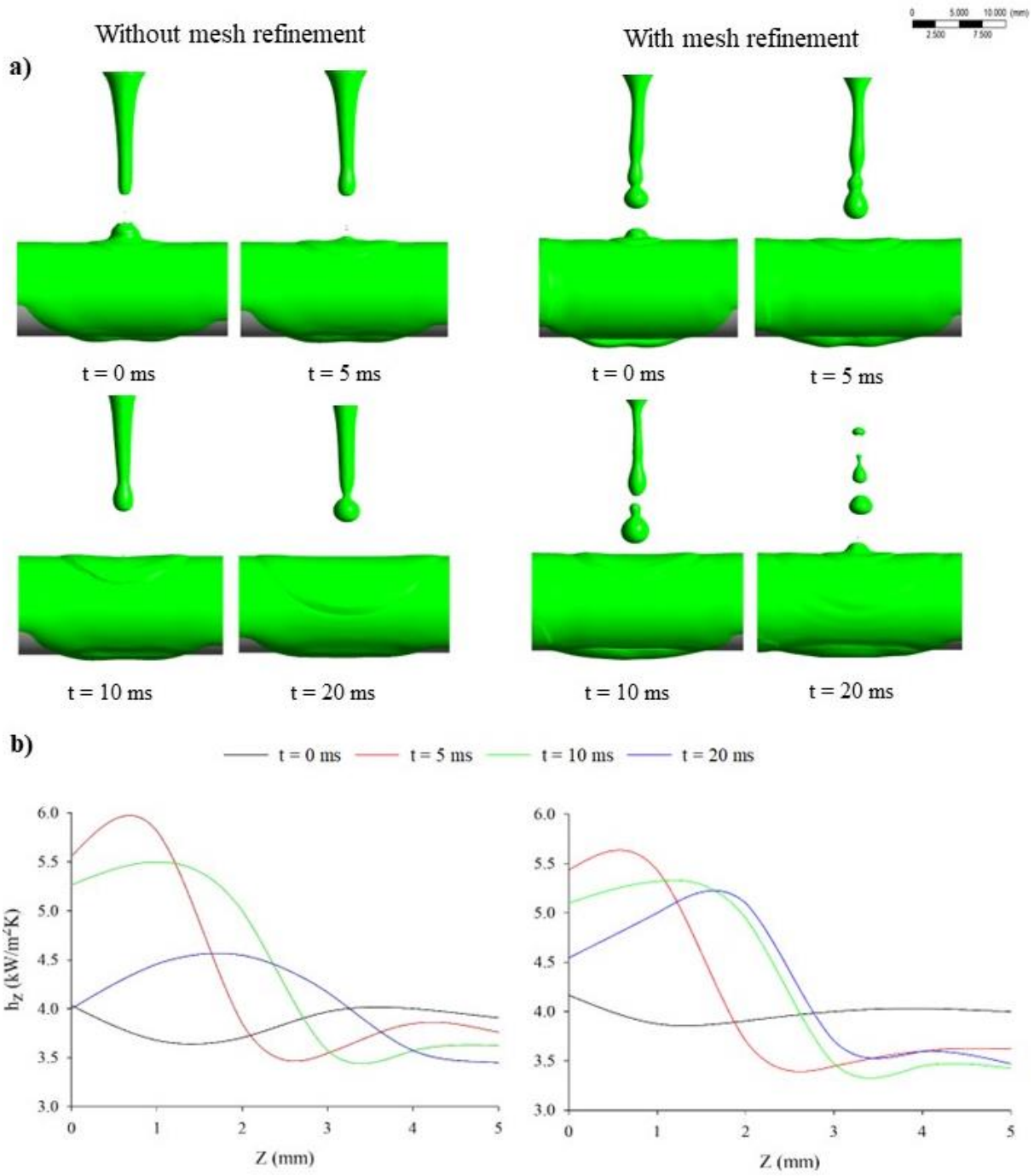

Figure 4.11. a) Jet instability behaviour with and without mesh refinement on the second tube just after satellite droplet impaction. b) Axial heat transfer coefficient within the liquid film where Z = 0 mm is taken from the centre of droplet impaction.

To explore the mechanism of the Rayleigh-Plateau instab–ility, **Figure 4.12** demonstrates the velocity contours of the jet just after the ligament breaks away from the leading droplet whilst **Figure 4.13** depicts the axial velocity and pressure variation within the liquid jet.

In **Figure 4.12a**/**Figure 4.13a**, the tip of the liquid jet contracts away from the droplet as the interfacial tension force starts to overcome the viscous forces. As doing so, capillary waves begin to generate at the apex of the formulating satellite droplet. As a consequence, the axial pressure gradient begins to fluctuate around the droplet and decrease towards the bulk region of the jet according to the Young-Laplace equation:[32,33]

$$\Delta p = \frac{2\gamma_{lv}}{r_j} \tag{4.24}$$

where r_j is the radius of the jet (m). The capillary waves then start to propagate parallel to the direction of recoil (caused by capillary tension) in the form of a harmonic sinusoidal wave (**Figure 4.12b**) and disperses its kinetic energy. Subsequently, the axial velocity falls and inversely increases the amplitude of the pressure gradient along the necked region of the jet but then suddenly increases once reaching towards the undisturbed region of the jet (**Figure 4.12b**). Due to the harmonic oscillations subsided from the capillary wave, the interface of the jet is perturbated. As a result, the interfacial surface tension starts to become unbalanced and takes the harmonic form of the generated capillary wave. Notably, more subsequent satellite droplets form from the unstable jet as the capillary waves further travel up the jet as displayed in **Figure 4.12c/Figure 4.13c**. The formation of these droplets is due to the change in the sinusoidal Laplace pressure gradient along its local maxima and minima points, which create regions of convex and concave curvatures along the jet. These observations coincide well with previously reported results for axial pressure variations.[34] Interestingly, the axial velocity starts to increase in magnitude near towards the necked regions of the jet. This is due to the amplitude of the capillary wave being high, which causes the surface tension force (along the convex regions) to become dominant over the concave regions.[35] Therefore, the axial velocity of capillary waves is dependent upon the its' wavelength.[34] This can be shown in **Figure 4.13c** onwards where the

wavelength appears to be longer within the bulk region of the jet with also having a smaller amplitude.

In **Figure 4.12d/Figure 4.13d** and beyond, the satellite droplets begin to detach from the liquid filament as the jet starts to become thinner due to capillary tension which pulls the jet towards the tube. Therefore, the diameter of the jet starts to decline which further increases the Rayleigh instability as the capillary wavelength can surpass the lowered jet diameter.

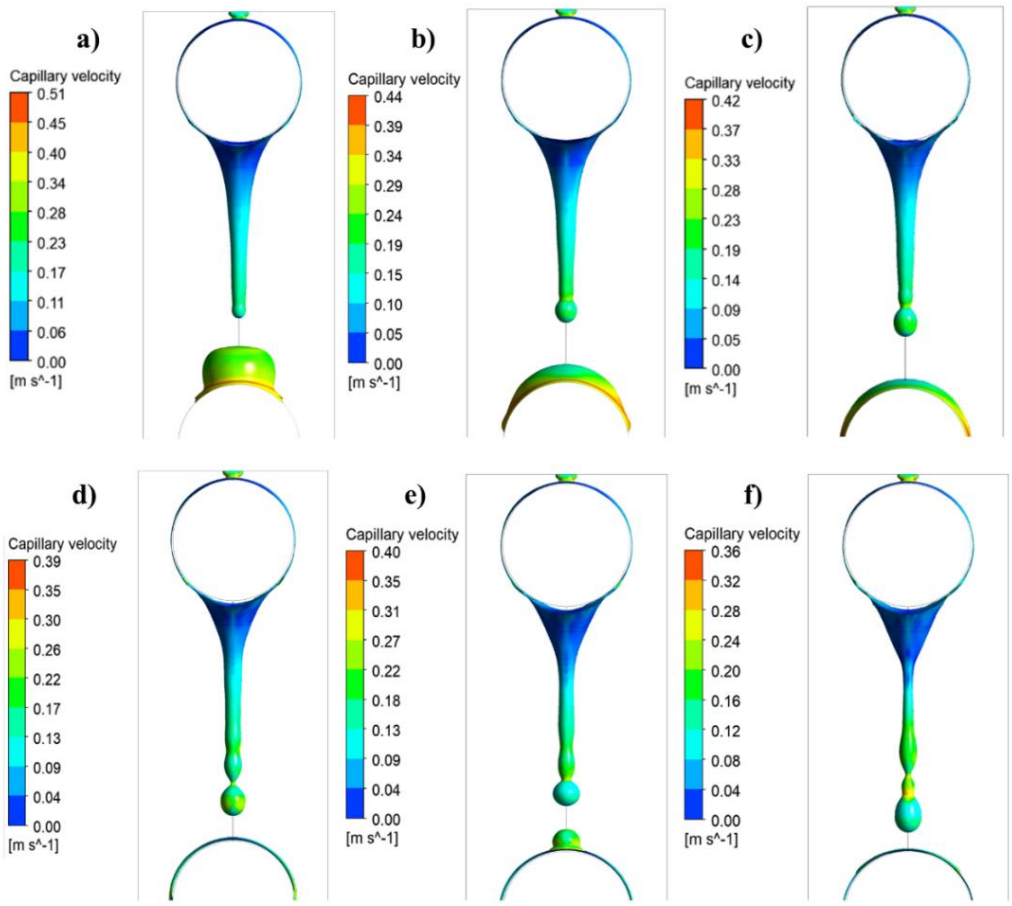

Figure 4.12. Velocity contours of first droplet impaction onto second tube following on to Rayleigh-Plateau instability.

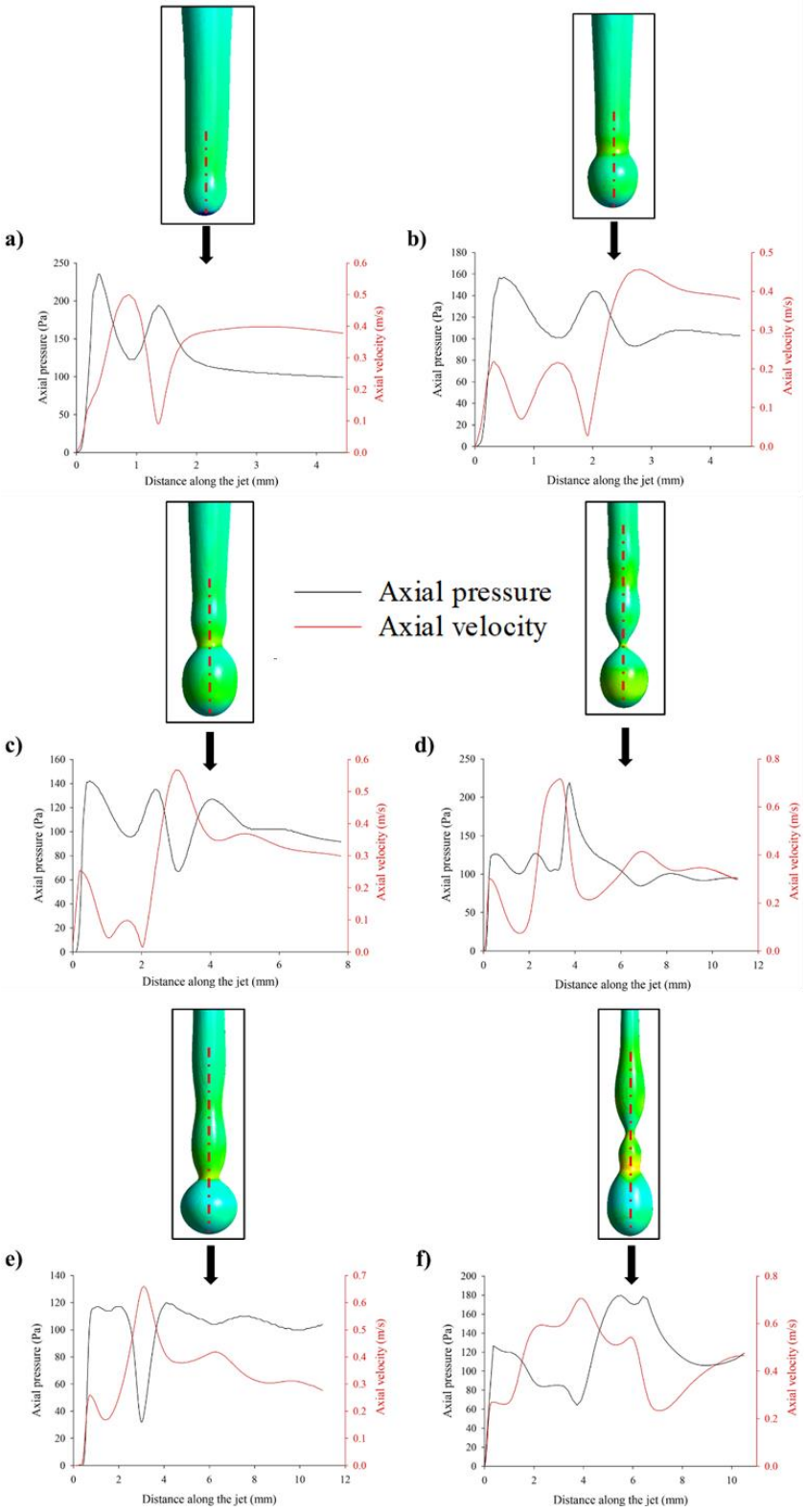

Figure 4.13. Axial velocity and pressure fluctuations within the central region of the unstable jet over time.

4.3.3 Falling-Film Flow Behaviour at Different Contact Angles

To briefly describe the flow behaviour on a completely wetted tube (contact angle of 0°), as shown in **Figure A.1a**, when exiting out of the inlet feeder, the liquid spreads rapidly to form a thin film around the entity of the tube. Due to the inertia force provided by the feeder and gravitational force acting in the direction of the flow, the liquid is accelerated towards the bottom of the tube where a droplet begins to nucleate. Once the hydrostatic pressure (gravitational force) is able to overcome the surface tension, the droplet departs and impacts the second tube where it also fully wets the surface. The same can be found on the third tube as well. Noticeably, just after 0.8 s, the droplet nucleation site has slightly shifted towards the left. This is mainly due to the Taylor wavelength instability where the amplitude of the wavelength changes as the liquid jet is recoiled back to the tube. The recoil velocity directly affects the interfacial surface tension forces, which alters the growth rate of the wave amplitude hence increasing the instability of the droplet formation site.[8,36,37]

For a tube contact angle of 30° the falling-film mode illustrates a dropwise flow (shown in **Figure A.1b**) by resolving the Rayleigh instability. This is shown from the small successive satellite droplets that form from the liquid jet as the jet recoils back to the tube after droplet impaction (seen at $t \geq 0.4$ s). In comparison to the work by Ding *et al*., the flow shows a laminar liquid jet throughout with no sign of jet instability or satellite droplets.[18] Notably, the spreading of the liquid along the first tube is substantially smaller than that of a tube with a contact angle of zero degree. It forms a circumferential ring around the centre of the tube where its axial thickness near the top of the tube is larger than the bottom (shown from $t \geq 0.2$ s). The reason is due to the reduced surface adhesion force the fluid experiences which causes the inertia, surface tension and gravitational force experienced by the feeder to become highly dominant. This prevents the liquid from

spreading more axially than circumferentially as the surface tension force is able to overcome the viscous force at a smaller axial distance. The point where the liquid no longer spreads axially on the tube is where the surface tension and viscous forces balance. This effect is particularly evident at larger contact angles. Since the surface tension force withdraws the liquid towards the centre of the tube, the film thickness starts to increase, which creates a rise in the hydrostatic pressure hence increasing the film flow rate.

As the fluid flows in the circumferential direction, a droplet swiftly forms and starts to depart from the tube at t = 0.2 s. Since the surface adhesion force is reduced, the gravitational force is able to overwhelm the surface tension at a smaller magnitude therefore increasing the droplet departure rate. The same can be found on the tubes beneath where the spreading area of the liquid has decreased causing the liquid to rapidly be removed off the surface whilst still being in dropwise mode (for the second and third tube). The formation of the sequential satellite droplets that impact the film is what causes the flow to be dropwise since the film thickness is unable to reach a steady state value, hence, increasing film instability.[11] At a contact angle of 60° (**Figure A.1c**), the flow is primarily in a dropwise/jet flow state due to the increased surface tension force and the Rayleigh instability capture as explained previously.

These observations are valid up to a critical contact angle of 90° where the flow no longer exhibits a falling-film manner as seen in **Figure A.1d**. At this point, the surface tension force has become so prevalent that the liquid film breaks into two droplets (formed on either side of the tube) before reaching the bottom of the tube when $t \geq 0.16$ s. The droplets then start to detach towards the bottom of the tube with a thin liquid film still being attached onto the tube. As the droplets wet the tubes beneath, macroscopic droplets are formed on the surface with some being restored to a hemispherical shape. This indicates that the adhesion force of the surface has minimised to the point where the surface tension

force is beginning to overcome the inertia force generated from droplet impact. Nevertheless, at even larger contact angles from 120 to 150°, (**Figure A.1e-f**) droplets no longer impact the tubes beneath but roll off the first tube and escape the fluid domain. Due to the amply reduced surface adhesion force, the tangential component of the gravitational force and surface tension force have become large enough to cause the droplet to depart from the tube at a relatively small circumferential angle.[38]

In the early stages of film formation (when t = 0.08 s), as the contact angle of the tubes increase, the film thickness along the circumferential direction begins to thicken. This is because the amplified surface tension force pulls the liquid towards the feeder. By 0.1 s, for a contact angle of 150°, the droplet has already detached itself from the liquid film and has begun to leave the tube. At 0.12 s, the droplet has completely left the tube and the fluid domain leaving the tube completely bare as doing so. This flow behaviour described simply repeats itself every 0.12 s. Notably at the same time for 120°, a droplet is formed and is separated from the film. When t = 0.4 s, the film has mostly covered the entirety of the first tube for contact angles of 0, 30 and 60°. Clearly at this stage, the film thickness is shown to rise between 0 and 60° (**Figure 4.14**), which has been explained earlier.

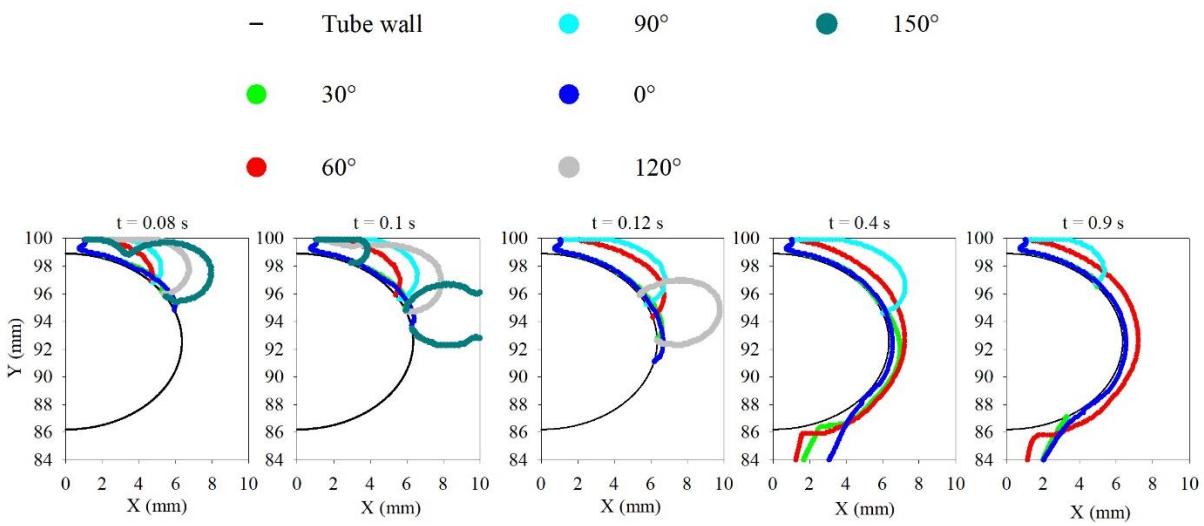

Figure 4.14. Contour plots of the flow behaviour around the first tube at multiple contact angles.

Particularly at 60°, the film has already separated itself from the second tube whereas for 30°, the film is just beginning to expand along the tube. At 0°, the film is still developing to initiate droplet nucleation. The film flow for 0° ultimately starts to catch to the other contact angles when t = 0.6 s where the droplet has already impacted the second tube and the jet has been broken into small satellite droplets. Remarkably, at t = 0.9s for a contact angle of 30°, the film in the circumferential direction splits in the middle and is divided axially. However, the flow behaviour still remains dropwise. Finally, when t = 2 s the final state of the flow pattern is revealed for each contact angle in **Figure 4.15**. For 0°, the flow remains dropwise. At 30° and 60° the flow pattern indicates a consistent dropwise and dropwise/jet flow up to 2 s. As for 90°, the flow does not follow a falling-film behaviour, and there are just continuous droplets that mitigate off the tubes. The same is applicable for 120° and 150°, although the droplets do not interact with the tubes beneath as stated before.

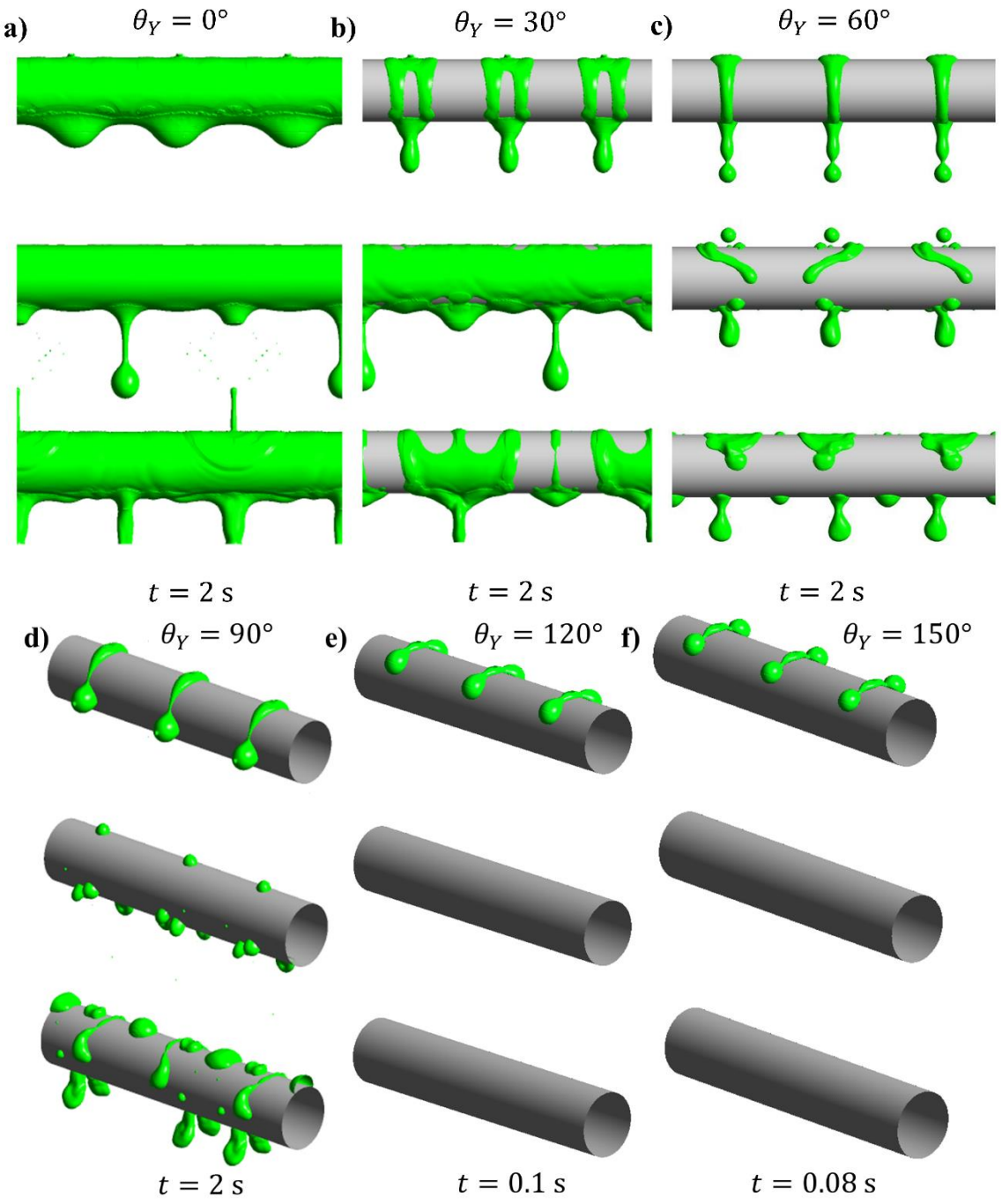

Figure 4.15. Hydrodynamic flow of liquid falling over the configurated pipes at different static contact angle states namely (a) 0°, (b) 30°, (c) 60°, (d) 90°, (e) 120° and (f) 150°.

Figure 4.16 illustrates the velocity vector plot of the fluid flow within the liquid at different contact angles when t = 0.08 s. Initially, for contact angles of 0° and 30°, the velocity is relatively large at the necking region due to the reduction in the fluids' surface

area. However, within the bulk region, the velocity of flow is reduced from the effects of increased surface adhesion. At larger contact angles, the velocity at the inlet region appears to be approximately the same as the prescribed velocity inlet since the interface of the fluid is undisturbed. Nevertheless, due to the growth in the circumferential film thickness between the contact angles, the velocity gradient of the fluid begins to increase. Most of the fluid is retained in the circumferential direction rather than the axial direction causing an increase of the inertial force, although, at a contact angle of 150°, the velocity begins to increase again due to the reduced surface area, which causes the droplet to be swiftly removed off the tube in comparison to lower contact angles.

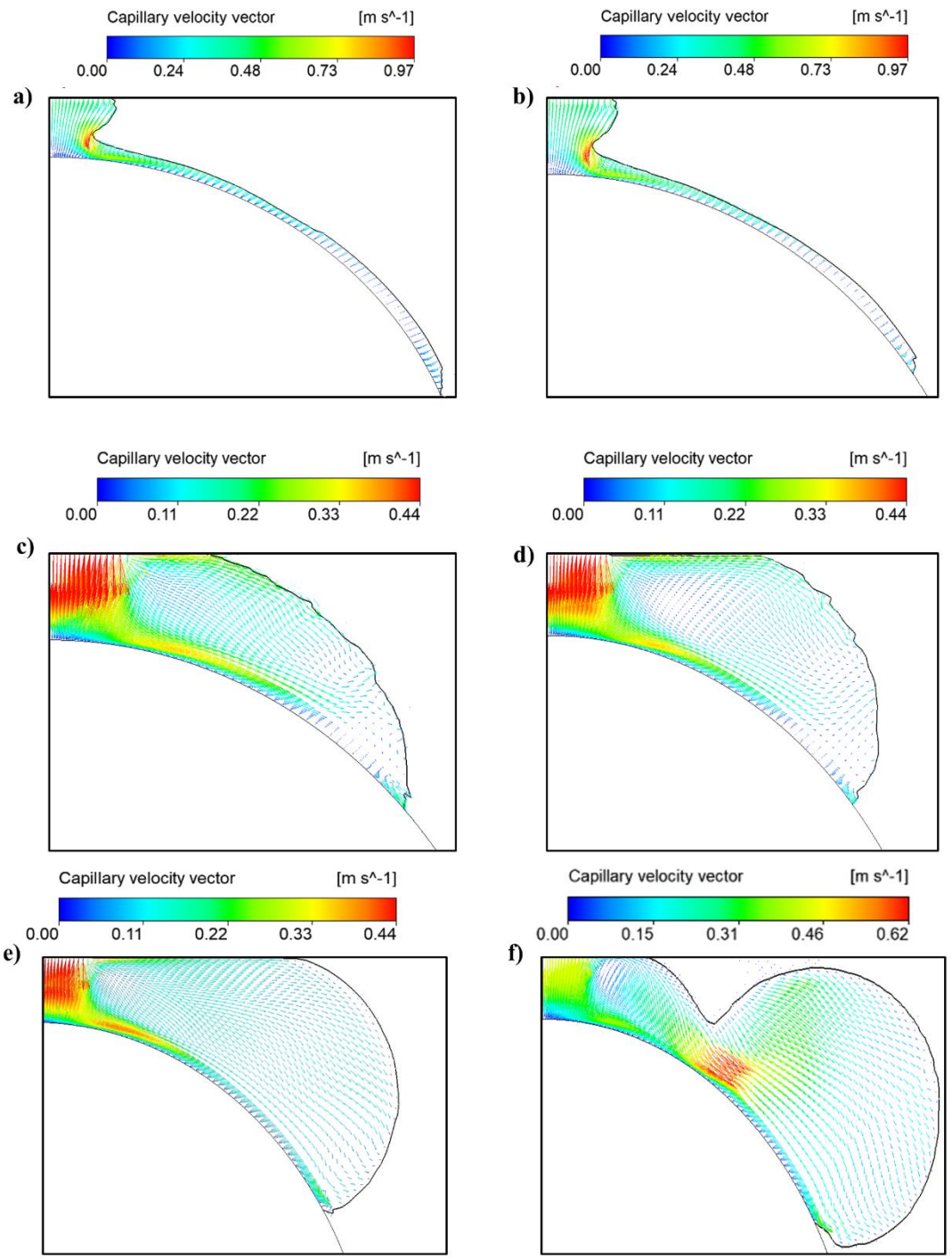

Figure 4.16. Velocity vector plot of the fluid exiting the inlet in the circumferential direction at different contact angles when t = 0.08 s. (a) 0° (b) 30° (c) 60° (d) 90° (e) 120° (f) 150°.

4.4. Conclusion

Numerical simulations capturing the Rayleigh-Plateau instability of liquid jets have been performed in this work by refining the mesh where the liquid jet is propelled. The fluid dynamics of the flow has been successfully verified against previously published experimental results on the first and second tubes alongside the axial and circumferential capillary waves. Additionally, the film thickness, velocity profiles, average and local heat transfer coefficients across the first tube was reasonably calibrated against numerical solutions. A suitably resolved Rayleigh-Plateau instability has also been verified against previous results for axial pressure variations within an unstable liquid jet. Furthermore, the hydrodynamics of the flow pattern at different contact angles have been investigated and scrutinized. The following aspects of this investigation are summarised as follows:

- Increasing the Rayleigh instability capture causes more satellite droplets to form towards the expected amount seen in experimental results as the jet recoils back to the tube. This further increases the number of capillary waves seen on the impacted tube as each individual droplet increases the film waviness and instability. As a result, the local heat transfer coefficient is also increased due to the sudden reduction in film thickness. The enhanced film instability causes the film to be abruptly removed off the tube, affecting droplet departure rates and droplet nucleation.

- Axial pressure capillary wave variations within the liquid jet displays a sinusoidal profile during jet contraction. This is what causes the Rayleigh-Plateau instability to occur, due to increased Laplace pressure gradient inflicted by the restored surface tension force. The points of minima and maxima inflexion seen on the axial pressure profile indicates the necking regions of the liquid jet which eventually

forms satellite droplets. The change in the axial velocity is associated with the variation in the capillary wavelength along the jet.

- Increasing the contact angle of the tubes causes the film thickness along the circumferential direction to promptly rise with the axial film thickness being substantially smaller. It should be noted that, only contact angles of 0°, 30° and 60° lead to a falling-film flow. For the contact angle of 90°, the flow shows no falling-film effects but constant removal of macroscopic droplets that impacted the tube beneath. At even higher contact angles up to a superhydrophobic state, the formulated droplets simply rolled off the fluid domain.

- For a contact angle of 30° and 60°, by introducing the Rayleigh instability capture, the falling film pattern has constantly remained to be in a dropwise and dropwise/jet state throughout the 2 seconds.

Future studies on falling films should extend the analyses under real industrial environments such as the effect of laminar or turbulent vapour flow orthogonal to the pipes. Multiple adjacent tube banks could be simulated for highly hydrophobic tubes (more than 120°) as the droplets that depart off the tube could interact with adjacent tubes beneath or on the first tube. Most importantly, the Rayleigh-Plateau instability should be carefully considered in relation to falling films, since this phenomenon will determine whether the flow pattern is either jet or dropwise/jet as examined here which will have implications on the wetting phenomena of the tubes beneath. Additionally, this will affect the heat and mass transfer characteristics of the tube as the enhanced film waviness promoted from the numerous satellite droplets will increase the rate of convection and mass transfer within the film. Likewise, this allows numerical flow patterns to be directly compared against experimental observations for different tube contact angles.

4.5. References

1. D. Popov, K. Fikiin, B. Stankov, G. Alvarez, M. Youbi-Idrissi, A. Damas, J. Evans, T. Brown, Cryogenic heat exchangers for process cooling and renewable energy storage: A review, Appl. Therm. Eng. 153 (2019) 275-290.
2. A. Stärk, K. Krömer, K. Loisel, K. Odiot, S. Nied, H. Glade, Impact of tube surface properties on crystallization fouling in falling film evaporators for seawater desalination, Heat Transf. Eng. 38 (2017) 762-774.
3. A. Austegard, M. Bandopadhyay, S. W. Løvseth, A. Brunsvold, Flow pattern transitions in and hysteresis effects of falling film flow over horizontal tubes related to LNG heat exchangers, Energy Procedia 64 (2015) 23-32.
4. Y. Zhang, M. T. Munir, I. Udugama, W. Yu, B. R. Young, Modelling of a milk powder falling film evaporator for predicting process trends and comparison of energy consumption, J. Food Eng. 225 (2018) 26-33.
5. I. Kyung, K. E. Herold, Y. T. Kang, Model for absorption of water vapor into aqueous LiBr flowing over a horizontal smooth tube, Int. J. Refrig. 30 (2007) 591-600.
6. Y.Zheng, X.Ma, Y. Liu, R. Jiang, K. Wang, Z. Lan, Q. Liang, Experimental study of falling film evaporation heat transfer on superhydrophilic horizontal-tubes at low spray density, Appl. Therm. Eng. 111 (2017) 1548-1556.
7. X. Hu, A. M. Jacobi, The intertube falling film: Part 1—Flow characteristics, mode transitions, and hysteresis, Trans. Am. Soc. Mech. Eng. J. Heat Transfer. 118 (1996) 616-625.
8. J.D. Killion, S. Garimella, Gravity-driven flow of liquid films and droplets in horizontal tube banks, Int. J. Refrig. 26 (2003) 516-526.

9. J. Eggers, E. Villermaux, Physics of liquid jets, Rep. Prog. Phys. 71 (2008) 036601.

10. S. D. Hoath, Fundamentals of Inkjet Printing: The Science of Inkjet and Droplets, JWS (2016).

11. W. van Hoeve, S. Gekle, J. H. Snoeijer, M. Versluis, M. P. Brenner, D. Lohse, Breakup of diminutive Rayleigh jets, Phys. Fluids 22 (2010) 122003.

12. F. Gallaire, P. T. Brun, Fluid dynamic instabilities: theory and application to pattern forming in complex media, Philos. Trans. R. Soc. London, Ser. A 375 (2017) 20160155.

13. L. Rayleigh, On the capillary phenomena of jets, Proc. R. Soc. London 29 (1879) 71-97.

14. K. Graessel, C. Bächer, S. Gekle, Rayleigh–Plateau instability of anisotropic interfaces. Part 1. An analytical and numerical study of fluid interfaces, J. Fluid Mech. 910 (2021)

15. R. Mead-Hunter, A. J. King, B. J. Mullins, Plateau Rayleigh instability simulation, Langmuir 28 (2012) 6731-6735.

16. G. H. McKinley, Dimensionless groups for understanding free surface flows of complex fluids, (2005) 1-8.

17. S. S. Deshpande, L. Anumolu, M. F. Trujillo, Evaluating the performance of the two-phase flow solver interFoam, Comput. Sci. Discov. 5 (2012) 014016.

18. H. Ding, P. Xie, D. Ingham, L. Ma, M. Pourkashanian, Flow behaviour of drop and jet modes of a laminar falling film on horizontal tubes, Int. J. Heat Mass Transfer 124 (2018) 929-942.

19. J. Shinjo, A. Umemura, Simulation of liquid jet primary breakup: Dynamics of ligament and droplet formation, Int. J. Multiphase Flow 36 (2010) 513-532.

20. S. M. Hosseinnia, M. Naghashzadegan, R. Kouhikamali, CFD simulation of water vapor absorption in laminar falling film solution of water-LiBr — Drop and jet modes, Appl. Therm. Eng. 115 (2017) 860-873.

21. D. Bonn, J. Eggers, J. Indekeu, J. Meunier, E. Rolley, Wetting and spreading, Rev. Mod. Phys. 81 (2009) 740-793.

22. B. Köroğlu, K. S. Lee, C. Park, Nano/micro-scale surface modifications using copper oxidation for enhancement of surface wetting and falling-film heat transfer, Int. J. Heat Mass Transfer 62 (2013) 794-804.

23. R. Armbruster, J. Mitrovic, Heat transfer in falling film on a horizontal tube, Trans. Am. Soc. Mech. Eng. (1995) 13-21.

24. A. Karmakar, S. Acharya, Numerical simulation of falling film sensible heat transfer over round horizontal tubes, Int. J. Heat Mass Transfer 190 (2022) 122727.

25. D. L. Youngs, Numerical methods for fluid dynamics, AP (1982).

26. R. B. Bird, W. E. Stewart, E. N. Lightfoot, Transport phenomena, JWS (2006).

27. J. Rogers, Laminar falling film flow and heat transfer characteristics on horizontal tubes, Can. J. Chem. Eng. 59 (1981) 213-222.

28. S. Inada, Y. Miyasaka, R. Izumi, A study on the laminar-flow heat transfer between a two-dimensional water jet and a flat surface with constant heat flux, Bull. JSME 24 (1981) 1803-1810.

29. V. Patnaik, H. Perez-Blanco, A study of absorption enhancement by wavy film flows, Int. J. Heat Fluid Flow 17 (1996) 71-77.

30. S. Jayanti, G. Hewitt, Hydrodynamics and heat transfer of wavy thin film flow, Int. J. Heat Mass Transfer 40 (1996) 179-190.

31. I. Mudawar, R. A. Houpt, Measurement of mass and momentum transport in wavy-laminar falling liquid films, Int. J. Heat Mass Transfer 36 (1993) 4151-4162.

32. J. Pellicer, V. Garcia-Morales, M. Hernandez, On the demonstration of the Young-Laplace equation in introductory physics courses, Phys. Educ. 35 (2000) 126.

33. B. E. Rapp, Microfluidics: Modelling, Mechanics and Mathematics, Elsevier (2017).

34. A. Umemura, Self-destabilizing mechanism of a laminar inviscid liquid jet issuing from a circular nozzle, Phys. Rev. E 83 (2011) 046307.

35. A. Karmakar, S. Acharya, Numerical simulation of falling film flow hydrodynamics over round horizontal tubes, Int. J. Heat Mass Transfer 173 (2021) 121175.

36. R. Bellman, R. H. Pennington, Effects of surface tension and viscosity on Taylor instability, Q. Appl. Math. 12 (1954) 151-162.

37. N. El-Ansary, G. Hoshoudy, A. Abd-Elrady, A. Ayyad, Effects of surface tension and rotation on the Rayleigh–Taylor instability, Phys. Chem. Chem. Phys. 4 (2002) 1464-1470.

38. F. Tahir, A. Mabrouk, M. Koc, Review on CFD analysis of horizontal falling film evaporators in multi effect desalination plants, Desalin. Water Treat 166 (2019) 296-320.

Chapter 5

Droplet Impact on Doubly Re-entrant Structures

Navdeep Sangeet Singh[1], Thanaphun Jitniyom[1], Miguel Navarro-Cía[1,2], Nan Gao[,1]*

[1]School of Engineering, University of Birmingham, Birmingham, B15 2TT, United Kingdom

[2]School of Physics and Astronomy, University of Birmingham, Birmingham, B15 2TT, United Kingdom

This chapter was published in the journal of Scientific Reports, (Singh, N. S., Jitniyom, T., Navarro-Cía, M. & Gao, N. Droplet impact on doubly re-entrant structures. Scientific Reports 14, 2700 (2024).).

Author Contributions: N.S.S. and N.G. formulated the research idea. N.S.S. computed, visualized and assessed the numerical simulations alongside analysing the experimental data. T.J. 3D-printed the doubly re-entrant pillars. M.N.-C. supported the 3D printing process. T.J. and N.G. performed the droplet impact experiments. N.S.S. drafted the manuscript. N.G. guided the manuscript preparation. All authors reviewed and approved the manuscript.

Abstract

Doubly re-entrant pillars have been demonstrated to possess superior static and dynamic liquid repellency against highly wettable liquids compared to straight or re-entrant pillars. Nevertheless, there has been little insight into how the key structural parameters of doubly re-entrant pillars influence the hydrodynamics of impacting droplets. In this work, numerical simulations and experimental studies were carried out to portray the fundamental physical phenomena that can explain the alteration of the surface wettability from adjusting the design parameters of the doubly re-entrant pillars. On the one hand, three-dimensional multiphase flow simulations of droplet impact were conducted to probe the predominance of the overhang structure in dynamic liquid repellency. On the other hand, the numerical results of droplet impact behaviours are agreed by the experimental results for different pitch sizes and contact angles. Furthermore, the dimensions of the doubly re-entrant pillars, including the height, diameter, overhang length and overhang thickness, were altered to establish their effect on droplet repellency. These findings present the opportunity for manipulations of droplet behaviours by means of improving the critical dimensional parameters of doubly re-entrant structures.

5.1. Introduction

Liquid repellent surfaces can be used to improve many industrial applications or processes. These include self-cleaning coatings,[1,2] drag reduction,[3,4] anti-icing surfaces,[5,6] enhancement of boiling,[7,8] and condensation.[9,10] In practice, liquid repellent surfaces can be realised by chemically modifying micro-structured substrates, such as those consisting of pillars, with low-surface-energy coatings. Conventional pillars are typically straight, that is, having a vertical sidewall perpendicular to the interface. However, the liquid repellence of regular pillars is largely limited to superhydrophobicity.

Tuteja *et al*. fabricated re-entrant structures by introducing a horizontal overhang structure on top of the straight pillars parallel to the interface.[11] This allowed the surface to become omniphobic, where the surface can repel both high- and low-surface-tension liquids. Liu *et al*. then further made doubly re-entrant structures by adding an additional vertical overhang to the re-entrant structure.[12] As a result, the structures were able to resist fluorinated solvents, including perfluorohexane (C_6F_{14}) that has a low surface tension value of 10 mN/m.

The concept behind the superior liquid repellency of the doubly re-entrant structure is related to manipulating the interfacial surface tension forces to be perpendicular against the direction of droplet penetration or impact. In other words, the vertical overhang provides a maximal suspension force compared to re-entrant or straight pillars,[12] suspending the liquid from wicking further into the cavities. Nonetheless, a sufficiently small solid fraction (~ 6%) is required to maintain superomniphobicty against the wetting liquids and large external pressures.[12] However, there have been many variants of the doubly re-entrant design. For example, Yun *et al.* created hierarchical surfaces where doubly re-entrant pillars were applied on a micro-wrinkled surface,[13] inspired by the inherent surface topography of springtail cuticles.[14] It was noted that the presence of the doubly re-entrant pillars on top made the surface resistant to elevated external pressure, enabling the repellency of much faster liquid droplets with low surface tension, with the Weber number (*We*) up to 287.

Sun *et al.* 3D printed hierarchical doubly re-entrant pillars consisting of multiple layers of doubly re-entrant overhangs.[15] The notion behind the design was to create additional pressure barriers, in order to prevent the droplet from further penetrating the cavity. This was accomplished by increasing the diameter of the overhangs along the length of the pillar, which consequently reduced the pitch of the cavity at each layer. The overall

breakthrough pressure was reported to be much higher than single layered doubly re-entrant structures as the hierarchical surface was able to repel water droplets at Weber numbers that were larger than 25. Here, the breakthrough pressure is defined as the maximum suspension pressure generated by the liquid surface tension that is acting around the perimeter of the pillars across the liquid-gas interface.[12,16,17] For the pillars to suspend the liquid, this maximum pressure must be greater than or equal to the downward directed dynamic pressures.

In addition, Liu *et al.* utilised triply re-entrant structures by allocating an additional horizontal overhang to the vertical one of the doubly re-entrant structure.[18] However, the additional overhang structures did not improve the droplet repellency (contact angle hysteresis) over the previously reported doubly re-entrant structures. On the other hand, surfaces consisting of isolated doubly re-entrant cavities have been reported to obtain more robust liquid repellency than those consisting of doubly re-entrant pillars in various scenarios, including droplet impact.[19,20] However, as the solid fractions of these cavities are higher than those of doubly re-entrant pillars, the apparent contact angle is reduced, causing the surface to partially lose their superhydrophobicity. Particularly, the contact angle hysteresis of doubly re-entrant cavities can be greater than 30°, significantly higher than that of doubly re-entrant pillars.[19,20] This is because some of the liquid will be trapped within the cavities as the liquid recedes, especially during capillary condensation.

It should also be noted that, while doubly re-entrant structures have been demonstrated to be superior, there is still a lack of quantitative investigations into the effect of the design parameters on the liquid repellency of the surface. Numerical simulations can provide such insight by depicting the principal hydrodynamic aspects that are involved during droplet impact, although there are limited successful studies related to numerical simulations of droplet impact on doubly re-entrant structures. In fact, most numerical

studies examine droplet impact on plain or macro-scale surfaces.[21-24] Recently, a study by Hu *et al.* simulated droplet impact on straight superhydrophobic micro-structured pillars.[25] Their investigation included a parametric analysis of droplet impact behaviours as a function of droplet velocities, intrinsic contact angles and pillar heights, noting whether the droplet rebounded or flooded the surface. A numerical study by Panter *et al.* conducted a parametric analysis of re-entrant and doubly re-entrant structures against various breakthrough pressures.[26] However, the relevant numerical model did not include droplet repellency.

Here, the numerical study of droplet impact is further extended towards doubly re-entrant pillars in which, the simulations are compared against experimental results to investigate the fundamental phenomena. It is observed that the behaviours of the impacting droplet can be manipulated by altering the dimension and pitch of the doubly re-entrant pillars. Further, hydrophobizing the pillars enables the droplet to bounce off the surface at a faster rate. Nonetheless, once the impacting pressure exceeds the breakthrough pressure, the droplet will flood the interstices of the doubly re-entrant pillars regardless of being hydrophobized. This leads to further questions of how the design parameters of the doubly re-entrant pillars, including the length and thickness of the vertical overhang, can be optimised in order to prevent the meniscus from touching the bottom of the surface. Through analysing the interfacial pressure and velocity contours plots, the regions of significance are illustrated that play an important role in droplet repellency.

5.2. Methodology

5.2.1 Setup of Fluid Domain and Boundary Conditions

The arrangement of the fluid domain and boundary conditions is configurated as shown in **Figure 5.1a** and **b**. A water droplet is initially placed at the XYZ axis containing a liquid volume fraction (α_l) of one with a diameter of 0.8-1.2 mm (λ_c) (**Figure 5.1a**). This is followed by an initial velocity condition applied on the droplet parallel to the direction of gravity which corresponds to a We = 1.25-1.7. As only a quarter of the simulation domain is used, a symmetry boundary condition is applied at YZ and XY planes where the droplet is placed. This particular setup is used to save computational resources, such as the number of mesh elements and computation time, as the flow is considered to be symmetric. Furthermore, a pressure-outlet condition is applied at the faces opposite to the position of the droplet to allow the liquid to escape either when it is spreading or bouncing. To simulate the ambient environment, the operating pressure chosen is equal to the atmospheric pressure (given as 101325 Pa). A wall boundary condition is applied at the pillars, having an intrinsic contact angle of 70°, 105° and 120°, with a no-slip condition (V_w = 0 m/s). For millimetric sized drops, the slip velocity at the liquid-solid interface is deemed to be insignificant. The dimensions of the fluid domain (i.e. width, length and height) are dependent on the diameter of the droplet (**Figure 5.1b**). This is to allow proper visualization of droplet impact behaviour as the liquid spreads, and rebounds towards the positive y-direction.

The properties of water employed in the simulation are isothermal (at ambient temperature), as previously stated in Chapter 4.2 (thermal conductivity and specific heat capacity are excluded here). Additionally, the dimensional parameters to be configured for the pillars are displayed in **Figure 5.1c**. The intrinsic contact angles used for each case

are listed in Appendix B (Chapter 1, **Table B.2**). In order to compare the numerical simulations against the experimental results, the intrinsic contact angles are set to match the values (70° before being hydrophobized and 120° after being hydrophobized) of the photoresin which was used to fabricate the pillars via laser lithography. More information on the contact angle measurements can be seen in Appendix B (Chapter 1, **Table B.2**). **Figure 5.1d** and **e** display the SEM (Scanning Electron Microscopy) images of the fabricated doubly re-entrant pillars and their cross section revealing the overhang structure. Details of fabrication can be seen within the Appendix B (Chapter 6). It is important to note that if the breakthrough pressure of the surface is greater than the total impacting pressure of the droplet, the droplet will be cushioned on a thin layer of air and emanate capillary waves instead of contacting the bottom of the cavity.[27-29] For functional surfaces having a composite interface, this air layer is present within the composite structure (**Figure 5.1f**).[5] With low Weber numbers, the air layer on a planar surface is considered to be incompressible. This is based upon the gas compressibility factor, ε, which must be much greater than one to ensure incompressibility:[28,30]

$$\varepsilon = \frac{P_a}{\sqrt[3]{R_d {\mu_v}^{-1} {\rho_l}^4 V^7}} \tag{5.1}$$

where P_a is the ambient pressure of the air (Pa) and R_d is the radius of the droplet (m). In our case, the gas compressibility factor was calculated to be more than 40, which suggests the flow remain incompressible in the absence of any micro-pillars. Nonetheless, the air within the vicinity of the pillars' cavities may become more compressible as air is trapped underneath the droplet.

Additionally, to prevent the hydrostatic force (i.e. the weight of the droplet) altering the hydrodynamics during impaction, the droplet diameter must be lower than the capillary length of the selected liquid. From the given fluid properties at ambient temperature, the

capillary length for water is calculated as 2.7 mm as determined previously. Therefore, based on the calculated capillary length, the droplet diameter chosen for this study will not be influenced by gravitational forces. Details of the governing equations used for the simulations and mesh refinement techniques are included in Appendix B (Chapter 1 and Chapter 3).

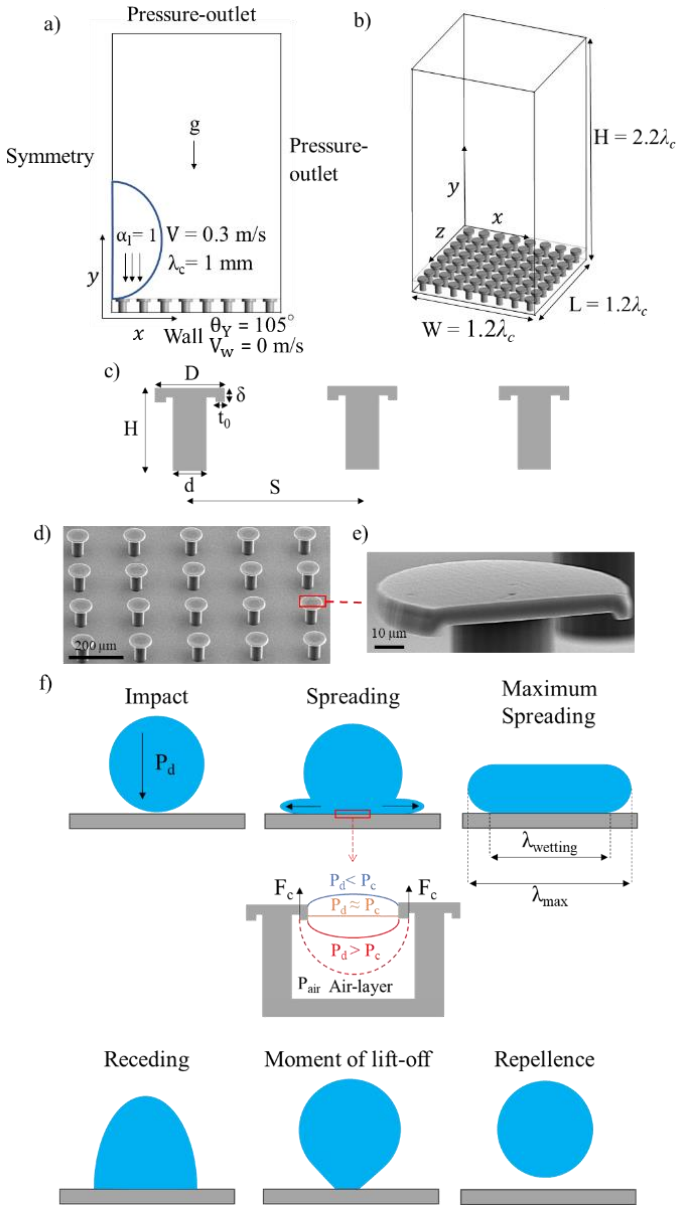

Figure 5.1. Fluid domain design with prescribed boundary and initial conditions: (a) side view and (b) iso view. (c) Key dimensions for doubly re-entrant pillars. (d) SEM image of the fabricated doubly re-entrant pillars, with D=100 µm, H=100 µm, S=200 µm, t_o=10 µm and δ=10 µm. (e) Cross-sectional image of the doubly re-entrant pillar. (f) Schematic illustration of the droplet impact process, where P_d is the total droplet impact pressure (Pa), F_c and P_c are the capillary force (N) and pressure (Pa) (see Appendix B, Chapter 5 for more details), P_{air} is the air pressure within the air-layer (Pa), λ_{max} and $\lambda_{wetting}$ are the maximum spreading diameter and wetting diameter of the droplet (m).

5.3. Results and Discussion

5.3.1 Numerical Validation against Experimental Results.

Figure 5.2 demonstrates the comparison between simulation and experimental results of droplet impact on doubly re-entrant pillars having a pitch spacing of 150 µm. The numerical results tend to agree very well with the experimental results regarding droplet spreading and repulsion at their respective timeframes. Initially, for the uncoated surface (**Figure 5.2a**), the doubly re-entrant pillars manage to sustain the droplet due to the breakthrough pressure (P_c) being greater than the total impacting pressure (P_d) (1-5 ms). As the droplet attempts to recoil away from the pillars (7 ms), the droplet is instead pinned at the interface. This is primarily due to the hydrophilic nature of the uncoated photoresin, which prevents the generated capillary force to overcome the interfacial adhesion force. However, for the hydrophobized pillars (**Figure 5.2b**), the interfacial adhesion force is greatly reduced, which allows the droplet to spread and retract on top of the pillars. The droplet eventually bounces off the surface (7.5-9.5 ms) instead of being pinned.

Increasing the pitch further to 200 µm increased droplet repellency as shown in **Figure 5.3**. This is illustrated by the reduced contact area and increased stretching of the droplet as it attempts to withdraw from the uncoated doubly re-entrant surface at 8.3 ms. Although the droplet remains pinned at the surface (seen at 14 ms), it reaches a reduced contact area, eventually, in comparison with the surface that has a 150-µm pitch. From **Figure 5.3b**, hydrophobizing the pillars shows similar results to **Figure 5.2b**, although in this case the droplet manages to bounce off the surface at an earlier time period (7-7.8 ms). The main difference is shown by the convex meniscus at the overhang which further bulges into the cavity (seen at various timeframes) since the breakthrough pressure is reduced due to the increase in pitch size (see Appendix B, Chapter 5 for further details). From a kinetic point

of view, increasing the pitch of the pillars reduces the interfacial adhesion force as the liquid-gas fractional area increases and the solid-liquid fractional area decreases. Nonetheless, up to a certain extent, the decline in the breakthrough pressure will inevitably reduce the droplet repellency of the surface as the amount of air pressure allowed to escape through the cavities will become dominant over the reduction in adhesion force. Therefore, a balance between the capillary and adhesion force can establish an optimal pitch value for droplet repellency. Indeed, the reduced droplet repellency performance at an even larger pitch size of 250 μm is highlighted in **Figure 5.4** where the droplets flood the interstices of the surfaces regardless of being hydrophobized. **Figure 5.4a** shows that the droplet spreads whilst flooding the interstices. There is a negligible lift-off (6 ms), showing that the capillary force (F_c) is insufficient to stop the liquid from penetrating the cavities. With the hydrophobized pillars in **Figure 5.4b**, the droplet is instead confined within a smaller area of pillars where it fails to either spread or bounce off the surface. It should be noted that for the Weber numbers used for droplet impact, most of the droplets either stuck onto the pillars or flooded the cavities unless they were hydrophobized. This is attributed to the relatively large fraction of the solid area of the pillared surface (on the order of 20-50%). Here, the solid fraction (φ_s) is referred to as the ratio of the interfacial area to the projected area of a composite surface. For doubly re-entrant pillars, this is calculated as:[12,31]

$$\varphi_s = \frac{\pi D^2 + 4\pi D\delta}{4S^2} \tag{5.2}$$

The surface area of the vertical overhang is included to the interfacial area which is given as $\pi D\delta$ as seen above. The derivation of the equation can be seen in the Appendix B (Chapter 7).

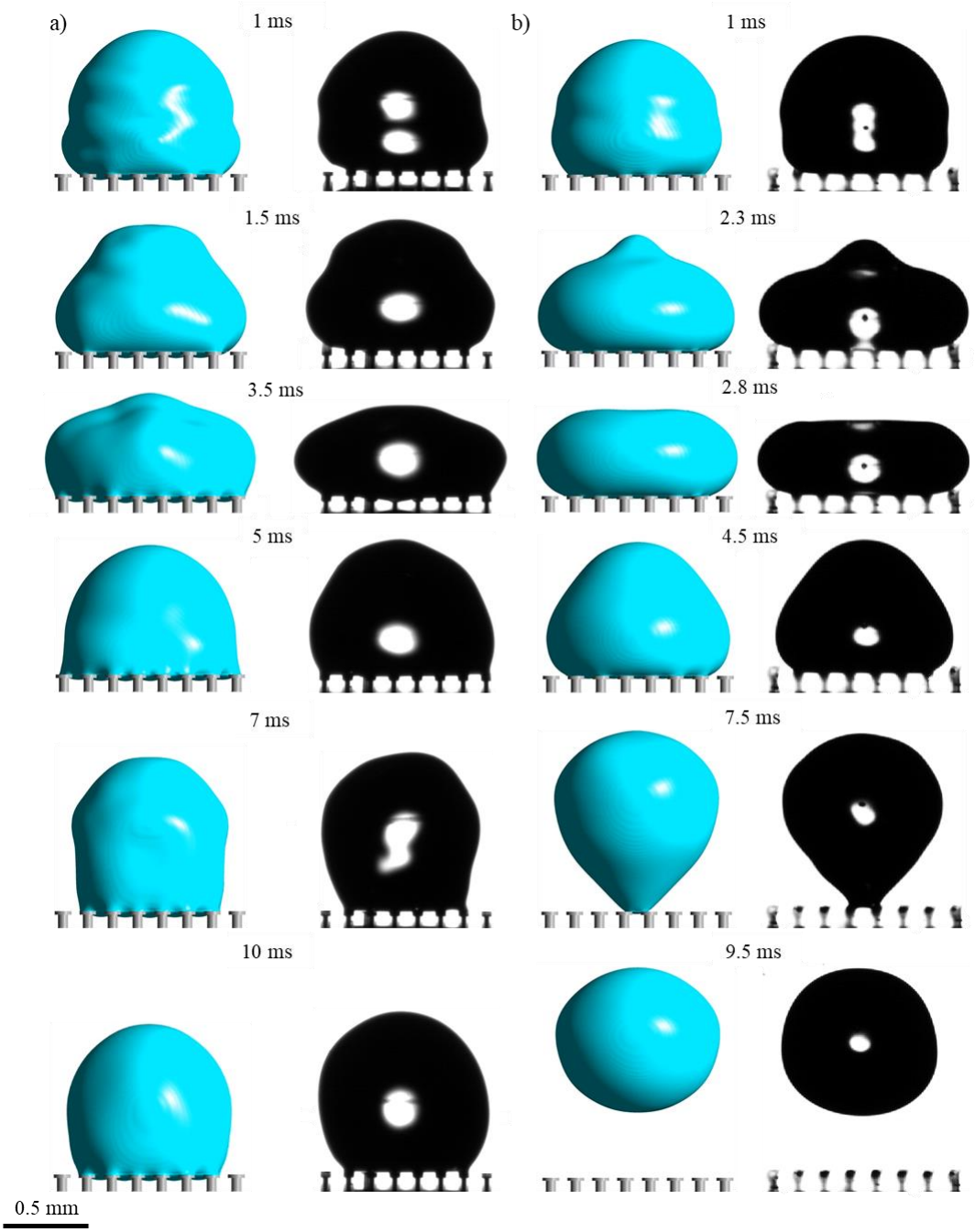

Figure 5.2. Comparison between numerical and experimental results of droplet impact at different time periods on doubly re-entrant pillars for the pitch size of 150 µm: (a) Pillars made of bare photoresin: V = 0.32 m/s, λ_c = 1.1 mm, We = 1.6; (b) pillars made of photoresin coated with Trichloro (1H,1H, 2H, 2H-perfluorooctyl) silane: V = 0.33 m/s, λ_c = 1 mm, We = 1.5.

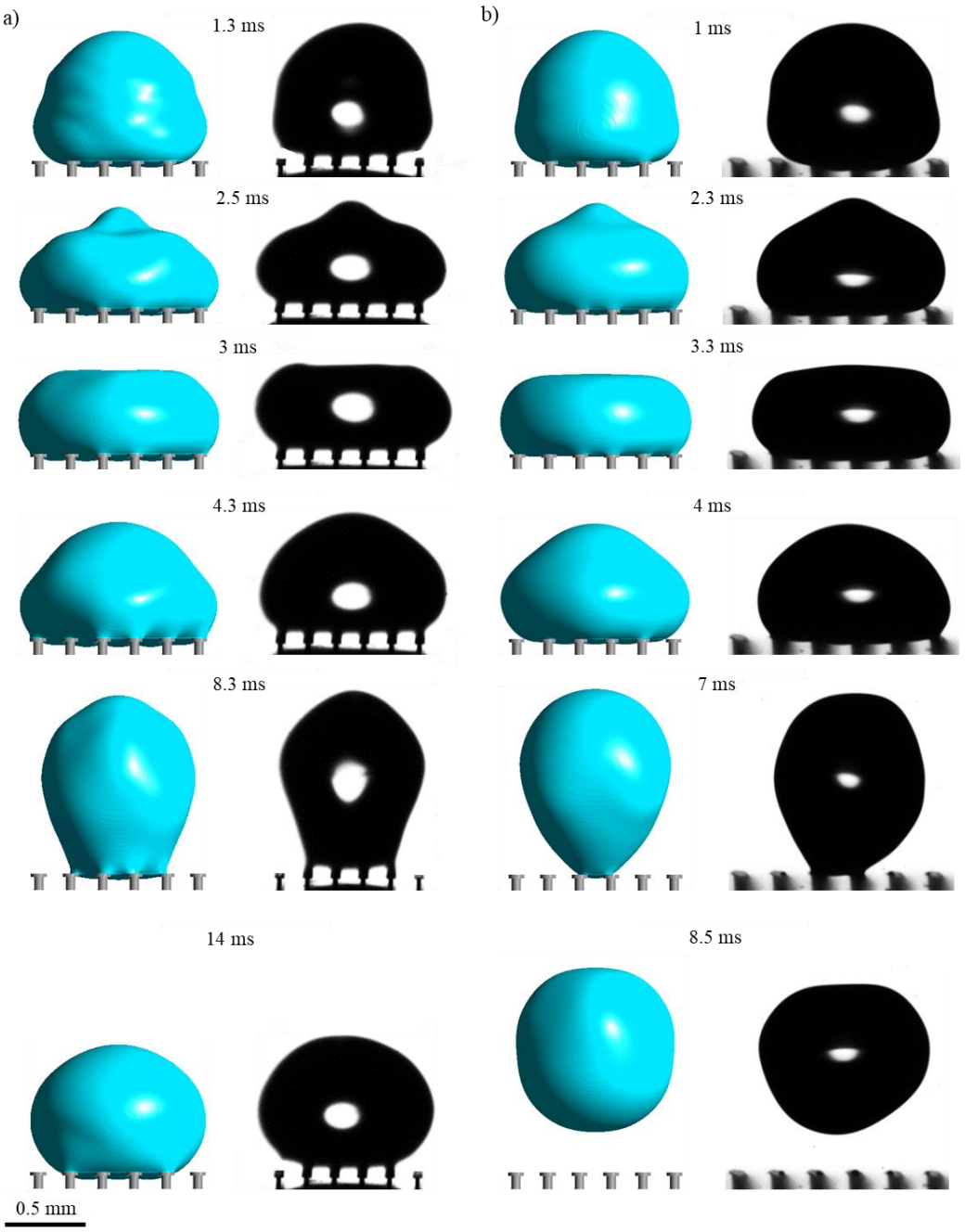

Figure 5.3. Comparison between numerical and experimental results of droplet impact on doubly re-entrant pillars at different time periods for the pitch size of 200 µm: (a) Pillars made of bare photoresin: V = 0.33 m/s, λ_c = 1.1 mm, We = 1.7; (b) Pillars made of photoresin coated with Trichloro (1H,1H, 2H, 2H-perfluorooctyl) silane: V = 0.34 m/s, λ_c = 0.8 mm, We = 1.3

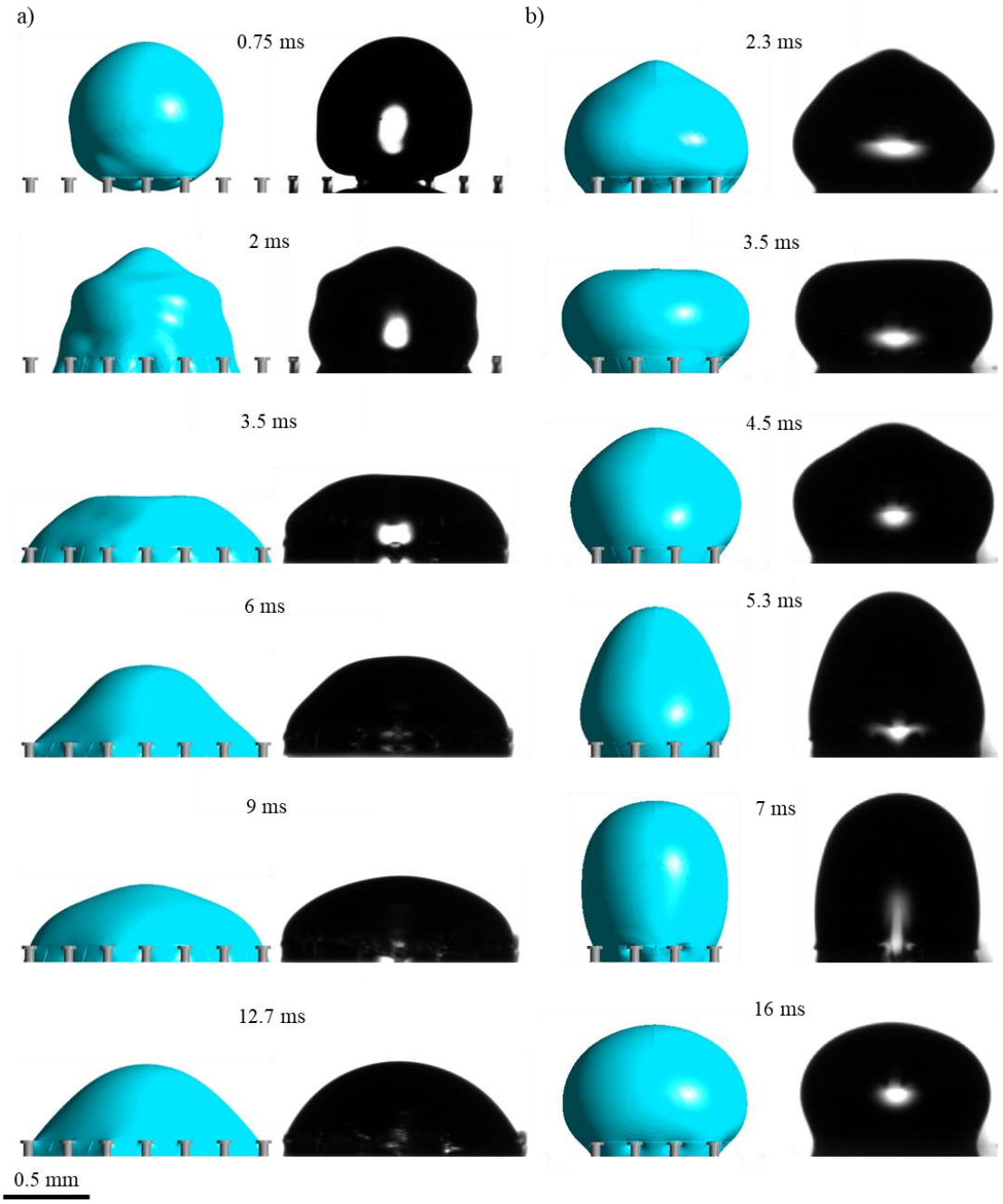

Figure 5.4. Comparison between numerical and experimental results of droplet impact on doubly re-entrant pillars at different time periods for the pitch size of 250 µm: (a) Pillars made of bare photoresin, V = 0.31 m/s, λ_c = 1.2 mm, We = 1.6; (b) Pillars made of photoresin coated with Trichloro (1H,1H, 2H, 2H-perfluorooctyl) silane, V = 0.32 m/s, λ_c = 1.1 mm, We = 1.6.

To quantify the experimental results, **Figure 5.5** displays the ratio of the maximum wetting diameter to the diameter of the droplet, $\lambda_{wetting}/\lambda_c$, against contact time, τ, for the processes of droplet impact corresponding to **Figure 5.2** to **Figure 5.4**. In general, the results further indicate good agreement between the numerical predictions and experimental results, especially for the immediate spreading regime upon impact. However, the experimentally obtained wetting diameter is shown to divert away from the numerically predicted wetting diameter in part of the retraction regime for droplets that have stayed in the Cassie state (suspended) while interacting with the pillars. This is attributed to the dissipation caused by the rupture of the thin film pinned at the top of the pillars while the contact line recedes.[32] The increase in the pitch size made this discrepancy more noticeable, because the rupture of the capillary bridge from each pillar becomes more influential when there is less solid-liquid contact area. To further note, for the two different pitch sizes of the doubly re-entrant pillars with the same intrinsic contact angles, the maximum ratios of the Cassie-state droplets are very similar, likely because of the inertia effect that has dominated the spreading regime, especially for relatively small intrinsic contact angles.[33] Specifically, the numerically predicted maximum ratios are 1.16 and 1.12, respectively, for the untreated pillars with the pitch sizes of 150 and 200 µm, as shown in **Figure 5.5a** and **b**. For the hydrophobized pillars with the pitch sizes of 150 and 200 µm, the numerically predicted ratios decrease to 0.95 and 1.09, respectively, as shown in **Figure 5.5d** and **e**. By contrast, for the Wenzel-state droplets, the liquid that penetrates inside the cavities influenced the droplet behaviours by preventing the liquid from further lateral motion. Nonetheless, increasing the intrinsic contact angle has allowed the ratio to be significantly reduced for both the spreading (from 1.51 to 0.97) and retraction stages, as shown in **Figure 5.5c** and **f**.

Other possible reasons for deviations between the comparison is due to the overhang not being perfectly straight (i.e. overhang angle ~ 90°) which can alter the net capillary force against the droplet. This is due to the difficulty in fabricating overhang structures through laser lithography since the 3D printer prints the geometry layer by layer. Thus, when printing the first layer of the overhang, the structure is thin and unstable which can easily be displaced by vibrations caused by stage movements and the microscope objective.[34] Moreover, inhomogeneities within the hydrophobic coating may result in an uneven coating layer across the pillars. This can potentially alter the advancement and recession of the contact line as the intrinsic contact angle will fluctuate within specific regions. In addition, the complexity of the geometry can also make it difficult to obtain a homogeneous coating through using chemical vapor deposition especially within the overhang structure. Details of the fabrication process is shown in Appendix B, Chapter 4.

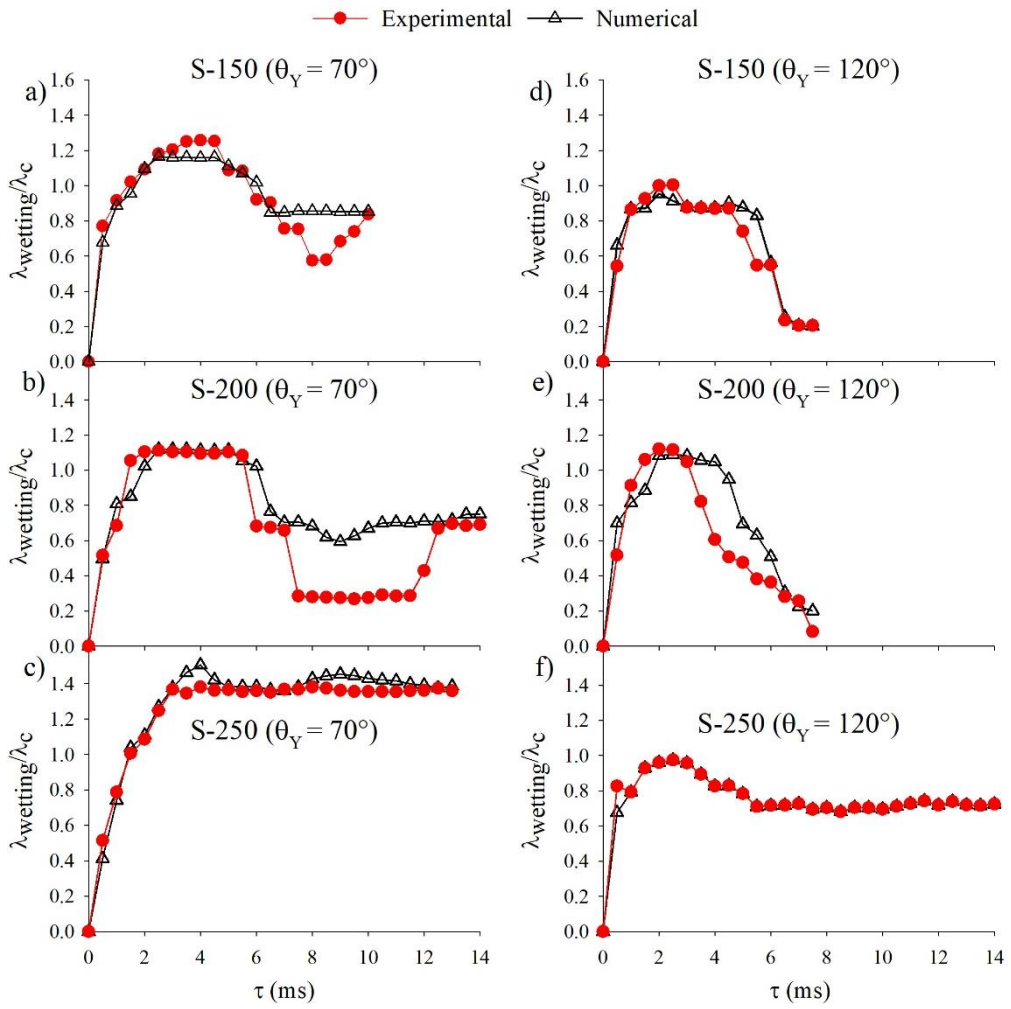

Figure 5.5. Numerical and experimental results of $\lambda_{wetting}/\lambda_c$ against contact time for different doubly re-entrant pitch sizes and intrinsic contact angles. a) S = 150 µm, θ_Y = 70°; b) S = 200 µm, θ_Y = 70°; c) S = 250 µm, θ_Y = 70°; d) S = 150 µm, θ_Y = 120°; e) S = 200 µm, θ_Y = 120°; f) S = 250 µm, θ_Y = 120°.

5.3.2 Droplet Repellency Performance Against Pillar Overhangs

As briefly discussed, applying a horizontal and vertical overhang upon micropillars directs the surface tension force of the liquid against the direction of impact. To quantify this, the interfacial pressure profile within the pillars is depicted (**Figure 5.6**). The interfacial pressure is the pressure experienced at the liquid-gas interface, which illustrates the pressure distribution of the air-layer confined within the cavities. Correspondingly, the

penetration depth is directly related to the interfacial pressure since the penetration depth increases as the air-layer thickness is reduced. Therefore, the maximum pressure experienced beneath the droplet has been reported to be inversely proportional to the square root of the minimum air-layer thickness observed.[30] Nonetheless, it is noted that this correlation is valid for a flat surface with a two-dimensional droplet striking the surface.[28,30] **Figure 5.6a** displays the droplet impact behaviour at various timesteps for straight and re-entrant pillars having an intrinsic contact angle of 70°. Immediately upon the impact (0.25 ms), the droplet penetrates into the cavities for straight pillars, whilst on the re-entrant pillars, the droplet remains pinned at the overhang. The reason for this penetration is associated with the increased interfacial pressure, as shown in **Figure 5.6b**. Here onwards, the droplet continues to spread within the straight pillars. As the droplet has fully flooded the interstice for straight pillars after 0.25 ms, the interfacial pressure cannot be depicted. By contrast, for re-entrant pillars, the overhang structure allows the surface tension force to act against the direction of motion. This occurs when the three-phase contact line advances and suspends itself towards the bottom of the surface. Therefore, the interfacial pressure is lessened, as shown in **Figure 5.6c** as the penetration depth is greatly reduced. The interfacial pressure profile continues to flatten and reduce as the droplet settles upon the re-entrant pillars (10 ms). Notably, the re-entrant pillars allow the droplet to recede.

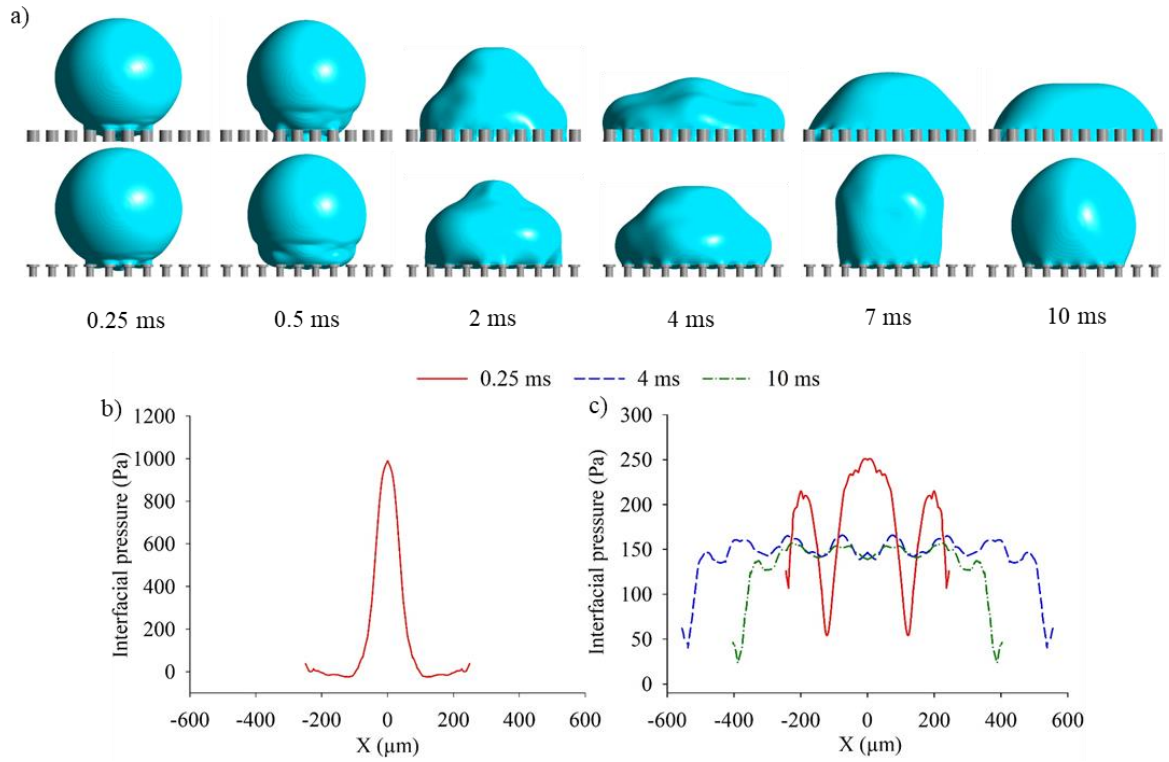

Figure 5.6. (a) Droplet impact behaviour at different timesteps on re-entrant and straight pillars having an intrinsic contact angle of $\theta_Y = 70°$. Interfacial pressure profiles within the cavities during droplet impact for straight pillars (b) and re-entrant pillars (c), $V = 0.3$ m/s, $\lambda_c = 1$ mm, $We = 1.25$.

5.3.3 Parametric Dimensional Analysis of Doubly Re-entrant Pillars Against Liquid-Repellency

To determine how the dimensional parameters of the pillars affect the droplet repellence of the surface, the diameter, height, overhang length and thickness are varied. **Figure 5.7** displays the droplet impact behaviours at various timeframes for different configurations of the doubly re-entrant pillars with the intrinsic contact angle of 105°. **Figure 5.8a** shows the interfacial pressure profiles. Increasing the diameter of the pillars from 100 to 200 μm causes the contact area of the droplet to increase before the droplet bounces (8 ms). This is primarily due to the increased adhesion force as the solid fraction of the surface becomes

greater with diameter. Nevertheless, at 10 ms, the droplet manages to bounce off the surface for both the diameters of 150 and 200 µm at a lower height compared to the diameter of 100 µm.

Further, as indicated by the contours, decreasing the height of the pillars from 100 to 50 µm increases droplet repellency as the droplet departs off the surface by 8 ms. This is attributed to the increased compression of the air layer as the meniscus protrudes closer to the bottom of the cavities. Nonetheless, decreasing the pillar height towards 30 µm causes the droplet to fully wet the cavities. A sufficient height of the pillars allows the meniscus to be away from the bottom of the surface. **Figure 5.8b** displays this phenomenon clearly: the air pressure (absolute value) rises as the droplet protrudes closer to the bottom of the surface between 0.25 and 0.5 ms, which increases the overall resistive force against the liquid-gas interface. After 0.5 ms, the increased capillary pressure generated from air compression causes the liquid-gas interface to be repelled away from the cavities, reducing the compression, as shown from the reduced air pressure difference. It is noted that a gap between the air-layer and liquid-gas interface exists as the diffusive zone between the liquid and gas phases (see Appendix B, Chapter 3 for further details). The same concept is observed from expanding the pitch of the pillars up to a critical value where the meniscus is stretched further downwards. Assuming the compression is adiabatic, the ideal gas law can also be used to describe the change in pressure of the air layer as the liquid-gas interface expands further into the cavities:[19,35]

$$P_{air} = P_a \left[\left(\frac{v_i}{v_{air}} \right)^{\kappa} - 1 \right] \tag{5.3}$$

where P_{air} is the air pressure within cavity after being compressed (Pa), v_i is the initial volume of air inside the cavity (m^3), v_{air} is the volume of air after compression (m^3). For adiabatic gas compression, κ is equal to 1.4. Hence, from decreasing the air volume after

compression, $\left(\frac{v_i}{v_{air}}\right) > 1$, the pressure of the air layer will rise, which deflects the liquid-gas interface away.

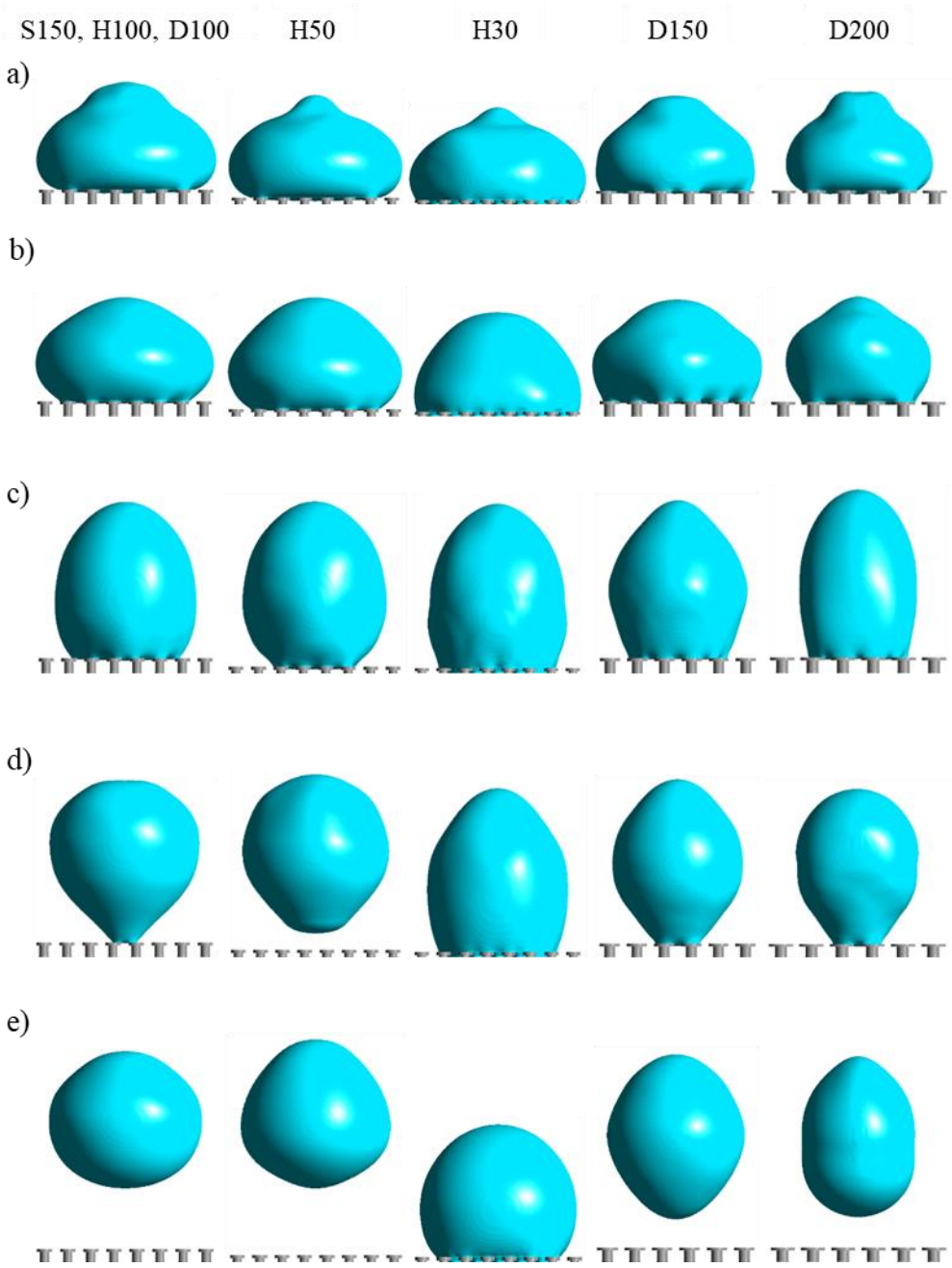

Figure 5.7. Droplet impact behaviours for various doubly re-entrant pillars with an intrinsic contact angle of θ_Y = 105° at (a) 2ms, (b) 4 ms, (c) 6 ms, (d) 8 ms and (e) 10 ms, V = 0.3 m/s, λ_c = 1 mm, We = 1.25.

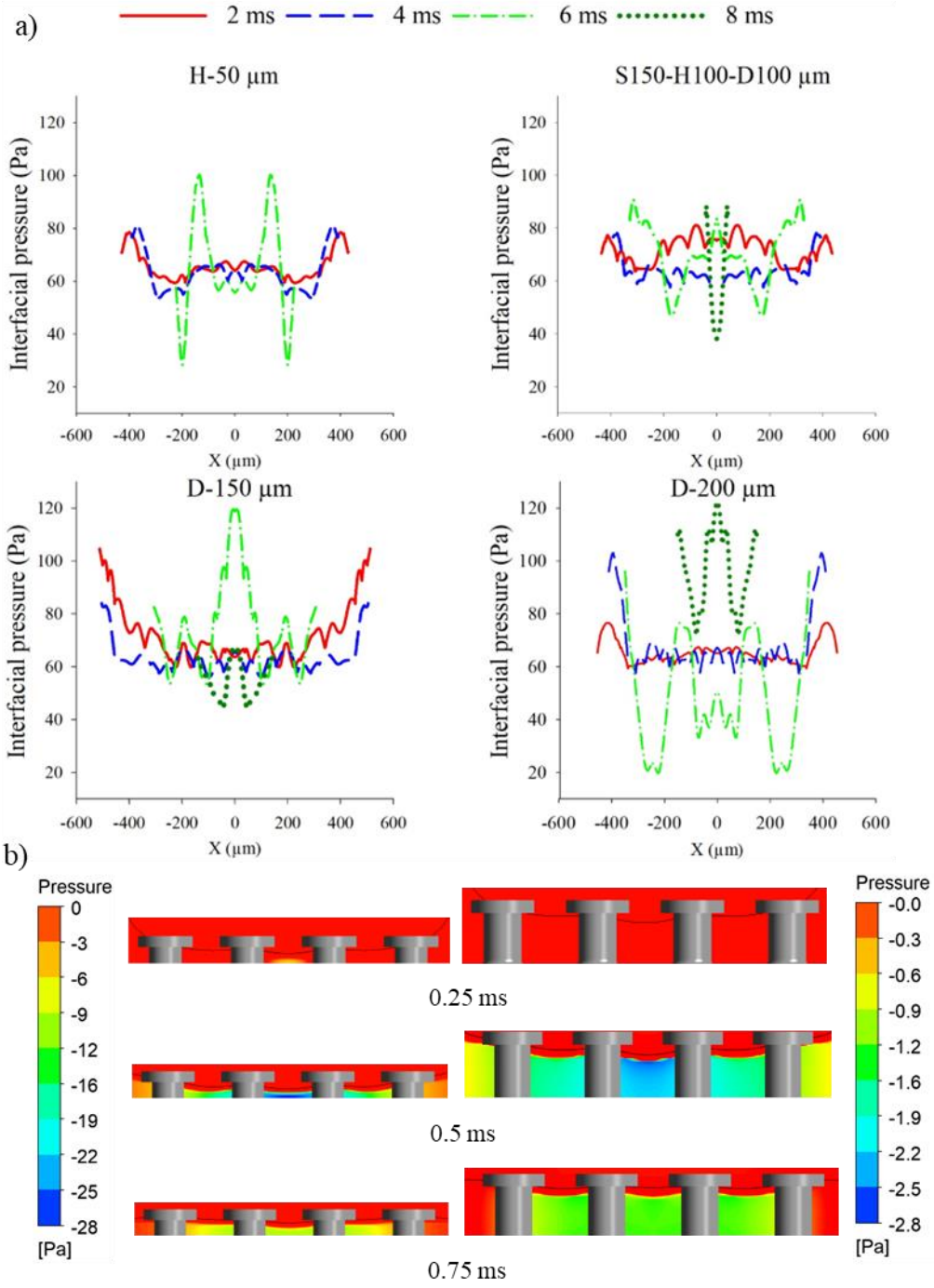

Figure 5.8. (a) Interfacial pressure profiles for each of the configured cases that are not flooded, (b) air pressure contours just after the moment of impact compared between the heights of 50 µm and 100 µm.

To explore the effects of the overhang length (δ) on the droplet repellency of the surface, **Figure 5.9** represents the velocity contours of the droplet at different time periods for the configured overhang lengths. Initially, as the droplet begins to recoil back (3 ms), the velocity is shown to be larger at the apex of the droplet for larger overhang lengths. At 8.25 ms, the droplet is still in contact with the pillars that have an overhang length of δ = 15 µm. By contrast, for the smaller overhang lengths of 10 µm and 5 µm, the droplets have already departed off the pillars. This is due to the increased projection of the meniscus at the centre of impact, which delays the onset of repellency. As shown in **Figure 5.1f**, for doubly re-entrant pillars, the liquid meniscus can be pinned at the bottom of the vertical overhang. Increasing the length of the overhang further will not only cause the meniscus to approach the bottom of the cavities, but also require more time for the receding liquid to detach from the pillars. Therefore, while the presence of the vertical overhang is essential for the pillars to suspend the wetting liquid, the length of the vertical overhang should be minimised to keep the solid fraction that can be contacted by the wetting liquid at bay.[12]

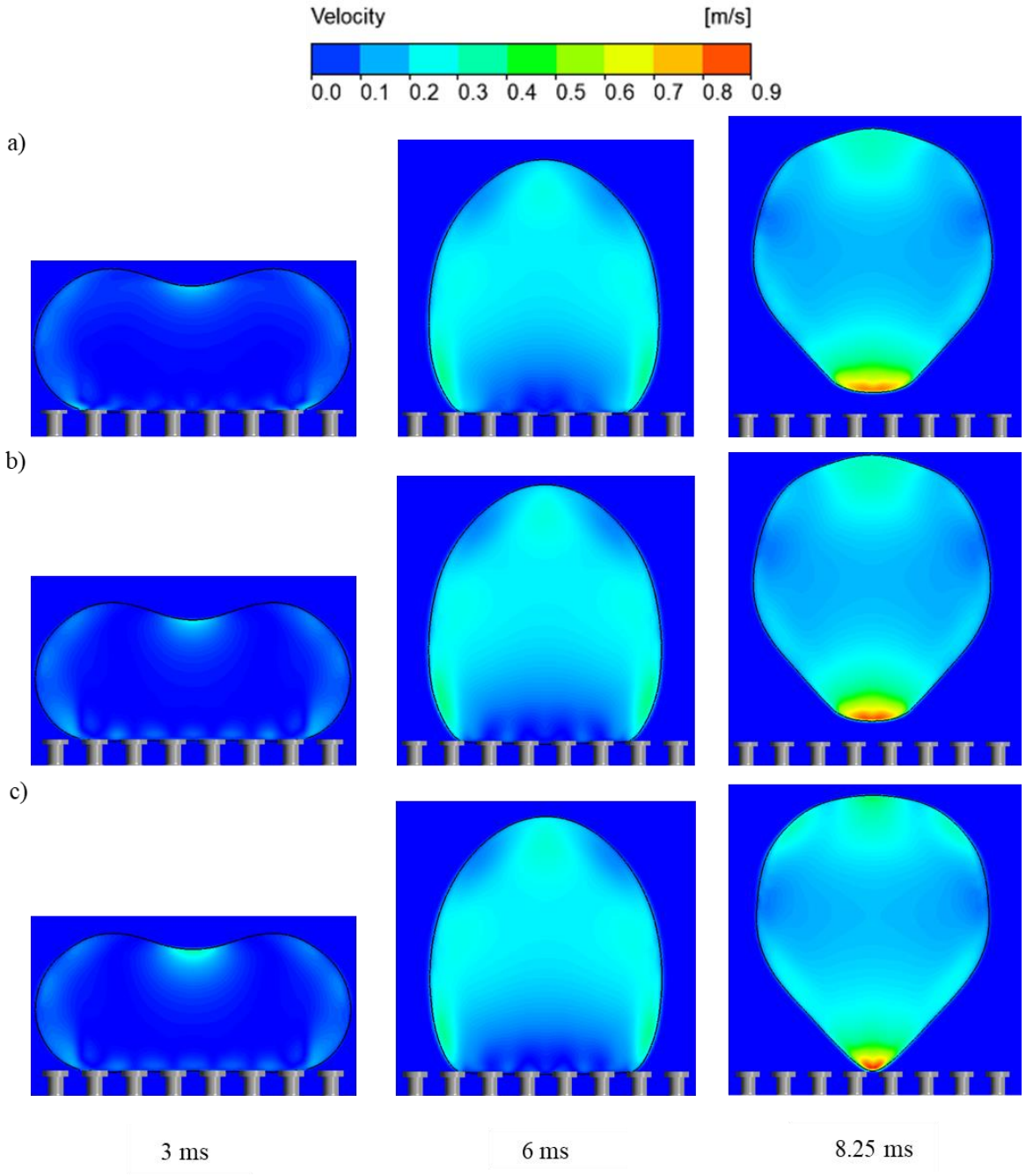

Figure 5.9. Velocity contours of droplet impacting doubly-re-entrant pillars at different time periods with different overhang lengths. (a) δ = 5 µm, (b) δ = 10 µm, (c) δ = 15 µm.

Figure 5.10 displays the pressure contours during droplet impact for various timesteps and overhang thicknesses. From decreasing the thickness (t_o) from 15 µm to 5 µm, the base of the droplet experiences an increase in capillary pressure that is demonstrated at 8 ms due to the reduction in the wetting diameter. The additional pressure experienced

against the droplet at lower overhang thickness can be predicted (Appendix B, Chapter 5, Equation B.7). Reducing the overhang thickness causes the diameter of the circular contact line at the bottom of the vertical overhang (D') to become nearly equal to diameter of the pillars ($D' \approx D$). Nevertheless, as indicated from the results, varying the thickness between 5 and 15 μm provides only a slight change in droplet repellency.

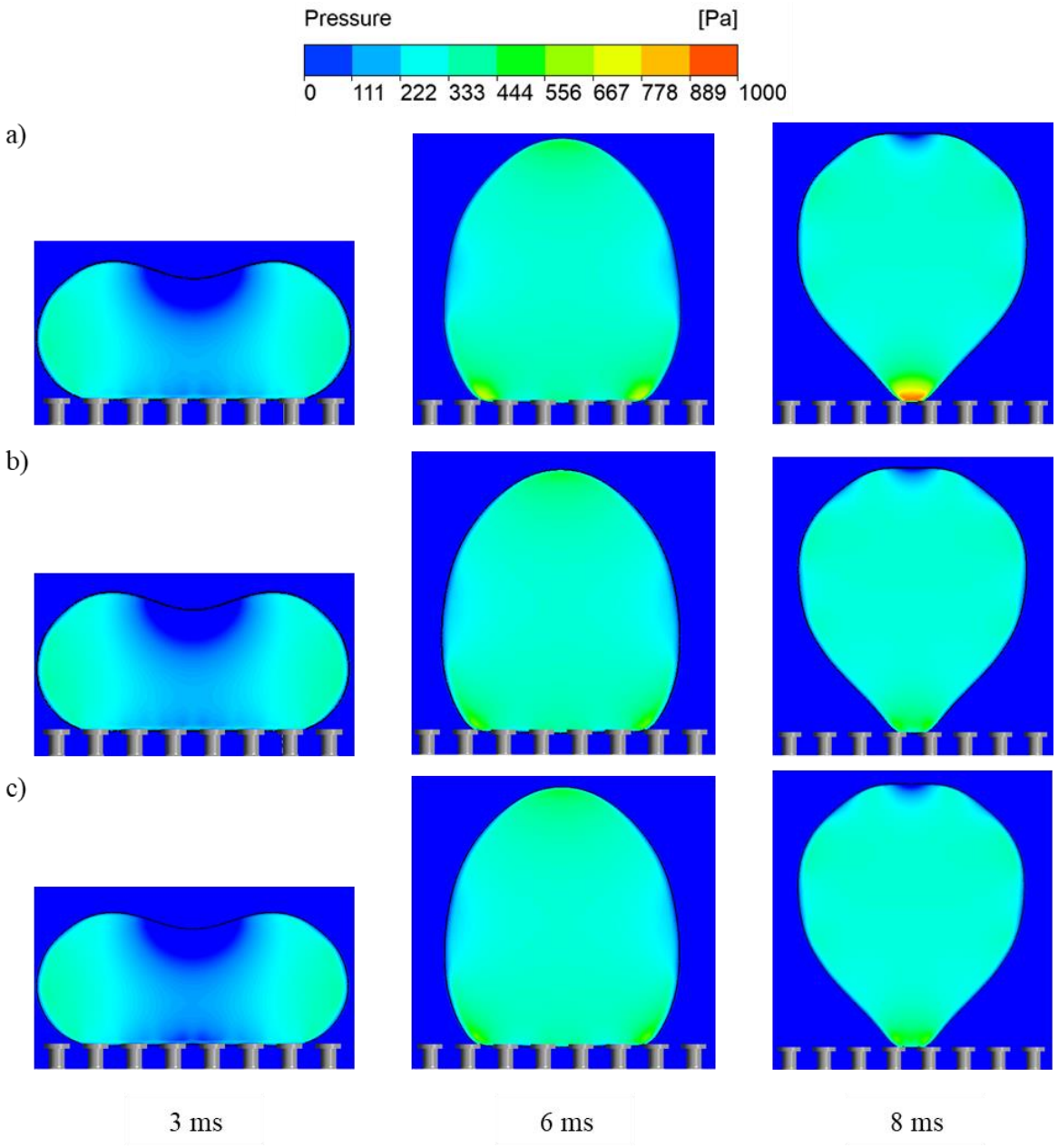

Figure 5.10. Pressure contours of impacting droplets on doubly re-entrant pillars at multiple time steps for various overhang thicknesses: (a) t_o = 5 µm, (b) t_o = 10 µm, (c) t_o = 15 µm.

Figure 5.11 demonstrates the ratio of the maximum wetting diameter to the diameter of the droplet, $\lambda_{wetting}/\lambda_c$, against contact time for the doubly re-entrant pillar dimensions with the intrinsic contact angle of 105° varied in the simulations. From **Figure 5.11a**, increasing the pitch size from 150 to 200 µm results in an initial increase in droplet

spreading. However, the droplet manages to detach from the 200 µm surface at an earlier contact time. This is primarily due to the reduction in the solid fractional area. Further increasing the pitch towards 250 µm causes $\lambda_{wetting}/\lambda_c$ to dramatically increase and remain roughly within the same range (around 1.3) throughout the contact time (between 2 to 10 ms). This is due to the fact that the droplet does not bounce off the surface. It, instead, remains on the surface. It should be noted that, when comparing **Figure 5.11a** to **Figure 5.5** for different intrinsic contact angles and pitch sizes, increasing the intrinsic contact angle from 70° to 105° reduces $\lambda_{wetting}/\lambda_c$ as the droplet rebounds instead of being pinned for pitch sizes of 150 and 200 µm. When the intrinsic contact angle is increased from 105° to 120°,$\lambda_{wetting}/\lambda_c$ remains approximately the same throughout the spreading period. However, it takes longer for the droplet to recede and rebound at 105° compared to 120°. As mentioned previously, increasing the intrinsic contact angle reduces the interfacial adhesion force, which then reduces $\lambda_{wetting}/\lambda_c$ for a given pitch size.[25,36] For the pitch size of 250 µm, the magnitude of $\lambda_{wetting}/\lambda_c$ at 105° is also placed between 120° and 70° (**Figure 5.5**).

Figure 5.11b shows that reducing the height of the pillars from 100 to 30 µm also causes $\lambda_{wetting}/\lambda_c$ to gradually increase. It should be noted that, even for the smallest pillar height of 30 µm that allows the droplet to spread, $\lambda_{wetting}/\lambda_c$ still manages to reach a value of around 0.8 at roughly 6 ms. This indicates that the spreading of the droplet is less triggered by the reduced height than by the increased pitch of the doubly re-entrant pillars. **Figure 5.11c** illustrates the values of $\lambda_{wetting}/\lambda_c$ for pillar diameters between 100 to 200 µm. Increasing the diameter from 100 to 150 µm causes $\lambda_{wetting}/\lambda_c$ to increase, because of the increased solid fraction. When increasing the diameter from 150 and 200 µm, however, $\lambda_{wetting}/\lambda_c$ reduces slightly by 0.2 between 2 to 5 ms. As the droplet is in contact with a smaller number of pillars when increasing the diameter to 200 µm (as seen from **Figure**

5.7), the contact line is pinned at a smaller distance (Appendix B, Chapter 8). In spite of this, the droplet still sits longer on the doubly re-entrant pillars with a diameter of 200 µm than on those with a diameter of 150 µm, where the droplet starts receding after 5 ms, and eventually, bounces off the surface prior to that of the larger pillar diameter of 200 µm. In contrast, the length and thickness of the vertical overhang have only negligible effect on $\lambda_{wetting}/\lambda_c$ as shown in **Figure 5.11d** and **Figure 5.11e**.

Since the pitch of the doubly re-entrant pillars has exhibited the most significant effect on $\lambda_{wetting}/\lambda_c$ among the factors, **Figure 5.11f** further scrutinises the correlation between the dimensionless contact time, τ^*, and the pitch size. τ^* is defined as the ratio of the contact time to the inertial-capillary contact time ($\tau^* = \frac{\tau}{\tau_o}$). The inertial-capillary contact time is specified as the contact time for a droplet impacting on a flat superhydrophobic surface which is scaled as:[37,38]

$$\tau_o = \sqrt{\frac{\rho_l {R_d}^3}{\gamma_{lv}}} \tag{5.4}$$

For *We* > 1, the inertial-capillary contact time is independent of the impact velocity.[38] For a water droplet with a diameter of 1 mm, the inertial-capillary contact time is equal to 1.32 ms. From the chart, increasing the pitch size from 150 to 200 µm gradually decreases the overall contact time. Specifically, the time taken for the droplet to spread ($\tau_{spreading}$) slightly decreases. Further increasing the pitch towards 250 µm displays a substantial increase in the contact time as the liquid fully penetrates the cavities of the pillars and floods the surface. As a consequence, the time taken for the droplet to recede is substantially longer since the liquid is adhered to the bottom of the pillars.

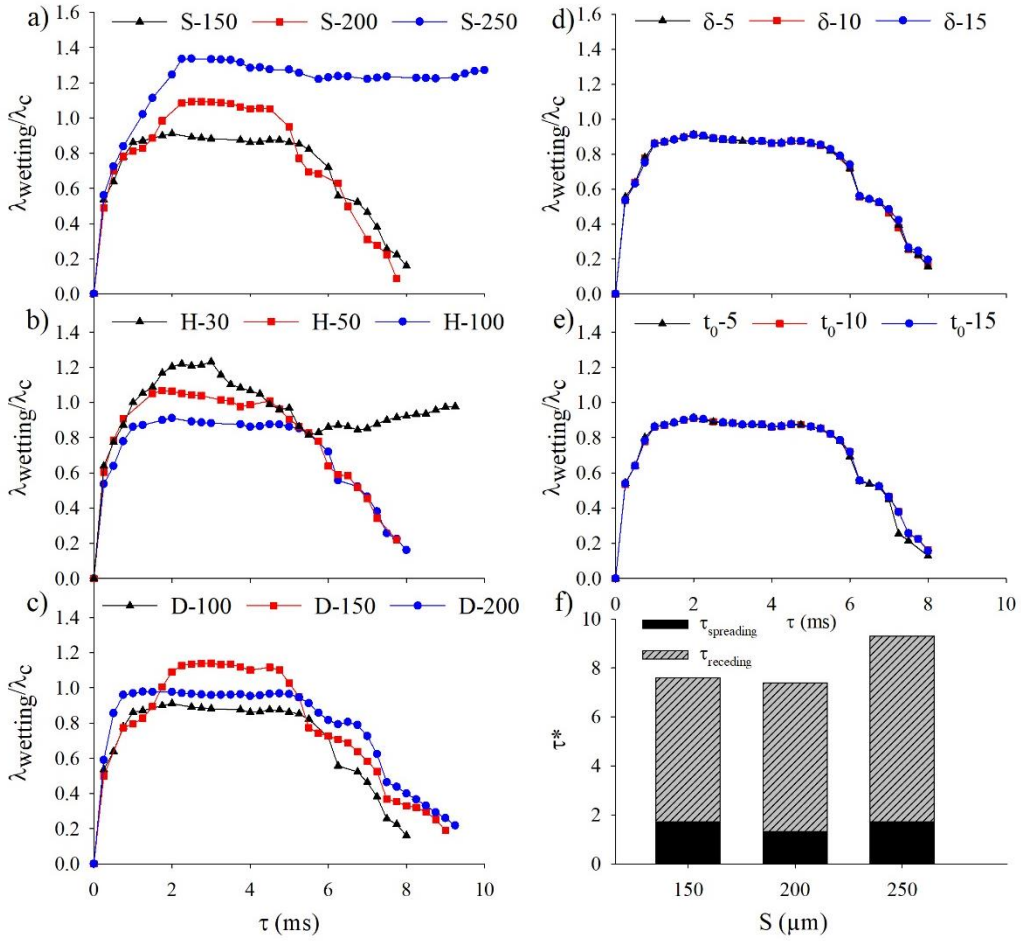

Figure 5.11. $\lambda_{wetting}/\lambda_c$ against contact time for each of the dimensional parameters varied: a) the pitch spacing (S); b) pillar height (H); c) pillar diameter (D); d) length of the vertical overhang (δ); and e) the thickness of the vertical overhang (t_o). $\theta_Y = 105°$. (f) dimensionless contact time (τ^*) against pitch spacing (S) chart highlighting the time taken for the droplet to spread ($\tau_{spreading}$) and recede ($\tau_{receding}$) on each of the configured surfaces.

5.4. Conclusion

Numerical simulations and experimental studies of droplet impact against doubly re-entrant pillars have been conducted to probe the underlying physical phenomena. Good agreement concerning the droplet behaviours has been found between the numerical and experimental results. This is demonstrated through both the comparison of the contour images and the quantitative analysis of the ratio of the maximum wetting diameter to the diameter of the droplet, $\lambda_{wetting}/\lambda_c$, against contact time for the various processes of droplet impact. Therefore, direct numerical simulations based on a Volume-of-Fluid method can be used to further support our understanding of droplet behaviours resulting from impacting complex surface structures. Specifically, the pitch, height, diameter, overhang length and thickness of the doubly re-entrant pillars have been varied to illustrate their roles in governing droplet repellency. Among these dimensional parameters, the pitch of the doubly re-entrant pillars has exhibited the most significant effect on the evolution of $\lambda_{wetting}/\lambda_c$. Additionally, the velocity and pressure contours have been displayed to identify the region of significance. This study provides an improved understanding of how adding the horizontal and vertical overhang to straight pillars enables droplet repellency for re-entrant and doubly re-entrant pillars.

Future studies may choose to study droplet impact on doubly re-entrant pillars under quasi-static conditions where a hydrostatic pressure is applied upon the droplet instead of utilizing dynamic pressures. Quasi-static studies have been shown to emulate the kinematics of droplet impact under dynamic conditions for Weber numbers much less than one where interfacial surface tension forces are dominant over inertial forces resulting in minor droplet deformations.[39,40] For Weber numbers greater than one, inertial forces are shown to be more dominant resulting in the effect of the water hammer pressure to act more strongly against impacting droplets due to the sudden and greater change in

momentum (further details are highlighted in Appendix B, Chapter 5). As the shift in droplet momentum is relatively small in quasi-static droplet impact conditions, the subsequent impacting pressure would be less in comparison to dynamic conditions which would establish different droplet dynamics for each stage of droplet impact (i.e. contact diameter and time would be bigger and longer under dynamic conditions).[41,42] Therefore, simulating droplet impact under quasi-static conditions on doubly re-entrant pillars must be limited to Weber numbers much less than one in order to remain valid within the dynamic criteria.

5.5. References

1. F. Geyer, M. D'Acunzi, A. Sharifi-Aghili, A. Saal, N. Gao, A. Kaltbeitzel, T.-F. Sloot, R. Berger, H.-J. Butt, D. Vollmer, When and how self-cleaning of superhydrophobic surfaces works, Sci. Adv. 6 (2020) 9727.
2. K. M. Wisdom, J. A. Watson, X. Qu, F. Liu, G. S. Watson, C.-H. Chen, Self-cleaning of superhydrophobic surfaces by self-propelled jumping condensate, Proc. Natl. Acad. Sci. U.S.A. 110 (2013) 7992-7997.
3. R. J. Daniello, N. E. Waterhouse, J. P. Rothstein, Drag reduction in turbulent flows over superhydrophobic surfaces, Phys. Fluids 21 (2009) 085103.
4. P. Tsai, A. M. Peters, C. Pirat, M. Wessling, R. G. Lammertink, D. Lohse, Quantifying effective slip length over micropatterned hydrophobic surfaces, Phys. Fluids 21 (2009) 112002.
5. T. Maitra, M. K. Tiwari, C. Antonini, P. Schoch, S. Jung, P. Eberle, D. Poulikakos, On the nanoengineering of superhydrophobic and impalement resistant surface textures below the freezing temperature, Nano Lett. 14 (2014) 172-182.

6. S. Farhadi, M. Farzaneh, S. A. Kulinich, Anti-icing performance of superhydrophobic surfaces, Appl. Surf. Sci. 257 (2011) 6264-6269.
7. Y. Song, C. D. Díaz-Marín, L. Zhang, H. Cha, Y. Zhao, E. N. Wang, Three-Tier Hierarchical Structures for Extreme Pool Boiling Heat Transfer Performance, Adv. Mater. 34 (2022) 2200899.
8. T. P. Allred, J. A. Weibel, S. V. Garimella, Enabling highly effective boiling from superhydrophobic surfaces, Phys. Rev. Lett. 120 (2018) 174501.
9. S. Sett, P. Sokalski, K. Boyina, L. Li, K. F. Rabbi, H. Auby, T. Foulkes, A. Mahvi, G. Barac, L. W. Bolton, Stable dropwise condensation of ethanol and hexane on rationally designed ultrascalable nanostructured lubricant-infused surfaces, Nano Lett. 19 (2019) 5287-5296.
10. N. Miljkovic, R. Enright, Y. Nam, K. Lopez, N. Dou, J. Sack, E. N. Wang, Jumping-droplet-enhanced condensation on scalable superhydrophobic nanostructured surfaces, Nano Lett. 13 (2013) 179-187.
11. A. Tuteja, W. Choi, J. M. Mabry, G. H. McKinley, R. E. Cohen, Robust omniphobic surfaces, Proc. Natl. Acad. Sci. U.S.A. 105 (2008) 18200-18205.
12. T. Liu, C.-J. Kim, Turning a surface superrepellent even to completely wetting liquids, Science 346 (2014) 1096-1100.
13. G.-T. Yun, W.-B. Jung, M. S. Oh, G. M. Jang, J. Baek, N. I. Kim, S. G. Im, H.-T. Jung, Springtail-inspired superomniphobic surface with extreme pressure resistance, Sci. Adv. 4 (2018) 4978.
14. R. Hensel, C. Neinhuis, C. Werner, The springtail cuticle as a blueprint for omniphobic surfaces, Chem. Soc. Rev. 45 (2016) 323-341.
15. J. Sun, P. Zhu, X. Yan, C. Zhang, Y. Jin, X. Chen, Z. Wang, Robust liquid repellency by stepwise wetting resistance, Appl. Phys. Rev. 8 (2021) 031403.

16. C. Extrand, Designing for optimum liquid repellency, Langmuir 22 (2006) 1711-1714.

17. H.-J. Butt, D. Vollmer, P. Papadopoulos, Super liquid-repellent layers: The smaller the better, Adv. Colloid Interface Sci. 222 (2015) 104-109.

18. X. Liu, H. Gu, M. Wang, X. Du, B. Gao, A. Elbaz, L. Sun, J. Liao, P. Xiao, Z. Gu, 3D printing of bioinspired liquid superrepellent structures, Adv. Mater. 30 (2018) 1800103.

19. D. Liao, M. He, H. Qiu, High-performance icephobic droplet rebound surface with nanoscale doubly reentrant structure, Int. J. Heat Mass Transfer 133 (2019) 341-351.

20. E. M. Domingues, S. Arunachalam, H. Mishra, Doubly reentrant cavities prevent catastrophic wetting transitions on intrinsically wetting surfaces, ACS Appl. Mater. Interfaces 9 (2017) 21532-21538.

21. H. Chen, X. Liu, K. Wang, H. Liu, S. Shen, Numerical study on dynamic characteristics of double droplets impacting a super-hydrophobic tube with different impact velocities, Int. J. Comput. Fluid Dyn. 33 (2019) 222-233.

22. J. Luo, F. Chu, Z. Ni, J. Zhang, D. Wen, Dynamics of droplet impacting on a cone, Phys. Fluids 33 (2021) 112116.

23. Z. Lin, H. Zhang, J. Tao, Y. Jin, Z. Zhu, Numerical analysis of droplet impact on the convex surface with liquid film, Langmuir 38 (2022) 7593-7602.

24. T. Xavier, D. Zuzio, M. Averseng, J.-L. Estivalezes, Toward direct numerical simulation of high speed droplet impact, Meccanica 55 (2020) 387-401.

25. A. Hu, D. Liu, 3D simulation of micro droplet impact on the structured superhydrophobic surface, Int. J. Multiphase Flow 147 (2022) 103887.

26. J. Panter, Y. Gizaw, H. Kusumaatmaja, Multifaceted design optimization for superomniphobic surfaces, Sci. Adv. 5 (2019) 7328.

27. Y. Liu, P. Tan, L. Xu, Compressible air entrapment in high-speed drop impacts on solid surfaces, J. Fluid Mech. 716 (2013) R9.

28. P. D. Hicks, R. Purvis, Air cushioning and bubble entrapment in three-dimensional droplet impacts, J. Fluid Mech. 649 (2010) 135-163.

29. F. Smith, L. Li, G. Wu, Air cushioning with a lubrication/inviscid balance, J. Fluid Mech. 482 (2003) 291-318.

30. S. M. M.Mani, M.P. Brenner, Events before droplet splashing on a solid surface., J. Fluid Mech. 647 (2010) 163-185.

31. A. Torkkeli, Droplet microfluidics on a planar surface, VTT Technical Research Centre of Finland (2003).

32. H.-J. Butt, N. Gao, P. Papadopoulos, W. Steffen, M. Kappl, R. Berger, Energy dissipation of moving drops on superhydrophobic and superoleophobic surfaces, Langmuir 33 (2017) 107-116.

33. G. Wang, L. Fei, T. Lei, Q. Wang, K. H. Luo, Droplet impact on a heated porous plate above the Leidenfrost temperature: A lattice Boltzmann study, Phys. Fluids 34 (2022)

34. D. E. Marschner, S. Pagliano, P.-H. Huang, F. Niklaus, A methodology for two-photon polymerization micro 3D printing of objects with long overhanging structures, Addit. Manuf. 66 (2023) 103474.

35. R. Zhang, P. Hao, X. Zhang, F. He, Dynamics of high Weber number drops impacting on hydrophobic surfaces with closed micro-cells, Soft Matter 12 (2016) 5808-5817.

36. C. Shinan, D. Liang, S. Mengjie, L. Mengyao, Numerical investigation on impingement dynamics and freezing performance of micrometer-sized water droplet on dry flat surface in supercooled environment, Int. J. Multiphase Flow 118 (2019) 150-164.

37. Y. Xu, L. Tian, C. Zhu, N. Zhao, Reduction in the contact time of droplet impact on superhydrophobic surface with protrusions, Phys. Fluids 33 (2021)

38. D. Richard, C. Clanet, D. Quéré, Contact time of a bouncing drop, Nature 417 (2002) 811-811.

39. J. Moláček, J. W. Bush, A quasi-static model of drop impact, Phys. Fluids 24 (2012)

40. T. Kärki, I. Pääkkönen, N. Kyriakopoulos, J. V. Timonen, Quasi-two-dimensional pseudo-sessile drops, Commun. Phys. 7 (2024) 333.

41. Y. Zong, A. Oron, H. Liu, Y. Jiang, Dynamic and quasi-static droplet penetration through meshes, Langmuir 39 (2023) 9808-9815.

42. M. Tenjimbayashi, Production of small powder-stabilized droplets using superhydrophobic mesh, Appl. Phys. Lett. 122 (2023)

Chapter 6

Conclusions, Future Prospects and Contributions Made

6.1. Contributions Made to Literature

This Thesis imposes various multiphase flow and phase-change simulations to improve and provide hindsight into the existing numerical results provided in literature in relation to condenser and absorber heat exchanger systems. As such, the findings presented here encompasses a foundation for future academics to build upon in order to accurately mimic the environmental settings on intricately designed functional tubes seen in experimental investigations as highlighted in Chapter 2. Firstly, the ability to adequately simulate dropwise/jumping-droplet condensation on a macro-scaled heat pipe at multiple intrinsic contact angles and contact angle hysteresis for large subcooling temperatures (~ 30 K) is a significant step into characterizing the fundamental requirements needed for establishing dropwise and even jumping-droplet condensation at various subcooling temperatures. Current studies within the literature have yet to provide any numerical data regarding the heat transfer coefficient/heat flux enhancements at various contact angles and contact angle hysteresis on circular heat pipes. In addition, being able to meticulously capture the Rayleigh-Plateau instability of liquid jets seen within falling-film flow is shown to severely modify flow behaviour on the impacting tubes and as such, further alter their heat transfer characteristics. This allows the simulated heat transfer performance/flow behaviour on the impinging tubes to further coincide towards experimental observations which demonstrates an improvement to the results provided by the current literature.[1-3] Furthermore, modelling liquid-repellency on doubly re-entrant pillars illustrates a baseline towards simulating these pillars and other complex functional surfaces under greater dynamic conditions seen within heat exchangers. Most studies have had limited success in simulating dynamic liquid-repellency on doubly re-entrant pillars as noted previously in Chapter 5.1.[4,5] The dimensional analysis conducted on the doubly re-entrant pillars also benefits in designing functional surfaces for or

against liquid impingement as the key dimensional parameters can be finely tuned to augment the heat transfer coefficients of condenser/absorber heat pipes based on their liquid-repellency performance. The articulation of these novelties are summarised below for each chapter.

6.2. General Conclusions

Chapter 3 portrays a two-dimensional multiphase flow with phase-change simulation of condensation on a heat pipe from utilizing the Volume-of-Fluid method. The numerical model was thoroughly calibrated against the Nusselt film theory and experimental results from literature. This is demonstrated from comparing the film thickness, temperature profiles in the circumferential direction at multiple tube angles, heat transfer coefficient and heat flux against various subcooling temperatures up to 50 K. The combination of the employing the Lee's mass transfer model and altering the vapour thermal conductivity is what allowed the model to be suitably stable and accurate under large subcooling temperatures. The numerical model is then used to investigate how changing the intrinsic contact angles and contact angle hysteresis of the tube can affect the flow behaviour of the condensate and the tubes' heat transfer performance. It is noted that, increasing the contact angle of the tube from 0° to 90° caused the condensate to transition from filmwise to dropwise condensation. Modifying the contact angle further from 90° to 150° resulted in the condensate to convert to jumping-droplet condensation as the contact length of the droplets were lessened to the point where the inertia force generated from coalescence was able to overcome the surfaces' adhesion force.

However, further increasing the contact angle beyond 150° may strengthen the longevity of jumping-droplet condensation as only a minute number of droplets were seen to jump off the surface during the initial stages of condensation. Nonetheless, the heat transfer

coefficient and heat flux of the tube were amplified significantly by 140% between contact angles 0° to 150°. Furthermore, increasing the subcooling temperature between 1-20 K for contact angles of 90° to 150° also enhanced the heat transfer coefficient and heat flux of the tube as magnifying the subcooling temperature allows the rate of condensation to increase which in turn, increased the droplet nucleation density of the tube. As a result, this intensified the frequency of coalescing droplets which resulted in droplets being removed off the tube promptly. Although, increasing the subcooling temperature further caused the heat transfer coefficient and heat flux to marginally decline due to the nucleating droplets being too large to depart off the tube which eventually led to droplets collapsing into a liquid film. This is seen from the heightened rate of condensation as the subcooling temperature is raised. On the other hand, for hydrophilic tubes, as the tube primarily displayed filmwise condensation, increasing the subcooling temperature only magnified the height of the liquid film which resulted in a 95% reduction in the heat transfer coefficient between subcooling temperatures 1 to 30 K. Therefore, it can be said that the enhancement in the heat transfer performance of the tube against the surface subcooling temperature is limited to heat pipes that display dropwise or jumping-droplet condensation up to a critical subcooling temperature threshold. This threshold, however, can be raised further by increasing the intrinsic contact angle of the tube.

Moreover, increasing the contact angle hysteresis between 0 and 20° caused formulating droplets to adhere more onto the tube and agglomerate towards the top of the tube between intrinsic contact angles of 30 to 150°. Subsequently, the heat transfer coefficients of the tube were seen to decrease for all intrinsic contact angles as the contact angle hysteresis is increased. Notably, the rate of reduction was more prevalent for contact angles less than 30° as the droplet nucleation density of the tube is raised whilst the

minimal droplet radius observed is lessened for as the intrinsic contact angle subsides. This observation correlates to previous experimental studies and theoretical models highlighted in Chapter 3.1 and Chapter 3.3. Thus, it is suggested that future numerical studies relating to surface wettability effects on condensation should consider the contact angle hysteresis as the flow pattern may be altered from dropwise to filmwise condensation for large contact angle hysteresis. Since, the simulation assumes that the contact angle hysteresis of the surface is equal to zero when the effects of the contact angle hysteresis are not included. Nevertheless, as the simulation is focused on a singular heat pipe, it remains unknown how the departing droplets influences the flow behaviour and heat transfer performance of the tubes beneath at various contact angles.

Chapter 4 then answered this issue from numerically investigating three-dimensional flow of subcooled water across multiple horizontal tube banks. Again, the numerical model was validated against analytical and experimental data. This is seen from exclusively comparing the film thickness, circumferential velocity profiles, average and local heat transfer coefficients, and the average Nusselt number on the first tube which demonstrated satisfactory agreement within the assumptions stated. Importantly, the flow behaviour of the liquid falling from the first to the second tube also illustrated excellent agreement compared to the experimental data for a completely wetted tube. The encapsulation of the Rayleigh-Plateau instability of the liquid jet is what allowed the simulation to further resemble the experimental data in which, other numerical studies related to falling-film flow (which compared their results to the same experimental data as shown) did not manage to apprehend or even take note of. By increasing the number of mesh elements within the diameter of the liquid-jet, the Rayleigh-Plateau instability was revealed as observed from previous case-studies. The resolution of this phenomenon can be seen through the variations in the axial pressure and velocity profiles within the

liquid jet as it recoils back to the tube. Notably, these variations are also verified against previous numerical results. Furthermore, the nature of these profiles correspond to a sinusoidal profile due to the harmonic nature of the capillary wave that travels upstream from the tip of the liquid jet. As a result, the interface of the liquid jet begins to take form of the capillary waves' profile, which establishes a Laplace pressure profile across the jet as exemplified from the maxima and minima inflexion points along the axial pressure profile. Once the surface tension force overcomes the viscous force the liquid, the jet begins to bifurcate into satellite droplets along the regions of high pressure. These satellite droplets that impacted the secondary tube induced film thinning and mixing which amplified the films' local heat transfer coefficient. Due to the additional capillary waves generated from the impacting droplets, the film became more unstable which affected the droplet departure and nucleation rates.

The influence of the Rayleigh-Plateau instability, however, is shown to be more prominent at different contact angles where the flow behaviour is altered significantly on the first tube. Specifically, at contact angles of 30 and 60°, the pattern of the falling film remained in a dropwise/jet flow within the simulation time (2 seconds). As seen from previous studies, without capturing the Rayliegh-Plateau instability, the falling-film pattern is shown to be jet flow throughout at the stated contact angles. This vastly alters the flow patterns and heat transfer performance on the secondary tubes in comparison to what the current literature presents. In addition, increasing the contact angles of the tube caused the axial film thickness to decrease while the circumferential film thickness rose due to the ample reduction in the surfaces' adhesion force, allowing the surface tension force to dominate. From reaching a contact angle of 90°, the flow pattern no longer displayed falling-film flow but instead constant removal of droplets that impede the secondary tubes. Raising the contact angles further to a superhydrophobic state caused

the formulating droplets to escape the fluid domain and not impact the tubes beneath. Therefore, it may be worth modelling various adjacent tube banks in future studies to observe how the escaping droplets influence the flow behaviour and heat transfer performance at other tube banks for large contact angles (greater than 120°).

As impinging droplets are observed to be ubiquitous within falling-film flow, it is necessary to undermine the fundamental behaviour of impacting droplets, so that future researchers can practically design elaborate functional surfaces that are able to enhance the performance of condenser or absorber heat exchanger tubes. This bring us forth to Chapter 5, where droplet impaction on doubly re-entrant pillars are numerically studied as they are notorious for repelling liquids under large impacting pressures. Unlike in the other chapters, the numerical results were directly compared with experimental data that were carried out from fabricating doubly re-entrant pillars through laser lithography of IP-S. Good agreement between the numerical and experimental results are illustrated from qualitatively and quantitatively analysing the contour images and the maximum wetting diameter to the diameter of the droplet ratios ($\lambda_{wetting}/\lambda_c$) during droplet impaction against pitch spacings between 150-250 μm and intrinsic contact angles of 70 and 120°. The structured hexahedral mesh refinement applied on the doubly re-entrant pillars (seen in Appendix B, Chapter 1), is what primarily permitted the numerical simulations to be accurately compared to experimental data. As such, this allowed the interfacial forces within the cavities to be suitably resolved. From thoroughly calibrating the developed numerical model, further investigations were carried out from analysing the droplet repellency performance against the pillars' overhang angle and its' key dimensions. Allocating vertical and horizontal overhangs to the straight pillar manipulates the interfacial surface tension force of the impinging liquid meniscus to act against the direction of impact. This, consequently, increases the breakthrough pressure of the

pillars, allowing the droplet to be pinned onto the pillars rather than flood the interstices as shown from the straight pillars. The interfacial pressure observed within the cavities quantifies these observations as it is shown to be 4 times larger at the centre of impact for straight pillars.

Furthermore, for doubly re-entrant pillars, increasing the pitch spacing from 150 to 200 µm reduced the total contact time of the droplet on the surface. This was due to the reduction in the solid-liquid fractional area which corresponds to a reduction in the interfacial surface adhesion force. Nevertheless, increasing the pitch greater than 200 µm illustrated surface flooding as the breakthrough pressure was lessened to the point where the liquid meniscus was able to protrude through and touch the surface, regardless of the further reduction in the solid-liquid fractional area. A similar observation is seen from reducing the height of the pillars between 100 to 50 µm as lowering the pillar height allows the protruding meniscus to deflect closer to the projected area. As a consequence, this increases the compression of the air-layer within the cavities, which in turn, increases the total net capillary pressure against the liquid meniscus hence, increasing droplet repellency. Additionally, reducing the pillar height to 30 µm allowed the meniscus to penetrate and touch the projected area which caused the droplet to flood the interstices. This may raise further questions as how the compression of the air-layer can be raised whilst preventing the meniscus from contacting the project area. On the other hand, increasing the diameter of the pillars from 100-200 µm reduced the droplet repellency performance as this allowed the solid-liquid fractional area to inevitably increase.

In spite of this, altering the overhang height and thickness provided a minimal change to the droplet repellency behaviour. Reducing the overhang height from 15 to 5 µm decreased the penetration depth of the liquid meniscus between the cavities which allowed the droplet to repel off the surface faster as less effort is required to withdraw the

liquid from the cavities. However, shortening the thickness of the overhang from 15 to 5 µm showed a negligible change in droplet repellency. Nonetheless, allocating an overhang thickness of 5 µm allowed the droplet to experience an additional capillary pressure at the base of the droplet due to the slight reduction in the wetting diameter. To summarise, manipulating the height of the protruding liquid meniscus is revealed to be the principal factor for establishing droplet repellency or surface flooding. The closer the liquid meniscus is towards the projected area, the more the air-layer becomes compressed which increases the net capillary pressure against the meniscus. However, if the meniscus protrudes too close to the projected area (i.e. touching the surface), the droplet will flood the interstices causing the droplet to be adhered onto the surface. The height of the meniscus is shown to be altered from adjusting the breakthrough pressure of the pillars which is directly proportional to the pillar dimensions and its' intrinsic contact angle as explained in Appendix B, Chapter 5.

6.3. Future Works

To conclude, the work presented in this Thesis is able to further bridge the gap between numerically applying intricately designed functional surfaces onto macro-scaled heat pipes in order to scrutinize and augment the experimental observations seen within literature. Thus, future academics may expand upon this work by combining the methodologies presented in Chapters 3 to 5, to numerically allocate doubly re-entrant pillars or other complex functional surfaces upon heat pipes under condensation and falling film flow as an example. Furthermore, for functional surfaces, the compression of the air-layer should be further optimised by meticulously controlling the height of the liquid meniscus for different under various droplet velocities and droplet diameters or even under consecutive droplet impacts as demonstrated within falling-film flow. In

addition, different design variants of the doubly re-entrant pillars as noted in Chapter 5.1, should be virtually simulated to further aid in this optimisation process. In conjunction, when allocating such functional surfaces onto heat pipes, the environmental settings could be expanded further from raising the film Reynolds number towards turbulent regimes and/or implementing vapour flow parallel or orthogonal to the direction of the tube either at laminar or turbulent regimes as noted in Chapter 4.4. This will further altar the tubes' heat transfer efficiencies as the formulating droplets will experience vapour shear flow (i.e. drag force) which will adjust the surfaces' droplet departure and nucleation rates depending on the magnitude of the vapour velocity (mentioned in Chapter 2.3.3). Consequently, this then may be worth investigating the effect of adding additional adjacent horizontal tube banks in order to observe how the condensate which departs radially from the tube may impede upon their heat and mass transfer characteristics especially for large tube contact angles observed in Chapter 4.3.3. More importantly, the fragility of such novel functional surfaces could also be analysed from conducting a multiphysics simulation which is able to simultaneously access their mechanical as well as their liquid-repellency performance against cyclic impinging liquids or vapour shear flow. Specifically, the deflection and von Mises stresses of micro/nanopillars could be interpreted against droplet impact or falling-film flow at various flow regimes (dropwise or jet-wise).[6] Additionally, the elastic strain generated in between the pillars due to capillary condensation is worth considering and can be analysed through utilizing the Kelvin-Laplace law.[7,8] This can easily be conducted through commercial softwares such as ANSYS and COMSOL. Investigating these particular aspects will allow engineers to optimise the surfaces' mechanical durability and liquid-repellency in order to establish their placement within industry.

Then again, numerically analysing the effects of non-condensable gasses is worthwhile considering especially in the presence of functional surfaces in order to thoroughly examine how non-condensable gasses can detrimentally affect the surfaces' heat transfer performance and how functional surfaces can be designed to enhance the entrapment of non-condensable gasses to prevent surface flooding. To further add, various types of hydrocarbons or binary fluids (such as Methane, Ethane and LiBr-Water) can also be examined alongside to establish their fundamental surface wettability requirements to formulate filmwise, dropwise condensation and jumping-droplet condensation or dropwise/jet flow particularly on functional surfaces. On the other hand, lubricant-infused surfaces may also be modelled within such intricately designed micro/nanopillars to further measure their liquid-repellency and heat transfer performance on heat pipes from parametrically optimising the pillars' key dimensions against the lubricants' film thickness and its' depletion rate. Minimising these particular factors would be of great interest to industry as high lubricant film thicknesses and depletion rates is what prevents these surfaces from entering into industrial heat exchangers as formerly highlighted in Chapter 1.

To evaluate the limitations of this thesis, one of the main limitations shown in Chapter 3 was simulating condensation through the use of an empirical coefficient known as the condensation frequency through implementing Lee's model. While this model is widely accepted within the literature to simulate condensation, it still requires the use of a trail-and-error approach which leaves room for improvement as it is unknown as to what the actual coefficient value should be to determine the mass transfer rate for the given boundary conditions. Employing the Energy jump condition or Schrages' model would be ideal in this scenario as it directly calculates the mass transfer rate between the two phases without the use of a coefficient as mentioned in Chapter 3. But also as mentioned,

this requires a liquid-vapour interface to be initially present when the simulation starts which limits its applicability against different surface contact angles. Hence, a developed mass transfer model for correctly calculating the mass transfer rate without the use of an initial liquid-vapour interface should be devised to improve the current validations.

To further add, the present work could also be extended by simulating condensation along various heat pipes within the 3rd dimension. Moreover, modelling micro/nanopillar designs on macro-scaled heat pipes would be very beneficial as this would be able to illustrate the dynamic liquid-repellency performance of the functional surfaces' design against condensation or falling-film flow. Although this would require much more computational power than HPC (High-Performance Computing) clusters currently provide due to the amount of memory required to interpret nanoscopic forces (i.e. van der Waals forces) within a macro-scaled environment.[9-11] Quantum computers may be able to solve this issue although quantum computing is still in its' development stage for CFD applications. In addition, the Rayleigh-Plateau instability captured in Chapter 4 could be further validated against quantitative data. An example can be through determining the critical Reynolds number of when capillary waves would be generated on a laminar film which would be directly proportional to the Rayleigh-Plateau instability. Then again, a developed critical Reynolds number criterion for the Rayleigh-Plateau instability for falling-film flow have yet to be seen within current studies. While the validation results in Chapter 5 show to have good agreement with experimental data, the validation may be further augmented through incorporating a numerical dynamic contact model specifically for three-dimensional flow for doubly re-entrant geometry. Current numerical dynamic contact angles available within the literature such as Kistlers', Shikhmurzaevs' and Coxs' model are limited to either modelling only the advancing contact angle, or valid for flat surfaces for two-dimensional axisymmetric

flows.[12-14] Future dynamic contact angle models should consider how to interpret the advancement and recession of the contact line and its' velocity along the edges of the pillars' overhang especially for Canthotaxis and Laplace breakthrough conditions (further details are shown in Appendix B, Chapter 7).

As with multiphase flow simulations, a high level of mesh refinement is required to interpret the liquid-vapour interface appropriately which results in large computational times. An approach to reduce computational time could be through implementing dynamic mesh refinement techniques where only the mesh around the liquid-vapour interface is refined with the rest of the fluid domain to remain course. Nevertheless, this could prove to be difficult for condensation due to the vast number of droplets nucleating and coalescing which may result in instability issues. Plus, utilizing the dynamic mesh refinement in conjunction with the adaptive time-stepping method may actually increase simulation times further due to the size of the mesh constantly changing at each timestep which in turn, can cause the time-step to continuously fluctuate alongside in order to reach the prescribed Courant number. This leads to further questions as to how an optimal balance between computational time and accuracy can be found for dynamic mesh refinement approaches. If one were able to address the following aspects stated above, the gap between numerical and experimental observations may eventually close, which would allow future academics and engineers to effortlessly mitigate the issues presented within industrial heat exchangers and optimise their heat transfer efficiencies to their fullest.

6.4. References

1. H. Ding, P. Xie, D. Ingham, L. Ma, M. Pourkashanian, Flow behaviour of drop and jet modes of a laminar falling film on horizontal tubes, Int. J. Heat Mass Transfer 124 (2018) 929-942.
2. S. M. Hosseinnia, M. Naghashzadegan, R. Kouhikamali, CFD simulation of water vapor absorption in laminar falling film solution of water-LiBr ─ Drop and jet modes, Appl. Therm. Eng. 115 (2017) 860-873.
3. C.-Y. Zhao, Z.-L. Yao, D. Qi, W.-T. Ji, A.-G. Li, W.-Q. Tao, Numerical investigation of tube bundle arrangement effect on falling film fluid flow and heat transfer, Appl. Therm. Eng. 201 (2022) 117828.
4. J. Panter, Y. Gizaw, H. Kusumaatmaja, Multifaceted design optimization for superomniphobic surfaces, Sci. Adv. 5 (2019) 7328.
5. X. Wang, L. Jia, C. Dang, The wetting transition of low surface tension droplet on the special-shaped microstructure surface, Colloids Interface Sci. Commun. 50 (2022) 100649.
6. S. Ganesan, C. L. Kumar, Investigation of fluid–structure interaction of micropillars in a three-dimensional microfluidic DLD array, J. Braz. Soc. Mech. Sci. Eng. 46 (2024) 571.
7. G. Y. Gor, A. V. Neimark, Adsorption-induced deformation of mesoporous solids, Langmuir 26 (2010) 13021-13027.
8. A. V. Neimark, I. Grenev, Adsorption-induced deformation of microporous solids: a new insight from a century-old theory, J. Phys. Chem. C 124 (2019) 749-755.
9. T. Takei, M. Chikazawa, T. Kanazawa, Validity of the Kelvin equation in estimation of small pore size by nitrogen adsorption, Colloid and Polymer Science 275 (1997) 1156-1161.

10. F. Casanova, C. E. Chiang, C.-P. Li, I. V. Roshchin, A. M. Ruminski, M. J. Sailor, I. K. Schuller, Gas adsorption and capillary condensation in nanoporous alumina films, Nanotechnology 19 (2008) 315709.

11. A. Wongkoblap, D. Do, G. Birkett, D. Nicholson, A critical assessment of capillary condensation and evaporation equations: A computer simulation study, J. Colloid Interface Sci. 356 (2011) 672-680.

12. J. Göhl, A. Mark, S. Sasic, F. Edelvik, An immersed boundary based dynamic contact angle framework for handling complex surfaces of mixed wettabilities, Int. J. Multiphase Flow 109 (2018) 164-177.

13. Y. D. Shikhmurzaev, Capillary flows with forming interfaces, Chapman and Hall/CRC (2007).

14. R. Cox, The dynamics of the spreading of liquids on a solid surface. Part 1. Viscous flow, J. Fluid Mech. 168 (1986) 169-194.

Appendix A

1. Falling-film Flow Behaviour of Water Flowing Over Several Stacked Tubes at Multiple Contact Angle Configurations

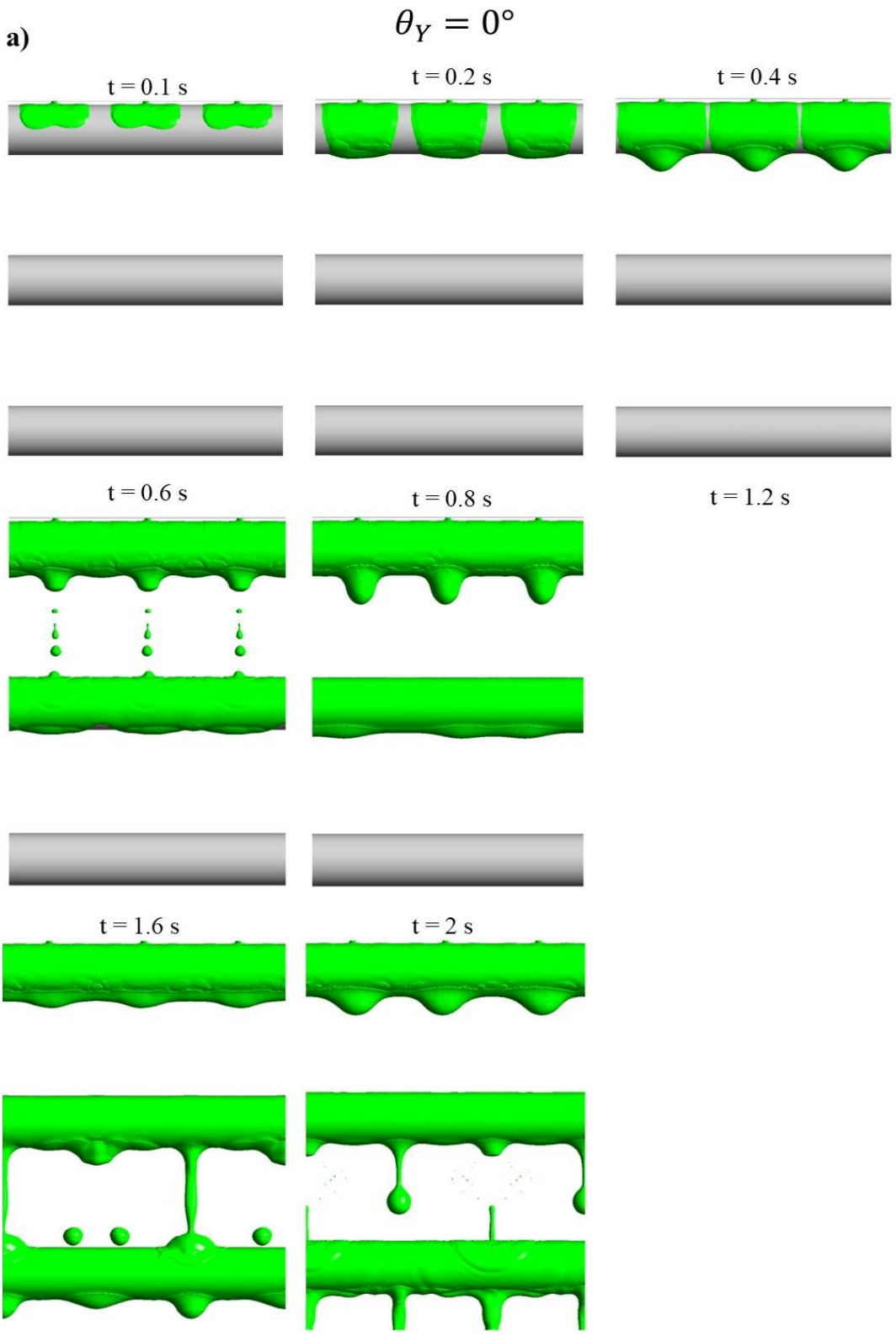

$\theta_Y = 30°$

b)

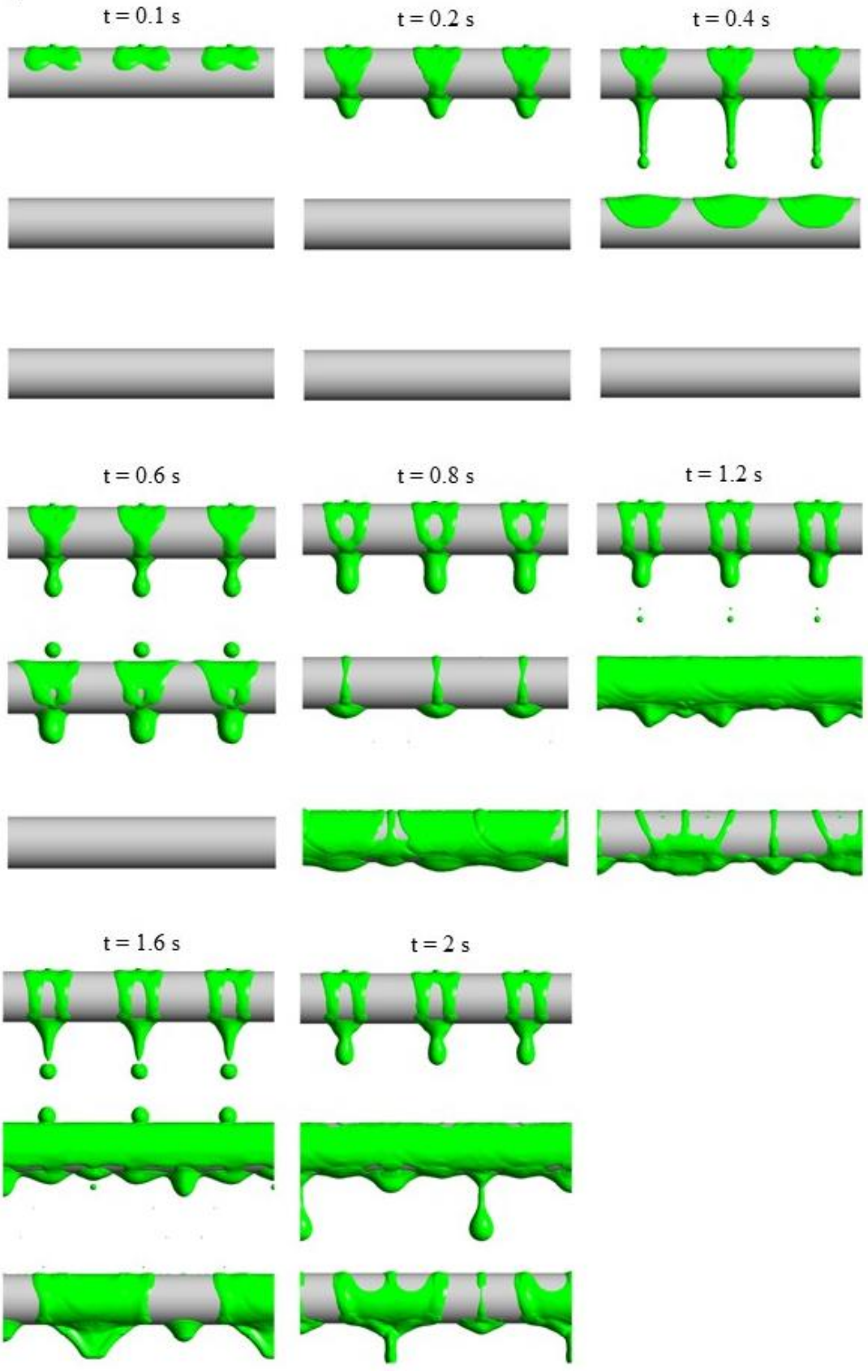

$\theta_Y = 60°$

c)

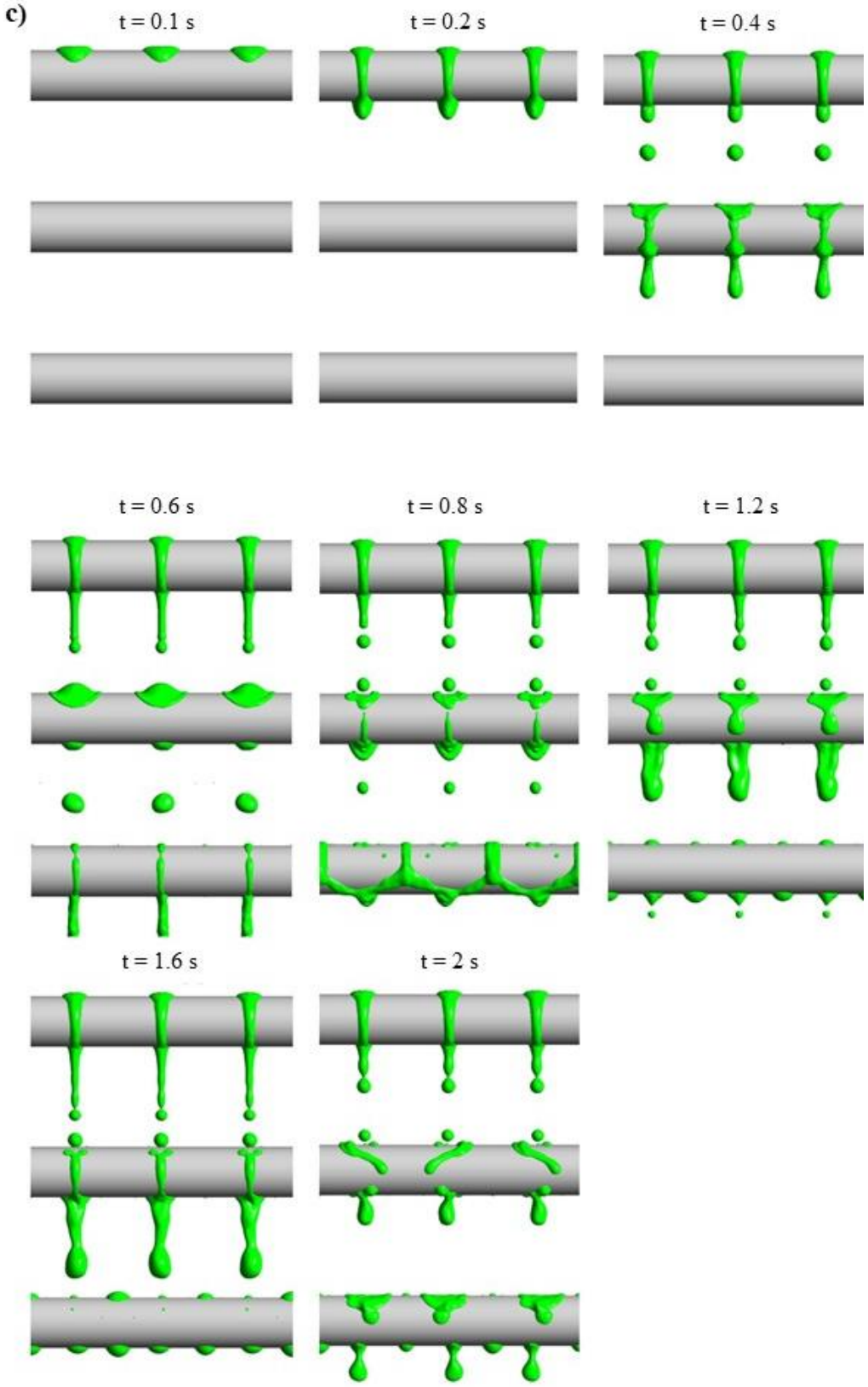

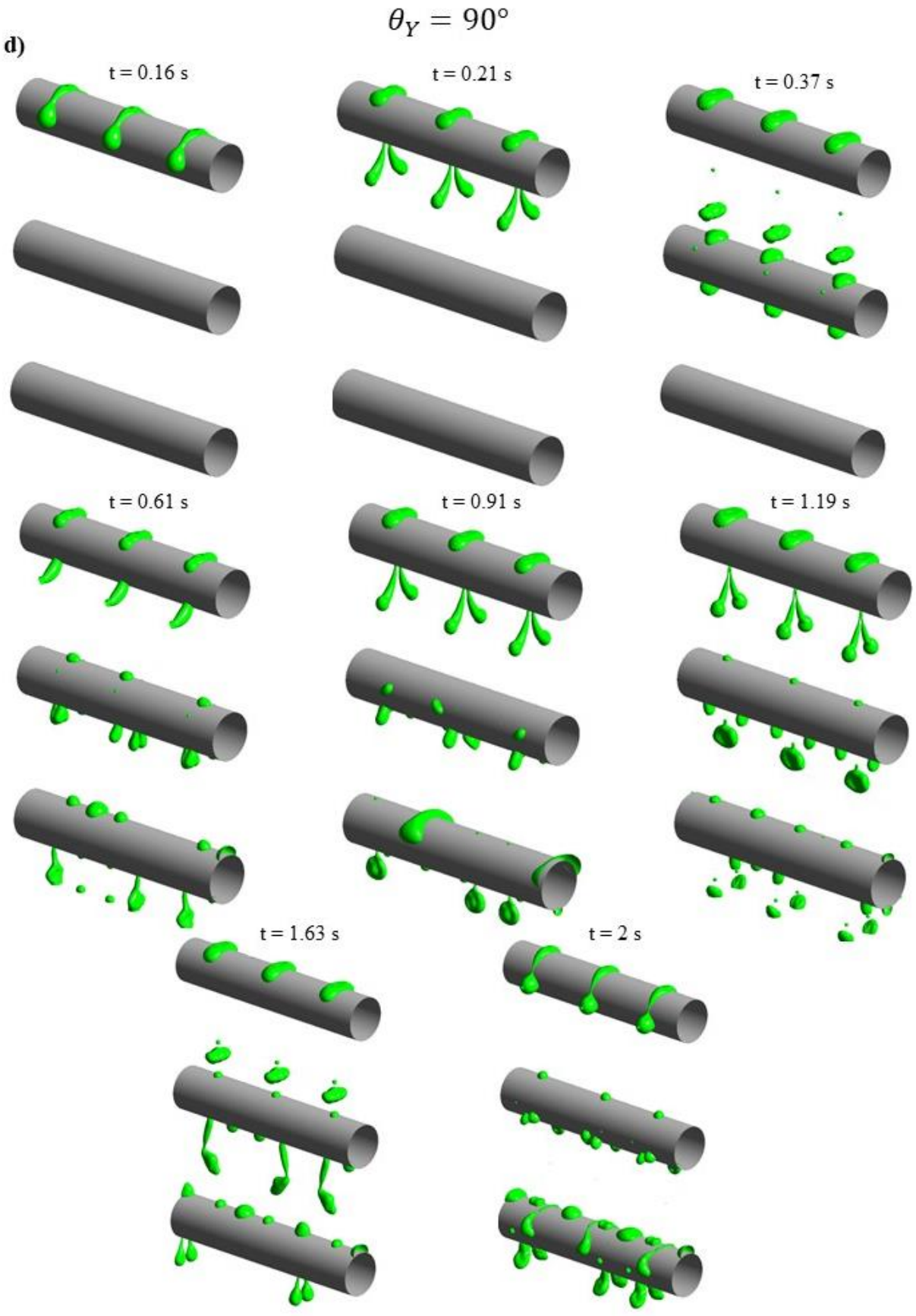
$\theta_Y = 90°$
d)
t = 0.16 s
t = 0.21 s
t = 0.37 s
t = 0.61 s
t = 0.91 s
t = 1.19 s
t = 1.63 s
t = 2 s

$\theta_Y = 120°$

e)

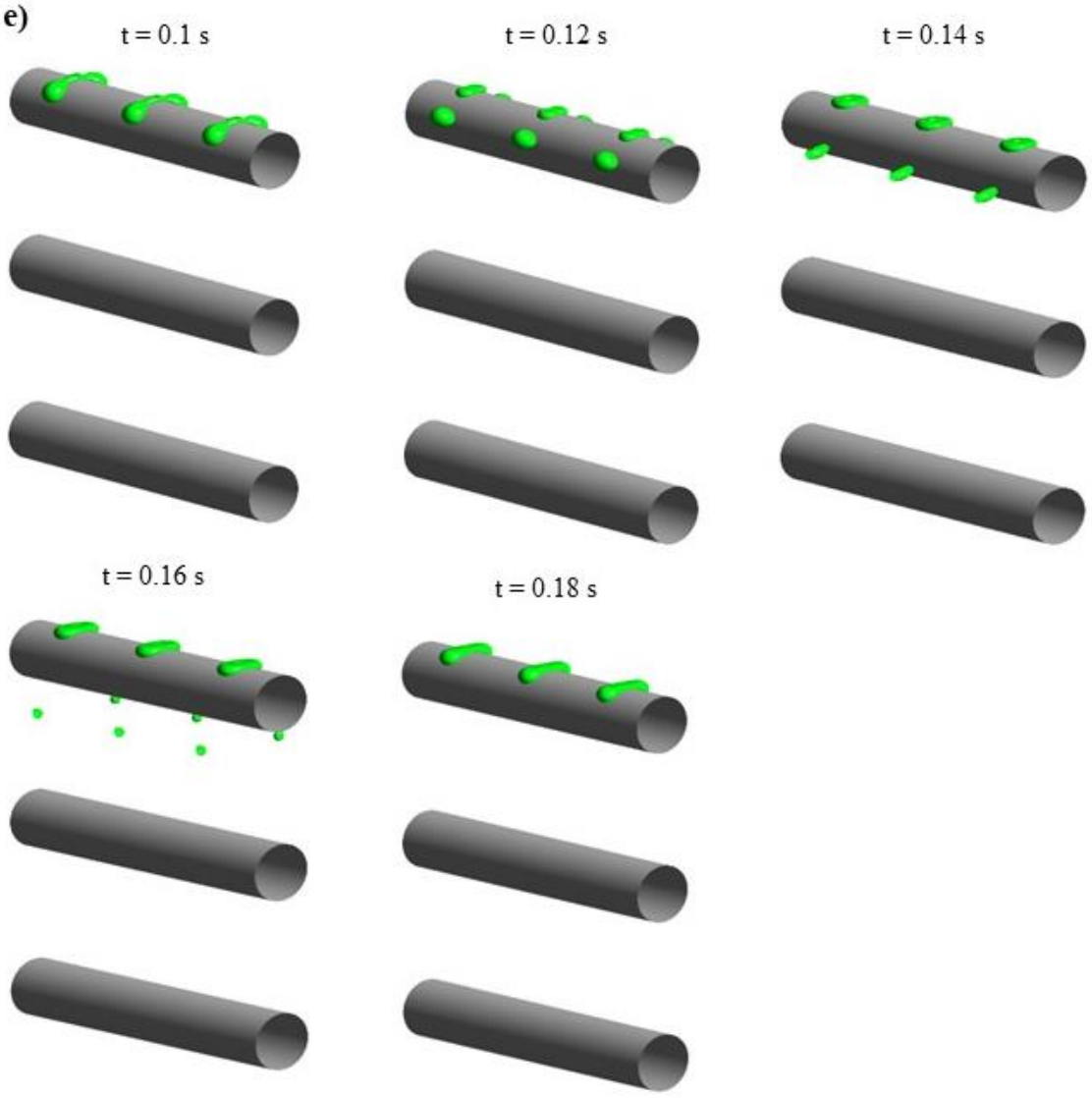

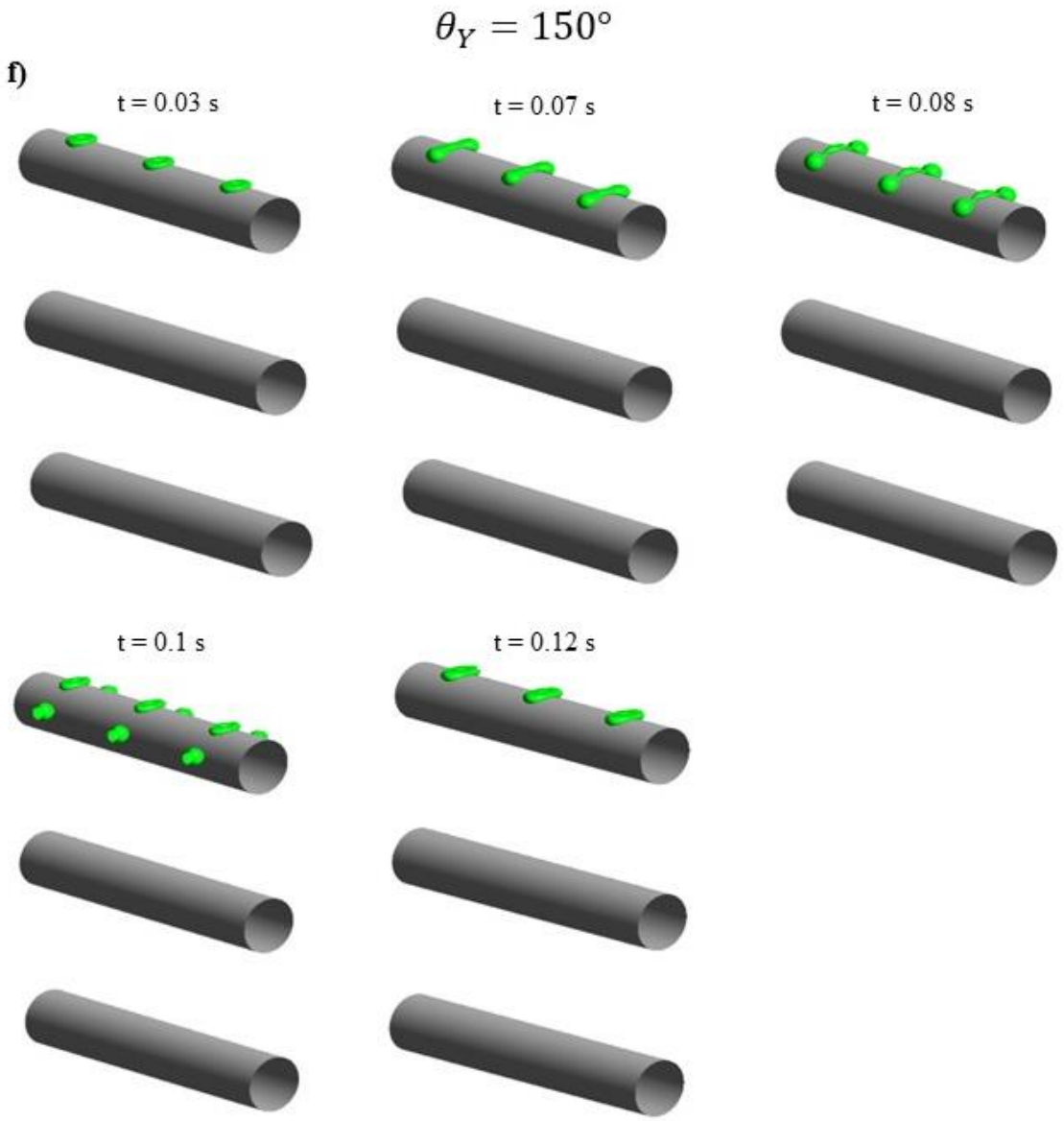

Figure A.1. General flow behaviour of fluid falling over parallel tubes for several contact angle conditions and time scales. (a) 0° (b) 30° (c) 60° (d) 90° (e) 120° (f) 150°.

Appendix B

1. Cases Ran for Simulation and Mesh Refinement

Table B.1 displays the cases run for each of the configurated pillars, illustrating their dimensions and intrinsic contact angles settings. Additionally, **Figure B.1** highlights the key dimensions configured on each pillar type.

Table B.1. Dimensions and intrinsic contact angles of the pillars used for the simulations.

Pillar	**D (µm)**	**d (µm)**	**H (µm)**	**S (µm)**	**δ (µm)**	**t_o (µm)**	**θ_Y (°)**
Straight	**100**	**/**	**100**	**150**	**/**	**/**	**70**
Re-entrant	**100**	**50**	**100**	**150**	**10**	**/**	**70**
Doubly re-entrant	**100**	**50**	**100**	**150**	**10**	**10**	**70**
Doubly re-entrant	**100**	**50**	**100**	**150**	**10**	**10**	**70**
Doubly re-entrant	**100**	**50**	**100**	**150**	**10**	**10**	**120**
Doubly re-entrant	**100**	**50**	**50**	**150**	**10**	**10**	**105**
Doubly re-entrant	**100**	**50**	**30**	**150**	**10**	**10**	**105**
Doubly re-entrant	**100**	**50**	**100**	**200**	**10**	**10**	**70**
Doubly re-entrant	**100**	**50**	**100**	**250**	**10**	**10**	**70**
Doubly re-entrant	**100**	**50**	**100**	**200**	**10**	**10**	**120**
Doubly re-entrant	**100**	**50**	**100**	**250**	**10**	**10**	**120**
Doubly re-entrant	**100**	**50**	**100**	**150**	**5**	**10**	**105**
Doubly re-entrant	**100**	**50**	**100**	**150**	**15**	**10**	**105**
Doubly re-entrant	**100**	**50**	**100**	**150**	**10**	**5**	**105**
Doubly re-entrant	**100**	**50**	**100**	**150**	**10**	**15**	**105**
Doubly re-entrant	**150**	**50**	**100**	**150**	**10**	**15**	**105**
Doubly re-entrant	**200**	**50**	**100**	**150**	**10**	**15**	**105**
Doubly re-entrant	**100**	**50**	**100**	**200**	**10**	**15**	**105**
Doubly re-entrant	**100**	**50**	**100**	**250**	**10**	**15**	**105**

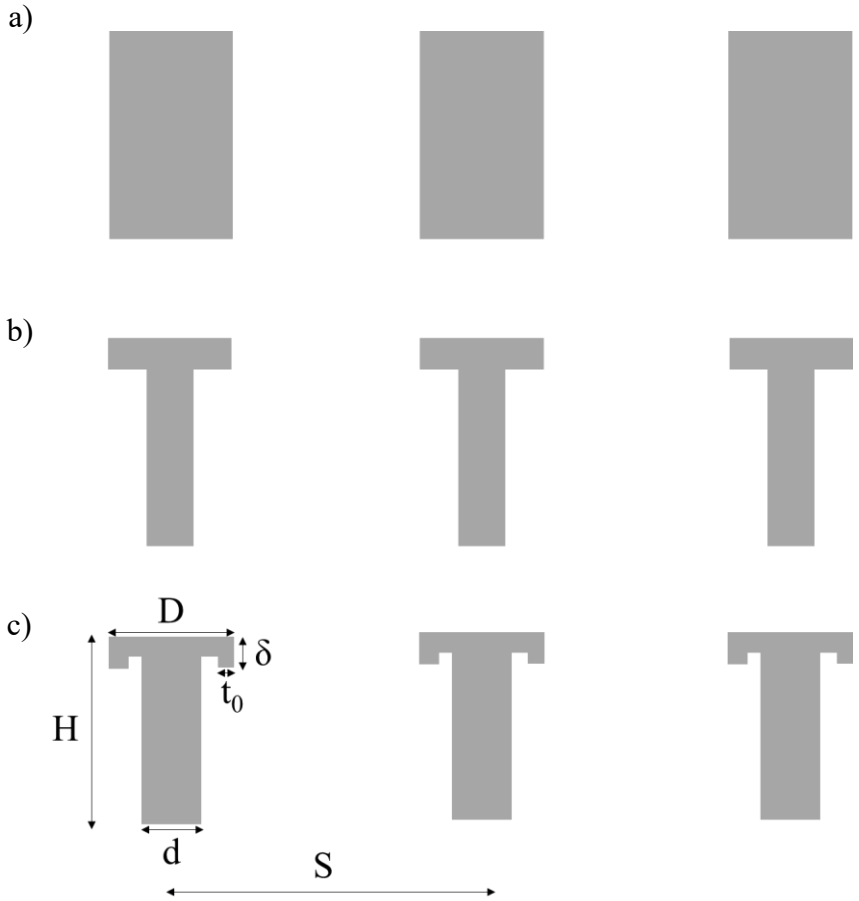

Figure B.1. Key dimensions for a) straight circular, b) re-entrant and c) doubly re-entrant pillars.

Figure B.2 illustrates the hexahedral elements that were used to mesh the fluid domain and pillars. To adequately interpolate the liquid-gas interface of the droplet during impaction and repulsion, mesh adaption was applied at the bottom and top sections of the fluid, with a level one octree mesh refinement where the mesh elements were split into quarters. According to the mesh sensitivity study by Hu *et al.*, the thickness of the air layer within the capillaries was able to be appropriately captured for element numbers greater than or equal to one million.[1] This was quantified through measuring the penetration depth of the liquid meniscus within the cavities at various number of elements. Increasing the number of elements beyond one million resulted in a negligible change in the

penetration depth.[1] Therefore, the number of mesh elements in all our cases was ensured to be more than one million.

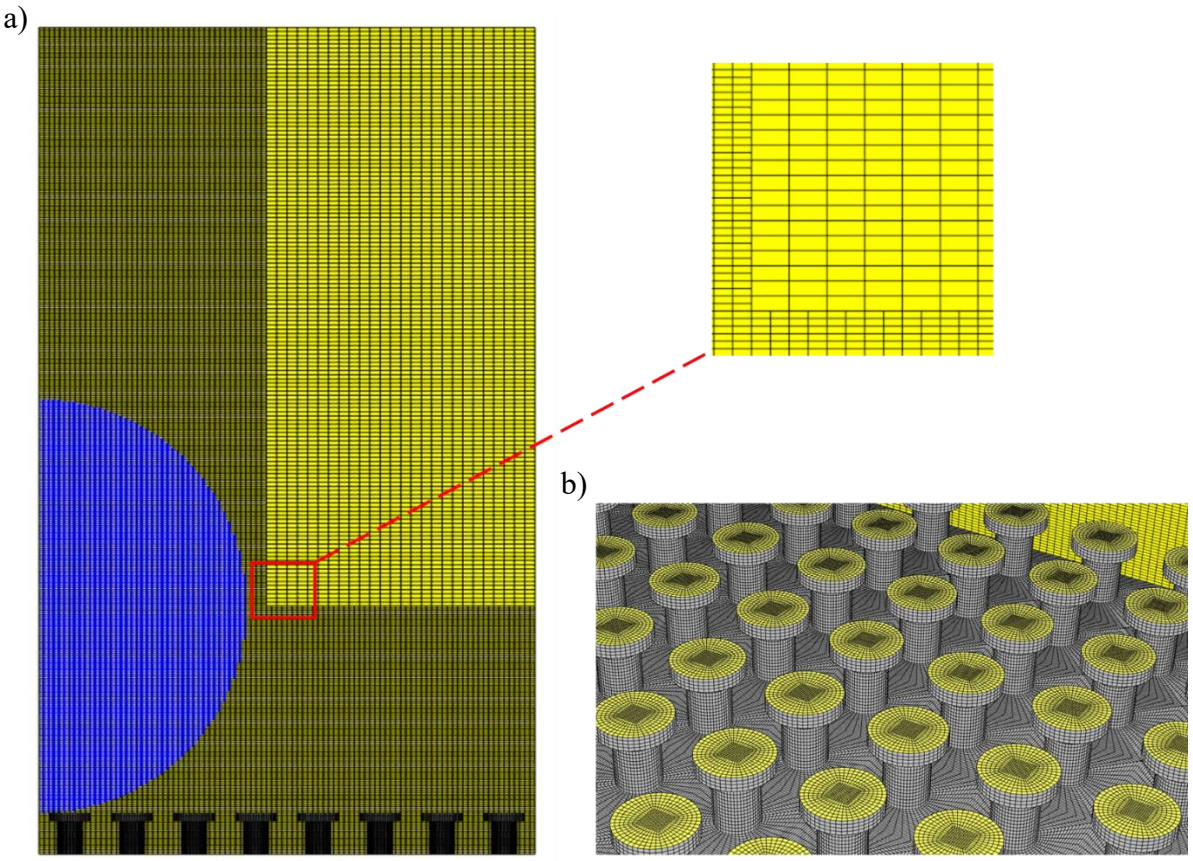

Figure B.2. a) Mesh topology of fluid domain having a level one octree mesh adaption which is applied within the vicinity of the droplet impact and repulsion area as elucidated from the darker regions, b) Structured mesh refinement applied upon the doubly re-entrant pillar arrays.

2. Contact Angle Measurements

The static and dynamic contact angles on each of our plain and structured surfaces were measured using a goniometer (Data-Physics OCA 15) at room temperature. A sessile drop (6 μL) method was used to measure the static contact angles. For the dynamic contact angles, the volume of the sessile drop was increased and decreased to measure the

advancing and receding contact angles, respectively, whilst performing drop shape analysis. For example, the minimum dosing rate used to add and withdraw the liquid was 0.16 µL/s. The measurements were repeated 3 times for each surface type to determine the average contact angles and the standard deviations. **Table B.2** presents the contact angle measurements for each surface type alongside the calculated contact angle hysteresis.

Table B.2. Static and dynamic contact angle measurements of water on the fabricated doubly re-entrant pillars with and without the (trichloro (1H,1H, 2H, 2H-perfluorooctyl) silane (PFOCTS) coating.

Surface type	θ_{CB} **(°)**	θ_a **(°)**	θ_r **(°)**	$\Delta\theta$ **(°)**
IP-S	70.7 ± 1.0	81.8 ± 2.0	37.2 ± 8.7	44.6 ± 8.9
IP-S + PFOCTS	112.9 ± 4.9	113.4 ± 2.6	73.3 ± 4.3	40.1 ± 5.0
IP-S (S-150 µm)	139.3 ± 0.3	152.5 ± 3.2	132.3 ± 3.4	20.2 ± 4.7
IP-S (S-200 µm)	141.0 ± 0.4	151.0 ± 3.7	135.0 ± 4.1	16.0 ± 5.5
IP-S (S-250 µm)	142.9 ± 0.2	153.7 ± 2.5	137.7 ± 3.1	16.0 ± 4.0
IP-S + PFOCTS (S-150 µm)	140.8 ± 0.3	154.5 ± 4.4	136.0 ± 4.0	18.5 ± 6.0
IP-S + PFOCTS (S-200 µm)	142.4 ± 0.8	153.4 ± 3.3	139.4 ± 2.7	14.1 ± 4.2
IP-S + PFOCTS (S-250 µm)	143.9 ± 0.4	153.5 ± 2.1	140.4 ± 1.6	13.1 ± 2.7

3. Numerical Methods

The numerical methods used are identical to the equations employed in Chapter 3.2.2, and Chapter 4.2.2. Specifically, the Volume-of-Fluid method and the mass and momentum conservation equations (Equation 4.12 and 3.13-3.15) are utilized to establish the volume fraction of each phase at the corresponding cell as well as the velocity field in order to calculate the velocity and pressure of each phase. Additionally, the CSF and wall adhesion model (Equation 3.16-3.18 and 4.14) are introduced to prescribe the surface tension force at the liquid-vapour interface and to also incorporate the effect of the surfaces' intrinsic contact angle. Finally, the Courant number and Compressive scheme (Equation 3.25-3.26) is applied. The Compressive scheme is used in this case as using sharper discretisation schemes may result in spurious oscillations at the liquid-gas interface. These instabilities typically proliferate throughout the flow (for example, during droplet spreading and receding) and produce fictitious flow instabilities.[2] Furthermore, the unsteady-state variable in the continuity equations is solved implicitly using the bounded second-order implicit method. Combining this with the Compressive scheme produces a stable robust liquid-gas interface, as the diffusive zone near the interface is decreased. As noted formerly, this will further lessen any conjured flow fluctuations. It should be noted that a droplet will induce a shock pressure that is generated upon impact. Due to the sudden rise in pressure, a capillary wave is generated at the liquid-solid interface which propagates against the direction of impact.[3] To appropriately apprehend the capillary wave without creating flow instability, a Courant number of 0.2 was set,[1] where the time-step routinely alters its value to satisfy this condition by utilizing an adaptive time-stepping method.

As noted in Chapters 3 and 4, the coupling of the pressure and velocity equations are conducted using the PISO method where the calculations (or iterations) are repeated until

the mass and momentum equations contain a normalized residual value of $\leq 10^{-3}$. A second-order upwind scheme is implemented alongside to discretise the continuity equations which enhances the accuracy of the solution.

4. Fabrication of Doubly Re-entrant Pillars

The configured doubly re-entrant pillars were designed using Autodesk 360 fusion and saved as a stereolithography file (STL), which was imported into Describe (Version 2.7, Nanoscribe GmbH, Germany) to prepare for laser lithography via a Nanoscribe Photonic Professional GT+ 3D printer. For all 3D printing processes of the doubly re-entrant pillars, a commercially available liquid photoresin (IP-S, Nanoscribe GmbH, Germany) was utilised. The photoresin was first applied onto indium tin oxide coated glass substrates (ITO glass). A 25x/NA 0.8 objective lens (Carl Zeiss AG, Germany) was then used to construct the pillars from the photoresin. The printing process was carried out with a piezo setting time of 10 ms, galvo acceleration of 10 V/s^2, stage velocity of 200 μm/s, laser power of 100 mW, and scan speed of 100 mm/s. The slicing and hatching distances were 1 μm and 0.5 μm, respectively, when the solid printing mode was used with no contour count and a base slice count of 2.

Following the printing process, the structures were developed in propylene glycol methyl ether acetate (PGMEA) for 20 minutes, followed by development in isopropyl alcohol (IPA) for 5 minutes. After the completion of the development process, the pillars were then air-dried at room temperature. By using scanning electron microscopy (SEM) imaging, the 3D printed objects were visually examined for their consistency in terms of their dimensions and overall structure. To improve the quality of the images, the structures were coated with gold before being observed using SEM.

To hydrophobize the surfaces, the fabricated doubly re-entrant pillars were placed in a vacuum desiccator at room temperature with 30 µL of (trichloro (1H,1H, 2H, 2H-perfluorooctyl) silane (PFOCTS) (97%, Sigma Aldrich) placed on a glass slide next to the surfaces for 90 minutes to allow chemical vapour deposition to occur. Once coated, the surfaces were removed from the vacuum desiccator and left overnight for 20 hours. This further increased the intrinsic contact angle to 112.9° ± 4.9° from 70.7° ± 1.0°, as shown in **Table B.2**. For simplicity, the intrinsic contact angle was rounded up to 120° to represent the doubly re-entrant pillars that had been hydrophobized.

5. How Micro-Pillars Repel Impacting Droplets

If the total impacting pressure is greater than the breakthrough pressure, the liquid droplet will penetrate through the interstices and flood the surface. In order to design pillars that prevent surface flooding, the breakthrough pressure should be pre-determined to be higher than the total impacting pressure. Simplifying the problem for a liquid column under capillary action, the critical breakthrough pressure (P_c) is defined as:

$$P_c = \frac{F_c}{A_c} \tag{B.1}$$

F_c is the capillary force (N), and A_c is the capillary area (m). Assuming the capillary is balanced under the weight of the liquid and taking into account of the pillars' overhang angle (relative to the interface), the capillary force is written as $F_c = \gamma_{lv} L_c \cos(\theta_e - (\theta_Y - 90°))$ where L_c is the capillary perimeter (m) and θ_e is the overhang angle (°). Inserting the capillary force into the breakthrough pressure equation above gives:[4,5]

$$P_c = \frac{\gamma_{lv}\, L_c \cos(\theta_e - (\theta_Y - 90°))}{A_c} \tag{B.2}$$

By simplifying the problem for a unit pillar cell configuration (4 × 4), where the liquid forms a meniscus at the centre of impact, the dashed area as highlighted in **Figure B.3** is described as the capillary area. Furthermore, the perimeter of the capillary can be determined from taking the total length of the meniscus along the contact lines of the solid-liquid and liquid-gas interfaces.[4]

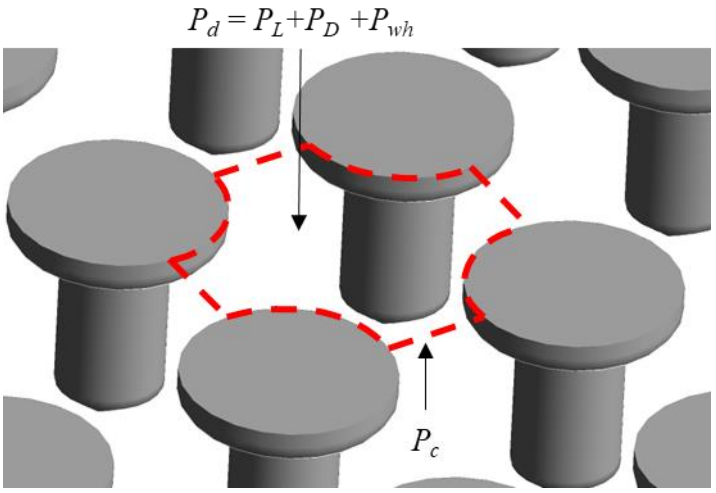

Figure B.3. Doubly re-entrant unit cell array highlighting the liquid-solid interface of the capillary area during droplet impaction. The working pressures involve the Laplace pressure (P_L), dynamic pressure (P_D), water hammer pressure (P_{wh}) and the breakthrough pressure (P_c).[1,6]

The pressures as aforementioned in the diagram will be explained within the chapter. Notably, the capillary perimeter and area are distinctive to the geometry of the pillars. Firstly, for circular pillars in a rectangular pattern as a unit cell, the capillary perimeter is given as $L_c = \pi D$ with the capillary area being equal to $A_c = S^2 - \frac{\pi D^2}{4}$ and the pillars' overhang angle equal to 90°. Substituting into the breakthrough pressure equation gives:[4,7]

$$P_{c,p} = \frac{4\pi D \gamma_{lv} \cos\theta_Y}{4S^2 - \pi D^2} \qquad \text{(B. 3)}$$

where $P_{c,p}$ is the breakthrough pressure for circular straight pillars (Pa). For re-entrant pillars, the capillary perimeter and area are given to be the same as circular pillars, except that the overhang angle is equal to 0°. Therefore, the breakthrough pressure for re-entrant pillars, $P_{c,re}$, is given as:

$$P_{c,re} = \frac{4\pi D\gamma_{lv} \sin\theta_Y}{4S^2 - \pi D^2} \quad \text{(B. 4)}$$

Importantly, however, this equation is only valid if $\theta_Y \leq 90°$. To explain why, there are two main wetting phenomena that occur when pillars are under capillary action. These are known as the Canthotaxis and Laplace breakthrough effect. The Canthotaxis effect states that as the hydrostatic pressure of the fluid increases through the capillaries, the apparent contact angle of the meniscus begins to increase up to a critical value where the three-phase contact line (initially pinned at the pillars' edge) begins to slide downwards along the sidewalls. This critical apparent contact angle is given as:[8]

$$\theta_{max} = \theta_Y + (180° - \theta_e) \quad \text{(B. 5)}$$

As a result, partial wetting (where the liquid wicks the cavities but does not wet the projected area) or homogenous wetting may occur from this effect.[9] On the other hand, the Laplace breakthrough effect is given when the pressure difference between the droplet and the capillary is greater than the breakthrough pressure before reaching the maximum apparent contact angle. This causes the meniscus to bulge further into the cavity whilst the three-phase contact line remains to be pinned. As a consequence, the penetration depth of the liquid-gas interface is now dependent on the surface tension force and the pitch of the interstice. To summarise, two boundary conditions can be derived to determine the stability of the wetting state: if $\theta_Y \leq \theta_e + 90°$, the Canthotaxis effect will take place; but if $\theta_Y > \theta_e + 90°$, the Laplace breakthrough effect will occur.[5] Regarding the

breakthrough pressure equation for re-entrant pillars, if the θ_Y > 90°, the Laplace breakthrough effect will take place therefore reducing the equation to:

$$P_{c,re} = \frac{4\pi D\gamma_{lv}}{4S^2 - \pi D^2} \tag{B.6}$$

Furthermore, for doubly re-entrant pillars, the capillary perimeter and area are slightly altered from circular pillars giving $L_c = \pi D'$ and $A_c = S^2 - \frac{\pi D'^2}{4}$. Here, D' is given as $D' = D - 2t_o$. As the overhang angle is determined to be -90°, the Laplace breakthrough effect will always take place for any intrinsic contact angle (as $\theta_Y > 0°$) from the Laplace breakthrough condition. Therefore, the breakthrough pressure for doubly re-entrant pillars, $P_{c,dre}$, is given as:

$$P_{c,dre} = \frac{4\pi D'\gamma_{lv}}{4S^2 - \pi D'^2} \tag{B.7}$$

For the case of a sessile droplet placed on a composite interface, the breakthrough pressure only needs to, ideally, overcome the Laplace pressure which is generally stated as:

$$P_L = \frac{2\gamma_{lv}}{R_d} \tag{B.8}$$

For millimetric sized droplets, the effect of the Laplace pressure can be considered to be negligible. Nonetheless, for impacting droplets, additional external pressures are involved, namely, the dynamic pressure derived from Bernoulli's principle ($P_D = \frac{1}{2}\rho_l V^2$) and the water hammer (or shock) pressure. The water hammer pressure is essentially the pressure due to the rapid deacceleration of a liquid which is given as:[10]

$$P_{wh} = W\rho_l cV \tag{B.9}$$

where W is the water hammer pressure coefficient and c is the speed of sound within the liquid (m/s).[6,11] Notably, the water hammer pressure coefficient is mainly determined experimentally which is based on the critical impact velocity that allows the droplet to transition from a non-wetting to a wetting state.[6] However, the coefficient can be estimated based on the pressure balance equation between the breakthrough pressure and the dynamic pressures involved with $P_c = P_D + P_{wh}$. Re-arranging the equation for the shock pressure coefficient gives:[6]

$$k = \frac{P_c - P_d}{\rho_l c V} \tag{B.10}$$

In summary, to prevent the impacting droplet from either partially or fully wetting the composite interface, the net pressure, that is, the total impacting pressure proportional to the droplets' size and velocity must be less than the breakthrough pressure generated from the pillars' dimensions and design ($P_c > P_D + P_{wh} + P_L$).

6. Droplet Impact Imagery

The droplet impact process was experimentally imaged using a high-speed camera (Photron, FASTCAM Mini UX100; image analysis software PFV4). The frame rate of the high-speed camera was 2000 fps with a resolution of up to 1280 x 1024. The volume of the droplet was matched to the value used for the simulations. The height between the syringe that delivered the droplet and the top of the sample surface was adjusted to create a free fall velocity of 0.3-0.34 m/s.

7. Solid Fraction of Doubly Re-entrant Pillars

From **Figure B.3**, the interfacial area is the sum of the planar cross-sectional area and the surface area of the vertical overhang $\pi D\delta/4$ (neglecting t_0).[4] The calculation of the solid fraction is given below:

$$\varphi_s = \frac{\left(\frac{\pi D^2}{16} + \frac{\pi D\delta}{4}\right) \times 4}{S^2}$$

$$\varphi_s = \frac{\pi D^2 + 4\pi D\delta}{4S^2} \quad \text{(B. 11)}$$

8. Interfacial Pressure, Penetration Depth and Spreading Diameter

Figure B.4 displays the wetting area, interfacial pressure and penetration height profiles of the droplet impacting the configurated pillars by varying the width between 100 to 200 µm. As expected, increasing the width causes the maximum and minimum wetting diameter to increase as the droplet struggles to recede once it is fully spread. **Figure B.5** shows the spreading diameter, interfacial pressure, and penetration depth profiles for each of the pitch variations from 150 to 250 µm. The effects of the pillar height against wettability are displayed in **Figure B.6**. To explore the effects of the length of the overhang on droplet repellency of the surface, **Figure B.7** demonstrates the wetting diameter, interfacial pressure, and droplet penetration profiles against various overhang lengths. **Figure B.8** depicts the contact area, interfacial pressure and penetration depth of the droplet for each of the overhang thickness values. **Figure B.9** displays the spreading factor results against contact time for various pitch, height and diameter sizes with an intrinsic contact angle of 105°. The spreading factor (β) is defined as the ratio of the maximum spreading diameter to the diameter of the droplet ($\beta = \frac{\lambda_{max}}{\lambda_c}$).

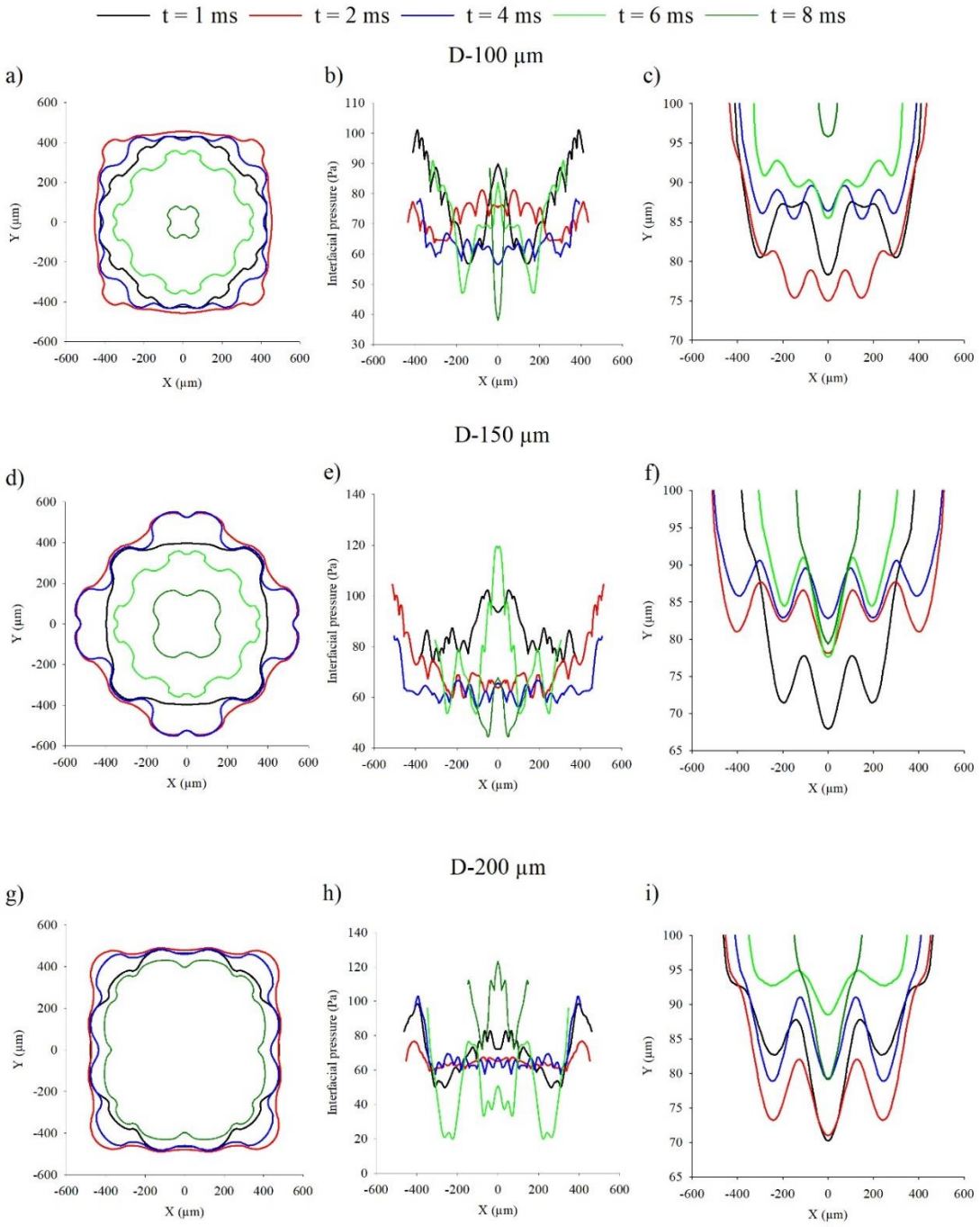

Figure B.4. Plots of contact area (a, d and g), interfacial pressure (b, e and h) and penetration depth (c, f and i) of droplet impacting configurated doubly re-entrant pillars at different timescales for an θ_Y = 105°. (a-c): D=100 µm. (d-f): D=150 µm. (g-i): D=200 µm.

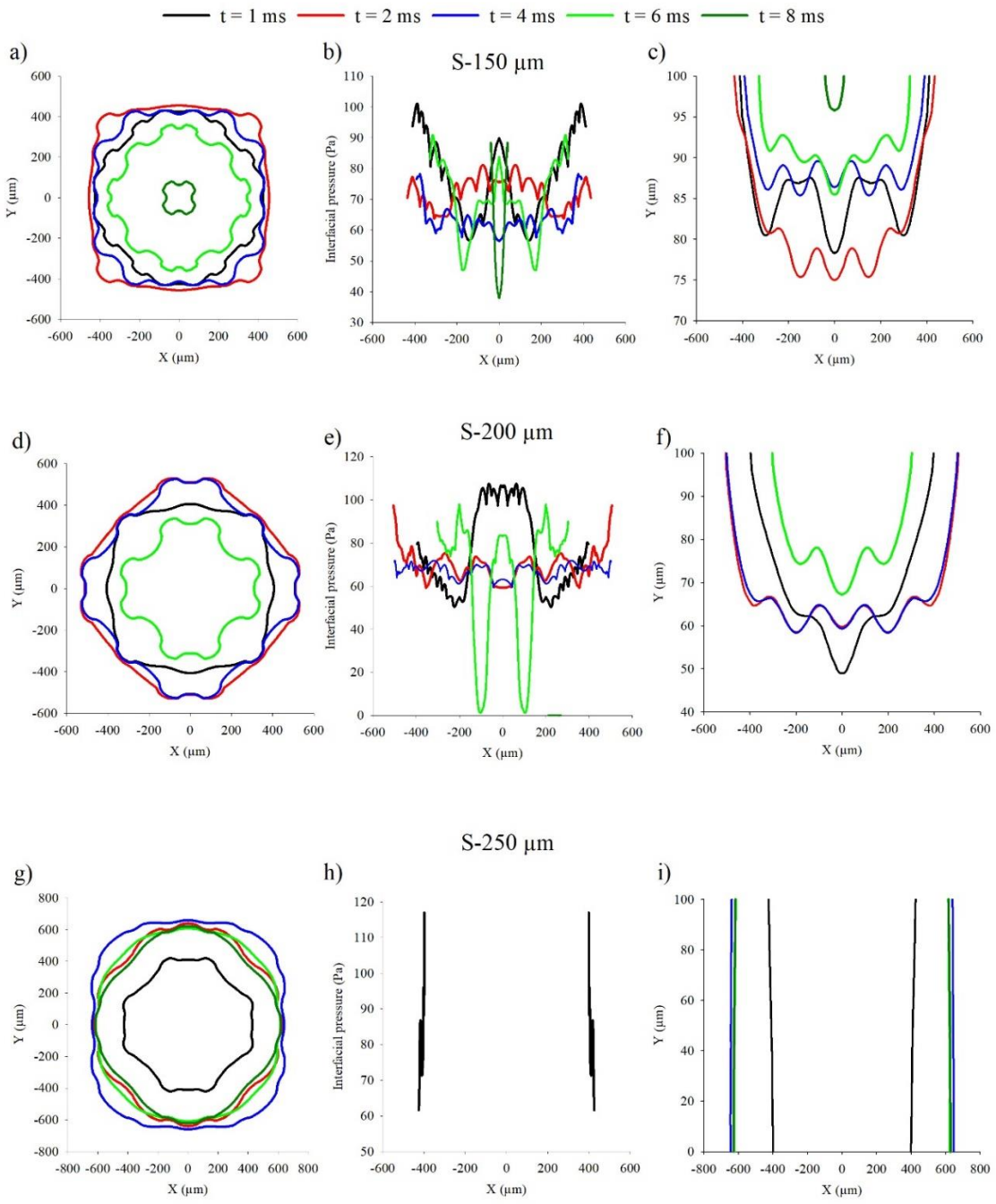

Figure B.5. Plots of contact area (a, d and g), interfacial pressure (b, e and h) and penetration depth (c, f and i) of droplet impacting configurated doubly re-entrant pillars at different timescales for θ_Y = 105°. (a-c): S=150 µm. (d-f): S=200 µm. (g-i): S=250 µm.

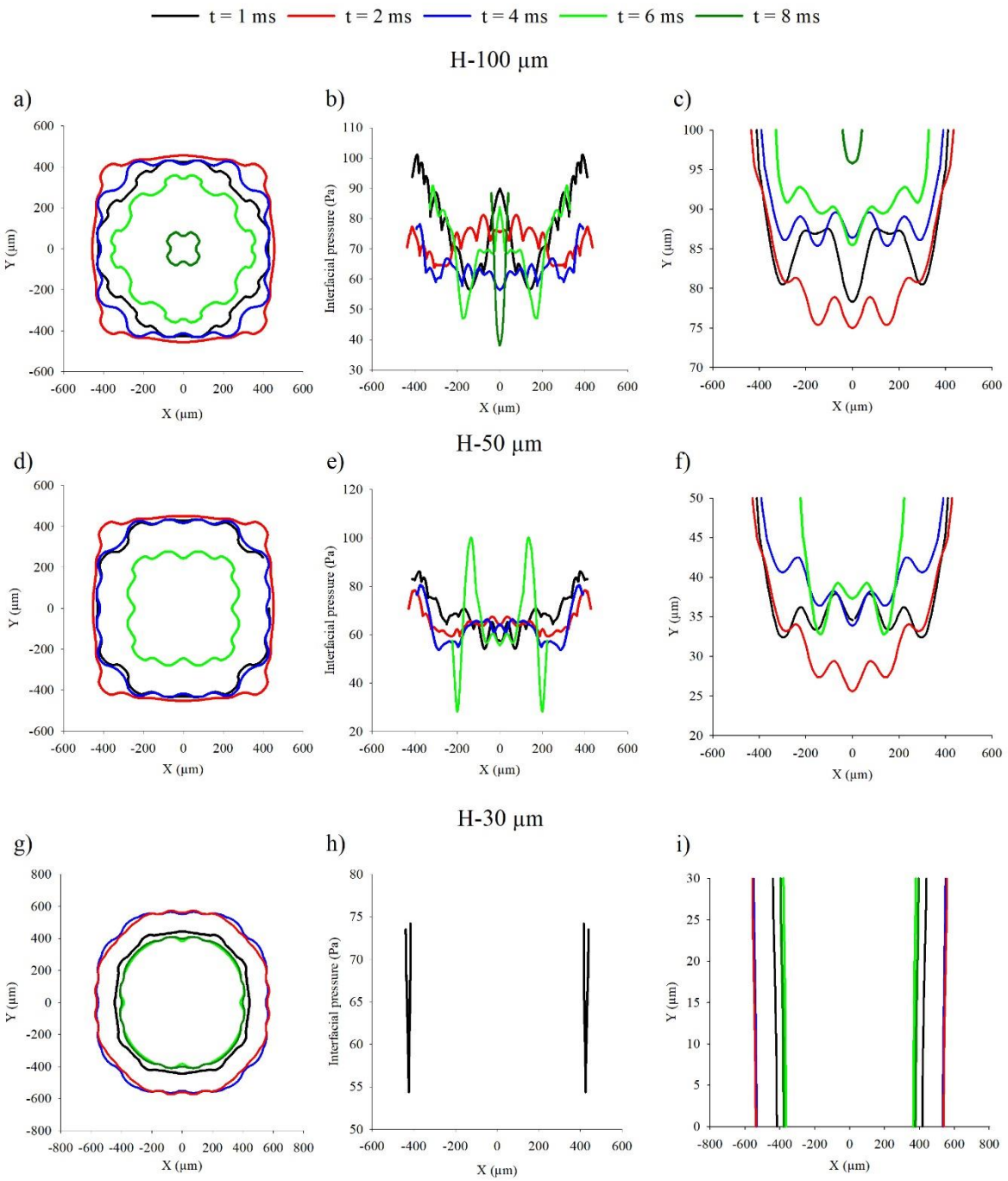

Figure B.6. Plots of contact area (a, d and g), interfacial pressure (b, e, and h) and penetration depth (c, f and i) of droplet impacting configurated doubly re-entrant pillars at different timescales for θ_Y = 105°. (a-c): H=100 µm. (d-f): H=50 µm. (g-i): H=30 µm.

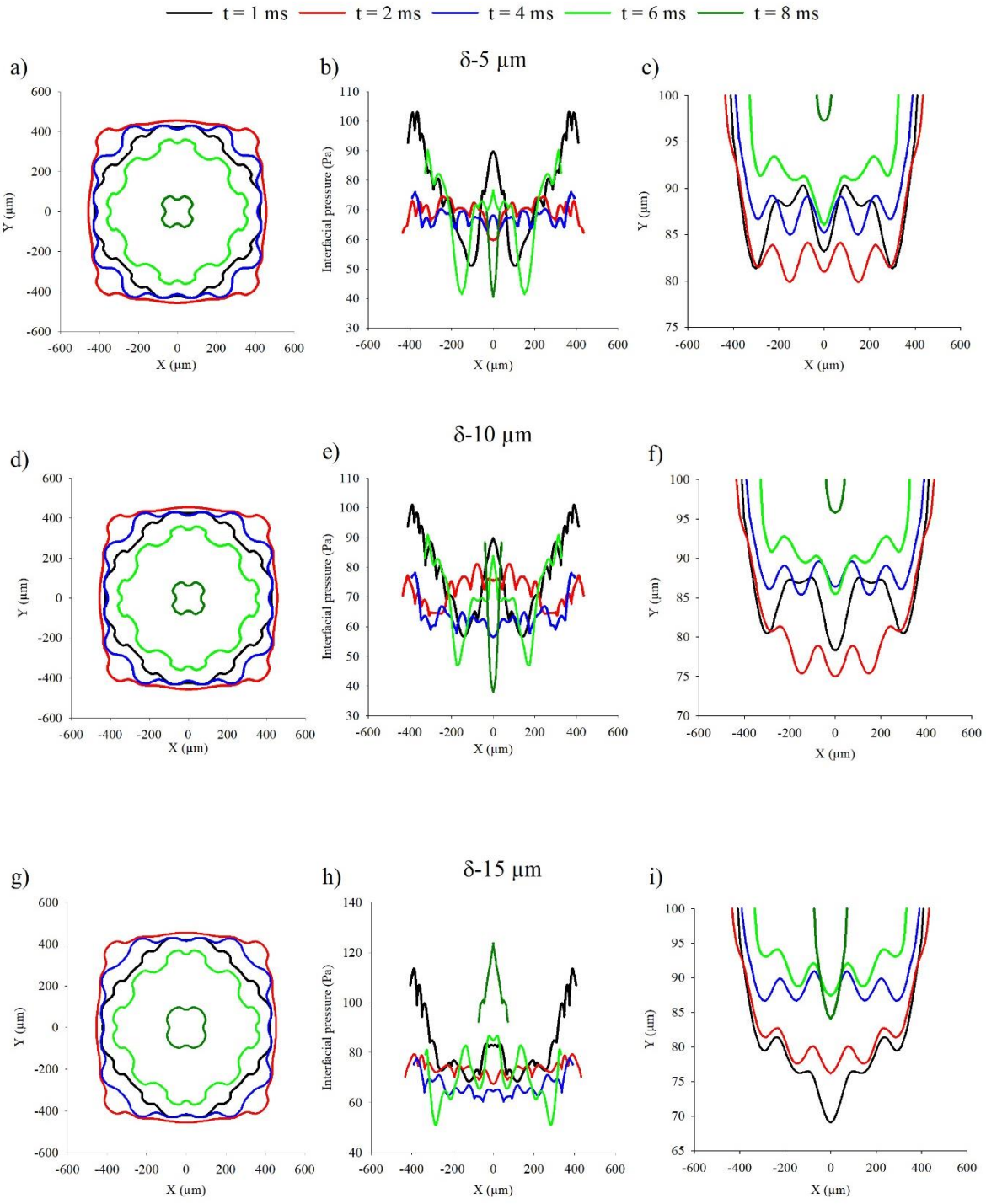

Figure B.7. Plots of contact area (a, d and g), interfacial pressure (b, e and h) and penetration depth (c, f and i) of droplet impacting configurated doubly re-entrant pillars at different timescales for θ_Y = 105°. (a-c): δ=5 µm. (d-f): δ=10 µm. (g-i): δ=15 µm.

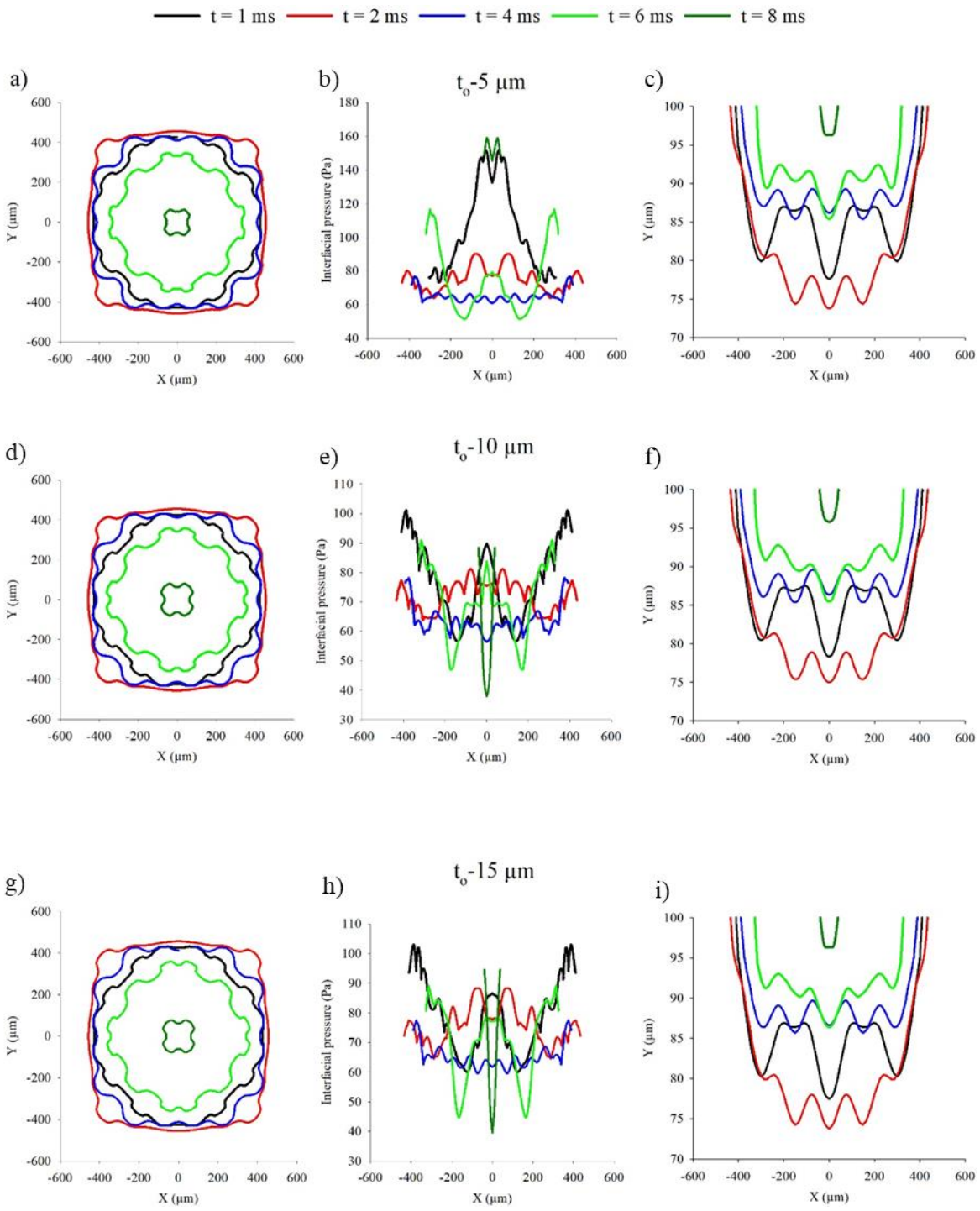

Figure B.8. Plots of contact area (a, d and g), interfacial pressure (b, e and h) and penetration depth (c, f and i) of droplet impacting configurated doubly re-entrant pillars at different timescales for θ_Y = 105°. (a-c): t_o=5 µm. (d-f): t_o=10 µm. (g-i): t_o=15 µm.

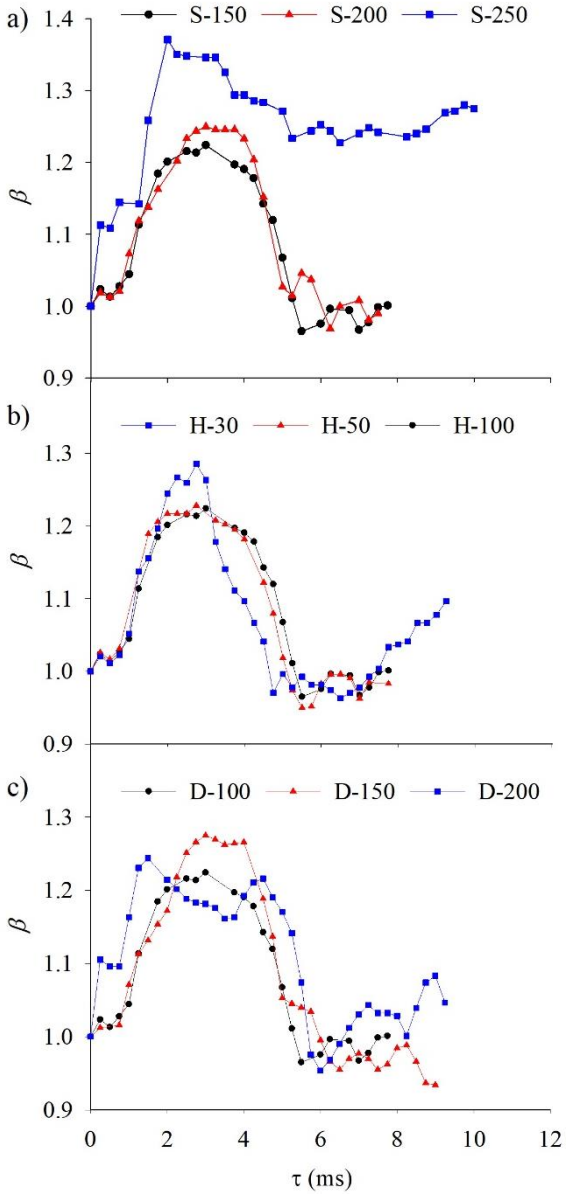

Figure B.9. Spreading factor against contact time for various dimensional sizes of the doubly re-entrant pillars with an intrinsic contact angle of θ_Y = 105°. (a): pitch spacing. (b): height. (c): diameter.

9. References

1. A. Hu, D. Liu, 3D simulation of micro droplet impact on the structured superhydrophobic surface, Int. J. Multiphase Flow 147 (2022) 103887.
2. E. Johnsen, Spurious oscillations and conservation errors in interface-capturing schemes, CTR Ann. Res. Briefs (2008) 115-126.
3. Y. Tatekura, M. Watanabe, K. Kobayashi, T. Sanada, Pressure generated at the instant of impact between a liquid droplet and solid surface, R. Soc. Open Sci. 5 (2018) 181101.
4. A. Torkkeli, Droplet microfluidics on a planar surface, VTT Technical Research Centre of Finland (2003).
5. J. Berthier, F. Loe-Mie, V.-M. Tran, S. Schoumacker, F. Mittler, G. Marchand, N. Sarrut, On the pinning of interfaces on micropillar edges, J. Colloid Interface Sci. 338 (2009) 296-303.
6. S. Dash, M. T. Alt, S. V. Garimella, Hybrid surface design for robust superhydrophobicity, Langmuir 28 (2012) 9606-9615.
7. D. Liao, M. He, H. Qiu, High-performance icephobic droplet rebound surface with nanoscale doubly reentrant structure, Int. J. Heat Mass Transfer 133 (2019) 341-351.
8. J. Oliver, C. Huh, S. Mason, Resistance to spreading of liquids by sharp edges, J. Colloid Interface Sci. 59 (1977) 568-581.
9. R. Hensel, R. Helbig, S. Aland, H.-G. Braun, A. Voigt, C. Neinhuis, C. Werner, Wetting resistance at its topographical limit: the benefit of mushroom and serif T structures, Langmuir 29 (2013) 1100-1112.

10. T. Maitra, M. K. Tiwari, C. Antonini, P. Schoch, S. Jung, P. Eberle, D. Poulikakos, On the nanoengineering of superhydrophobic and impalement resistant surface textures below the freezing temperature, Nano Lett. 14 (2014) 172-182.

11. D. Hee Kwon, S. Joon Lee, Impact and wetting behaviors of impinging microdroplets on superhydrophobic textured surfaces, Appl. Phys. Lett. 100 (2012) 171601.